Battery Electrical Vehicles-Analysis of Thermal Modelling and Thermal Management

Ahmadou Samba

To cite this version:

Ahmadou Samba. Battery Electrical Vehicles-Analysis of Thermal Modelling and Thermal Management . Electric power. LUSAC (Laboratoire Universitaire des Sciences Appliquées de Cherbourg), Université de caen Basse Normandie; MOBI (the Mobility, Logistics and Automotive Technology Research Centre), Vrije Universiteit Brussel, 2015. English. NNT : 2015CAEN2003 . tel-01298416

HAL Id: tel-01298416
https://hal.science/tel-01298416v1

Submitted on 5 Apr 2016

UNIVERSITÉ DE CAEN BASSE NORMANDIE
U.F.R. de Sciences
Ecole doctorale *SIMEM*

THÈSE

présentée et soutenue le : *26/03/2015*
par

Ahmadou SAMBA

En vue de l'obtention du

DOCTORAT de l'UNIVERSITÉ de CAEN
Spécialité **:** *Génie Electrique*

préparée dans le cadre d'une cotutelle internationale de thèse
entre l'Université de Caen Basse-Normandie et Vrije Universiteit Brussel/Belgique

---

Battery Electrical Vehicles- Analysis of Thermal Modelling and Thermal Management

---

Contribution à la Modélisation et à la Gestion Thermique des Batteries Lithium-Ion pour des Applications de Véhicules Electriques

---

Jury
Daniel Hissel, Professeur, Université de Franche-Comté (Rapporteur)
Brayima Dakyo, Professeur, Université du Havre (Rapporteur)
Stéphane Raël, Professeur, ENSEM Nancy
Hasna Louahlia-Gualous, MCF-HDR, Université de Caen Basse-Normandie
Noshin Omar, Professeur, Vrije Universiteit Brussel/Belgique
Joeri Van Mierlo, Professeur, Vrije Universiteit Brussel/Belgique
Hamid Gualous, Professeur, Université de Caen Basse-Normandie, (directeur de thèse)

Composition of the Jury

Chairman of the jury:

- Professor **Annick Hubin**: Vrije Universiteit Brussel – Research Group Electrochemical and Surface Engineering (SURF), Belgium

Vice-Chairman of the jury:

- Professor **Rik Pintelon**: Vrije Universiteit Brussel – Department of Fundamental Electricity and Instrumentation (Vakgroep Elektriciteit – ELEC), Belgium

Promoters:

- Professor **Joeri Van Mierlo**: Vrije Universiteit Brussel – Research Group Mobility and Automotive Technology (Vakgroep Electrotechniek en Energietechnologie – ETEC), Belgium
- Professor **Hamid Gualous**: Université de Caen Basse Normandie, Laboratoire Universitaire des Sciences Appliquées de Cherbourg (LUSAC), France
- Professor **Noshin Omar**: Vrije Universiteit Brussel – Research Group Mobility and Automotive Technology (Vakgroep Electrotechniek en Energietechnologie – ETEC), Belgium

Secretary of the jury:

- Professor **Peter Van den Bossche**: Vrije Universiteit Brussel – Research Group Mobility and Automotive Technology (Vakgroep Electrotechniek en Energietechnologie – ETEC & Vakgroep Industriële Wetenschappen - INDI), Belgium

Members of the jury:

- Professor **Daniel Hissel**: Université de Franche-Comté, Franche-Comté Electronique, Mécanique, Thermique et Optique - Sciences et Technologies (FEMTO-ST), France
- Professor **Brayima Dakyo**: Université du Havre, Groupe de Recherche en Electrotechnique et Automatique du Havre (GREAH), France
- Professor **Hans Jürgen Seifert**: Karlsruhe Institute of Technology, Institute for Applied Materials – Applied Materials Physics, Germany

- Professor **Hasna Louahlia-Gualous**: Université de Caen Basse Normandie, Laboratoire Universitaire des Sciences Appliquées de Cherbourg (LUSAC), France
- Professor **Stéphane RAEL** : Ecole Nationale Supérieure d'Electricité et de Mécanique Nancy, Groupe de Recherche en Électrotechnique et Électronique de Nancy (GREEN), France
- Assistant Professor **Tala-Ighil Boubekeur** : Université de Caen Basse Normandie, Laboratoire Universitaire des Sciences Appliquées de Cherbourg (LUSAC), France

Acknowledgments

First and foremost, I offer my sincere gratitude to my supervisors Prof. Hamid Gualous, Prof. Joeri Van Mierlo and Prof. Noshin Omar for offering me the opportunity to perform a joint PhD between the Vrije Universiteit Brussel and the University of Caen and for their continuous support and motivation during my year of research. Without their enthusiasm, inspiration and expertise, this thesis would not have been possible.

Special thanks go to Prof. Noshin Omar, for his help, encouragement and the fruitful discussion during the hardest time of my year research. Furthermore, I would like to thank Prof. Peter Van den Bossche, Prof. Noshin Omar and Prof. Joeri Van Mierlo for all the time that they spent in reviewing and correcting the manuscript.

I would also like to extend my appreciation to the Jury members for their comments and suggestions during the private defense.

Special thanks goes to Tala-Ighil Boubekeur for his guidanceduring the first part of my PhD and his support for designing the battery tester in LUSAC laboratory and Jelle Smekens for translating the summary of my PhD into Dutch.

I also wish to express my warm thanks to my colleagues at ETEC department: Omar Hegazy, Mohamed Monem, Yousef Firouz, Odile Capron, Thierry Coosemans, Alexandros Nikolian, Joris De Hoog, Shovon Goutam, Elisabeth Leloup, Sylvia Heyvaert, Rahul Gopalakrishnan, Jean-Marc Timmermans, Karel Fleurbaey, Mohamed El Baghdadi, Maarten Messagie, Luis Hernandez, Maria Oliveira, Maitane Berecibar, Nils Hooftman, Surendraprabu Rangaraju, Yang, Cedric De Cauwer for their friendship and the nice working atmosphere they created in the team.

I also would like to thank my colleagues at LUSAC laboratory: Amrane Oukaour, Youssef Slamani, Moataz Elsied, for their friendship and the nice working atmosphere.

Last but not the least; I would like to express my appreciation to my beloved wife, for her love, sacrifice, patience, tolerance and encouragement.

I would like to express my deepest gratitude and sincere appreciation towards my parents, brothers, sisters, and relatives for their love, support and encouragement.

Finally, I would like to dedicate my dissertation to my godfather Ahmadou Kane.

Brussels, March 2015

Table of Contents

List of Figures

List of Tables

List of Acronyms

ARC	Accelerating Rate Calorimeter
BEV	Battery Electric Vehicle
BMS	Battery Management System
BTMS	Battery Thermal Management System
CFD	Computational Fluid Dynamics
CH_4	Methane
CO	Carbon monoxide
CO_2	Carbon Dioxide
COP	Conformity of Production
Ch	Charge
Disch	Discharge
DoD	Depth of Discharge
DMC	Dimethylene Carbonate
DSC	Differential Scanning Calorimeter
EDLC	Electric Double–Layer Capacitor
ECM	Electrical Circuit Model
EEC	European Economic Community
EMC	Ethyl Methyl Carbonate
EV	Electric Vehicle
EIS	Electrochemical Impedance Spectroscopy
EU	European Union
FDM	Finite Differential Method
FEM	Finite Element Method
FVM	Finite Volume Method
GHG	Greenhouse Gas
HC	hydrocarbons
HEV	Hybrid Electric Vehicle
HPPC	Hybrid Pulse Power Characterization
ICE	Internal Combustion Engine
LFP	Lithium Iron Phosphate
LiBF4	Lithium tetrafluoroborat
$LiCoO_2$	Lithium Cobalt Oxide
$LiFePO_4$	Lithium iron phosphate
$LiMn_2O_2$	Lithium Manganese Spinel Oxide
$LiNiCoAlO_2$	Lithium nickel cobalt aluminum oxide
$LiNiMnCoO_2$	Lithium Nickel Manganese Cobalt Oxide
$LiNiO_2$	Lithium Nickel Oxide
$LiPF_6$	Lithium hexafluorophosphat
$LiTiO_2$	Lithium titanate oxide
LMO	Lithium Manganese Oxide

LTO	Lithium Titante Oxide
LCO	Lithium cobalt oxide
NCA	Nickel Cobalt Aluminum Oxide
NiMH	Nickel–Metal Hydride
NMC	Nickel Manganese Cobalt Oxide
NOx	Mono-Nitrogen Oxide
N_2O	Nitrous Oxide
OCV	Open Circuit Voltage
PC	Propylene Carbonate
PCM	Phase Change Material
PHEV	Plug–In Hybrid Electric Vehicle
PM	Particulate Matter
RESS	Rechargeable Energy Storage System
RoH	Rate of Hybridization
SEI	Solid Electrolyte Interface
SIMPLE	Semi-Implicit Method for Pressure-Linked Equations
SoC	State of Charge
TECM	Thermal Equivalent Circuit Models
TIS	Thermal Impedance Spectroscopy
VRLA	Valve Regulated Lead–Acid

List of Symbols

A_{tab}	Cross section of the tab	(m^2)
A	cross section of the cooling channel	(m^2)
c_1	Concentration of lithium in the active material particles	(mol/m^3)
c_2	Concentration of lithium in the electrolyte	(mol/m^3)
C_{dl}	Electrical double layer capacitance,	(F/m^2)
C_p	Thermal capacitance	(J/kg.K)
c_F	inertial coefficient of liquid state of the PCM	
d_h	hydraulic diameter	
dH	the latent heat	(kJ.kg^{-1})
D_1	Diffusion coefficient of lithium in the solid phase	(m^2/s)
D_2	Diffusion coefficient of lithium in the electrolyte	(m^2/s)
ΔS	Entropy	(J.K^{-1})
$Ea_{D_{s,j}}$	Activation energy for particle diffusion	(J/mol)
$Ea_{R,j}$	Activation energy for reaction	(J/mol)
$\frac{dE}{dT}$	entropy coefficient	(V.K^{-1})
$f_{\pm}$	Average molar activity coefficient	
F	Faraday's constant	(C.mol^{-1})
$F_{gravity}$	body force due to the gravity	(N)
f_D	Darcy friction factor	
h	Convective heat transfer coefficient	(W/m^{2}K)
i_1	Electronic current density in the solid phase	(A/m^2)
i_2	Ionic current density in the liquid phase	(A/m^2)
i_N	Normal inward current density trough the electrode/CC interfaces	(A/m^2)
i_{app}	Total applied current density	(A/m^2)
I	applied current	
J_0	Exchanged current density	(A/m^2)
J_n	Local charge transfer current density	(A/m^2)
k_0	Reaction rate constant	(m$^{2.5}$/mol$^{0.5}$ s)
K	Permeability of the aluminum-foam	(m^2)
L_{PCC}	Positive current collector thickness	(m)
L_P	Positive electrode thickness	(m)
L_S	Separator thickness	(m)
L_{NE}	Negative electrode thickness	(m)
L_{NCC}	Negative current collector thickness	(m)

n	Number of electrons transferred	
N	Total number of single cell	
Nu	Nusselt number	
p	Pressure of the fluid	(Pa)
p_a	atmospheric pressure	(Pa)
Pg	total heat generation	(W.m^{-3})
Pr	Prandtl number	
q	Heat source per volume	(W.m^{-3})
$q_{v,0}$	Volumetric flow rate	(m^3.s^{-1})
r	Radius distance variable of the solid particles	(m)
Re	Reynolds number	
R	Gas constant, 8.314	(J/mol.K)
R_s	Radius of electrode particle	(m)
R′	Internal Resistance of the battery	(Ω)
R''	Electrical resistance	(Ω)
Rth	conductive thermal resistance	(K W^{-1})
Rcon	convective thermal resistance	(K W^{-1})
S_a	Specific surface area	(m^{-1})
S	Cross section	
t	Time	(s)
t_+	Transferring number of Li+	
T	Absolute temperature	(K)
u	velocity vector of liquid state in PCM	(m/s)
v	Averaged fluid velocity	(m/s)
V	Volume	(m^3)
Z	wetted perimeter of the cooling channel	(m)
ε_2	Electrolyte volume fraction	
ε_1	Active material volume fraction	
ϵ	emissivity	
Φ_1	Solid phase potential	(V)
Φ_2	liquid phase potential	(V)
Φ_{cc}	Current collector potential	(V)
α	Charge transfer coefficient	
γ	Bruggeman tortuosity exponent	
η	Local surface overpotential	(V)
σ_1	Electronic conductivity of solid matrix	(S/m)
σ_2	Ionic conductivity of electrolyte	(S/m)
β	thermal expansion coefficient of the liquid state of the PCM	(K^{-1})
φ	volume fraction of liquid state in PCM	
ρ	Density	(kg/m^3)

λ	Thermal conductivity	(W/m.K)
ρ''	Resistivity	(Ω.m)
σ	the Stefan–Boltzmann constant	($Wm^{-2}K^{-4}$)
μ	dynamic viscosity	(Pa.s)

Chapter 0: General Introduction

0. General Introduction

0.1 Goal

Global climate change and air pollution are key challenges for today's human society, affecting our thinking to new technological innovations. Major eco-friendly changes have to be made at each level and in each sector. For the automotive industry, this means that our main way of transport, now mainly based on the ICE (Internal Combustion Engine) has to innovate even more relating to a clean environment. One of the possibilities is the electrification of our fleet of cars, vans, motorcycles, buses, trucks... Hybrid Electric Vehicles (HEVs) and Plug in Hybrid Electric Vehicles (PHEVs) are the first steps to make the transition possible to the fullest electrification (Battery Electric Vehicles (BEVs)) of the automotive sector in the future. BEVs, HEVs and PHEVs today still are facing some technical and economic challenges related to the range, charging time, lifetime and battery cost. The batteries must operate in a certain envelope of voltage, current and temperature for optimal performance and for safety considerations. Regarding temperature, the BTMS (Battery Thermal Management System) is needed to maintain the operating temperature of the batteries within the operational range. The BTMS should be optimized in order to increase its effectiveness and the battery performance and to reduce its complexity, size, weight and cost.

0.2 Outline of performed research work

This PhD is divided in six chapters:

- Chapter 1: Background information

This chapter presents a brief description of the environmental impact of the transportation sector regarding energy consumption and gas emissions. In addition, the state-of-the-art of EVs, HEVs and PHEVs is presented as potential solution of the environmental issues. Furthermore, the characteristics and specifications of the different batteries used in these vehicles are compared and analyzed. Finally, the specifications of some recent commercial vehicles are also reported.

- Chapter 2: State-of-the-Art of Battery thermal management

This chapter is mainly focused on the review of the different battery thermal models that have been developed, their characteristics and their applications. The shortcomings of these models are also described. Furthermore, the different battery thermal management used in the literature is also discussed in depth. Some basic numerical methods and software tools are also analyzed and documented.

- Chapter 3: Electrical-Thermal Model for Large Size Lithium-Ion Cells

In this chapter, a two dimensional electrical-thermal model has been developed in order to investigate and to analyze the temperature distribution over the battery surface. The ANSYS FLUENT software has been used to solve the model development. The model is validated by experimental results. In addition, a new estimation tool has been developed for the estimation of the proposed thermal model parameters. Furthermore, the thermal behavior of the battery has been investigated at different environmental conditions as well as during abuse conditions.

- Chapter 4: Pouch Cell Design: Impact of Tab Location

Following chapter 3, the developed model has been extended to three-dimensional (3D) level and in particular for large lithium iron phosphate oxide (LiFePO4) pouch cells. 3D simulations of the Li-ion battery behavior are highly nonlinear and computationally demanding. Integration of the electrochemical model to the thermal models represents an important step towards accurate simulation of the thermal behavior of Li-ion batteries. Non-uniform temperature, potential and current density through the battery induce non-uniform use of the active material and can have a negative impact on cell performance and lifetime. Different pouch cell designs, with different tab locations, have been investigated in terms of performance, current density, potential and heat distributions. The developed model has been validated against experimental data at different current discharge rates. Afterwards, the electrochemical, thermal and electrical behaviors over each cell design at high discharge current rate (4 I_t) are compared between different design configurations.

- Chapter 5: Numerical Analysis of Different Battery Thermal Management Systems

In this chapter different thermal management strategies such as water cooling and passive cooling using phase change material embedded in an aluminum foam (liquid-solid phase change) have been investigated by using the developed electrochemical-thermal model in chapter 4 coupled with fluid dynamics. The model has been developed in COMSOL Multiphysics. At first, different liquid cooling plate's configurations have been investigated in order to obtain the suitable and efficient cooling architecture, which allows to decrease the temperature and to obtain a more uniform temperature distribution over the surface of the battery cell. Secondly, the performances of the battery thermal management system (BTMS) of a battery module with 10 cells, cooled by the efficient cooling plate architecture have been investigated by varying the cold plate locations. The select BTMS design with the efficient cold plate arrangement is analyzed at different load conditions, liquid inlet (temperature and flow rate), and initial temperature. Finally, the passive cooling using phase change material embedded in an aluminum-foam have been investigated and compared to the liquid cooling method. The impact on the cost of the different solutions are also discussed.

- Chapter 6: Conclusions, Contributions and Future Work

The different results obtained in this PhD are summarized. The added value of this thesis as well as the future work have been discussed.

Chapter 1: Background Information

1. Background Information

1.1 Introduction

Since the urban areas and populations are expanding worldwide [1], the world energy consumption is constantly increasing. The transportation sector in particular is one of the major global consumers of energy. It remains the main driver of economic growth and social opportunities. Between 1990 and 2010, final energy consumption from overall transport in EU-28 have increased by more than 30% as shown in Figure 1.1a. This trend can be explained by the growth in number of vehicles particularly in new member countries of the EU. In addition, transportation in EU-28 remains highly oil dependent, more than 75% are derived from crude oil as illustrated in Figure 1.1b. Because the technology of the transportation sector is still dominated by the conventional internal combustion engine (ICE), which uses mainly gasoline or diesel.

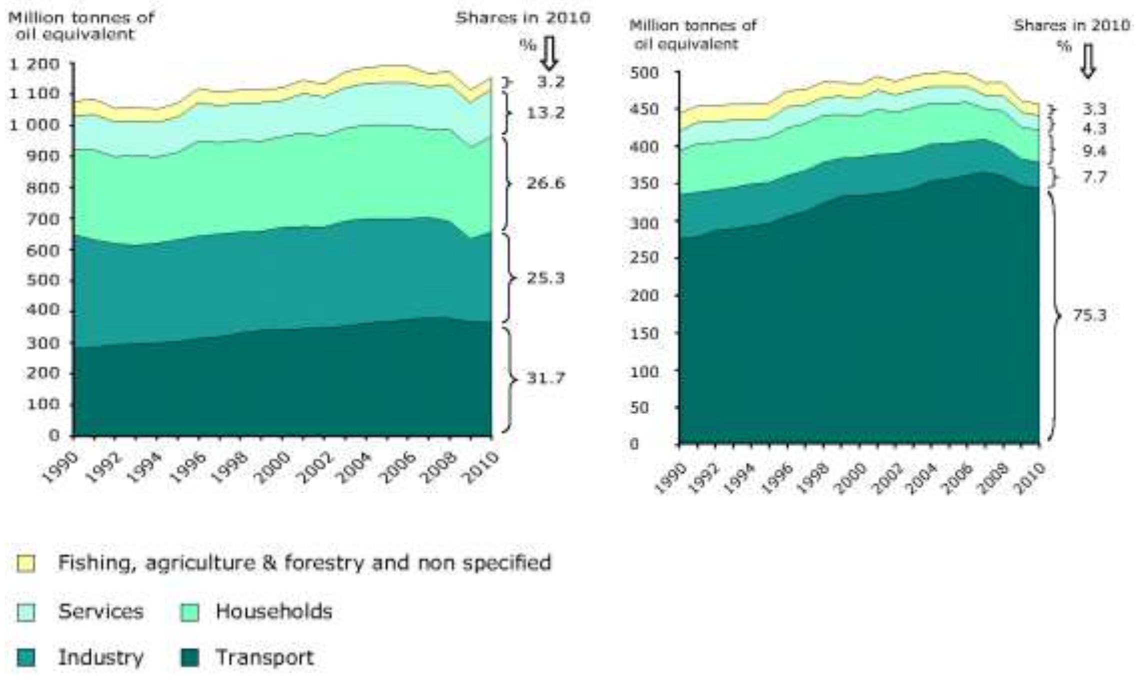
(a) (b)

Figure 1.1: final energy consumption (a) total and (b) petroleum products by sector in the EU-28, 1990-2010 [2]

Furthermore, the transport sector is one of the main contributors of greenhouse gas (GHG) emissions (CO2, CH4 and N2O), representing 25% above level, which has been defined in 1990 [3]. As illustrated in Figure 1.2, from 1990 to 2012, only the GHG emissions from overall transport in the EU-28 are increasing while emissions from others sector are generally decreasing. The GHG emissions are also directly related to the fuel consumption. The greenhouse gas emissions are responsible for the air pollution, which harms human health and environment, and contributed to the global warming.

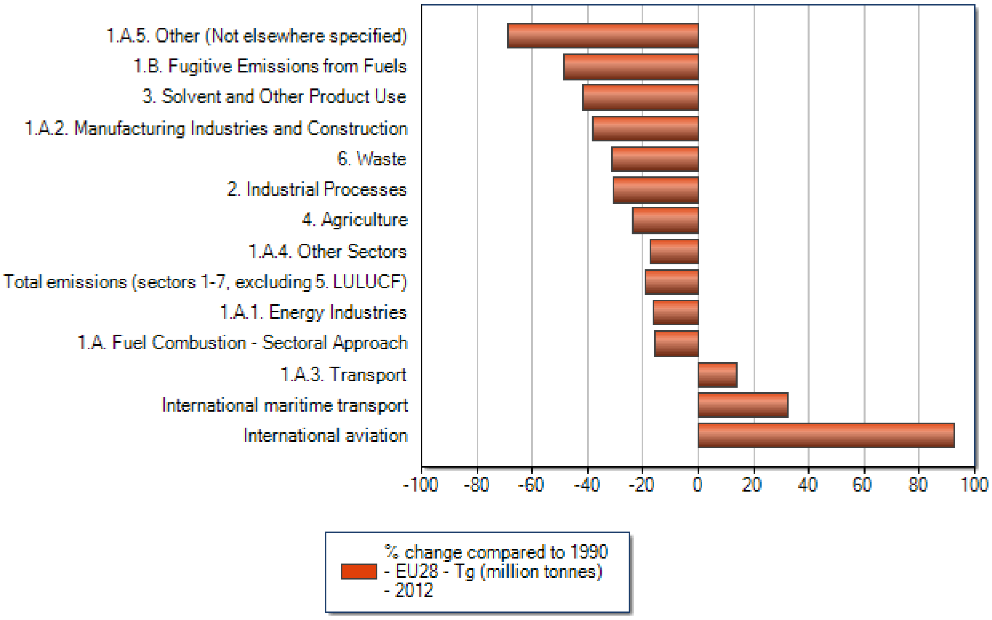

Figure 1.2: change of Greenhouse gas (GHG) emissions from 1990 to 2012 in CO2 equivalents (Tg) by sector in the EU-28 [4].

In the last decade, some efforts are being made to reduce the fuel consumption and GHG emissions in the transportation sector. From the vehicle manufacturers' point of view, this reduction of fuel consumption GHG emissions involved the lightening of the vehicle body structure, the reduction of the aerodynamic drag coefficient and the improvement of engine efficiency. Beside, from a political point of view, several European policies and regulations have been established aiming at the reduction of GHG emissions from transport. Among the well-known, one can mention:

- The council directive 70/220/EEC [5], introduced in 1970, is related to reduce the air pollution from the engine of motor vehicles,
- The Euro regulations: Different Euro emissions regulations [5]–[9] for light–duty vehicles are introduced. They define the mandatory limit in g/km for a list of

pollutants (carbon monoxide (CO), nitrogen oxides (NOx), hydrocarbons (HC) and particulate matter (PM10)).

To achieve these targets, the transport has to innovate even more related to a clean environment. The vehicles with electric propulsion are considered as an attractive option on the pathway to reduce GHG emissions.

Due to major progress in rechargeable energy storage system (RESS), the sales of vehicles with electric operation mode are expected to increase. The overall target of a 50% reduction in global energy-related CO2 emissions by 2050 [10] compared to 2005 levels can be achieved by performing annual sale of about 50 million of electrical vehicles by 2050 as shown in Figure 1.3.

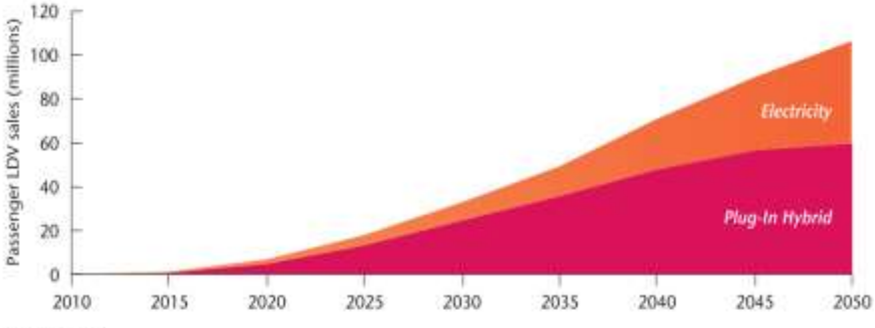

Source: IEA 2010.

Figure 1.3: Annual global EV and PHEV sales [11]

1.2 Alternative powertrains

1.2.1 Hybrid Electrical Vehicles (HEVs)

Hybrid Electric Vehicles (HEVs) are the first steps to make the transition possible to the fully electrification of the automotive sector in the future. In principle, there are two energy sources in HEVs: the conventional internal combustion engine (ICE), which uses mainly gasoline or diesel operates in combination with an electric motor generally powered by battery or a combination of battery and electrical double-layer capacitors (EDLCs). The HEVs have the advantage of reducing the fuel consumption and emissions. The electric motor allows energy recovery to the battery system during braking, provides additional power to assist the ICE during pick power demand, and then allows reducing the size and power of the ICE.

The main hybrid topologies are the series hybrid (Figure 1.4), the parallel hybrid (Figure 1.5) and the series-parallel combined hybrid (Figure 1.6). In the series topology, the traction is obtained by only the electric motor and an ICE works as a generator to power the electric motor or recharge the battery. As the different energy sources are decoupled, the series hybrid has the advantage of operating the ICE only when needed. Thus, it can run at optimum speed and efficiency [12]. However, the disadvantage of the series hybrid topology is that it implies higher losses due to the double energy conversion. This topology is usually used in heavy vehicles (buses, locomotives, military vehicles, etc…).

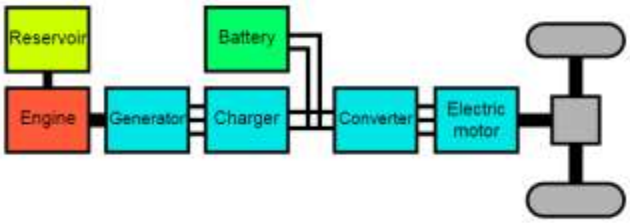

Figure 1.4: Series hybrid topology [12]

In parallel hybrid technology, the traction is obtained through a mechanical coupling of the ICE and the electric motor. They can supply the vehicle traction individually or together. The major advantage of this topology is that the energy loss due to the conversion is small. In addition, it required small traction motor and due to the missing of the generator, the system is compact. Passenger cars usually use the parallel configuration. The main disadvantage is the ICE operation still depending on vehicle speed.

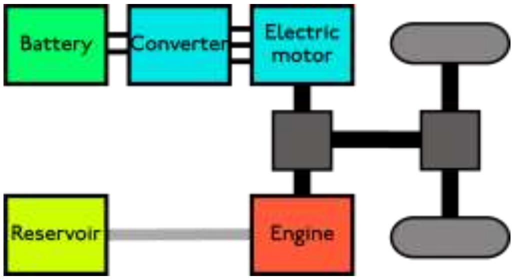

Figure 1.5: Parallel hybrid topology [12]

In the combined hybrid topology, the advantages of previous two topologies are combined. It often makes use of a planetary gear to connect the ICE and the two electric machines with the wheels of the vehicles.

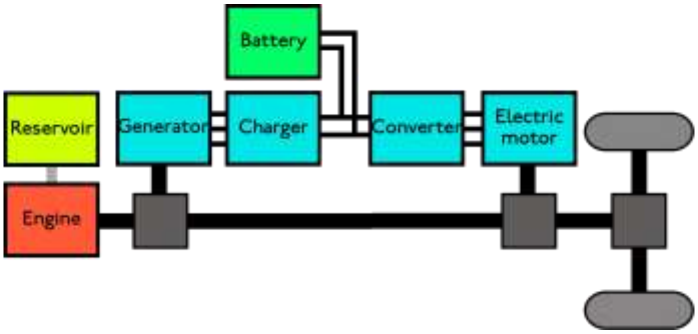

Figure 1.6: Combined hybrid topology [12]

Several hybrid concepts are created based on the rate of hybridization (RoH) [12] such as the Micro-HEVs, the Mild-HEVs, the Full-Hybrid and the PHEVs. According to the RoH, the functions performed by the electric motor are different. The RoH is equal to 1 if the both energy sources (ICE and electric motor) have an equal contribution to the vehicle traction effort. If only one of both energy sources is used, the RoH is equal to zero. Table 1.1 summarized the functions of the different HEVs according to the RoH. In Table 1.2, the performances and characteristics of different commercial HEVs, from the manufacturer values, are compared.

System	Function				
	Stop & Start	Electric traction	Regenerative Braking	Electric driving only	External Battery Charge
Conventional vehicle (ICE)	Possible	No	No	No	No
Micro-HEV	Yes	No	Minimum	No	No
Mild-HEV/medium HEV	Yes	Limited	Yes	Minimum	No
Full HEV	Yes	Yes	Yes	Yes	No
PHEVs	Yes	Yes	Yes	Yes	Yes

Table 1.1: Different HEVs types and their main functions/Characteristics [13]

1.2.2 Plug-in Hybrid Electric Vehicles (PHEVs)

The PHEVs are based on the three basic hybrid topologies described above. They are generally using with high capacity batteries, with a typically energy content up to 15 kWh, for passenger cars that can be charged externally from the power grid. They can store enough electricity to decrease significantly the petroleum consumption. This allows having an all electricity range from 15 to above 100 km [14]. In Table 1.3, the performances and characteristics of different commercial PHEVs, from the manufacturer values, using Lithium ion battery, are compared. The charging can be standard charge (220V, 10 or 16 A) or Fast charge (400V, 32 or 63 A) [13].

1.2.3 Battery Electric Vehicles (BEVs)

Battery Electric Vehicles (BEVs) are using an electric motor powered by the battery packs for traction. With the advancement of new battery technology, such as Lithium ion battery, BEVs become more attractive. They are expected to perform more acceleration with a speed up to 200 km/h and ranges up several hundred kilometers with top-range commercial BEV such as the Tesla [13]. In Table 1.4, the performances and characteristics of different commercial BEVs, from the manufacturer values, using Lithium ion battery, are compared. The BEVs can be recharged at home through a standard 230V connection, or at charging station, or wireless charging with inductive technology.

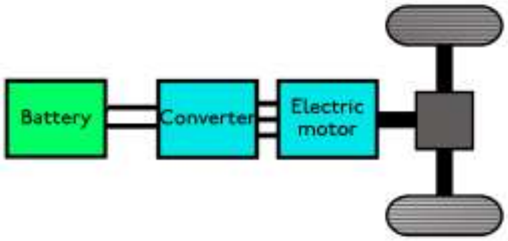

Figure 1.7: Battery electric vehicle topology [12]

Model	Battery type	Energy content (kWh)	Electric motor power [kW]	Electric range [km]	Max vehicle speed in pure electric [km/h]	Battery thermal management
Audi Q5 Hybrid (Full HEV)	Li-ion (266V/5Ah)	1.3	40	3	100	Air-cooling
BMW ActiveHybrid 3 (Full HEV)	Li-ion (317V/2Ah)	0.675	41	4	70	Air-cooling
BMW ActiveHybrid 5 (Full HEV)	Li-ion (317V/2Ah)	0.675	40.5	4	60	Air-cooling
BMW ActiveHybrid 7 (Mild HEV)	Li-ion (120V/6.6Ah)	0.8	15	4	60	Liquid-cooling
Nissan Infiniti M35h (Full HEV)	Li-ion (346V/3.7Ah)	1.4	50	No data available	80	Air-cooling
Mercedes S400 Class Hybrid (Mild HEV)	Li-ion	0.8	20	No data available	No data available	Air-cooling

Table 1.2: Prototypes/commercial HEVs [13], [15]

Model	Battery type	Energy content (kWh)	Electric motor power [kW]	Electric range [km]	Max vehicle speed in pure electric [km/h]	Battery thermal management
Mercedes Vision S500 Plug-in HYBRID (PHEV)	Li-ion	10	85	33	140	Water-cooling
Toyota Prius Plug-in (PHEV)	NiMH	4.4	60	22	100	Air-cooling
Volvo V60 Plug-in Hybrid (PHEV)	Li-ion	11.2	51	49	112	Water-cooling

Table 1.3: Prototypes/commercial PHEVs [13], [15]

Model	Battery type	Energy content (kWh)	Electric motor power [kW]	Electric range [km]	Max vehicle speed [km/h]	Battery thermal management
BMW i3 (EREV)	Li-ion	23	126	225	150	Air-cooling
Chevrolet Spark EV 2014 (BEV)	Li-ion	21	110	130	193	Liquid-cooling
Chevrolet Volt (EREV)	Li-ion	16.5	110	60	160	Liquid-cooling
Citroën C-Zero (BEV)	Li-ion	16	47	150	130	Air-cooling
Fiat 500e (BEV)	Li-ion	24	83	140	115	Liquid-cooling
Ford Focus EV (BEV)	Li-ion	23	108	160	136	Liquid-cooling
Honda FIT EV (BEV)	Li-ion	20	92	130	70	Air-cooling
Mini E (BEV)	Li-ion	35	150	200	152	Air-cooling
Nissan Leaf (BEV)	Li-ion	24	80	175	93	Air-cooling
Peugeot iOn (BEV)	Li-ion	16	47	150	130	Air-cooling
Renault Fluence Z.E. (BEV)	Li-ion	22	70	160	135	Air-cooling
Renault Kangoo Z.E. (BEV)	Li-ion	22	44	160	130	Air-cooling
Renault Zoe Z.E. (BEV)	Li-ion	22	65	160	140	Air-cooling
Toyota eQ (BEV)	Li-ion	12	46	100	125	Liquid-cooling
Volvo C30 (BEV)	Li-ion	21.5	40	150	130	Liquid-cooling

Table 1.4: Prototypes/commercial BEVs [13], [15]

1.3 Lithium-ion battery

Lithium-ion battery (LIB) has received considerable attention for traction uses due to the higher energy density (70-170 Wh/kg), power capabilities, lowest standard reduction voltage (Eo=-3.04V) and low atomic mass compared to previous battery technologies. Figure 1.8 shows the relationship between various types of secondary batteries in a Ragone plot. The required amount of energy stored in PHEVs and EVs is much higher than for HEVs in order to be able to travel long distances in all electric range. In the 2000s, the LIB are considered as one of the most promising solutions for environment-friendly transportation such as HEVs, PHEVs and EVs.

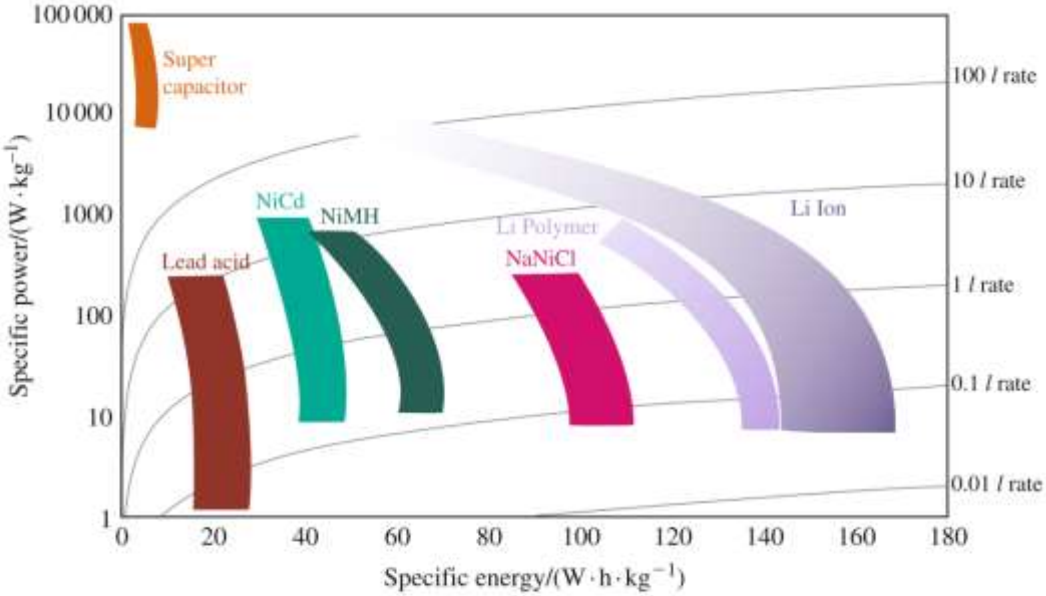

Figure 1.8: Specific energy and specific power of different battery types [16]

Basically, LIB includes different components (cathode, anode, separator and electrolyte) and work according to the so-called “extraction/insertion” process. The LIB cells are configured in various shapes such as coin, cylindrical, pouch and prismatic as shown in Figure 1.9. The basic working principle of the LIB is described in Figure 1.10. During charging lithium-ions are extracted from the cathode and migrate via the electrolyte into the anode. The reverse mechanism occurs during discharging

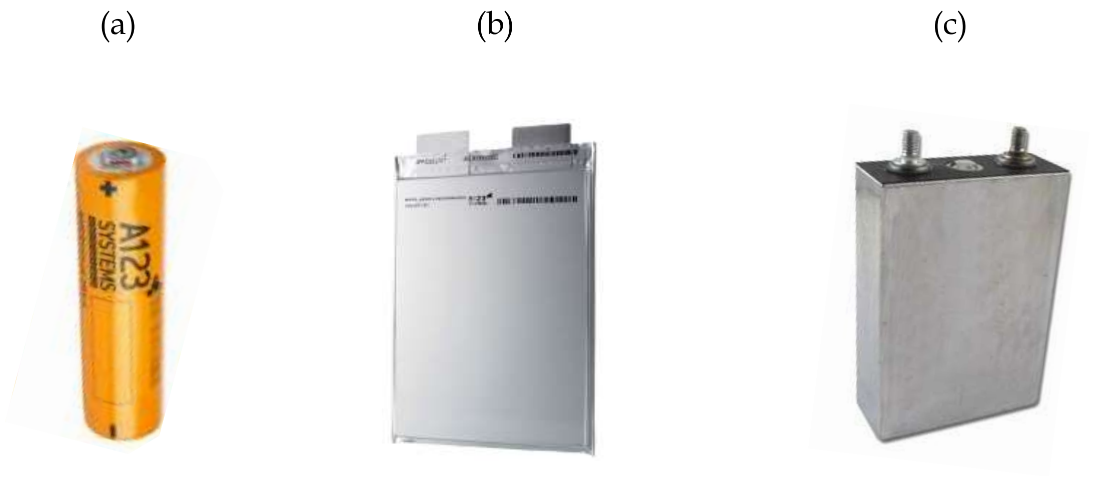

Figure 1.9: Different lithium-ion battery design concepts: (a) cylindrical, (b) pouch and (c) prismatic cells [17]

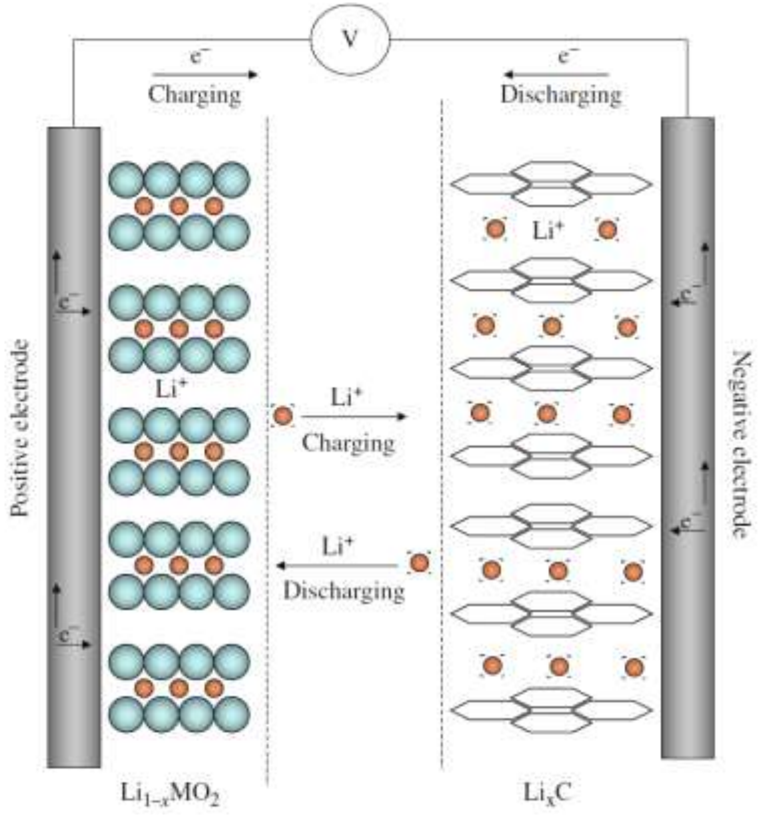

Figure 1.10: working principle of LiB [18]

Based on the used cathode and anode materials, different types of LIB have been adopted and show different performance, cost and safety characteristics.

1.3.1 Cathode material

According to the cathode material, different LIB can be categorized by material crystal structure, including the layered compounds $LiMO_2$, the spinel compounds LiM_2O_4 and the olivine compounds $LiMPO_4$ as illustrated in Figure 1.11. In recent years, new structure intercalation such as silicates Li_2MSiO_4, borates $LiMBO_3$ and tavorites $LiMPO_4F$ compounds are also gaining attention.

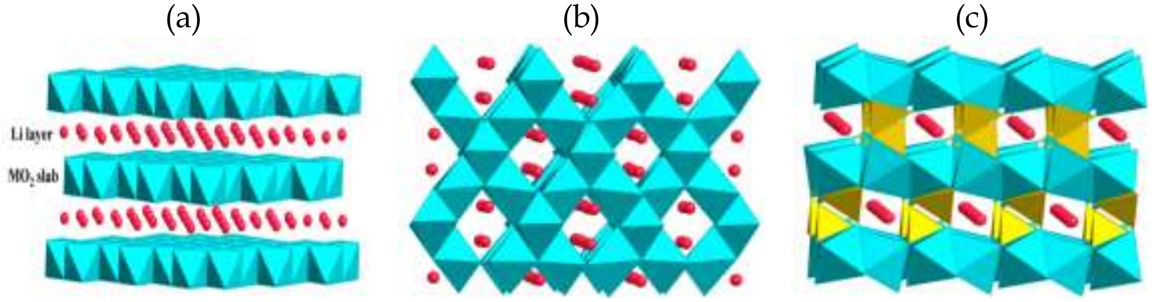

Figure 1.11: crystal structure of: (a) layered, (b) spinel and (c) olivine [19]

For the Layered compounds $LiMO_2$: the transition metal intercalation oxides MO_2 and the Li layers are stacked alternatively. The most common lithium ion candidate taking part to this group are listed below [18], [19]:

- Lithium cobalt oxide ($LiCoO_2$ or LCO): The LCO batteries are widely used in portable applications. The presence of toxic, the high cost and the structural instability of the material that raised some safety issues, are the main disadvantages of this material. The LCO batteries can deliver only 140 mAh/g capacity (compared to 160 mAh/g of theoretical capacity) and are not suitable for HEV and EV applications[19].

- Lithium nickel cobalt aluminium oxide ($LiNi_{0.8}Co_{0.15}Al_{0.05}O_2$ or NCA): in order to improve the stability of the LCO, the nickel has replaced some cobalt atoms because nickel is cheaper than cobalt and then it can reduce the battery cost. Aluminium doping is beneficial to stabilize the charge transfer impedance on the cathode side and improving the electrolyte stability. The NCA has a specific capacity of 200 mAh/g, however the cycle life remains short [19].

- Lithium nickel manganese cobalt oxide ($LiNi_{1/3}Mn_{1/3}Co_{1/3}O_2$ or NMC), which have a specific capacity of 180 mAh/g. The NMC batteries are less costly than the others layers compounds battery due to the presence of the Manganese (Mn).This technology becomes a good candidate for BEVs.

For the spinel compounds LiM_2O_4, in this crystal structure, the Li-ions occupy the tetrahedral sites in the transition metal layers. The spinel Lithium manganese oxide ($LiMn_2O_4$ or LMO) is a promising cathode electrode due to its high operating voltage (3.5-4.5V), lower cost and lower toxicity. They are now powering the Nissan Leaf and the Chevrolet Volt.

For the olivine compound $LiMPO_4$, these crystal structures are receiving more attention because of these stabilities compared to the layered and spinel compounds. Among them, the Lithium iron phosphate ($LiFePO_4$ or LFP) has been proposed as a promising candidate to overcome the weakness of the earlier cathode material. The LFP have an excellent thermal stability, show high cycle life, and are low cost and less toxic. However, the operating voltage (3.3 V) and energy density are rather low.

1.3.2 Anode material

As mentioned above, during discharge the Li ions are intercalated into the anode. The most common anode material are listed below:

- Graphite: due to its high specific capacity of 372mA [20], graphite seems to be the most appropriate anode material. However, graphite-based anodes have some limitation due to the poor performance at low temperature and the formation of a passive solid electrolyte interface (SEI) layer[21]. An SEI layer is formed because lithium intercalation reaction proceeds on graphite at such a low potential that the organic electrolyte, consisting of $LiPF_6$ dissolved in organic solvents, becomes unstable and reacts with the electrode[22]. This layer makes the graphite electrode less reactive towards further decomposition of the electrolyte and the reactions continue to some extent consuming the electrolyte during charging of the battery. Another drawback of a graphite anode, resulting from the low lithium insertion potential, is the deposition of metallic lithium on the electrode surface. This irreversible reaction occurs especially when charging at sub-zero temperatures or using too high a charging rate. Very reactive metallic lithium consumes the electrolyte and may result in dendrite formation and even in internal short-circuiting of the battery.

- LTO [23], [24] is a more ideal insertion material because of its high lithium insertion potential of about 1.55 V versus Li/Li^+ where the electrolyte is more stable and metallic lithium formation thermodynamically less favorable making the battery safer and more durable. LTO has also very small dimensional changes during lithium intercalation/de-intercalation and consequently, mechanical stress during battery cycling is low. As no electrolyte consuming SEI layer is formed and dimensional changes are low, batteries with an LTO anode show long cycle life. However, the specific capacity is only 175 mAh/g and thus the batteries have a low energy density. Because of the high anode potential, batteries with an LTO anode have low operating voltages, comparable to lead acid batteries. LTO has a spinel structure, whereby the surface area is typically much larger than that of carbon-based electrodes [25]. The larger surface area allows moving the electrical charges more quickly. Thus, the LTO does not suffer from high current rates. In the last few years, several companies such as Toshiba, EIG Batteries and Altairnano have begun commercializing this technology.

1.3.3 Electrolyte

In LIB, the lithium-ion migrate from electrode to electrode through the electrolyte. Several requirements must be satisfied by the electrolyte, such as larger ionic conductivity (higher than 10^{-3} S/cm[21]), a stabilized evolution of the solid electrolyte interface (SEI) (interface between electrolyte and electrode) and a higher thermal and electrical stability [22]. Several liquid electrolytes are used in LIB, such as Lithium hexafluorophosphate ($LiPF_6$), Lithium tetrafluoroborate ($LiBF_4$), lithium triflate ($LiSO_3CF_3$) and lithium tris (trifluoromethanesulfonyl) methide ($LiC(SO_2CF_3)_3$) [26]. Due to its higher ionic conductivity, the $LiPF_6$ is mostly used and they are often dissolved on carbonate-based aprotic solvents such as: propylene carbonate (PC), ethylene carbonate (EC), diethyl carbonate (DEC), ethyl methyl carbonate (EMC) or dimethylene carbonate (DMC).

1.3.4 Summary of commercial lithium ion batteries

As shown below, several materials have been adopted for use in commercial lithium ion batteries. The choice depends on the targeted application and the operation conditions. Table 1.5 shows the characteristic list of the most common lithium ion candidates for EV and HEV.

Positive/Negative Electrode Material	Nominal Cell Voltage/V	Specific Capacity
		Positive/Negative/(mA.h.g^{-1})
$LiCoO_2$ (LCO)/graphite	3.7	120/370
$LiMn_2O_4$(LMO)/graphite	3.7	100/370
$LiNiO_2$/graphite	3.7	170-180/370
$LiNi_{1/3}Mn_{1/3}Co_{1/3}O_2$ (NMC)/graphite	3.7	130-160/370
$LiCo_{0.2}Ni_{0.8}O_2$/graphite	3.7	200/370
$LiNi_{0.8}Co_{0.15}Al_{0.05}O_2$ (NCA)/graphite	3.7	180/370
$LiFePO_4$(LFP)/graphite	3.7	150-160/370
$Li_4Ti_7O_{12}$ (LTO)/LFP	3.7	150-160/150-160

Table 1.5: Characteristics of some commercial lithium Ion batteries [18], [27], [28]

1.3.5 Choice of the battery chemistry in this PhD

Due to the availability of the cells in the framework of research project, as well as to the properties of this technology, the lithium iron phosphate battery of 45Ah pouch type cell, as shown in Figure 1.12, was selected as high energy storage component. This cell is manufactured by the European Batteries. The performance parameter characteristics of cell is included in Table 1.6.

Figure 1.12: Pouch cell, European Battery (EB) 45 Ah

Nominal capacity BoL/Ah	45
Nominal Voltage/V	3.2
Max. voltage/V	3.65
Min. voltage/V	2
Weight/kg	0.99
Nominal Energy EoL/Wh	144
Spec. Energy BoL Wh/kg	145
Max. discharge current cont/A	135
Peak Current discharge 10s/A	180
Peak regen. Current 10s / A	90
Peak spec. discharge power 10s W/kg	580
Peak discharge power 10s /W	576

Table 1.6: Characteristics of EB 45Ah lithium Iron Phosphate battery

Chapter 2: General State-of-the-Art of Battery Thermal Management

2. State-of-the-Art of Battery Thermal Management

2.1 Goal

This chapter is mainly focused on the review of the different battery thermal models that have been developed, their characteristics and their applications. The shortcomings of these models are also described. Furthermore, the different battery thermal management used in the literature is also discussed in depth. Some basic numerical methods and software tools are also analyzed and documented.

2.2 Introduction

As mentioned in chapter 1, lithium-ion batteries have emerged as a key energy storage technology and are now the main technology for portable devices. Due to their high potential and their high energy and power densities, and also their good lifetime, they are now the preferred battery technology, which has been able to provide longer driving range and suitable acceleration for electrically propelled vehicles such as Hybrid Electric Vehicles (HEVs), Battery Electric Vehicles (BEVs) and Plug-In Hybrid Electric Vehicles (PHEVs) [16], [29]–[31]. However, cost, safety and temperature performance issues remain obstacles to its widespread application. As known, during the discharge or charge process, various exothermic chemical and electrochemical reactions occur. These phenomena generate heat that accumulates inside the battery and therefore accelerates the reaction between cell components. With higher discharge/charge current rates, the heat generation in a battery increases significantly. If heat transfer from the battery to the surroundings is not sufficient, the battery temperature can rise very fast and exceed the safe temperature range. In the worst-case scenario (Figure 2.1) thermal runaway can occur [32]–[34]. For optimal performance, safety and durability considerations, the battery must operate within the safe operating range of voltage, current and temperature as indicated by the battery manufacturer. Figure 2.1 shows the safe operating window for a typical LiFePO4/graphite cell [35]. The voltage range is between the maximum voltage (3.65V) and the minimum voltage (2V), the temperature range is depending on the operating mode (charge and discharge) and varies between [-20°C; 60°C] and [0°C; 40°C] during discharge and charge, respectively. These ranges can change according to the cell chemistry and battery manufacturer [36].

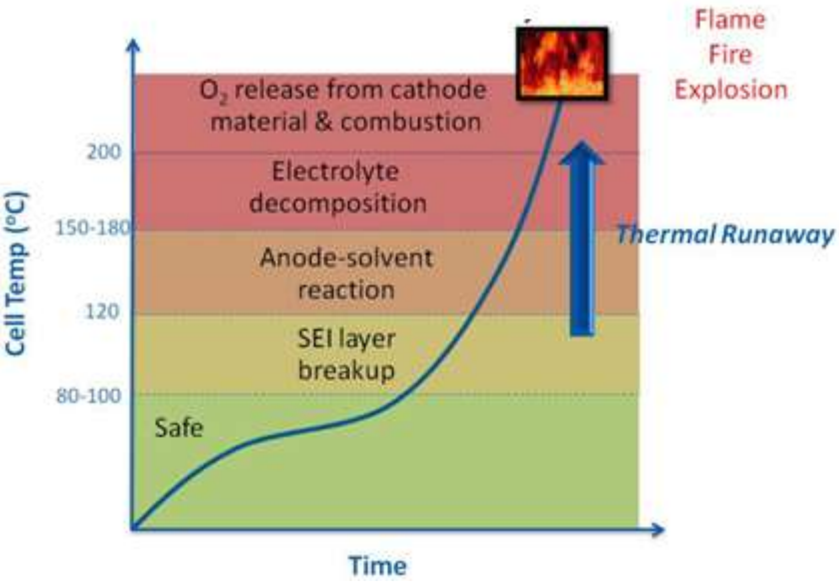

Figure 2.1: Thermal runaway process [37]

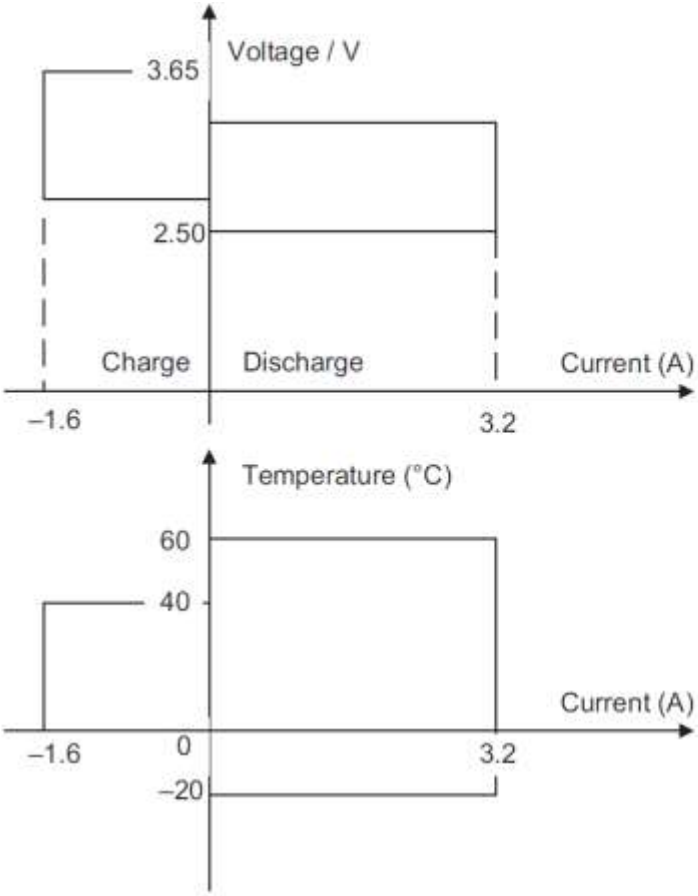

Figure 2.2: An example of a safe operating area of a typical LiFePO4/graphite cell [35]

Regarding the temperature issue, a Battery Thermal Management System (BTMS) as a part of the whole battery system is needed for implementation to maintain the operation temperature of the batteries between those boundaries. The BTMS must be optimized to suit the operational conditions specific for each application. A better understanding, evaluation and comparison of the different BTMS in an objective way is needed to have the optimum battery performances. This would also give the opportunity to make the BTMS smaller, cheaper, compact, efficient, and light, dedicated to its operation area… If less attention is spent on the BTMS, problems could arise around safety, durability and life cycle, range…

In this way the design, evaluation and comparison of BTMSs are crucial for better battery performance and setting future goals on the expectations of BEVs.

This chapter is firstly focused on giving a brief description of the temperature impact on the lithium ion battery cell. Then a review of the different battery thermal models that have been developed and their characteristics are analyzed. Furthermore, the different existing battery thermal management systems used in the literature are also discussed in depth. Some basic numerical methods and software tools are also analyzed and documented.

2.3 Battery thermal behavior, modeling and characterization

2.3.1 Battery geometry, external and internal structures

As shown in chapter 1, commercial lithium-ion batteries can be classified according to cell shape and component materials. The various forms of batteries include cylindrical, prismatic and pouch cells, as illustrated in Figure 2.3. This figure describes the key components in a LIB, such as the cathode active material, the anode active material the current collector (aluminium and copper), the separator the electrolyte and the tab outer casing. Cylindrical cells have spiral wound structure and are easier to manufacture with a good mechanical stability. However, they have relatively a low packing energy density. Prismatic cells have jelly roll or stacked layer structures with high packing efficiency and are more expensive to manufacture. Pouch cells, which could be considered as thin prismatic cells within a flexible enclosure. They have stacked layer structure with higher energy density than the prismatic and cylindrical cell, and provide more flexibility of the design aspect and are relatively less expensive. However, they remain mechanically vulnerable, and require a strong case for the module packaging. As mentioned in chapter 1, section1. 3, all these three types of LIB include several single battery layer with a dimension of 100 microns. Each single battery layer contains different components (cathode, anode, separator and electrolyte) and work according to the so-called "extraction/insertion" process.

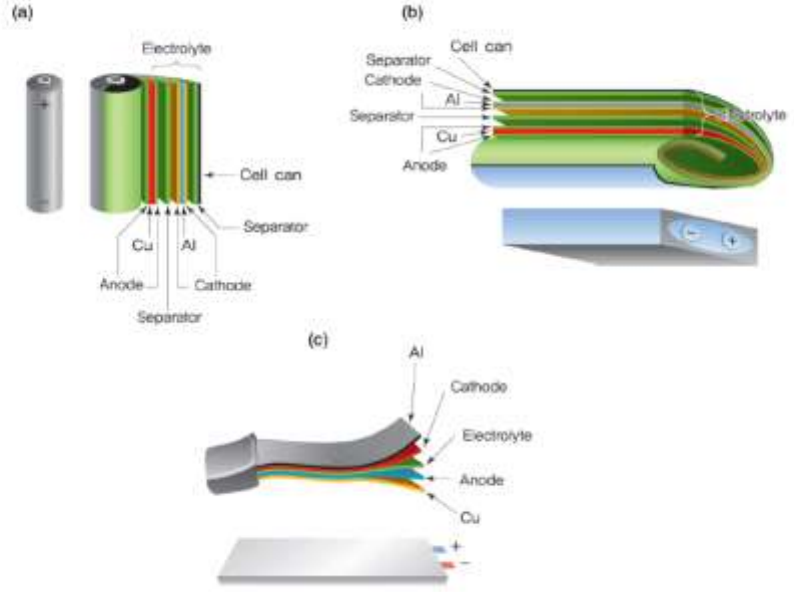

Figure 2.3: Internal structure of the different shape of LIB: (a) cylindrical, (b) prismatic and (c) pouch [38]

2.3.2 Impact of temperature on the battery behaviors

A thermal management system for batteries is needed because of the best optimal temperatures of the batteries do not comply completely with the possible operating temperatures of the vehicle. The best temperature range of ambient temperature for Li-ion batteries is situated between 25°C and 40°C [39], while the operation range of a vehicle is possible between -30°C and 60°C depending on the geographic regions and climatic zones.

Phenomena that occur when the temperature exceeds the prescribed limits are briefly summarized in Table 2.1 [39]. Global trends of battery behaviors are related to the chemistry, design and manufacturer of the battery package. Low temperature induces to the capacity drop and internal resistance increase due to the lower chemical activity. The increase in resistance will result in a higher heat generation. However, high temperature leads to an increase of the internal resistance, to self-discharge and in worst case to thermal runaway. These phenomena may reduce battery performance and lifetime [40]–[42].

Low temperature (<0°C)	- Capacity drop - Internal resistance increase
High temperature (>40°C)	- Internal resistance decrease - Accelerated aging phenomena - Higher self-discharge - Decomposition of electrolyte - Thermal runaway, safety considerations - Reduced life cycle

Table 2.1: Influence of temperature on working principle of batteries: global trends [39]

2.3.3 Effect of cell design on the cell behaviors

Advanced research in the field of rechargeable energy storage (RESS) enables to a wide use of large-format, high-capacity Li-ion cells in PHEVs and EVs. This format has the advantage of reducing the number of cells in the module, increasing the capacity and reducing the size and weight at the pack level. Increasing the current amplitude during the charge/discharge process subjects the large format battery to abuse situations and leads to non-uniform distributions of temperature, potential, current density and heat generation through the cell. Bad design and extreme operation conditions of large format cells may reduce battery performance and lifetime. Therefore, good cell design is necessary to avoid non-uniform distribution of the electrical and thermal parameters. The temperature differences within a cell and amongst the cells in battery pack should be smaller than 5°C [43]. Furthermore, the particle size and the electrode coating thickness have also a significant impact on battery behavior. Recently, Zhao et al [44] showed that small coin cells provide much better performance and energy density than large format cells, where uneven current density is observed, leading to lower utilization of the active material. In addition, the impact of the arrangements and the number of the current collecting tabs are investigated in the cases of wound design [44], [45] and stacked layer design [46], [47]. As a function of the number and location of tabs, the electron pathways become more or less long and thereby cause an increase or decrease of the ohmic resistance responsible for the voltage loss. Interaction between the cooling systems and the design of the battery pack is needed to ensure this uniformity of temperature.

2.4 Battery Models

In order to build an effective battery management system (BMS), designing the battery cell and dimensioning the cooling and heating systems, the development of an accurate model is crucial. Three categories of models are reported in the literature:

- The equivalent circuit model (ECM),
- The electrochemical models,
- The empirical model.

All these battery models are generally coupled with the thermal model. The ECM and the electrochemical models are the most widely used.

2.4.1 Electrical-thermal modeling

The coupling scheme between the electrical and thermal models with the model inputs and outputs are illustrated in Figure 2.4. The electrical parameters, such as the resistance and capacitance depend on the temperature and SoC. The resistance and the current are used to compute the battery heat source. The SoC is calculated based on Coulomb counting method, where:

$$SoC(t) = SoC(t_0) + \frac{\int_{t_0}^{t_0+t} I_t d\tau}{C_N} \tag{2.1}$$

With C_N the nominal capacity of the battery and I the current of charge or discharge.

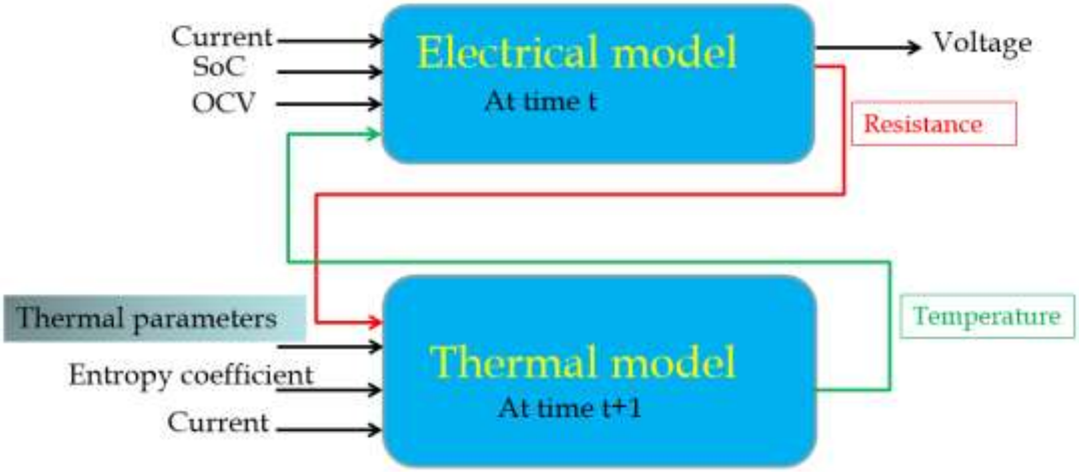

Figure 2.4: Electro-thermal model [48]

- Electrical Circuit Model (ECM)

Various ECM are developed and presented in the literature. All these models are summarized in Omar's PhD report [49]. The accuracy of them depends on the battery chemistry. Among the most relevant one, we can find:

- Shepherd Model [50],
- Rint battery model [51], [52],
- RC battery model [53],
- FreedomCar Battery model [54],
- Thévenin Battery model [54],
- Second order FreedomCar Battery Models [54].

The ECMs consists of electrical components such as capacitors, resistances (ohmic and polarization), and voltage sources (open circuit voltage). Figure 2.5 shows the voltage response of a lithium-ion cell after a pulse test, the voltage declines in three parts:

- The first part corresponds to the ohmic loss without any time delay
- The second part corresponds to the voltage loss caused by charge transfer runs after a time delay
- The third part corresponds to the voltage loss by diffusion of lithium in the active material

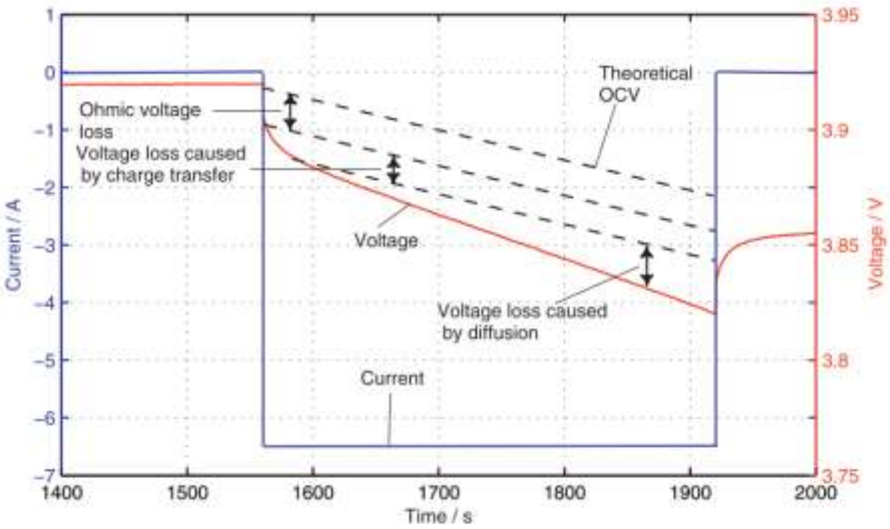

Figure 2.5: Voltage response of a lithium-ion cell after a current pulse[55]

These different phenomena are included in the ECM model. For example in Figure 2.6, the first order Thévenin battery model is illustrated, where:

- OCV represents the open circuit voltage of the battery
- Ro represents the ohmic resistance
- Rp represents the polarization resistance due to the charge transfer
- Cp represents the polarization capacitance in parallel with Rp
- V_L represents the battery voltage

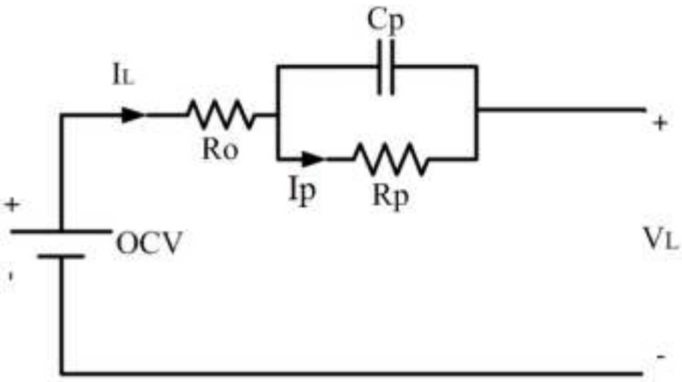

Figure 2.6: first order Thévenin Battery model [54]

The electrical parameters of these models can be extracted by performing tests such as the HPPC (Hybrid pulse power characterization test) [48] in the time domain model or by using the electrochemical impedance spectroscopy (EIS) [56] in the frequency domain. These tests are coupled with an estimation technique, such as generic algorithm (GA) optimization [57], nonlinear least squares curve fitting techniques [58] in order to extract the electrical parameters from the used model. These methods can be used without the need to access the innards of the battery cell. Afterwards, the battery model is built based on look-up tables with cell electrical parameters. As a function of the inputs (current, OCV (open circuit voltage) and temperature the model could be validated as illustrated in Figure 2.7.

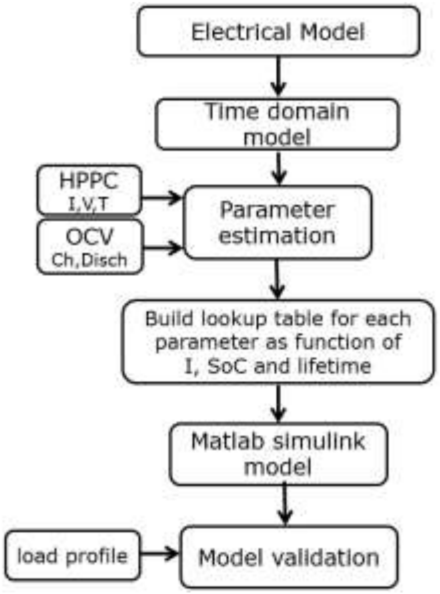

Figure 2.7: operating principle of the electrical model [48]

- Thermal Model

The thermal model delivers the temperature distribution of the cell, which depends on the electrical parameters and the operating conditions (current, cooling method and ambient temperature). The thermal model is based on the energy balance, taken in one, two or three-dimensional according to the geometric features of the battery. The heat source is mainly derived from three main phenomena [31] :

- The reversible heat corresponding to the chemical reaction, manifested by an entropy change,
- The irreversible heat including ohmic heat and polarization heat,
- The heat generated by side reactions, for example, corrosion reaction, overcharge, and chemical shorts.

The latter point is generally neglected. The irreversible heat is computed from the electrical parameters (internal and polarization resistances) including in the lookup table of the electrical model. While the reversible heat is computed from the entropy coefficient, based on the OCV change as a function of cell temperature [59]–[61].

To solve the electrical-thermal modeling, two types of techniques have been considered in the literature: Analytical techniques give continuous solutions and can show explicitly how the parameters affect the solutions [62]. Nevertheless, these techniques are only applicable in simplified cases [62], for example in the case of lumped-parameters approach where the battery surface temperature is considered as uniform or the Biot number is lower than 1 [63]. Several analytical techniques exist, such as Laplace transformation [64], [65], separation of variables [66], [67], Green's function [68][69], [70], etc. . . . Numerical techniques are performed based on complex models depending on the design and the multidirectional heat transfer of the battery. They use many discretization techniques such as a finite differential method (FDM) [71], finite volume method (FVM), the finite element method (FEM) [14,18] and etc. . .

To solve the energy balance equation, numerical methods are usually implemented in commercial software packages such as ANSYS Fluent, COMSOL Multiphysics, Star-CCM+, etc. . . .

Several one-dimensional thermal equivalent circuit models (TECM) applied to cylindrical and prismatic cell have been developed in the literature [30], [31], [72]–[75] ; they are more suitable for small cylindrical cells as illustrated in Figure 2.8, where the temperature gradient along the axial direction is almost negligible comparing to the radial direction. The one-dimensional model can be implemented easily in a BMS. Others multidimensional thermal models have been developed in the literature [34], [43], [61], [72], [73]. They are more suitable for large cells where asymmetric temperature distribution arises from geometric effects and from the cooling method.

Figure 2.8: Simplified thermal ECM for small cell [74]

One difficulty for developing accurate battery thermal models is that the thermal parameters are not easy to obtain. Different techniques have been established, such as parameters estimation and measurement techniques.

In the estimation technique, two methodologies have been used in the literature. The first one considered the active material as a continuous material with anisotropic properties that depend on the layered directions. Normally the active material is assumed to consist of several layers (anode, cathode, separator and current collectors). The thermal conductivity along and across the layers can be evaluated as a function of the thicknesses (l_i) of the different layers and the thermal conductivity (k_i) of the material constituting these layers as shown in Eq (2.1) and Eq (2.2). The density (ρ) and heat capacity) (C_p) of the active material are calculated similarly as a function of the density (ρ_i) and heat capacity (C_{p_i}) of the material constituting these layers, as illustrated in Eq (2.3) and Eq (2.4).

Thermal conductivity across the layers (k_n):

$$k_n = \frac{\sum_i l_i}{\sum_i \frac{l_i}{k_i}} \tag{2.2}$$

Thermal conductivity along the layers (k_t):

$$k_t = \frac{\sum_i l_i k_i}{\sum_i l_i} \tag{2.3}$$

Density (ρ) and thermal capacity (C_p) of the active material:

$$\rho = \frac{\sum_i l_i \rho_i}{\sum_i l_i} \tag{2.4}$$

$$C_p = \frac{\sum_i l_i {C_p}_i}{\sum_i l_i} \tag{2.5}$$

For a good accuracy of this model, the material composition of the layers should be well known. This is rarely the case in the competitive industry; the manufacturers do not want to reveal their secrets.

The second estimation technique is based on the solving of a first order thermal equivalent circuit model [74], [75]. By applying a micro-pulse test, one can estimate the different thermal resistances. However, this method is performed to estimate the thermal parameters in one direction and requires to insert a thermal sensor inside the battery in order to calculate the conductive resistance. The thermocouple inserted inside the battery can involve oxidation risks.

The thermal parameter measurement can be determined by using accelerating rate calorimeter (ARC) [76], differential scanning calorimeter (DSC) [77], thermal impedance spectroscopy (TIS) [78], [79], hot disc method [80], [81], flash method [82], [83], etc…

However, these devices are expensive and available in laboratories specialized on material characterization.

2.4.2 Electrochemical-thermal modelling

The electrochemical or physics based model is a multidimensional model that involves the resolution of the physical and electrochemical variable at the different length scale (particle, electrode and cell levels) as illustrated in Figure 2.9. This model has been firstly developed by Doyle, Fuller and Newman [84] based on the porous electrode theory.

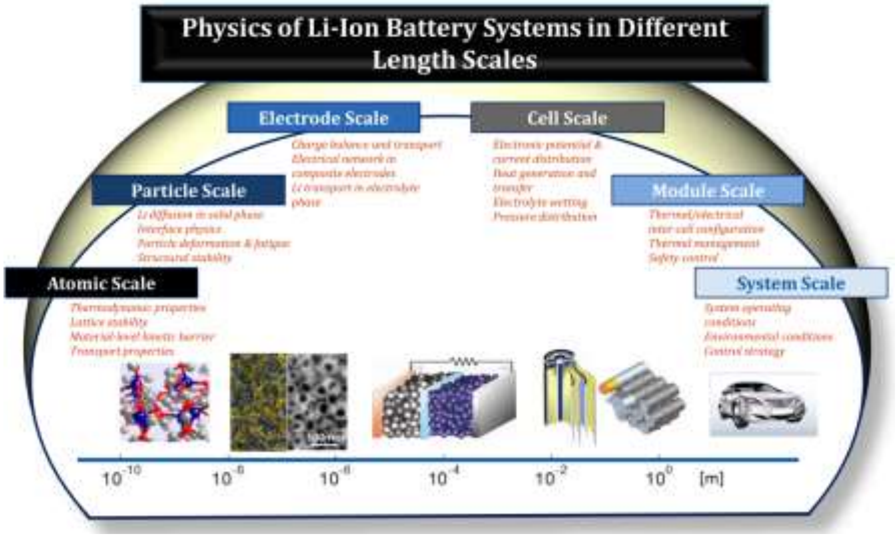

Figure 2.9: Governing equation at different length scale [85]

Electrochemical modeling techniques are more appropriate than the electrical modeling to investigate the battery designs, because they show a clear relation between the electrochemical parameters and battery geometry and have a relatively high accuracy. The main disadvantages of this model are the difficulty to obtain the required parameters and long computational times due to the lot of effort of meshing. Most of the electrochemical parameters depend on the temperature.

Several 1D electrochemical models are listed in the literature [86], [88]–[90]. These are more suitable for describing small-format batteries. They also provide average values for large-format batteries without taking into account the collector tabs. However, they are not sufficient to handle the issue of non-uniform thermal, electrical and electrochemical variable distributions observed in large-format cells. Recent advances in numerical simulation techniques applied to Li-ion batteries have given more attention to the development of 2D axisymmetric and 3D electrochemical-thermal modeling [44], [45], [91]–[93]. The multi-dimensional simulations are highly nonlinear and computationally demanding, and coupling electrochemical and thermal modeling represents an important step towards accurate simulation of the Li-ion battery. Most of the models in the literature use the electrochemical-thermal coupling model. As illustrated in Figure 2.10, the coupling method 1 is performed by using the volume-average temperature of the cell from the previous time step as inputs to update the electrochemical parameters and compute the heat source. This coupling method is less time and memory consuming. Little work focuses on the coupling method 2 [85]–[87]. This method shows results that are more accurate with time consuming.

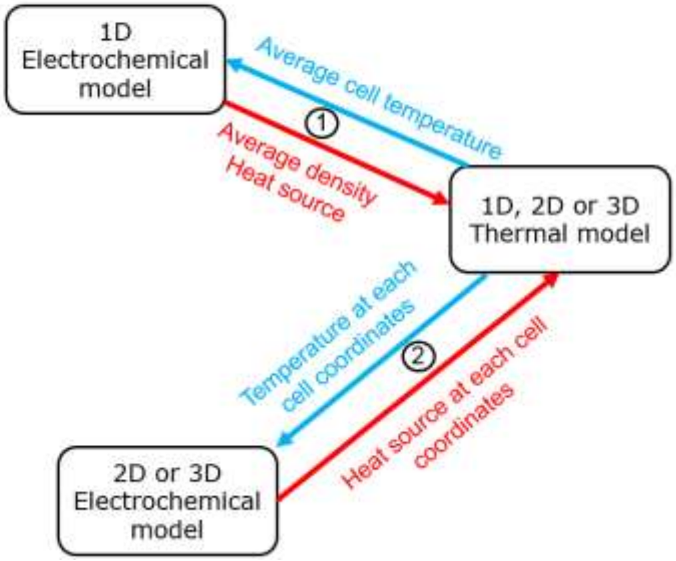

Figure 2.10: Different types coupling between electrochemical and thermal models

Most of 2D and 3D electrochemical-thermal models are applied to the spirally wound design in order to gain insight into large-scale battery behavior and to investigate the impact of the number of collecting tabs on the battery performance. However, little work is focused on stacked layered designs and the impact of the tab positioning on performance and variable distributions

2.5 Battery Thermal management

2.5.1 Global principles of a battery thermal management system

Figure 2.11 gives a global overview of the main possibilities of a BTMS. Depending on the application area and the type of battery, cooling and/or heating is required to work in the best temperature operating range. For the cooling aspect, it is important to distinguish three major cooling methods: liquid, air and Phase Change Material (PCM) cooling (or a combination of these). The choice of the method has a large impact on the performance, complexity and cost of the thermal management system.

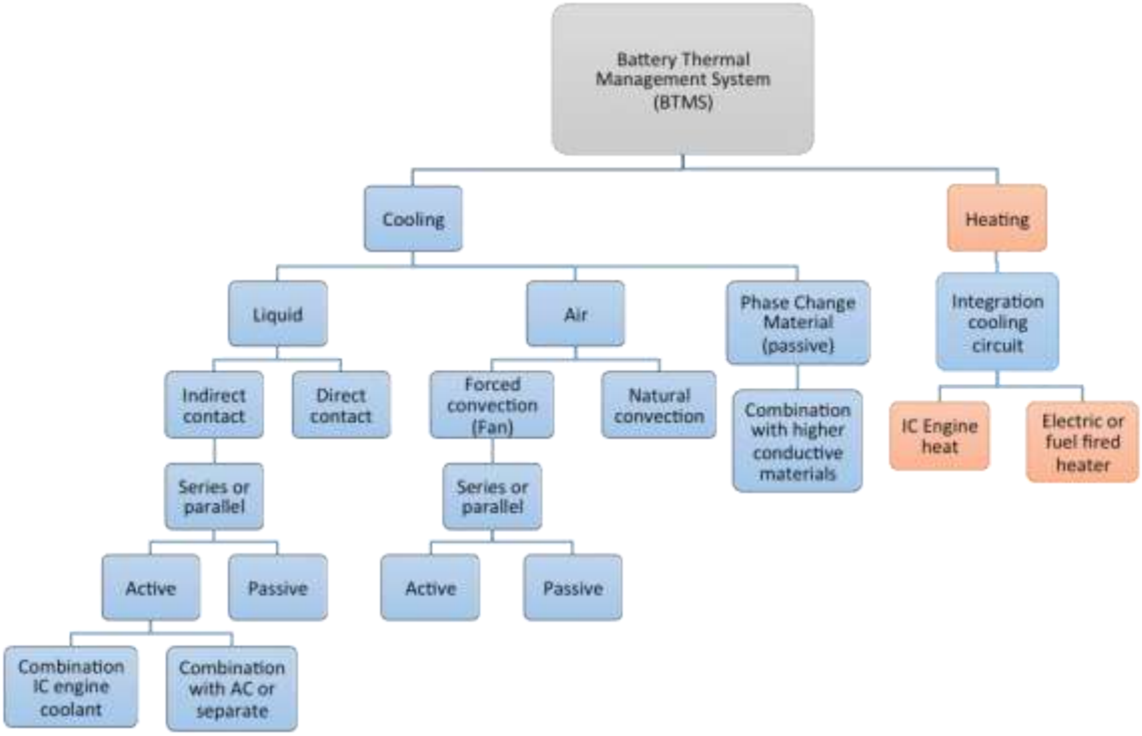

Figure 2.11: Flow chart of the BTMS for BEV [88]

- Liquid cooling system

Liquid cooling with direct contact means that the coolant involved, is in contact with the surface of the cell and have a property of a dielectric coolant (silicon-based or mineral oils could be used) in order to avoid cell short circuit. The advantage of direct contact with fluids is its high heat transfer coefficient rate. Due to the high viscosity of these fluids, more energy for pumping is needed, which results in a higher overall energy consumption. The liquid cooling shows a heat transfer coefficient 1.5 to 3 times larger than air [88].

The liquid indirect cooling is the most used system, where the coolant flows through pipes and channels between the different cells or in a jacket around the battery. Such configurations exist where all the cells are thermally connected to a fluid cooled plate [89]–[92].

Water/glycol is the most used coolant in liquid indirect cooling system; it has a lower viscosity and higher thermal conductivity than oils used in direct contact, which results in high heat transfer coefficients. In this way, it is interesting to use good thermal conductivity materials and high contact surface in the packaging between the cell and the fluid in order to enhance the heat transfer coefficient. Aluminium, copper and steel are good candidates for the packaging. In the Tesla Roadster for example, the cells have a steel packaging for strength and rigidity, but also to fasten the heat removal [93].

Due to their larger battery packs of BEVs and PHEVs, the liquid cooling system has shown to be more appropriate for the used BTMS.

In the recent year, passive liquid-vapor phase change processes [94]–[99] are investigated for battery cooling system using different refrigerant types. In general, passive liquid cooling has the advantage to operate passively with natural circulation of the refrigerant and no additional energy input is needed. They operate at a low temperature and pressure differences between heat source and condenser.

- Air cooling

In specific cases air-cooling and/or heating can deliver sufficient thermal management. Air cooling is often indirect. The natural convection is generally not sufficient for battery cooling [39] due to its low heat transfer coefficient. For this reason, a fan is generally used to create forced convection. Because of the use in mild climates, the early BEVs did not have specific cooling or heating equipment for thermal regulation of the batteries and only ambient air was used for the battery cooling. Around the year 2000, cabin air has been used for heating/cooling in HEVs like for example Honda Insight and Toyota Prius [88].

More problems of non-uniform temperatures rise with series cooling (the cool media is heated up by the first cells and is less able to cool the other cells because the same amount of air is provided for all the cells/modules). Advantage of series cooling is that the flow isn't split into different branches (like for parallel) such that the flow rate for series cooling is higher. In this way steady state can be achieved much faster and the absolute steady state temperature is also lower [100]. For parallel cooling the total airflow is split and this requires a very careful design of the air inlet manifold.

Explicit examples of series or series-parallel air cooling are GM EV1, Toyota RAV4-EV, Honda Insight HEV, Toyota Prius (Japanese version), while pure parallel air cooling is used in the Toyota Prius (North American version) [88] .

An overview of the main possibilities for passive and active cooling/heating is visible in Figure 2.11. For passive cooling, no explicit auxiliary equipment is used (except the fan for forced convection). This means only ambient or cabin air is used to cool the battery or the circulating fluid in the battery. For active cooling, interaction with auxiliary equipment like the ICE coolant (only for HEV), air conditioning or specific equipment is possible. Passive systems can be generally sufficient in mild climates when the ambient temperature is around 10°C to 35°C. Explicit examples of active water-cooling are Opel Ampera, Volvo C30, Volvo V60, BMW i3 and Volkswagen E-UP.

- Phase change material (PCM) cooling method

Generally, the PCM is used to capture the heat surrounds the cells of the battery pack. In this way, heat is stored in the PCM and the temperature is controlled in a uniform way. Because of the direct thermal energy capture of the PCM, it is clear that temperature variations are more attenuated. This means also that the heat storage is limited and residual heat can be present/stored from the previous operation of the batteries. PCM on its own has a low relative thermal conductivity and to prevent temperature increases, the generated heat must be removed quickly. For this reason, several techniques exist to improve the thermal conductivity of the PCM. Possible improvements are the encapsulation of PCM into metal-foam [73], [107]–[112], the attachment of aluminium cooling fins on the battery or cells and the PCM can also be used in a PCM-graphite composite. Of course, the combination of PCM cooling with air or liquid cooling is possible to solve the problem of the limited heat storage. Battery packs for a scooter or HEV applications are smaller compared to BEV battery packs and therefor PCM cooling with thermal improving conducting materials can be a simple, compact and cheap solution [101]. For BEV applications, the combination of the PCM with air or liquid cooling is recommended to ensure enough heat removal of the batteries. Problem of PCM is currently the slight increase of the battery volume due to the implementation of enough PCM between the cells. The advantage of using PCM is that different layers of different types of PCM can be used to ensure optimal temperature range of broader temperature conditions [102].

An illustration can be given by the specific study of changing the existing NiMH battery pack of the Ford Escape Hybrid (PHEV) by Li-ion battery pack with PCM cooling (by All Cell Technologies LLC [103]). The study claims that PCM cooling seems to be the ideal solution for flattening out peak temperatures in specific applications (peak and stressful loading of the battery) like Plug in Hybrid Electric Vehicles (PHEV) compared to forced air-cooling. The PCM cooling method, required less maintenance than the air and liquid-cooling method.

For specifying the phase change material[104], a very wide range of possible chemical species exist. An overview of the possibilities for vehicle applications is given in Figure 2.12 and they can be globally divided into organic, inorganic, metallic and solid-solid PCMs. In the past, many investigation focus on the PCM material with a high specific latent heat (200kJ/kg – 285kJ/kg) such as the paraffin waxes (e.g. Rubitherm RT-42 [105]). These paraffin have a wide melting range of temperatures (related to their composition from -30°C up to 115°C) and in this way, the operating temperatures can be easily turned around the right temperature. Recently, more attentions have been spent for materials with better volumetric latent heat and higher thermal conductivity compared to paraffin. Promising materials for battery thermal management with these better properties are suggested in Table 2.2.

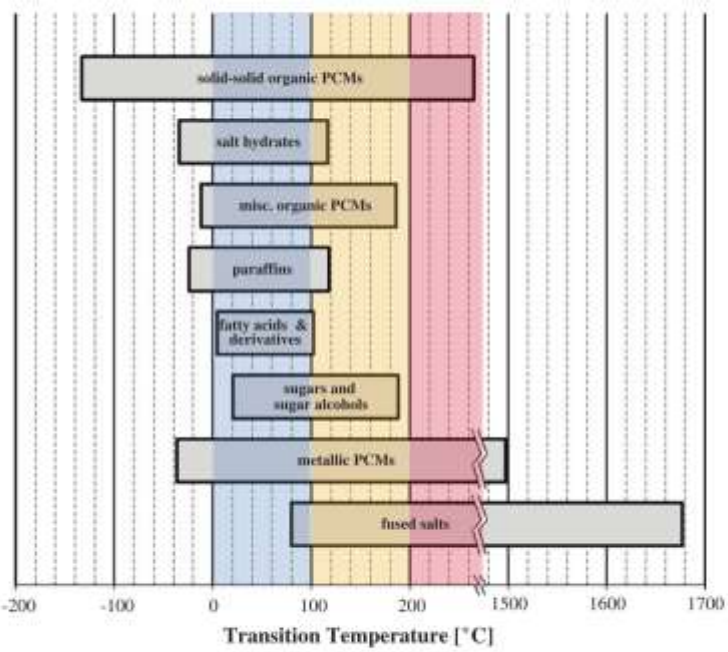

Figure 2.12: Temperature ranges of the surveyed material categories [104]

Name PCM	Type	T_M (°C)	H_f (kJ/kg)	$H_{f,v}$ (MJ/m^3)	$k_{th,s}$ (W/mK)
Gallium	Metallic	29.8-30	80.1-80.3	473-474	33.7
Lithium nitrate trihydrate	Salt hydrate	29.9-30.2	296	460	0.8
Lithium acetate dihydrate	Salt hydrate	58-70	150-377	-	-
Sodium hydroxide monohydrate	Salt hydrate	64.3	227.6-272	385-468	-

Table 2.2: Notable PCMs for battery pack buffer/protection [104]

2.5.2 Commercial applications of BTMS

The battery thermal management methods of different vehicle's brands are included in Table 1.2, Table 1.3 and Table 1.4. Air and liquid cooling have each their specific advantages and disadvantages and a specific comparison can be found in Table 2.3.

Specific aspects of BTMS	Characteristics
Air cooling	- Less complicated - Lower cost - Less uniform temperature distribution - Higher parasitic fan power
Liquid cooling	- Less space demanding - Higher cost - Cooling more effective so higher load of battery possible - Require higher maintenance - Higher weight

Table 2.3: Comparison (dis)advantages BTMS using air or liquid [88]

2.6 Conclusions

As shown in this chapter, the temperature is the major parameter influencing the battery performance and lifetime in many aspects. Two ways are identified to improve the battery behavior. The first one is to optimize the cell design in order to lower the temperature gradient and the second one is to associate the cell with a dedicated battery thermal management system that can keep the cell temperatures in the safe range. In addition, the pouch cells are specified as the most flexible design aspect and are relatively less expensive and easier to manufacture.

To tackle this, there is a need to develop a dedicated battery electrical-thermal model in order to investigate the cell thermal behavior. The model has to be based on a new methodology to estimate the battery thermal parameters, which avoids an insertion of thermal sensor inside the battery and which is able to estimate the thermal resistance in all directions of the battery cell. The pouch cell, less investigated in literature, is a good candidate for BEVs due to its large capacity and energy density.

At cell level, the safety improvements can be made by acting on the cell chemistry or the cell design. In this PhD dissertation, a methodology for battery cell design is proposed in order to improve the battery's effectiveness and safety. A good cell design requires therefore a less complex cooling strategy.

Finally, regarding the thermal management, the liquid and PCM cooling methods have shown to be more appropriate for BEV applications. In numerical and design aspect, some improvements are needed to increase the accuracy of the models with less effort of meshing.

Chapter 3: Electrical –Thermal Model for Large Size Lithium-ion Cells

3. Electrical –Thermal Model for Large Size Lithium-ion Cells

3.1 Goal

In this chapter, a two dimensional electrical-thermal model has been developed in order to investigate and to analyze the temperature distribution over the battery surface. The ANSYS FLUENT software has been used to solve the model development. The model is validated by experimental results. In addition, a new estimation tool has been developed for the estimation of the proposed thermal model parameters. Furthermore, the thermal behavior of the battery has been investigated at different environmental conditions as well as during abuse conditions.

3.2 Introduction

As mentioned in chapter 2, section 2.2.2, the temperature has a strong influence on the battery performance and safety. It is suggested also that the ECM is the most appropriate models that can be implemented in a BMS. Furthermore, the electrical parameters, including in the ECM model depend strongly on the cell temperature. This input can be obtained by real time recording through a thermocouple or by using thermal models.

In order to keep the battery temperature on the safe range on one hand and to increase its performance on the other hand, the knowledge of the battery temperature distribution under all environmental conditions is necessary. Different ECM models coupled with a thermal model are developed in the literature. In [75] a 1D thermal model for small cylindrical Electric Double–Layer Capacitors (EDLC) is proposed using a thermal sensor inside the battery in order to calculate the conductive resistance of the cell and then estimating the different thermal parameters. In [74], almost the same methodology is described as in [75] for simulation of the temperature of a small cylindrical LFP battery cell. In [106], the simulation of the temperature of a small cylindrical LFP battery cell is proposed based on some estimation routines. However, these models are more suitable for the thermal parameter estimation of small cylindrical cells, as specified in chapter 2, section 2.2.3.1. Large and high capacity cells, as widely used in BEV applications, are generally subject to heavy solicitation that can lead to non-uniform temperature distribution.

In [34], [43], [61], [72], [73], different 2D and 3D electrical-thermal models, more suitable for large cells, have been developed with known thermal parameters. From this investigation, we found the necessity to develop a dedicated battery electro-thermal model that can be applied for any type of battery cell (scale and chemistry), with a new methodology to estimate the battery thermal parameters in all directions, avoiding the insertion of thermal sensors inside the battery. The main advantage of this model is that the cell can be considered as a 'black-box approach' and without knowing the materials and layers composition, thermal parameters can be estimated by input and output signals (current voltage and cell surface temperature) and then included these parameters in the CFD models.

Taking into account the advantage of using the pouch cell, as mentioned in chapter 2, section 2.3.1, a large format pouch cell, characteristic for BEV applications, has been selected for in-depth investigation. The selected cell is 45Ah $LiFePO_4$/graphite. For this, an advanced electrical-thermal model is developed to simulate the thermal behavior at different operating conditions. The used input parameters are the heat generation and thermal properties. A new estimation tool has been developed in Matlab Simulink for estimation of the thermal model parameters, accurately, in each direction of the cell. Furthermore, the thermal behavior of the proposed battery has been investigated at different environmental conditions as well as during the abuse conditions by using the ANSYS FLUENT software.

3.3 Thermal modelling

3.3.1 Model assumptions and geometry features

Generally, soft pouch cells for BEVs and PHEVs have small thicknesses, which vary between 5 and 20 mm, depending on the battery cell capacity. The used $LiFePO_4$/graphite lithium-ion pouch cell with the size of the different domains (Tabs, case and electrode domains) is illustrated in Figure 3.1. These domains are made of different materials. Taking into account its thickness of 13 mm, the heat development in the y-direction has been neglected. Thus a two-dimensional transient heat conduction equation is sufficient to describe the thermal phenomena in the battery. However the convective term inside the battery (electrode-electrolyte) can generally be neglected [63]. As mentioned in chapter 2, section 2.3.1, the active material of the battery is assumed to consist of several single cell layers. Therefore, the thermal conductivities are anisotropic, with a higher value along the x and z-directions, than the normal direction to the layers. Furthermore, the thermal conductivity along x-direction is the same than the z-direction.

Therefore, an equivalent material is set up to model all different materials that the battery cell is consisting of. The radiative and convective heat transfer from the battery surface to the surrounding have been considered.

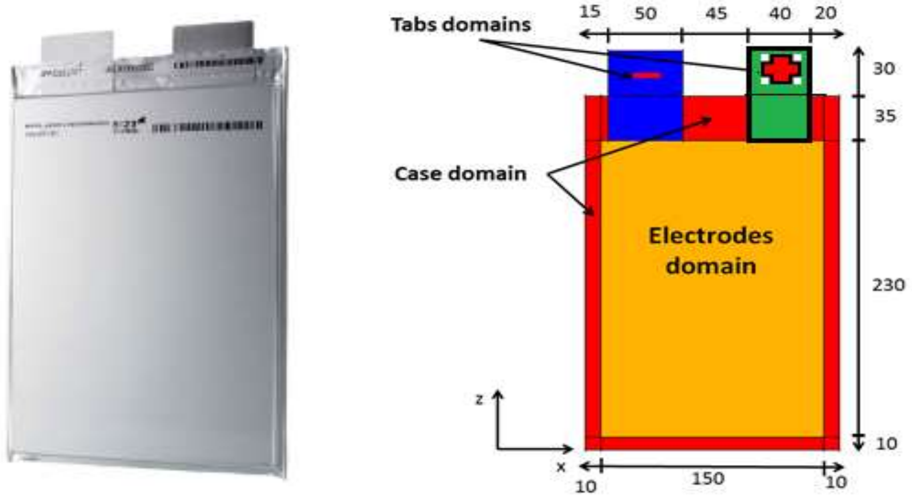
(a)

(b)

Figure 3.1: Pouch cell: (a) image and (b) schematic diagram and dimension (mm) of pouch Li-ion battery

3.3.2 Governing equations and boundary conditions

3.3.2.1 Governing equations

Based on the above assumption, the energy balance equation over a representative elementary volume (REV) in a battery, enable to predict the transient response of the temperature distribution for the 2D thermal modeling is formulated as:

- In the electrode and tabs domains:

$$k\left[\frac{\partial^2 T}{\partial x^2}+\frac{\partial^2 T}{\partial z^2}\right]+q_g=\rho.C_p\frac{\partial T}{\partial t} \tag{3.1}$$

For the electrodes domain, the heat generation is given by:

$$q_g=\frac{1}{V_{bat}}\left[R'I^2+\left(T\left[\frac{dE}{dT}\right]\right)I\right] \tag{3.2}$$

Where q_g (W m^{-3}) is the volumetric heat generation, where R'(Ω) is the battery internal resistance, $\frac{dE}{dT}$ (V.K^{-1}) the entropy coefficient and I(A) the applied current (negative in discharge and positive in charge).

For the Tab domain, the heat generation is given by:

$$q_g = \frac{R'' I^2}{V_{tab}}; \quad R'' = \rho'' \frac{l}{S} \tag{3.3}$$

- In case domains

$$\lambda \left[\frac{\partial^2 T}{\partial x^2} + \frac{\partial^2 T}{\partial z^2} \right] = \rho . C_p \frac{\partial T}{\partial t} \tag{3.4}$$

Where R'' (Ω), ρ''(Ωm), l(m), S(m^2) and V_{tab}(m^3) are the electrical resistance, resistivity, length, cross section and volume of the corresponding tab, respectively. Also ρ (kg m^{-3}), C_p (J kg^{-1} K^{-1}) and λ (W m^{-1} K^{-1}) are the average density, the average specific heat and the average thermal conductivity along the x-direction and z-direction, respectively. ρ is equal to 2247 kg m^{-3}, this value is calculated from the mass and the volume of the cell.

3.3.2.2 Boundary conditions

- Interface cell/ ambient air

The balance between the conductivity heat flux from the battery surface to the surrounding and both contributions of radiation and convection heat gives the boundary conditions:

$$q_s = -\lambda \left(\frac{\partial T}{\partial x} + \frac{\partial T}{\partial y} \right) |_{boundaries} = (h_{conv} + h_{rad})(T - T_a) \tag{3.5}$$

With

$$h_{rad} = \epsilon \sigma (T^2 + T_a^2)(T + T_a) \tag{3.6}$$

- The interface between two domains of cell made of different material

At this type of boundary the continuity is applied and formulated as follows:

$$\lambda\left(\frac{\partial T}{\partial x}+\frac{\partial T}{\partial y}\right)|_{domain\ 1}=\lambda\left(\frac{\partial T}{\partial x}+\frac{\partial T}{\partial y}\right)|_{domain\ 2} \tag{3.7}$$

Where h_{conv} (W m^{-2} K^{-1}), h_{rad} (W m^{-2} K^{-1}) represent the convective heat transfer and radiative heat transfer, ε the emissivity of the cell surface, σ (5.669 10^{-8} $Wm^{-2}K^{-4}$) the Stefan–Boltzmann constant [107], T the battery surface temperature and T_a the ambient temperature. Because of using a thermal imager, the battery has been painted black, and then the emissivity is taken equal to 1.

The case domains are made by aluminium; all related thermal parameters of this domain are taken from [107]. The thermal parameters used in the tab domains are summarized in Table 3.1

	Positive tab (aluminium) and case domain	Negative tab (copper)
ρ(kg m^{-3})	2719	8978
λ(W m^{-1} K^{-1})	202.4	387.6
C_p(J kg^{-1} K^{-1})	871	381

Table 3.1: Thermal parameters of tab domains

From the tab dimensions and the resistivity value, the electrical resistance of the aluminium positive tab is 4.3 mΩ and the electrical resistance of the copper negative tab is 1.09 mΩ. These resistances are computed from the Eq (3.3). Thus, the heat generated at the positive tab is higher than at the negative tab. Knowing the heat generation variation and thermal parameters, finite volume numerical is used to solve the energy balances by ANSYS Fluent software. The thermal model is validated by comparing with the experimental measurements.

3.3.3 Heat generation measurement

The expression of heat source is derived from Bernardi et al. [108] by applying the first law of thermodynamic energy balance on a cell control volume. Two main origins of heat source are taken into account: the first represents the overpotential heat due to ohmic losses in the cell, the charge-transfer overpotentials at the interface and the mass transfer limitations, and the second is the entropic heat from the reaction. The heat source from mixing effects (during relaxation after the current is turned off) and phase change are neglected in this expression. The internal resistance and the entropy coefficient have been extracted experimentally; these parameters allow to determine the heat source.

3.3.3.1 Internal resistance measurement

The measurement method of the internal resistance is described in [109], [110]. The battery is first placed in a climatic chamber to ensure constant battery temperature. Thereafter, the extended hybrid pulse power characterization (HPPC) test was applied, whereby at a specific SoC, different charge and discharge current pulse rates of 10 seconds, with a rest of 300 seconds in between is applied. The test procedure is repeated at different environment temperatures as summarized in Table 3.1. Based on the Levenberg-Marquardt minimization algorithm applied to the first order Thévenin model, the internal resistance is estimated based on the methodology described in Figure 3.2.

Step	Action	Duration
1	Tempering	3h
2	Constant current (CC) charge at 1 It up to 3.65V	<2 h
3	Constant voltage (CV) charge at 3.65V up to 1A with SoC=100%	<1h
4	Rest	30 min
5	– Charge current pulse at specific current rate – Rest – Discharge current pulse at specific current rate – Repeat step 5 at different current rates	– 10 s of charge – 300s of rest – 10s of discharge
6	Discharge of 5% SoC at ½ It	6 min
7	Rest	15 min
8	Repeat steps 5- 7 up to SoC = 0%	

Table 3.1: HPPC procedure at a specific temperature

In this PhD, the HPPC is performed at different temperatures (0°C, 10°C, 25°C, and 40°C), current rates (1/3I_t, 1I_t, 2I_t, and 3I_t) and SoC (100% to 0% by step of 5%). Where the I_t represents the current value corresponding to the battery capacity in Ah as defined in IEC61434[111]. In our case 1I_t corresponds to 45 A. The environment temperature is regulated by using climatic chamber as shown in Figure 3.15. The variation of internal resistance as a function of SoC and temperature at 1It charge and discharge current rates are plotted in Figure 3.3 and Figure 3.4. Between 100% and 90% SoC, the internal resistance decreases with the decrease of SoC. From 90% and downwards the internal resistance maintain more less stable. Below 20%, the resistance increases more as can be seen in both the resistance figures. At low temperatures, the internal resistance increases due to the increase of the electrolyte's viscosity, which is limiting the ionic transport reaction speed. It has been shown that the internal resistance decrease with the increasing of the current rate, as shown in Figure 7.1, Figure 7.2, Figure 7.3, Figure 7.4, Figure 7.5, and Figure 7.6 in Appendix I, section 7.1.

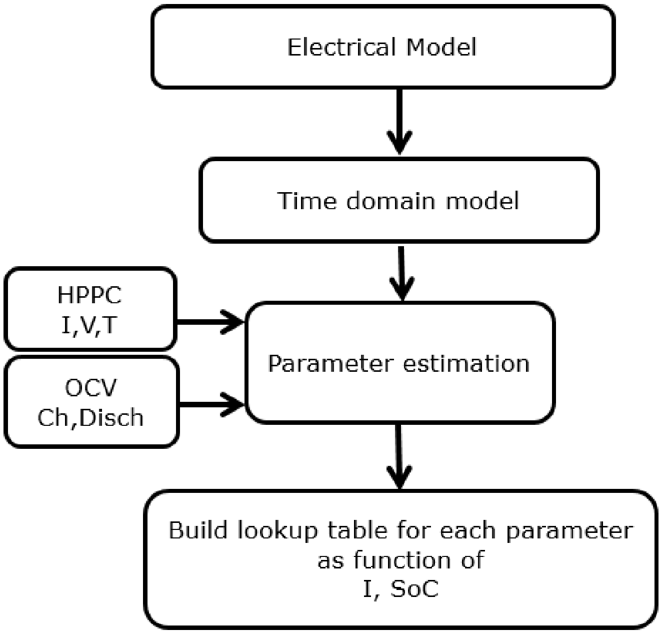

Figure 3.2: Methodology of the Electrical parameter estimation

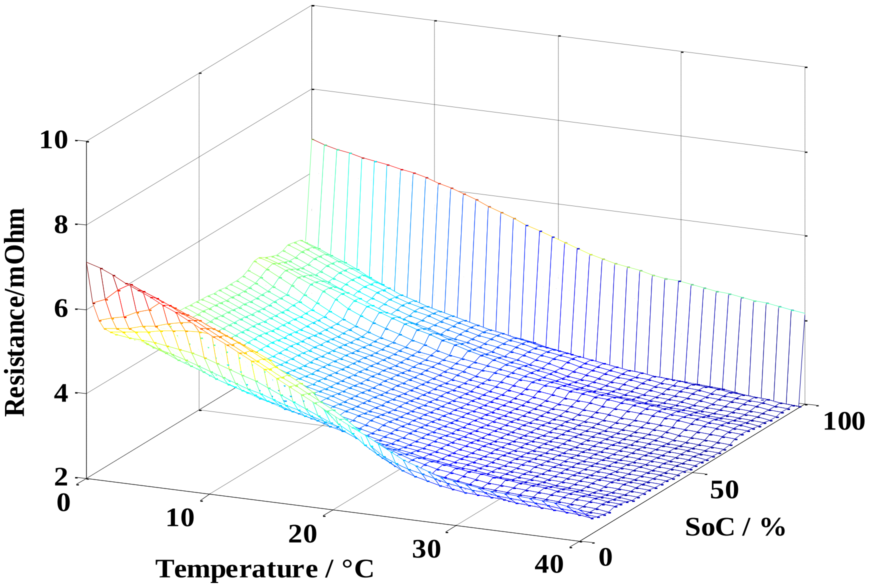

Figure 3.3: Internal resistance of charge as a function of SoC and Temperature at $1I_t$ current rate

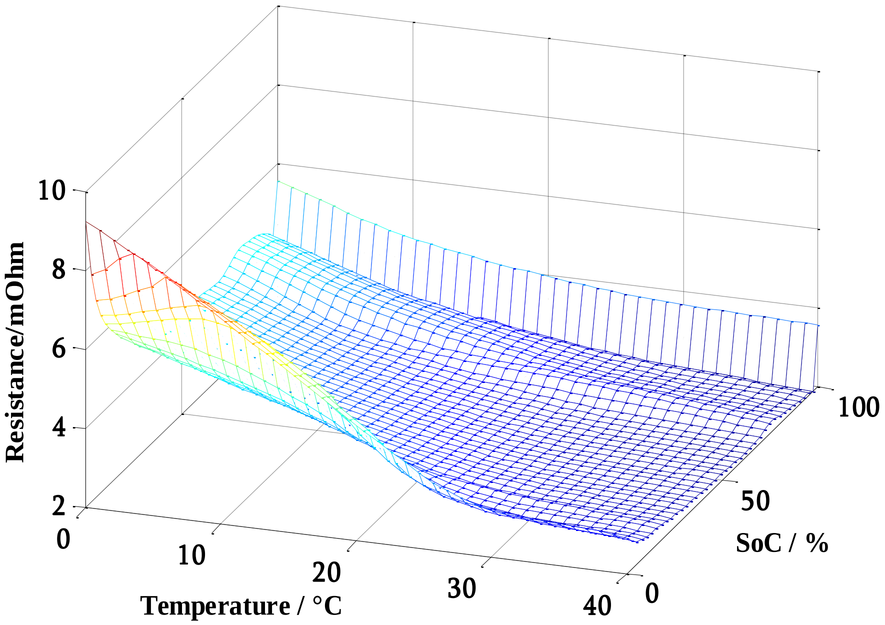

Figure 3.4: Internal resistance of discharge as a function of SoC and Temperature at $1I_t$ current rate

3.3.3.2 Entropy coefficient measurement

The entropy coefficient is based on the open circuit voltage (OCV) measurement as a function of battery temperature at different SoC levels. Several methods exist to measure the OCV such as linear interpolation method and potentiometric method or voltage relaxation method [76], [112]. In this work, the voltage relaxation method is used. The OCV measurement during charge, discharge process was performed as follows:

- The battery was first charged at $1/3I_t$ up to 3.65V, followed by a constant voltage charge of 3.65V up to 1A, corresponding to a SoC of 100%.
- The battery was left in open circuit for about 3h relaxation in order to reach a relatively stable state. Afterwards, the OCV in discharge at 100% of SoC was reached.
- With a programmable climatic chamber, the OCV in discharge was measured at different temperatures (10°C, 2°C, 15°C, and 30°C). For each temperature level, 3h was needed to ensure constant battery temperature.
- The battery was discharged at $1/3I_t$ by a step of 10% of SOC
- At each SoC, the battery was left in open circuit for about 3h relaxation in order to reach a relatively stable state. Afterwards, the OCV measurement as a function of temperature was repeated.

The OCV measurement is repeated in charge process by discharging completely the battery at $1/3\ I_t$ up to the cutoff voltage 2V, corresponding to a SoC of 100%. After relaxation time of 3h the OCV was measured at different temperatures. Figure 3.5 shows the illustration of the OCV in charge as a function of temperature at 0% of SoC, where at the end of each temperature variation the steady state was reached.

Afterwards the battery was charged at $1/3I_t$ by a step of 10% of SOC and at each SoC the OCV in charge was measured at different temperatures.

The entropy coefficient for a given SoC is obtained experimentally from the slope of the open circuit voltage (OCV) curve as a function of temperature. The entropy coefficient of 0% of SoC is illustrated in Figure 3.6. This calculation procedure is repeated at each SoC (90% to 0% by step of 10%) during both charging and discharging. The entropy coefficients from 10 to 50% of SoC during the charge process is illustrated in Appendix I, Figure 7.10, Figure 7.11, Figure 7.12, Figure 7.13, and Figure 7.14. Figure 3.7 describes the entropy coefficient as a function of SoC during charge and discharge process and shows a difference between both. This difference is due to the hysteresis of the open circuit voltage (OCV). The result has also been observed for various lithium-ion batteries [109], and is more pronounced at low SoC as reported by V. Pop et al [112].

For low charge or discharge current rates, the reversible heat becomes dominant respect to the irreversible heat. According to the reversible heat formula ($\left(T\left[\frac{dE}{dT}\right]\right)I$), this term may be positive or negative depending the sign of the current (positive in charge and negative in discharge) and also the sign of the entropy coefficient. If the reversible heat is positive, then the chemical reactions are exothermic otherwise, they are endothermic. Physically, an endothermic reaction is obtained when the chemical bonds of the reactants are higher than those of the product: then extra energy should be absorbed from the external environment to create new bonds. During exothermic reaction the opposite situation occurs. Generally the entropy ($\Delta S = nF\frac{dE}{dT}$) measures the degree of disorder in a system at the microscopic level, where n is the number of electrons transferred and F is the Faraday's constant. Indeed the higher entropy is high, the less its elements are ordered and the higher the system energy.

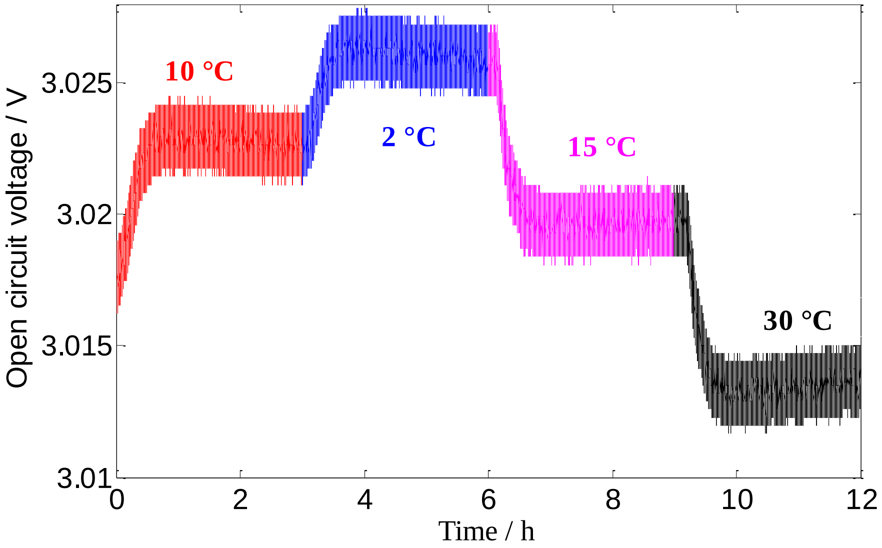

Figure 3.5: evolution of OCV as a function of battery temperature at 0% of SoC during charge process

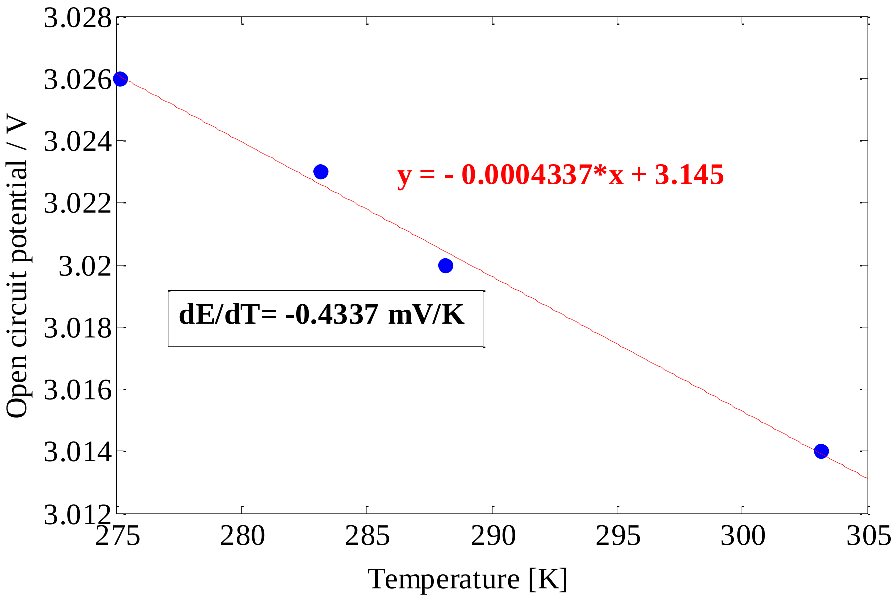

Figure 3.6: Entropy coefficient of 0% of SoC during charge process

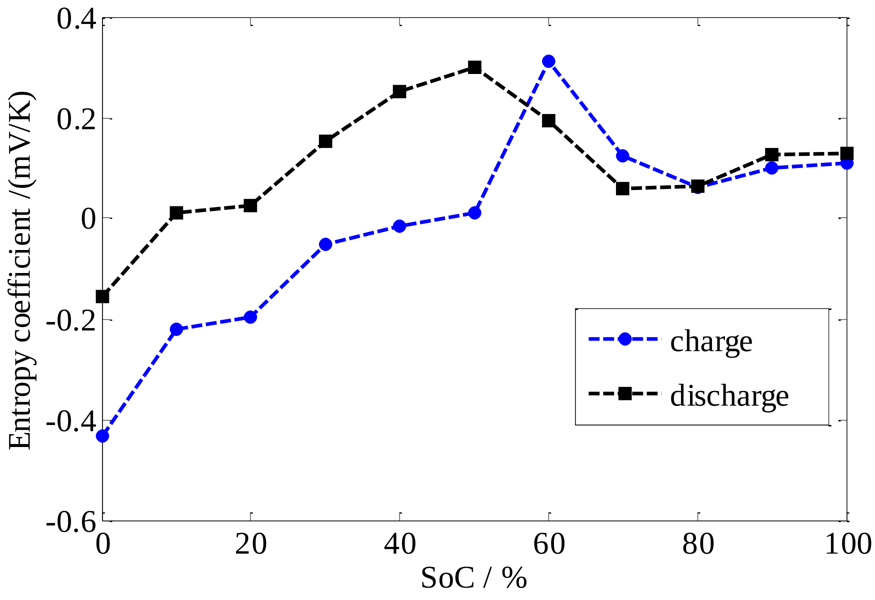

Figure 3.7: Entropy coefficient as a function of SoC during charge and discharge processes

3.3.4 Battery thermal model parameters

As the dynamic performances of cells and batteries during operation are related to their temperature, an accurate thermal model is essential to investigate the battery behavior in advance and during operation.

As the battery cell is considered as a "black-box" and consists of a combination of materials and layers not precisely mentioned, thermal parameters have to be estimated from the input and output signals. From a practical point of view, only current, voltage and surface temperature of the battery cell can be measured. Electrical parameters are estimated based a first order Cauer network, where the energy balance is represented by an equivalent circuit in each direction of the cell, as shown in Figure 3.8, where P_g represents the total heat generation, C_p stands for the thermal capacitance, R_{th} is the conductive thermal resistance and R_{con} represents the convection and radiation thermal resistance. This model has less assumptions comparing to some models used in the literature [48], [74], [75] where a thermal sensor was inserted inside the battery in order to calculate the thermal resistance R_{th} and also these models considered that all power generated by the battery goes through the normal direction, which is an ideal condition. These assumptions are only valid for cylindrical battery shape because in prismatic or pouch cell the dissipated power is not just released through the normal front and back directions to the ambient ($T_{s\,front}$ and $T_{s\,back}$ as demonstrated in Figure 3.8) but also along the surface directions to the ambient (T_{s1}, T_{s2}, T_{s3} and T_{s4} as presented in Figure 3.8). The thermocouple inserted inside the battery can involve oxidation risks. Taking account all these into consideration, the method described below is developed to estimate the thermal battery model parameters.

Firstly, a micro-pulse test is carried out at 3 I_t current rate until the battery surface temperature reached the steady state. As shown in Figure 3.9, the temperature at each surface is almost equal and the differences did not exceed 1 °C.

From these results, the percentage of power generation emitted along each direction is calculated. P_1, P_2, P_3 are defined as the part of heat generated through the front direction, the right direction and the down direction, respectively. At steady state, the heat accumulation is equal to zero, and then from Figure 3.8, the energy balance can be formulated as:

$$P_g = 2.P_1 + 2.P_2 + 2.P_3 \tag{3.8}$$

Where P_g is the generated heat in [W].

According to the Newton's law of cooling, each associated heat can be expressed as a function of temperature difference ΔT between surface and ambient, total heat transfer coefficient h (W/m^2 K) and surface. ΔT_1, ΔT_2 and ΔT_3 are the temperature differences associated to the direction of P_1, P_2 and P_3, and A_1, A_2 and A_3 are the related areas.

Then at the steady state, we have from Figure 3.8 and Figure 3.9 the following equations:

$$P_1 = hA_1\Delta T_1 \; ; \quad P_2 = hA_2\Delta T_2 \; ; \quad P_3 = hA_3\Delta T_3$$

$$\Delta T_1 = \Delta T_2 = \Delta T_3 \tag{3.9}$$

These equations also can be expressed as follows:

$$\frac{P_2}{P_1} = \frac{A_2}{A_1} \; ; \quad \frac{P_3}{P_1} = \frac{A_3}{A_1} \tag{3.10}$$

Substitution of (3.10) in (3.8):

$$P_g = 2.P_1 + 2\frac{A_2}{A_1}\,P_1 + 2\frac{A_3}{A_1}P_1 \tag{3.11}$$

According to cell dimensions, the results give:

$$P_1 = 0.45\,P_g \; ; \quad P_2 = 0.03\,P_g \; ; \quad P_3 = 0.02\,P_g \tag{3.12}$$

In each direction the calculated percentage of heat generated is used to estimate the associated thermal parameters with the least-square curve fitting method.

According to the flowchart as shown in Figure 3.10, the methodology of the estimation of the thermal battery model parameters is presented. For estimating thermal parameters, the surface temperature of the battery has to be stabilized. Therefore, the micro-pulses are applied until the temperature reaches the steady state condition. Considering the total resistance and battery current, total heat generation can be calculated. According to the methodology described for determining of the heat flow in each direction, the thermal parameters can be estimated. The associated heat generated at each direction is taken as input and the measured surface temperature is considered as output. As it mentioned above, the algorithm that is used for parameter estimation is least-square curve fitting. This algorithm uses a recursive procedure to optimize the cost function (thermal balance equation) and tries to fit the temperature curves.

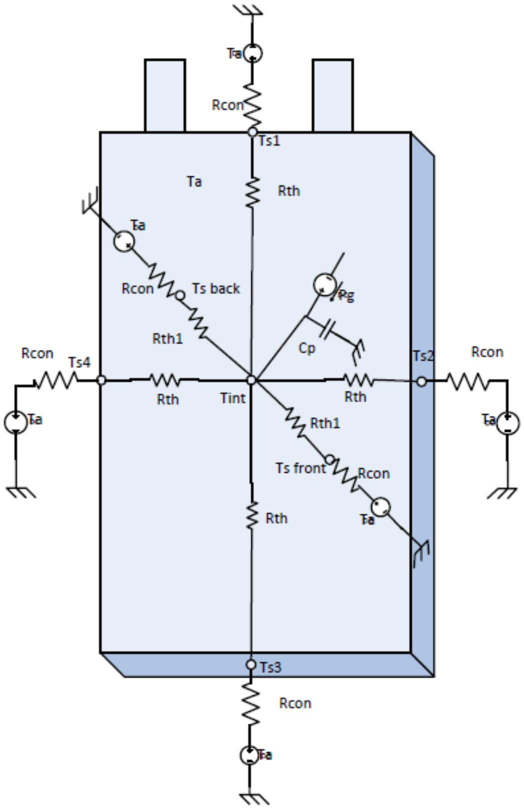

Figure 3.8: Cauer thermal model

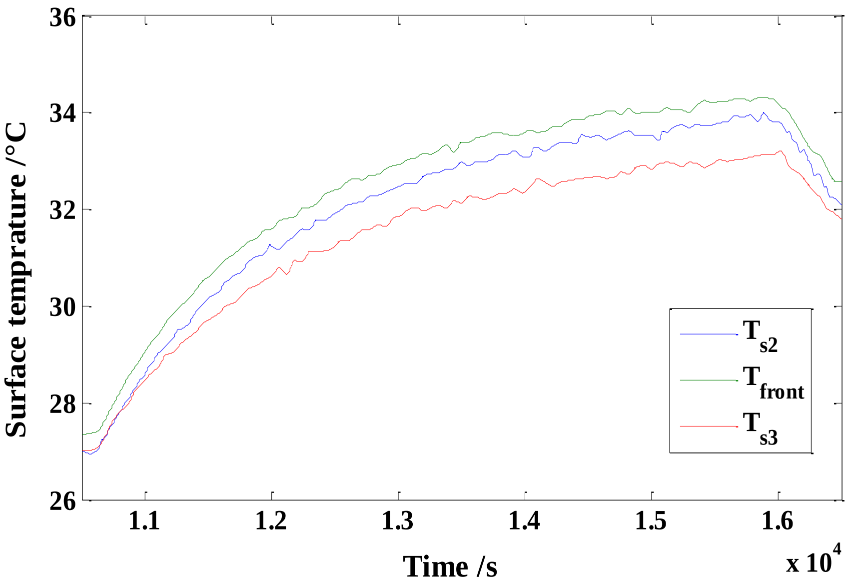

Figure 3.9: Battery surface temperature at $2\ I_t$ current rate micro-pulse and 27°C of environment temperature

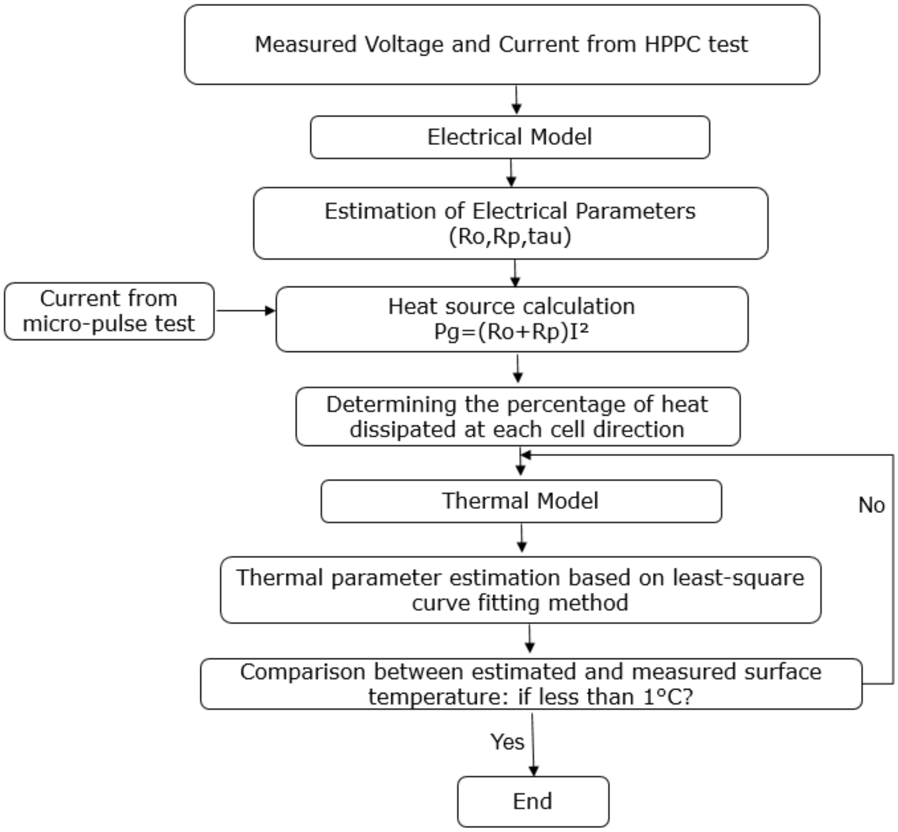

Figure 3.10: Estimation flowchart thermal battery model parameters

In order to ensure the validity of the results, the thermal parameters have been estimated at different current pulses ($1.5I_t$, $2I_t$, and $3I_t$). The results are shown in Table 3.2, where the thermal conductivity along the axial direction is 100 times bigger than the thermal conductivity along the normal direction of the battery. The reason is the layering of several materials in the direction of the front and back surfaces, thereby acting as an insulator. The estimated h is the combination of convection and radiation heat transfer. The estimated values are in the range of those used in the literature. However, the difference in function of current rate may from to the temperature increase during high current pulse test or from the error of the internal resistance estimation.

	C_p (J/kg.K)	R_{th1} (°C/W)	R_{th} (°C/W)	R_{con} (°C/W)	h (W/m^2.K)	λ_1 (W/m.K)	λ (W/m.K)
1.5 I_t	645,01	0,62	0,89	0,95	30,41	0,30	28,13
2 I_t	636,05	0,65	0,81	1,14	25,21	0,28	32,68
3 I_t	575,03	0,66	0,74	1,21	23,79	0,28	33,50

Table 3.2: Battery thermal parameters at different current rates and 27°C of environment temperature

3.4 Experimental

A test bench has been developed in order to characterize the battery and validate the model. The test bench is composed of a programmable DC power supply and DC active load to charge and discharge the battery, respectively, and four electric contractors, which are alternately closed and opened according to the battery processes (charge/discharge). These components are interconnected in series, as represented in Figure 3.11 and Figure 3.12. During the charge process the Contactors c1 and c2 are closed, d1 and d2 are opened, and the opposite will happen during the discharge process. A Labview application was developed to manage the battery process and to monitor the different measurements (current, voltage and temperature) by means of a Data acquisition system.

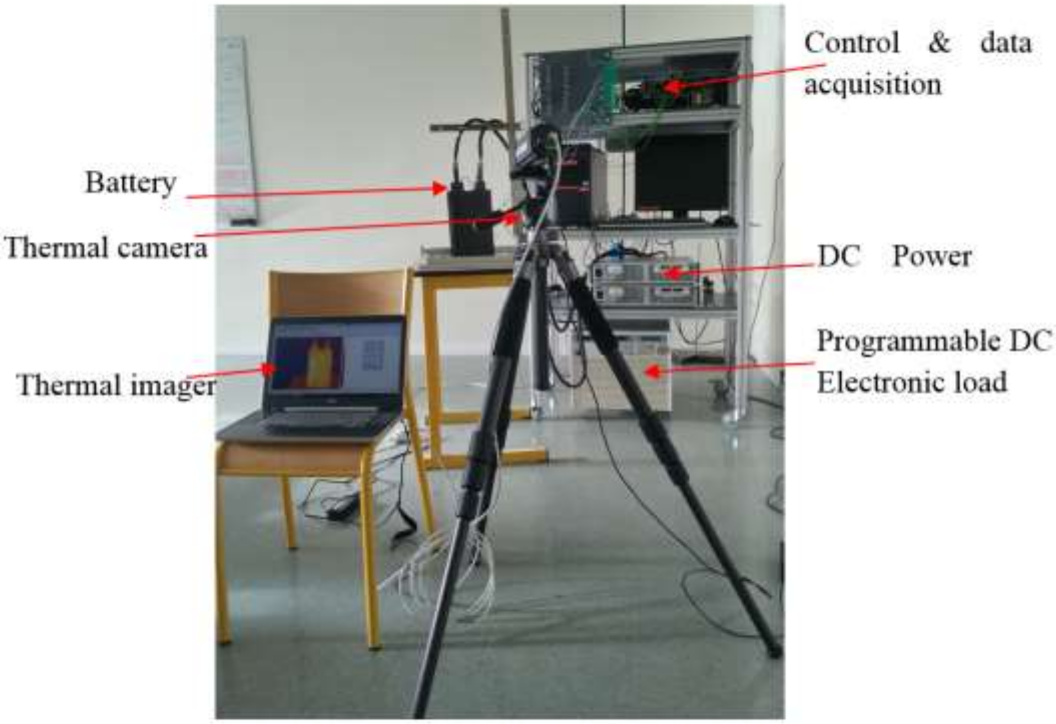

Figure 3.11: Battery tester

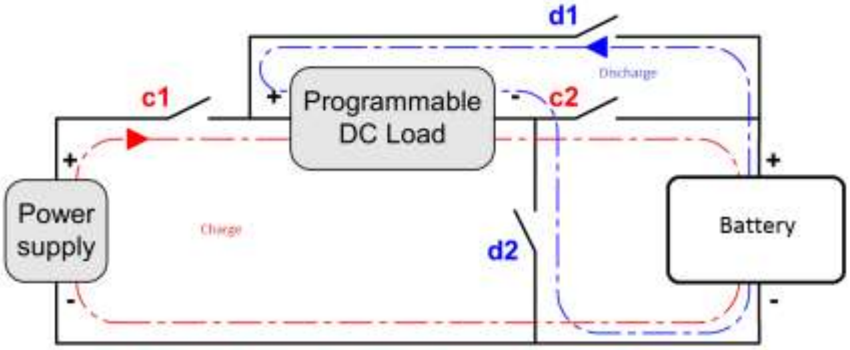

Figure 3.12: Charging and discharging circuits [113]

The battery was fully charged (100% SoC) by using the constant current (CC) charge process with the given current till the maximum allowed voltage (V_{max}= 3.65 V) following by constant voltage (CV) till the battery charge current is reduced till $0.01I_t$ as illustrated in typical current-voltage charging curve in Figure 3.13.

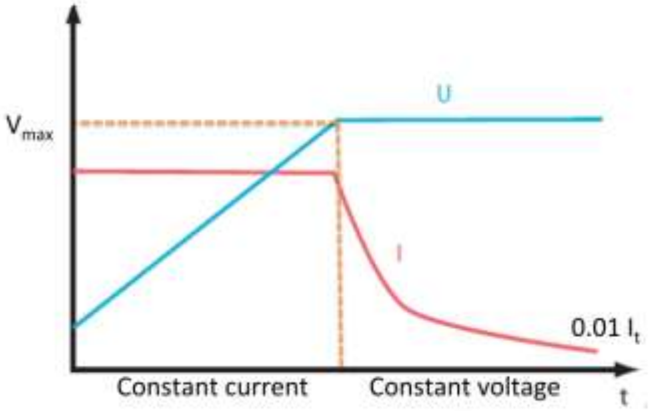

Figure 3.13: Constant current –constant voltage (CCCV) charging process [49]

The complete discharge is performed until the cut-off voltage (V_{min}=2V) is reached. Different charge and discharge current rates are performed. Due to the current limitation the charge process is performed at 1/3I_t, 2/3 I_t, and 1 I_t, against 2I_t, 3I_t and 4It for the discharge process. In addition. A computer, by means of the data acquisition system, monitors, displays and records continuously the current, voltage and temperature of the battery at each 0.01s. In order to analyze the thermal distribution of the battery, 11 thermocouples (K-type) have been placed on the battery surface as shown in Figure 3.14.

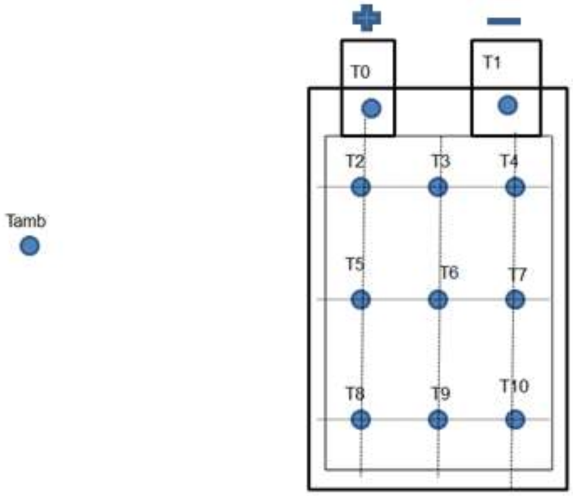

Figure 3.14: Thermocouples position on the battery

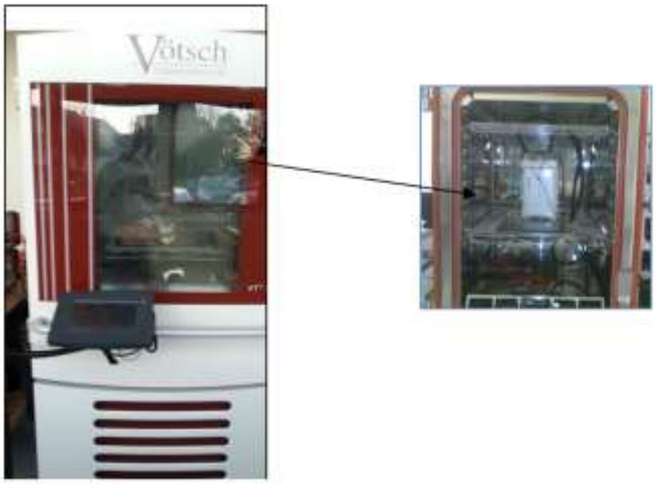

Figure 3.15: The pouch cell battery in the climatic chamber

In order to regulate the environment temperature a climatic chamber is used as shown in Figure 3.15. A FLIR A325SC IR camera is used to measure accurately the thermography imaging of the battery at each 5 seconds. The battery is coated with a black paint with 1 as emissivity. The Thermal camera is connected to a computer in order to display and save the images and videos at different time steps. During the test, we make sure that the room temperature remains almost constant with a temperature variation less than 2°C.

3.5 Results and discussion

3.5.1 Numerical aspect

All equations are simultaneously solved numerically in ANSYS FLUENT by using the Finite Volume Method (FVM). As the governing equations are nonlinear, the performance and accuracy of the calculation depend on the mesh and solver. A structured mesh is generated with GAMBIT software. To ensure the accuracy and the mesh independency of the solutions, 24,990 structured elements are used over the entire computational domain after testing several grid densities with refining zones at the junction between the tabs and the electrode domain, as illustrated in Figure 3.16. The energy equations are fully coupled with the electrical model by means of the lookup table as illustrated in Figure 3.17. For spatial discretization, the 1st-Order Implicit formulation is used. At each time step (taken at 1 second), the temperature is solved by using the SIMPLE (Semi-Implicit Method for Pressure-Linked Equations) Solver Algorithm. For each time step, the convergence is reached where the relative tolerance is below than 10^{-3} for all variables. Then, the time step progresses until the cut-off potential is reached

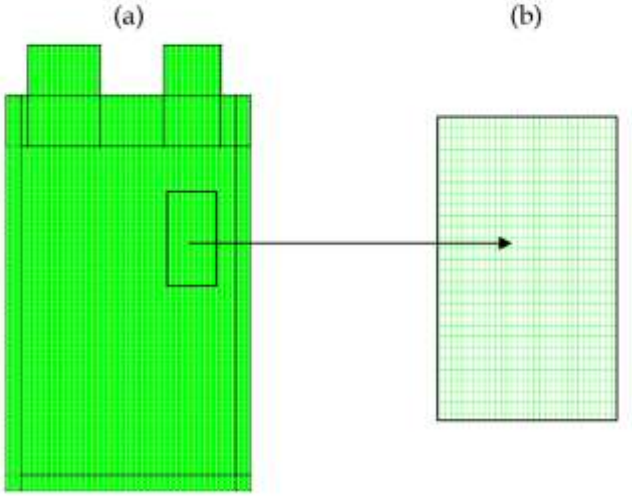

Figure 3.16: Meshing of battery (a), and zoom vision (b)

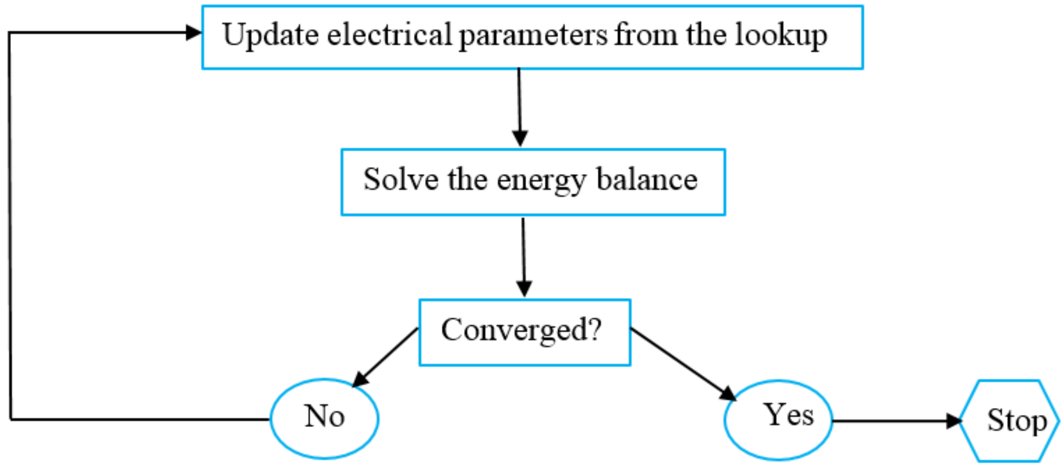

Figure 3.17: Procedure of the numerical solution at each time step

3.5.2 Model validation

The simulation results are compared with the experimental results during capacity tests at different current rates and operating conditions. The full modeling of thermal distributions at different time steps of 1 I_t charge and discharge, as shown in in Figure 3.18 and Figure 3.19, is compared with the thermal imager measurements. The comparison shows a good agreement, except at the tabs, because the tabs are connected during test to a heavy copper block, which conducts a lot of heat. This indicates that the battery surface temperature is nearly uniform, except in the middle where the maximum temperature is measured by the thermocouple T6. The maximum temperature gradient on the surface of the battery is about 0.7°C. This type of distribution is only shown for low current rate (less than 1 I_t) because the density of heat generation by tabs are negligible compared to the heat density of the battery's active material.

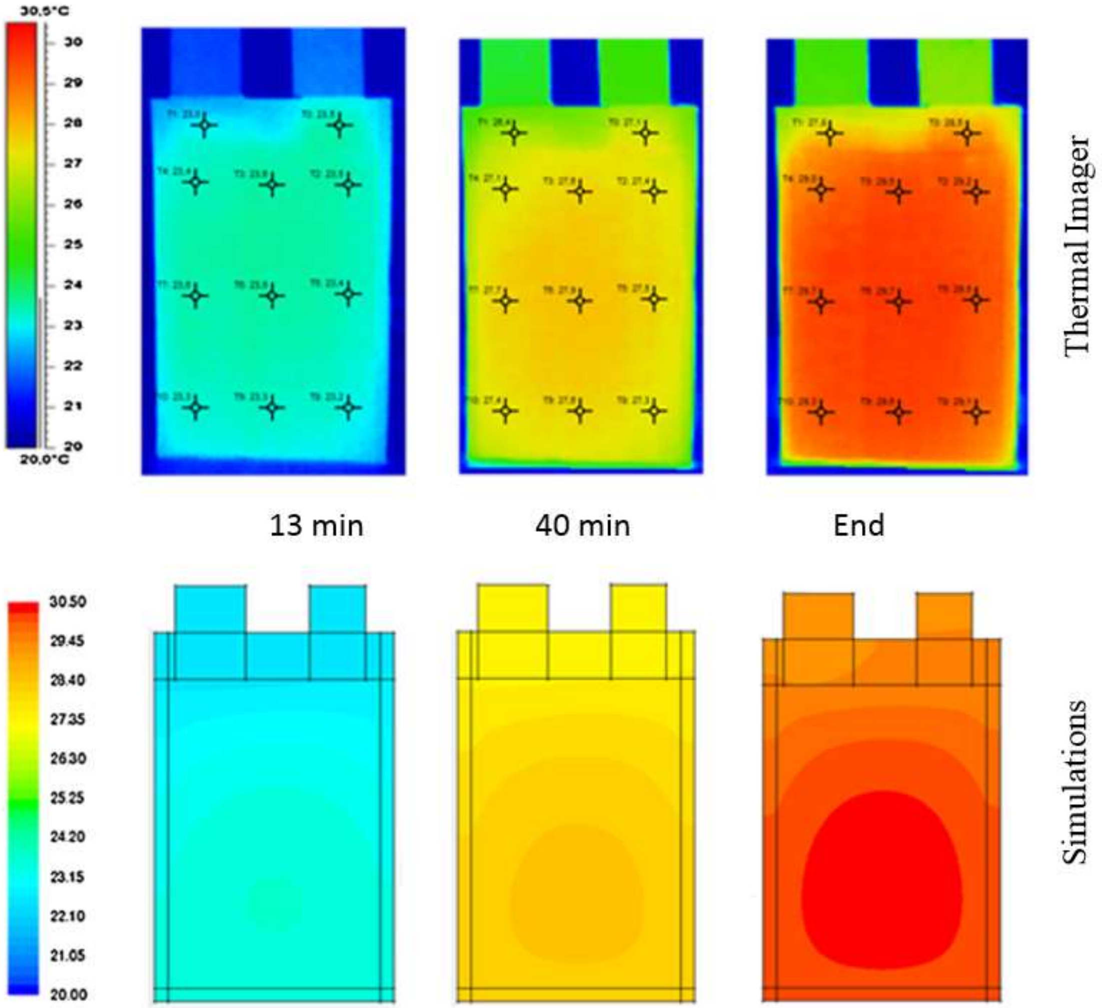

Figure 3.18: Thermal distributions based on thermal imager and modeling at 1 It charge current rate and 20°C of environment temperature

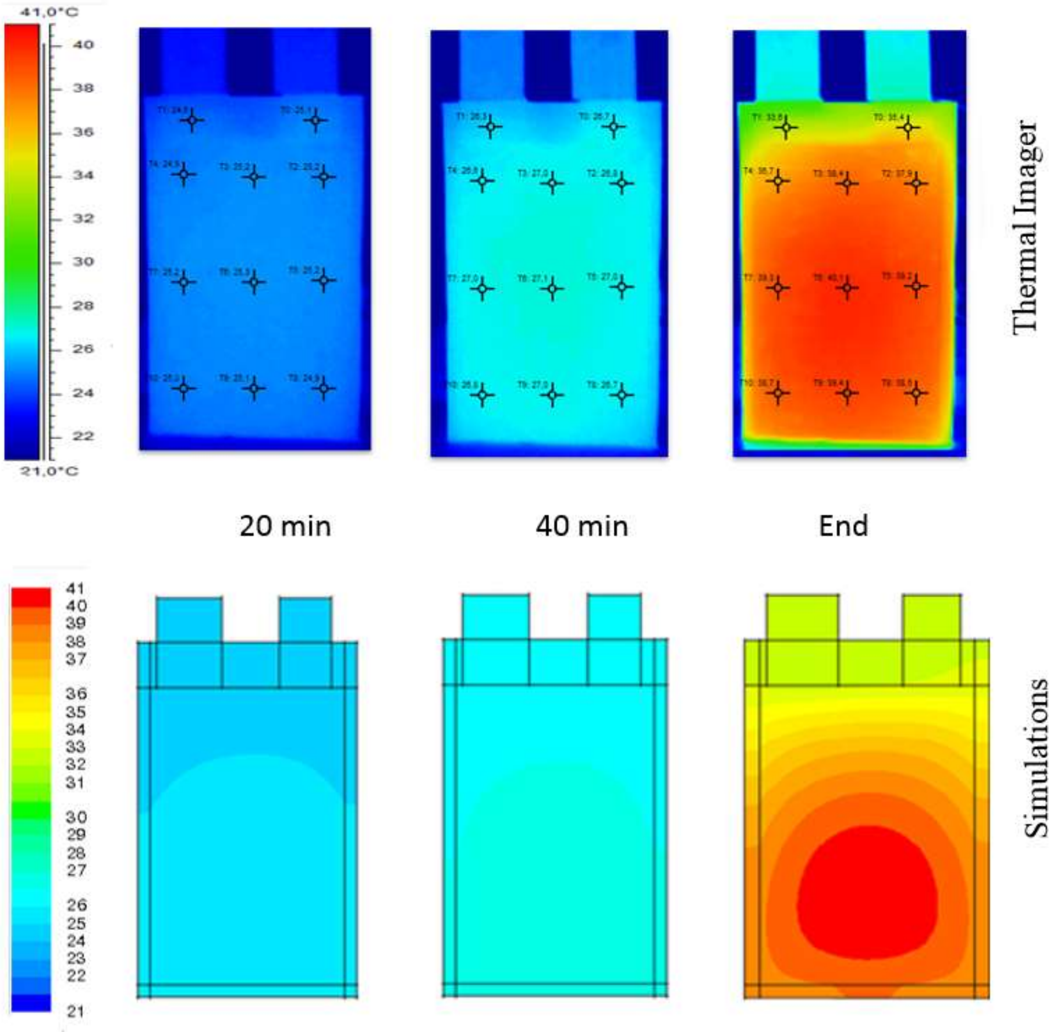

Figure 3.19: Thermal distributions based on thermal imager and modeling at 1 It discharge current rate and 20°C of environment temperature

As observed in Figure 3.20 and Figure 3.21, the simulation results at different charge and discharge rates are validated by the experimental results. The relative error is less than 3% at low current rate and 7% at high current rate. Similar results validation, based on the comparison between simulations and thermal camera results at different current rate, are included in Figure 7.7, Figure 7.8 and Figure 7.9 in Appendix I, section 7.2. By increasing the current rate, the battery temperature raises more due to the increase of the heat generation in the electrodes and tab domains.

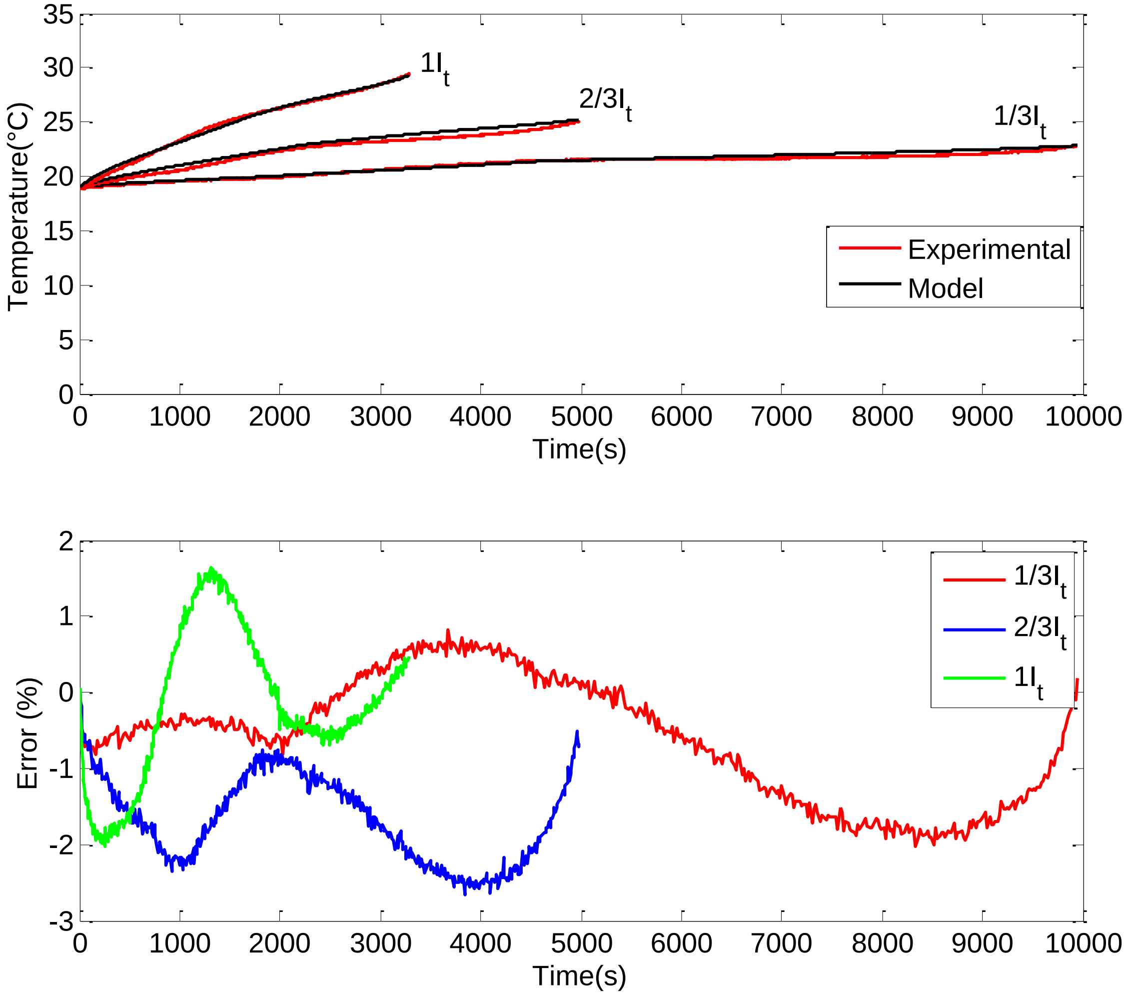

Figure 3.20: Maximum temperature and relative error variations from model and experiment during different charge current rates and 20°C of environment temperature

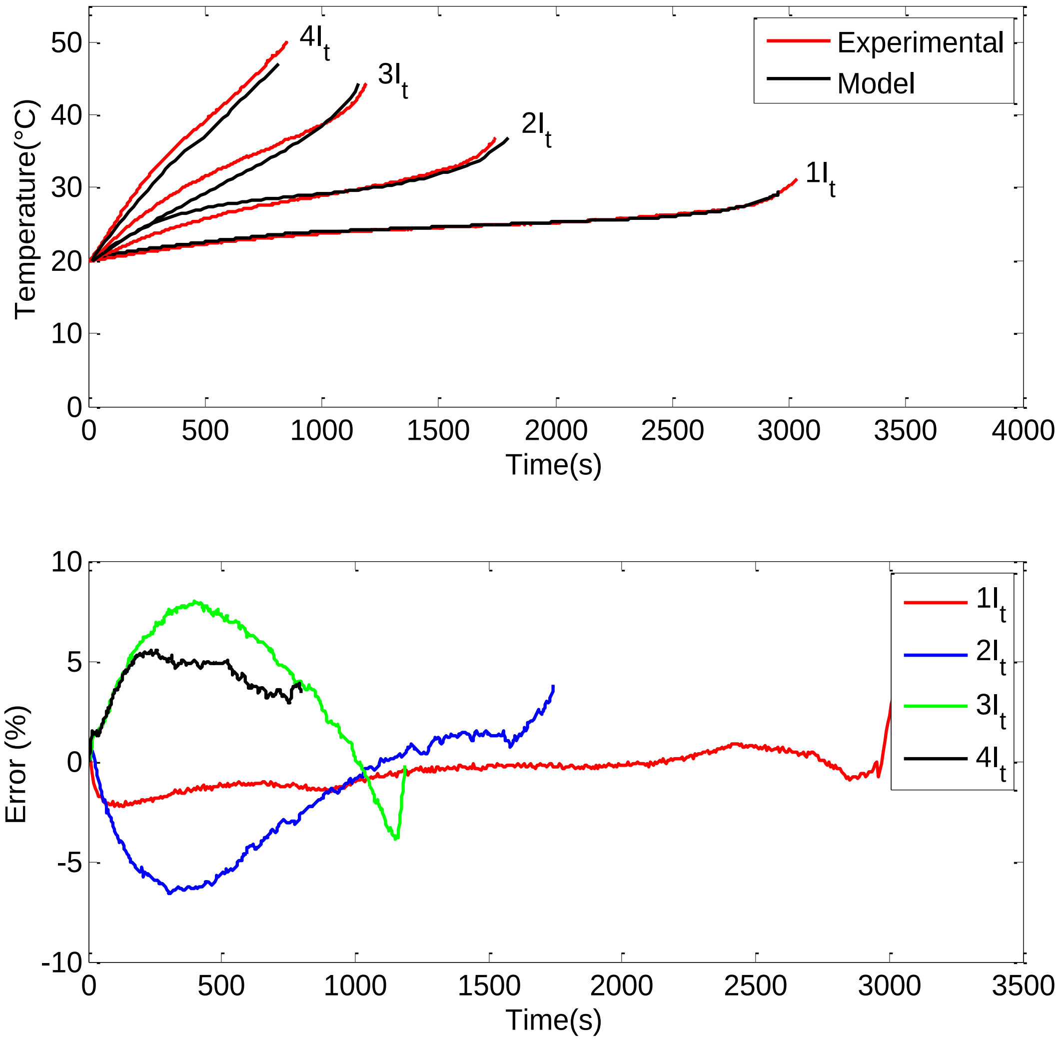

Figure 3.21: Maximum temperature and relative error variations from model and experiment during different discharge current rates and 20°C of environment temperature

Figure 3.22 shows the temperature distribution at high discharge rate (4 I_t). The maximum temperature is located near the positive tab due to the high amount of heat generated at the positive tab, because of the high resistivity of aluminium compare to the copper material at the negative tab.

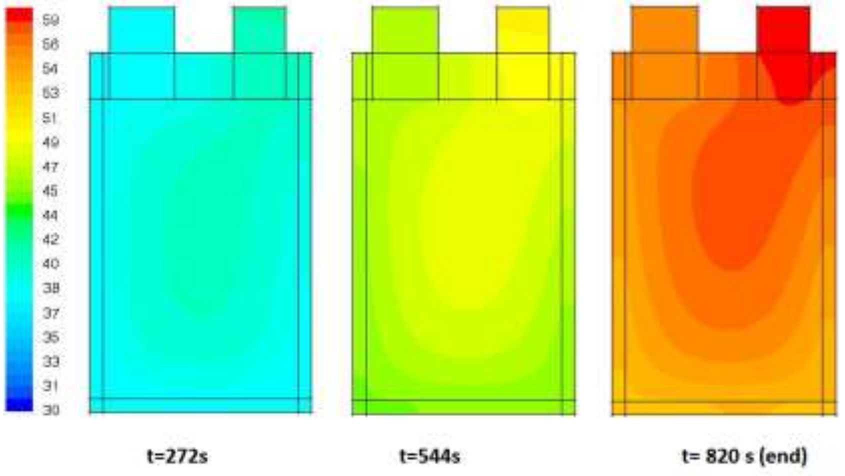

Figure 3.22: Thermal distributions based on modeling at 4It discharge current rate at 20°C of environment temperature

3.6 Conclusions

In this work, a 2D-thermal model is developed for a large size of Li-ion pouch battery for BEVs, which is able to predict the surface temperature distribution of the battery at different operating conditions. The simulation results are in good agreement with the experimental results where the relative errors are less than 7%. A new battery thermal parameter estimation is developed to estimate the related thermal parameters by using the first order Cauer model. This model involves a primary calculation in order to calculate the percentage of heat flows through each side of the cell. At high current rate (more than 1 I_t) the generated heat is higher than the dissipated heat and the maximum temperature is located near the positive tab. However, at low current rate, the maximum temperature is located at the middle of the battery cell.

Chapter 4: Pouch Cell Design: Impact of Tab Location

4. Pouch Cell Design: Impact of Tab Location

4.1 Goal

In this chapter, different pouch cell designs, with different tab locations, have been investigated in term of performance, current density, potential and heat distributions by using advanced three-dimensional electrochemical-thermal modeling. The model is first validated with experimental data at different current discharge rates. Afterwards, the electrochemical, thermal and electrical behaviors over each cell design under high discharge rate (4 I_t) are compared between configurations.

4.2 Introduction

As mentioned in chapter 3, large-format, and high-capacity Li-ion pouch cells are widely used in PHEVs and EVs, and the temperature has a strong influence on the battery performance and safety. As found in chapter 3, the increase of the current amplitude during the charge/discharge process can subject the large format battery cell to non-uniform temperature distributions. In Pesaran et al work [43] it is mentioned that the temperature gradient within the cell should be less than 5 °C in order to guarantee good battery performance and a long lifetime. Therefore, good cell design is necessary to avoid non-uniform distribution of the electrical and thermal parameters that can lead to a non-uniform utilization of the active material.

Particle size, electrode coating thickness and current collector dimensions also have a significant impact on battery behavior. Recently, Zhao et al [44] showed that small coin cells provide much better performance and energy density than large format cells, where uneven current density is observed, leading to lower utilization of the active material. In addition, the impact of the arrangements and number of the current collecting tabs is investigated in the cases of wound design [44], [45] and stacked layer design [46], [47]. As a function of the number and location of tabs, the electron pathways become more or less long and thereby cause an increase or decrease of the ohmic resistance responsible for the voltage loss. In order to investigate these battery designs, electrochemical modeling techniques are more appropriate than electrical modelling because they show a clear relation between the electrochemical parameters and battery geometry. As mentioned in chapter 2, the 1D electrochemical models are more suitable for describing small-format battery behavior. They also provide average values for large-format batteries without taking into account the collector tabs. However, they are not sufficient to handle the issue of non-uniform thermal, electrical and electrochemical variable distributions observed in large-format cells. Recent advances in numerical simulation techniques applied to Li-ion batteries have given more attention to the development of 2D axisymmetric and 3D electrochemical-thermal modeling [44], [45], [86], [87], [114]. This chapter presents an extensive fully coupled three-dimensional (3D) simulation of electrochemical-thermal modelling, describing the behavior of large $LiFePO_4$ pouch cells. Different pouch cell designs with various tab locations have been investigated in term of performance and distribution. The model is first validated with experimental data at different discharging current rates. Afterwards, the electrochemical, thermal and electrical behaviors of each cell design under high discharge rate (4 I_t) are compared in order to select the best configuration. Finally, the impact of the tab width on the temperature, potential and current density distributions is also investigated in depth.

4.3 Model Description

4.3.1 Model assumptions and geometry features

A 3D electrochemical-thermal model is developed for the same pouch cell as presented in chapter 3. As it is well-known, the battery is composed of several layers (current collectors (CC) (positive and negative) with collecting tabs, the positive electrode (PE), the separator and the negative electrode (NE)) in sandwich structure as described in chapter 2, section 2.2.1. Since the modeling of all layers required a lot of meshing effort and then long computational times, 1D electrochemical coupled with the thermal model applied to a single cell layer (composed by NCC, NE, separator, PE, PCC) has been used in several works [115]–[118]. The model was validated by comparing simulation to the experimental test performed on the whole battery. Therefore a single electrode plate pair approach can be modeled to describe the pouch cell behaviors. In this approach the electrochemical variable in length and large directions have been considered. The sandwich structure can be considered as a parallel circuit. The single cell potentials are almost equal. The total current is almost equal to the sum of the currents in each single cell. For this reason, we downscale the current by taking into account the current passing through representing other cell layers. The whole layers of the cell are bathed in the electrolyte (2 mol/L LiPF6 in EC/DMC solvent) as illustrated in Figure 4.1.

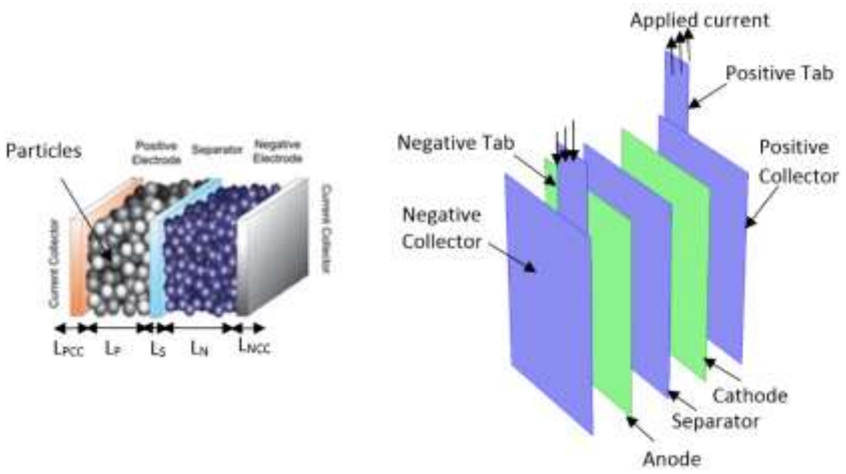

Figure 4.1: single electrode plate pair configuration and component thicknesses

Several designs of single electrode configuration are investigated, where the collecting tab positioning changes as shown in Table 4.2.

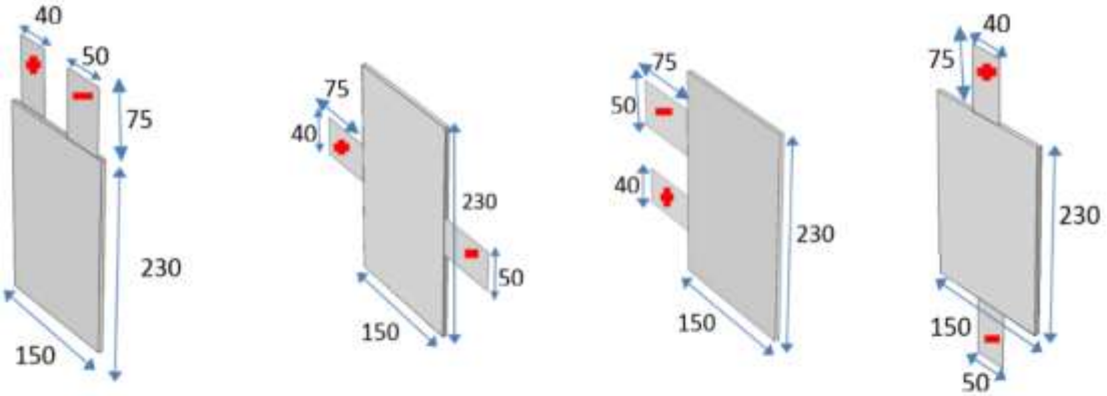

(a) Case1 (b) Case 2 (c) Case 3 (d) Case 4

Figure 4.2: different designs and dimensions (mm) of pouch cell

The geometrical details such as the electrodes, separator and current collectors, and tabs thicknesses and the particle radius are included in Table 8.1, in Appendix II, section 8.3.

4.3.2 Electrochemical modeling

The electrochemical process during discharge is mainly represented by energy conversion from the chemical to the electrical, and during charge the inverse process occurs. These conversions occur at the solid electrolyte interface (SEI) by mean of electrochemical reactions as described below:

$$Li_yFePO_4 \underset{discharge}{\overset{charge}{\longleftrightarrow}} Li_{y-z}FePO_4 + zLi^+ + ze^- \tag{4.1}$$

- At the negative electrode:

$$Li_xC_6 \underset{charge}{\overset{discharge}{\longleftrightarrow}} Li_{x-z}C_6 + zLi^+ + ze^- \tag{4.2}$$

In the charge process, lithium ions are deintercalated from the cathode material and an equal number of lithium ions and electrons are produced. Then the lithium ions migrate through the electrolyte where they are intercalated into the anode. The passing of an electron through the collectors compensates each passage of a lithium ion into the internal circuit of the battery because the electrons cannot cross through the separator. These processes are exothermic due to the ohmic losses, activation losses, and other irreversible processes. According to the above physical description, lithium-ion batteries are modeled using porous electrode theory coupled with various transport and reaction mechanisms. This theory determines the concentration of lithium ions, the potential in the electrolyte and in the intercalation particles, as well as in the collectors and tabs. The electrochemical reaction kinetics for lithium-ion intercalation/deintercalation at the SEI is also estimated. As the physical parameters depend on the cell temperature, the porous electrode theory is coupled with the energy balance. All the required variables are listed in Table 4.1.

Domain	Variable name	Symbol	SI Unity	Variable
Particle	Li concentration in solid phase	$c_{1,j}(j = p, n)$	mol. m^{-3}	t, r, x, y, z
Porous Electrode	Li+ concentration in the electrolyte Potential in solution phase Potential in solid phase Surface reaction rate	c_2 Φ_2 Φ_1 $J_j(j = p, n)$	mol.m^{-3} V V $\text{mol.m}^{-2}.\text{s}^{-1}$	t, x, y, z
Cell	Temperature Potential in collector& Tabs	T $\Phi_{cc,j}(j = p, n)$	K V	t, x, y, z

Table 4.1: variables of the model

The battery cell is divided into several geometrical domains. Each corresponds to a particular physical length scale as described in Figure 4.1. The dynamic performance of a lithium-ion cell is characterized by the solution of the electrochemical and thermally coupled equations as summarized in Table 4.2.

Physics	Governing equations and boundary conditions	Eq. Number
Mass balance in solid phase	$\frac{\partial c_{1,j}}{\partial t} = \nabla . \left(D_{1,j}\ \nabla . c_{1,j} \right)$ $-\nabla . c_{1,j}\Big\|_{r=0} = 0\ ; \quad -D_{1,j}\ \nabla . c_{1,j}\Big\|_{r=R_{s,j}} = \frac{J_{n,j}}{S_{a,j}\ F}\ ; \ \ (j = p, n)$	(4.4)
Mass balance in electrolyte phase	$\varepsilon_2 \frac{\partial c_2}{\partial t} = \nabla . \left(D_2^{eff}\ \nabla c_2 \right) + \frac{S_{a,j}\ J_{n,j}}{F} (1 - t_+)\ ; \quad D_2^{eff} = D_2 \varepsilon_2^{\gamma_2}$ $-\nabla . c_2\Big\|_{\substack{interfaces \\ NE/CC^- \ and \ PE/CC^+}} = 0\ ; \ -\nabla . c_2\|_{\substack{interfaces \\ PE/SP}} = -\nabla . c_2\|_{\substack{interfaces \\ NE/SP}}$	(4.5)
Electron transport in the solid phase	$\nabla . i_1 = -S_{a,j}\ \left(J_{n,j} + C_{dl} \left(\frac{\partial \Phi_1}{\partial t} - \frac{\partial \Phi_2}{\partial t} \right) \right)\ ;$ $i_1 = -{\sigma_1}^{eff}\ \nabla \Phi_1; \quad \sigma_1^{eff} = \sigma_1 \varepsilon_1^{\gamma_1}; \ \ S_{a,j} = \frac{3\varepsilon_{1,j}}{R_{s,j}}$ $-{\sigma_1}^{eff}\ \nabla . \Phi_1\Big\|_{\substack{interfaces \\ NE/CC^- \ and \ PE/CC^+}} = i_{N,j}\ ; \quad -{\sigma_1}^{eff}\ \nabla . \Phi_1\Big\|_{\substack{interfaces \\ NE/SP \ and \ PE/SP}} = 0; \qquad (j = p, n)$	(4.6)
Ionic transport in the solution phase	$\nabla . i_2 = S_{a,j}\ J_{n,j}$ $i_2 = -{\sigma_2}^{eff}\ \nabla \Phi_2 + \frac{2R\ T\ {\sigma_2}^{eff}}{F} (1 - t^+\ ) \left(1 + \frac{dln\ f_\pm}{dln\ c_2} \right) \nabla ln\ c_2$ $\nabla . \Phi_2\Big\|_{\substack{interfaces \\ NE/CC^- \ and \ PE/CC^+}} = 0$	(4.7)
Electrochemical kinetics	$J_{n,j} = J_{0,j} \left[exp \left(\frac{\alpha_a\ F}{RT} \eta_j \right) - exp \left(-\frac{\alpha_c\ F}{RT} \eta_j \right) \right] \ ; \quad J_{0,j} = Fk_{0,j} c_2^{\alpha_a} \left(c_{1,j,max} - c_{1,j,surf} \right)^{\alpha_a} c_{1,j,surf}^{\alpha_c}$ $\eta_j = \Phi_1 - \Phi_2 - U_j\ ; \quad c_{1,j,surf} = c_{1,j}\|_{r=R_s}$	(4.8)
Potential in collectors & Tabs	$\nabla . \left(-\sigma_{cc,j} \nabla \Phi_{cc\,j} \right) = -i_{N,j}$ at the PE/CC and NE/CC $i_{N,J} = 0$ at the tabs $n . \left(-\sigma_{cc,j} \nabla \Phi_{cc,j} \right) = i_{app,j} = \frac{I_{app}}{N * A_{tab}}$ at top of the tab $\Phi_{cc,n} = 0$ (*j=n*) at the top of the negative tab	(4.9)
Energy balance	$\rho_j c_{p,j}\ \frac{dT}{dt} - \lambda_j\ \nabla^2 T = q_{rea,j} + q_{act,j} + q_{ohm,j}$ $\lambda_j\ \ \Delta T\Big\|_{CC \ and \ Tabs/ambient} = h(T - T_a)$	(4.10)
reversible heat	$q_{rea,j} = S_{a,j}\ J_{n,j} \left(T \frac{dU_j}{dT} \right)$	(4.11)
polarization heat	$q_{act,j} = S_{a,j}\ J_{n,j}\ \ \eta_j$	(4.12)
Ohmic heat	$q_{ohm} = -i_1 \nabla . \Phi_1 - i_2 \nabla . \Phi_2 - i_{cc,j} \nabla . \Phi_{cc,j}\ \ ; (j = p, n)$	(4.13)

Table 4.2: Governing equation and boundaries conditions [84]

The electrodes are assumed to be porous material consisting of a lattice of several spherical particles (with ε_s the corresponding volume fraction) immersed in the electrolyte (with ε_l the corresponding volume fraction). The electrochemical processes and transport phenomena in the porous electrode and particles are described by an extended 3D porous electrode model derived from the work of Newman et al. [84]. The intercalated lithium concentration in the spherical particle is computed from the mass balance (Fick's second law), as shown in Eq. (4.4). Due to symmetry, the lithium flux is equal to zero at the center of the particle, while at the surface of the particle (SEI), the lithium flux is equal to the surface electrochemical reaction rate (J_j). Furthermore, the lithium-ion transport in the electrolyte phase is modeled by using the concentrated solution theory as shown in Eq. (4.5), where the flux is equal to zero (no reaction) at the electrode/collector interfaces; additionally there is continuity of species flux in the electrolyte at the electrode/separator interfaces. At the SEI, the surface electrochemical reaction rate is represented by the Butler-Volmer equation as shown in Eq. (4.8). The transport and kinetic parameters are dependent on the exchange current density, the overpotential and temperature variation of the system. The potential in the solid phase is derived from the charge balance governed by Ohm's law as described by Eq. (4.6). At the electrode/separator interfaces, there is no flux of charge (the separator acts as a barrier for the passage of the electrons), while at the electrode/collector interfaces the charge flux corresponds to the total current in the circuit. The potential in the electrolyte phase is also governed by Ohm's law, defined as a function of reaction current density and the local concentration of lithium, as shown in Eq. (4.7), where at the electrode/collector interfaces the potential gradient is equal to zero. A continuity of charge flux is considered in the electrolyte at the electrode/separator interfaces. The governing equations for the charge balance in the collectors are given by Eq. (4.9), where no transverse current is flowing through the tab domains. The current density is applied at the top cross-section of the positive tab, while the potential at the top of the negative tab is fixed at zero.

4.3.3 Thermal modeling

The electrochemical model is coupled to the thermal model in order to estimate the cell temperature change. As mentioned in chapter 3, a two-dimensional transient model can be used to model the thermal behavior of a pouch cell. Therefore a single cell sandwich, which can be likened to a 2D geometry is suitable to describe the thermal behavior. From this assumption, the heat equation is solved in the same geometry as used in the electrochemical model to ensure better spatial coupling of these two physics. As shown in Eq. (4.10), the energy balance is solved at each layer (electrodes, separator and current collectors and tabs included). Heat generation is mainly composed of the contributions of polarization heat, ohmic heat and reversible heat as expressed in Eq. (4.11)-(4.13). At the interfaces between cell components (current collectors/electrodes and electrodes/separator), the continuity of the heat flux is applied as an internal boundary condition. Furthermore, to match the experimental conditions, model validation is conducted by taking into account convective heat transfer. Convective heat transfer is calculated using the methodology as described in chapter 3 and included in Table 8.1 in Appendix II, section 8.3. Afterwards, the model is performed in adiabatic conditions in order to compare the performances and behaviors of the different cell designs.

4.3.4 Model Input

The effective parameters are obtained by multiplying the porosity (ε_j) power to the tortuosity (γ_j, Bruggeman coefficient) of the porous electrode. In addition, electrochemical parameters such as the diffusion coefficient of lithium in the solution and solid phases, the ionic electrical conductivity of the solution phase, the open circuit potential, the entropy coefficient and the reaction rate are affected by temperature change through the Arrhenius law and other empirical relations, as listed in Table 8.2, in Appendix II, section 8.3. To compute this model, the dimensions of the different components as well as the electrochemical and thermal parameters are needed. The used input data come from the literature and are listed in Table 8.1, in Appendix II, section 8.3.

4.3.5 Numerical method and Validation

4.3.5.1 Numerical aspects

All equations are simultaneously solved numerically in COMSOL Multiphysics 4.3b with the Batteries and Fuel cells toolbox by using the Finite Elements Method (FEM). As the governing equations are highly nonlinear, the performance and accuracy of the calculation depend heavily on the mesh and solver. A hexahedral mesh is used, generated by the swept method. To ensure the accuracy and the mesh independency of the solutions, 16,700 hexahedral elements are used over the entire computational domain after testing several grid densities with refining zones at each component thickness, especially at the electrolyte and also at the junction between the tab and the current collector, as illustrated in Figure 4.3.

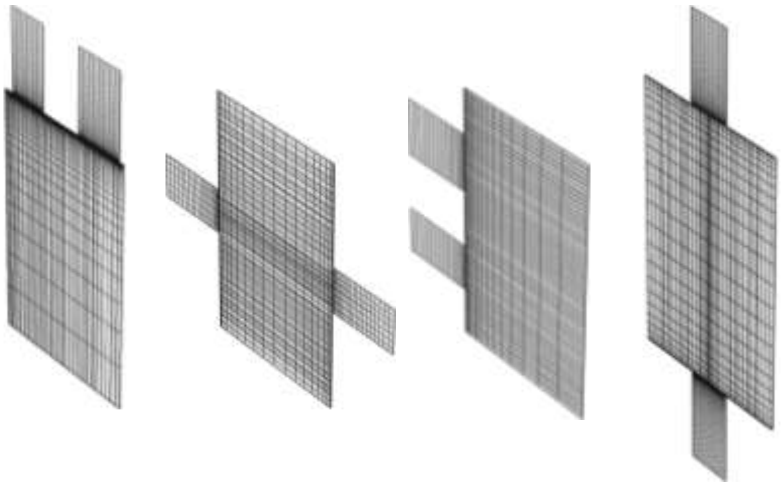

Figure 4.3: Meshing of different cell designs

In order to save memory and time, the equations are coupled, by using the segregated approach as shown in Figure 4.4. At each time step, two segregated steps are considered: first, the temperature is solved by keeping the electrochemical variables constant, and second, the results of temperatures at each mesh nodes are used to update the corresponding local electrochemical parameters and then the local electrochemical variables of each mesh nodes are calculated. The process is repeated at each node until the convergence is reached for all variables. The direct solver PARDISO (Parallel Direct Sparse Solver Interface) was chosen as linear solver. For each time step, the convergence is reached where the relative tolerance is below than 10^{-3} for all variables. Then, the time step progresses until the cut-off potential is reached.

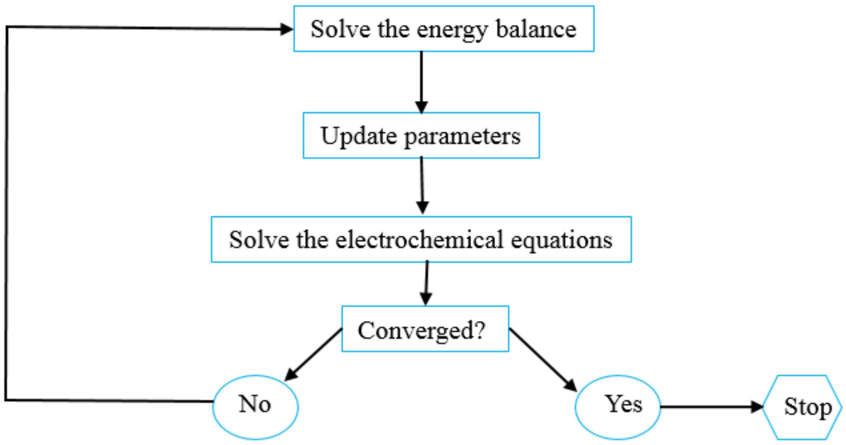

Figure 4.4: Procedure of the numerical solution at each time step

4.3.5.2 Model validation

Different capacity tests were carried out, as mentioned in chapter 3, section 3.4, at various charge current rates (1/3I_t, 2/3I_t and 1 I_t) and discharge current rates (1I_t, 2I_t, 3I_t and 4 I_t) under 20°C of ambient and initial temperatures. Pouch cell with the case 1 design, is used. The electrode dimensions are presented in both Figure 4.2 and Table 8.1 in Appendix II, section 8.3. During the capacity test the cell was cycled between 0%-80% DoD. The maximum and minimum cell potential are 3.65V and 2V, respectively. The battery tester, presented in chapter 3, was used to charge and discharge the battery and also to monitor the current, potential and temperature. 9 thermocouples (75 µm, K-type) were placed on the upper side of the battery surface as illustrated in chapter 3 with the accuracy of ± 0.1°C obtained from [119]. As the capacity of the cell is 45Ah in our simulation, an electrode plate pair is modeled with a capacity of (C=Capacity of the entire cell/total number of the electrode pair (N)), where N is 77, therefore the capacity used in the model is 0.58Ah and the applied current density is equal to

$$i_{app} = \frac{I_t}{N * positive\ tab\ cross - section} \tag{4.3}$$

The initial electrochemical parameters (concentration and potential in electrolyte and solid particle, state of charge) are obtained from model calibration. The model is validated by comparing the experimental temperature given by the thermocouples and the measured potential with the model results.

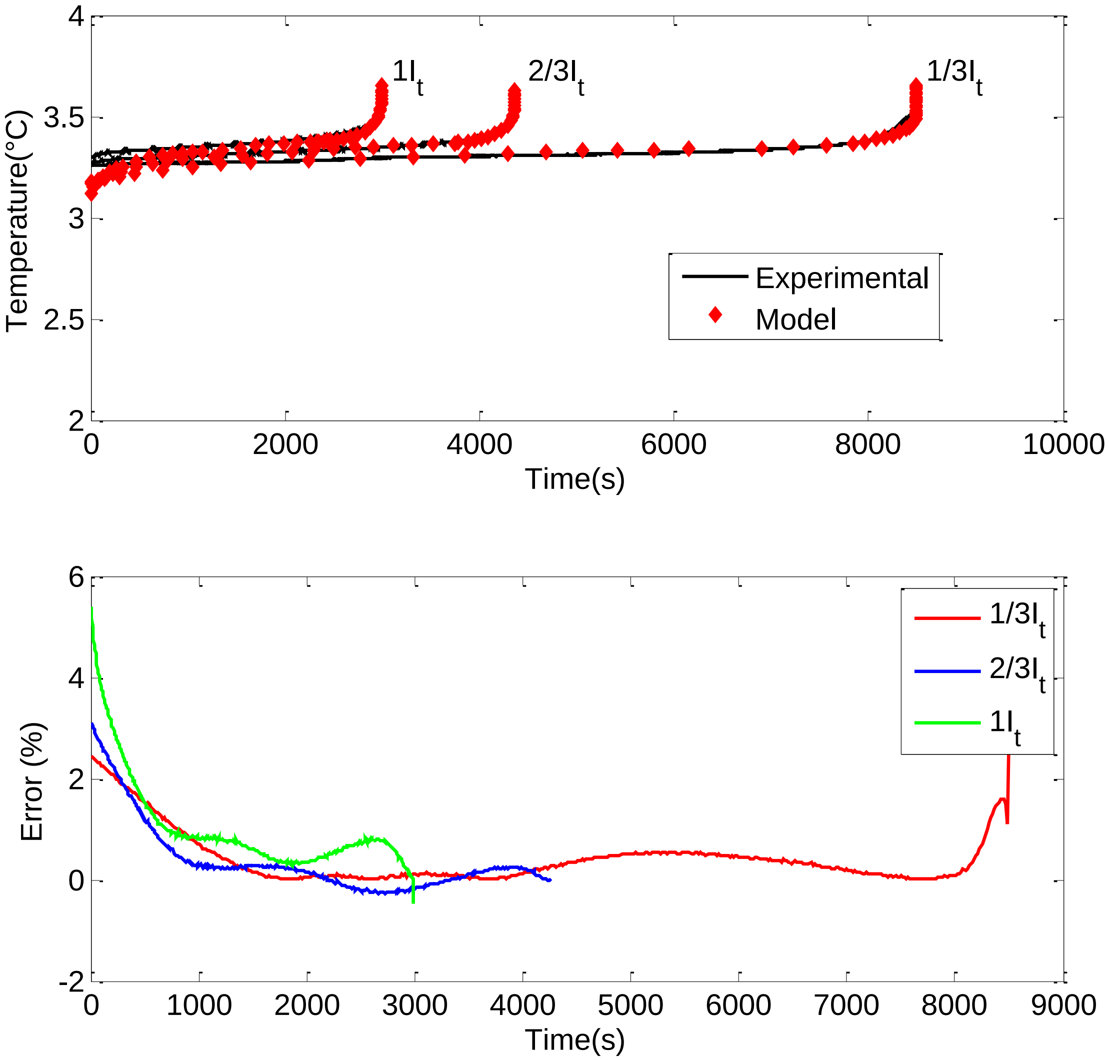

Figure 4.5: Comparison between experimental and modeling of cell potential at different charge current rates and the relative error

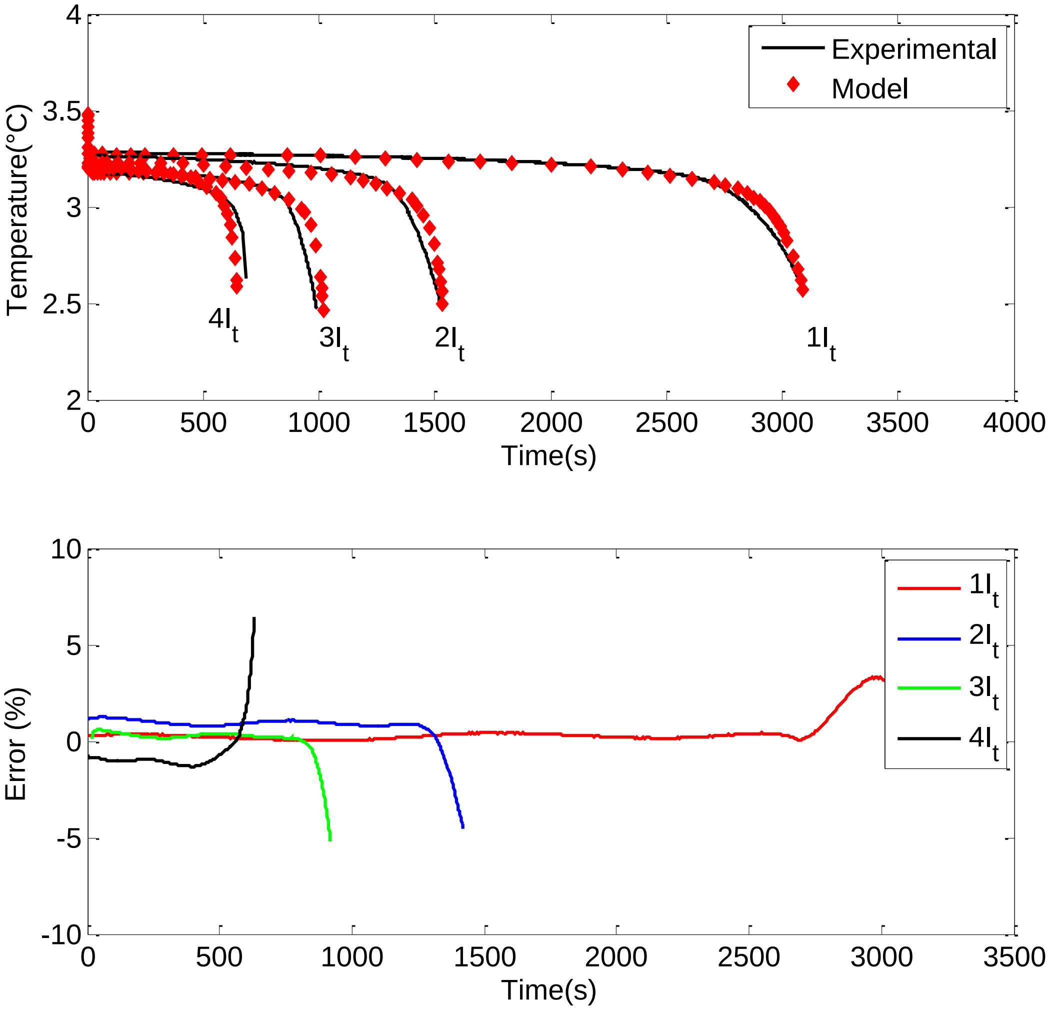

Figure 4.6: Comparison between experimental and modeling of cell potential at different discharge current rates and the relative error

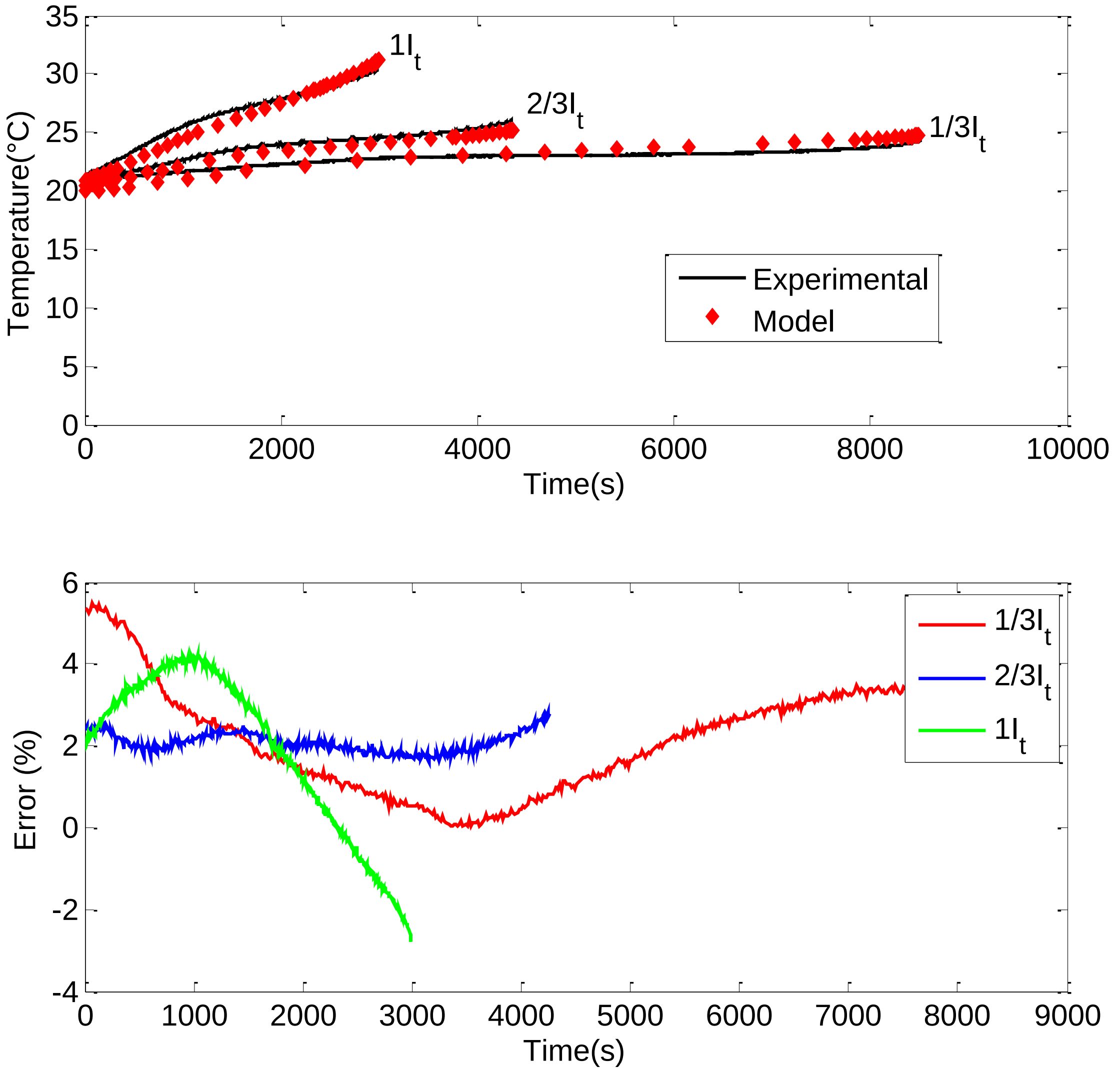

Figure 4.7: Comparison between experimental and modeling of the cell maximum temperature at different charge current rates

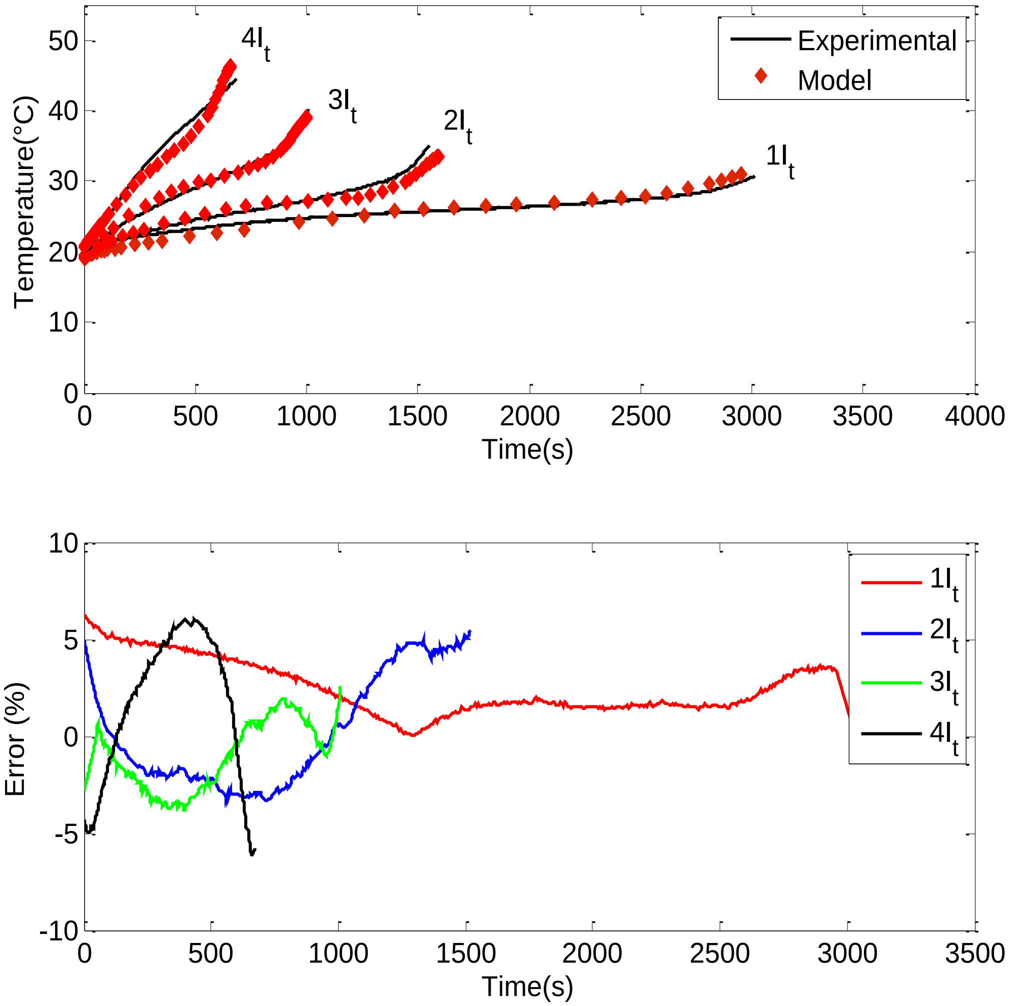

Figure 4.8: Comparison between experimental and modeling of the cell maximum temperature at different discharge current rates

In Figure 4.5 and Figure 4.6, the cell potentials from the simulations are compared with the experimental results and the evolution of the relative error at different constant charge and discharge current rates are represented. The cell potential was computed from the difference between the positive tab and the negative tab potentials. A good agreement is shown between the model and experimental data, except at the end of the discharge and the beginning of the charge processes, where a maximum relative error less than 5%, and this difference may result from the inaccuracy of the electrochemical parameters used, which did not take into account the battery lifespan. In chapter 3, the temperature distribution over the battery surface has been shown to be nearly uniform at low current rate (less than $1I_t$) and highly non-uniform at high current rate (more than $1I_t$), where the maximum temperature is located near the positive tab due to the higher resistance of the aluminium. For this reason, the maximum temperatures from the model and the simulation are compared at different discharge current rates in Figure 4.7 and Figure 4.8. The simulation results, at different discharge rates, validate the experimental results. The maximum relative error is less 6%. At high current rates, the battery temperature rises more due to increased heat generation.

The voltage and temperature distributions throughout the battery at different time step are included in Figure 8.1 and Figure 8.2 in Appendix II, sections 8.2 and 8.3. These results confirm the cell behaviour observed in chapter 3.

4.4 Results and discussion

After validation based on case 1, the model is extrapolated to others designs (case 2, case 3 and case 4) with different tab locations as illustrated in Figure 4.2. The same current density and physical parameters (electrochemical and thermal) are used for all designs. In order to investigate the impact of cell design on battery behavior, the discharge process under 4 I_t rate and 20°C of initial temperature is simulated in adiabatic conditions. In the validation part, convective heat transfer was considered in order to match the experimental conditions.

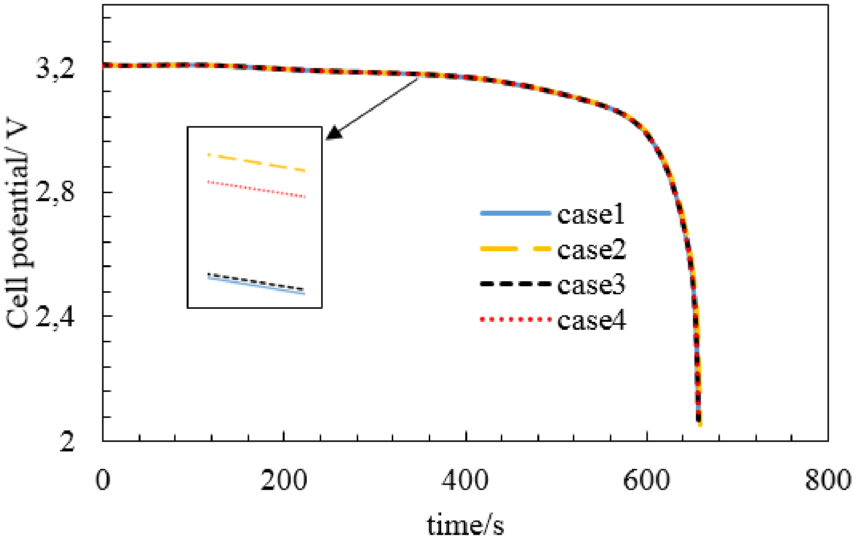

Figure 4.9: average cell potential for different cell designs versus time under 4 I_t discharge current rate

Figure 4.9 shows the average output potential profiles of the different cell designs. The curves have a similar shape, but small potential differences are observed. Case 2 shows less potential drop, followed by case 4, case 3 and case 1. The small differences in potential may be due to the use of cell components with the same dimensions. On the other hand, tab arrangement is responsible for the potential drop by changing the current pathways, which affect the active material utilization.

To highlight the origin of the potential drop, potential distributions relative to tab potential along the negative and positive current collector at 640s of discharge time are plotted in Figure 4.10 and Figure 4.11.

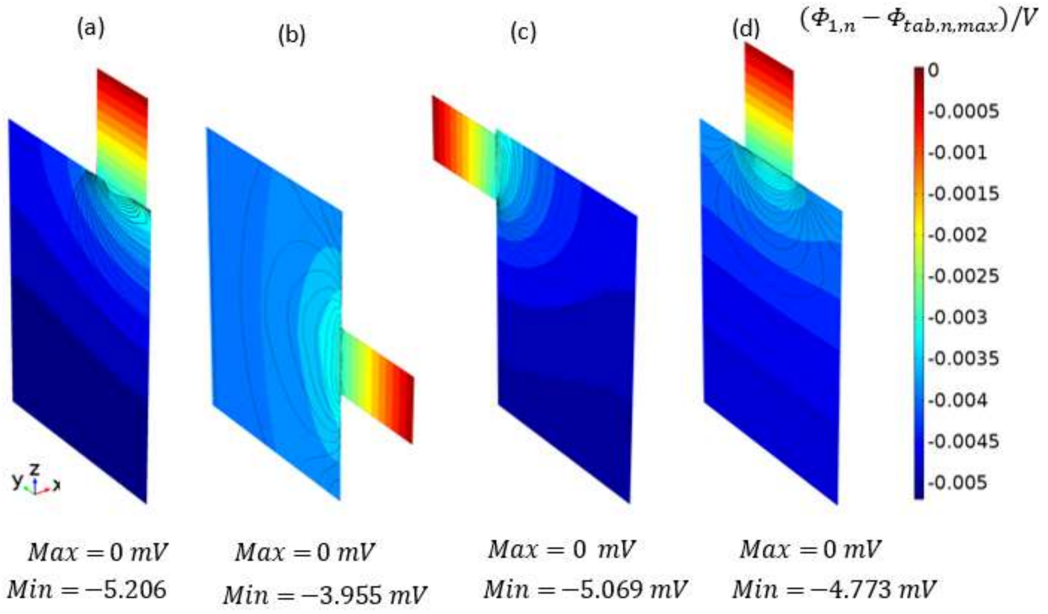

Figure 4.10: Potential gradient over the negative current collectors and tab under 4 I_t discharge current rate at 640s for different cell designs: (a) case 1, (b) case 2, (c) case 3 and (d) case 4

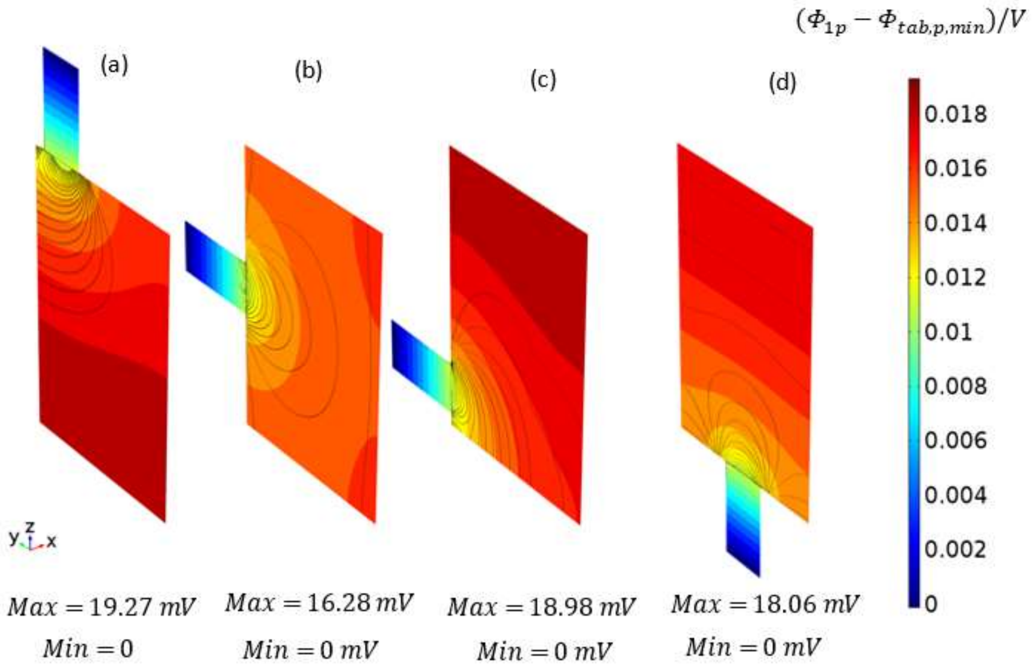

Figure 4.11: Potential gradient over the positive current collectors and tabs under 4 I_t discharge current rate at 640s for different cell designs: (a) case 1, (b) case 2, (c) case 3 and (d) case 4

Regardless of cell design, the potential gradient in both current collectors is mainly localized near the junctions between the tabs and the current collectors. At the beginning of the discharge process, the current enters through the negative tab. Due to resistance and the change of cross-section (between tab and current collector), the current amplitude (represented by the black line) decreases steeply along the flow direction and leads to a gradual potential drop along the negative collector. A similar trend of local overpotential therefore occurs along this current collector. According to the electrochemical kinetics (cf Eq. (4.8)), the same trend of current density is generated in the positive electrode and then flow out through the positive current collector. Finally, the generated current and the resistance of the Al foil are responsible for the non-uniform potential formed in the positive current collector. Comparing the different cell designs, case 2 shows the smallest potential gradient, followed by case 4, case 3 and case 1.

Due to the positions of their tabs, as described in Figure 4.12, L_1, L_2, L_3 and L_4, are proposed to illustrate the maximum current pathways in the current collector of case 1, case 2, case 3 and case 4, respectively. From this figure, it is shown that L_2 (~240 mm) < L_4 (~280 mm) < L_3 (~325 mm) <= L_1 (~325 mm). Resistance ($R= (\rho L_i)/S$) of the negative current collector is lowest with case 2, which generates the lowest potential gradient. In addition, the voltage drops in case 1 and case 3 are almost the same, due to the same maximum current pathways.

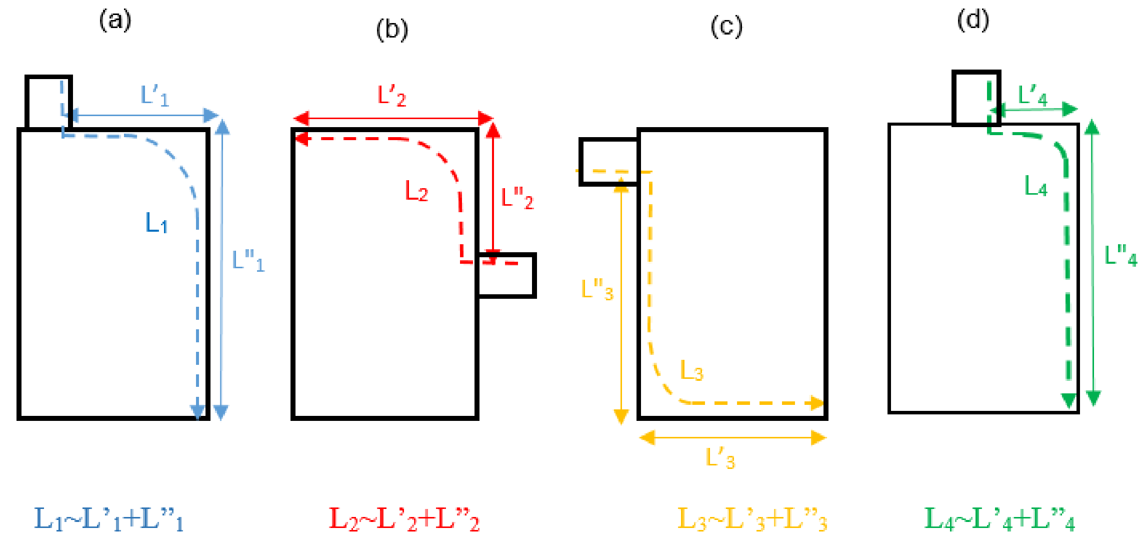

Figure 4.12: maximum current pathway on the negative current collector of different cell designs: (a) case 1, (b) case 2, (c) case 3 and (d) case 4

Due to charge conservation, similar trends of current density and potential gradient are generated in the positive current collector, as shown previously. However, the aluminium positive collector has a larger potential gradient due to its high electrical resistivity compared to the copper negative collector. The non-uniform utilization of active material can be quantified by the local depth of discharge (DoD). The DoD distributions along the electrode length are investigated in the different cell designs. Variation of the DoD through the thickness (due to the lithiation/delithiation mechanism) were examined in the literature [44], [120], [121].

Figure 4.13 and Figure 4.14 show DoD distributions at the middle planes of the anode and cathode. Due to the high local overpotential closer to the positive tabs, the active material in that region is used faster than the rest of the domain and showed higher DoD. As expected, case 2 shows more uniform local DoD compared to other cell designs, due to its uniform local overpotential. This uniform DoD distribution leads to high active material utilization and less potential drop, as observed in Figure 4.9.

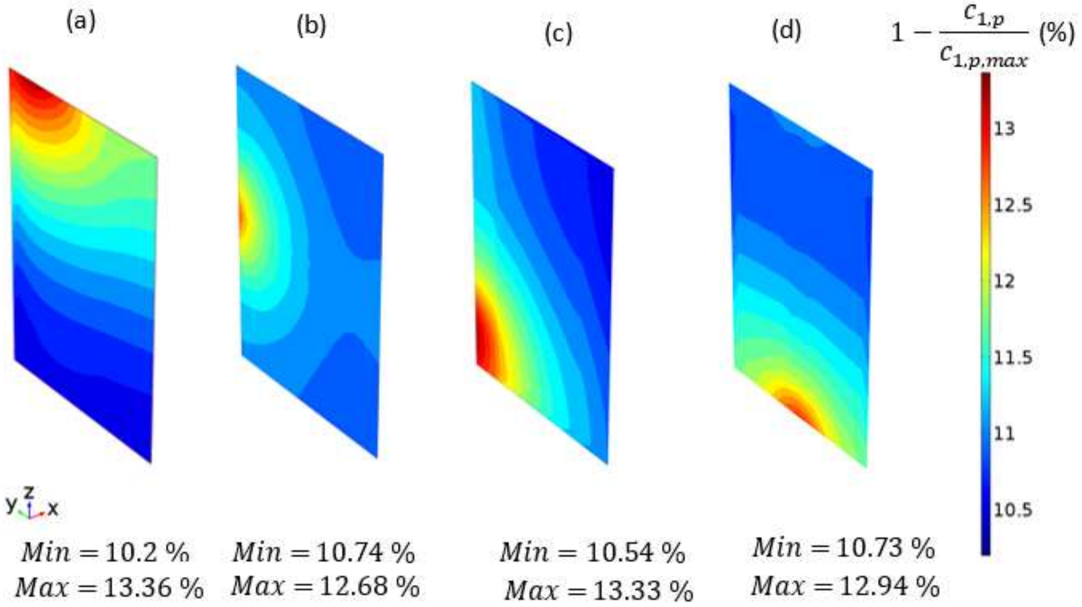

Figure 4.13: DoD distribution over the middle of the cathode under 4 I_t discharge current rate at 640s for different cell designs: (a) case 1, (b) case 2, (c) case 3 and (d) case 4, with $c_{1,p,max}$ the maximum stoichiometric lithium content in the cathode

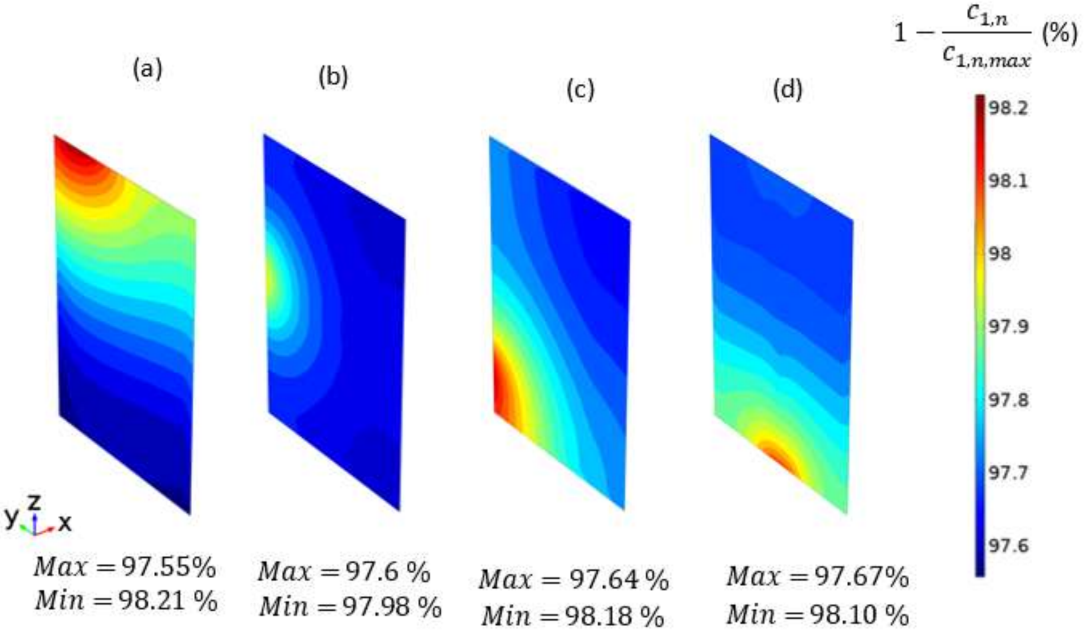

Figure 4.14: DoD distribution over the middle of the anode under 4 I_t discharge current rate at 640s for different cell designs: (a) case 1, (b) case 2, (c) case 3 and (d) case 4, with $c_{1,n,max}$ the maximum stoichiometric lithium content in the anode

Regarding thermal behavior, the average temperature of each cell design is represented in Figure 4.15. All cell designs have temperature profiles with similar trends, but small differences are observable. These differences may arise from the ohmic heat seen in Figure 4.17, which affects the total heat source (Figure 4.18).The high potential gradient drives the increase of ohmic heat (as conductivity multiplied by the gradient of potential squared). As mentioned above, the case 2 design is cycled more uniformly and generates less potential gradient and thus less temperature increase. The same logic can be used to explain the order of temperature increase (Figure 4.15) and deviation (Figure 4.16) among the different cell designs.

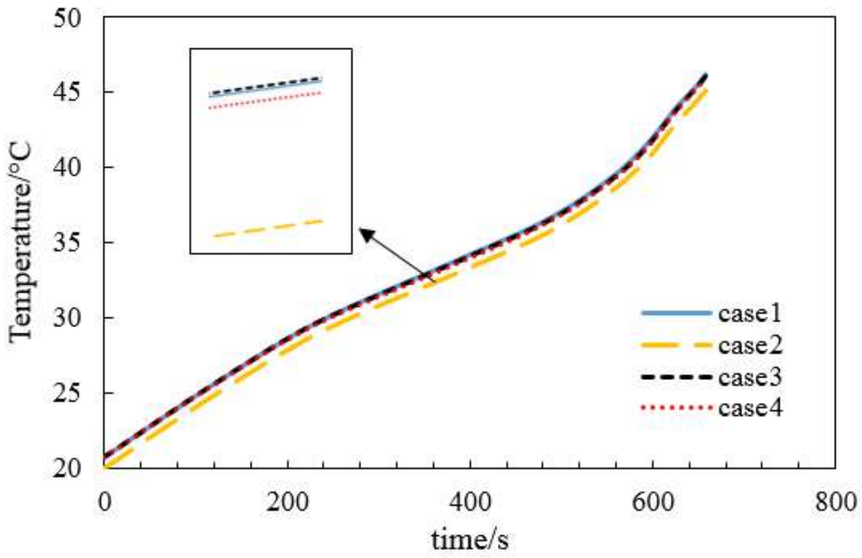

Figure 4.15: Comparison of the average temperature under 4 I_t discharge current rate for the different cell designs

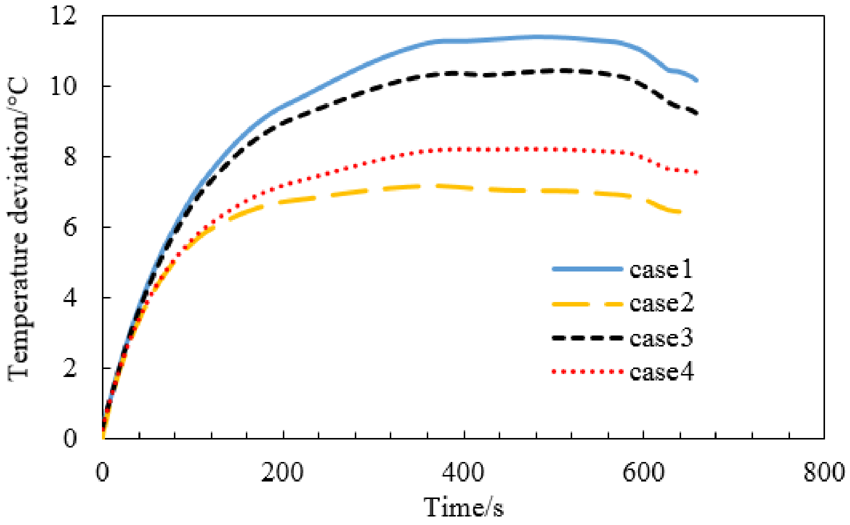

Figure 4.16: Comparison of the temperature deviation profiles under 4 It discharge current rate for the different cell designs

The total heat generation represented in Figure 4.18 shows nonlinear behavior, with a sharp peak followed by a drop in heat generation near the end of the discharge. To gain better insight into this behavior, different heat contributions (reversible and irreversible) are represented in Figure 4.19. It is well known that the reversible heat corresponds to the chemical reaction manifested by an entropy change, while the irreversible heat corresponds to the heat effects of ohmic resistance and polarization. At the beginning of the discharge process, the total heat slightly decreases due to the endothermic reaction (with a negative reversible heat). The contribution of ohmic heat to the irreversible heat is constant throughout the discharge process (cf. Figure 4.17). After that, the rapid increase of total heat corresponds to the exothermic reaction (with a positive reversible heat). Near the end of discharge, the rapid increase of total heat is caused by a significant increase in the irreversible heat by polarization heat.

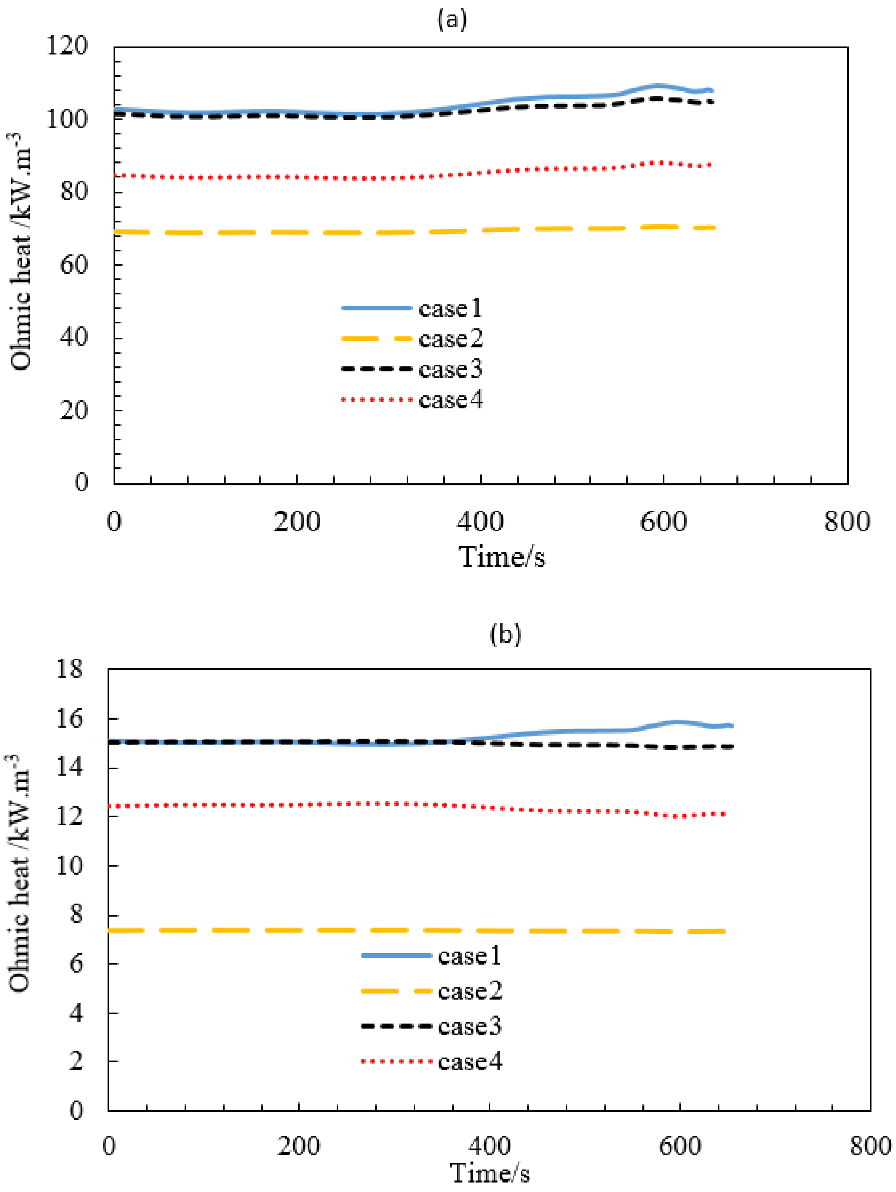

Figure 4.17: average ohmic heat sources profiles at (a) the positive current collector and (b) the negative electrode under 4 I_t discharge current rate

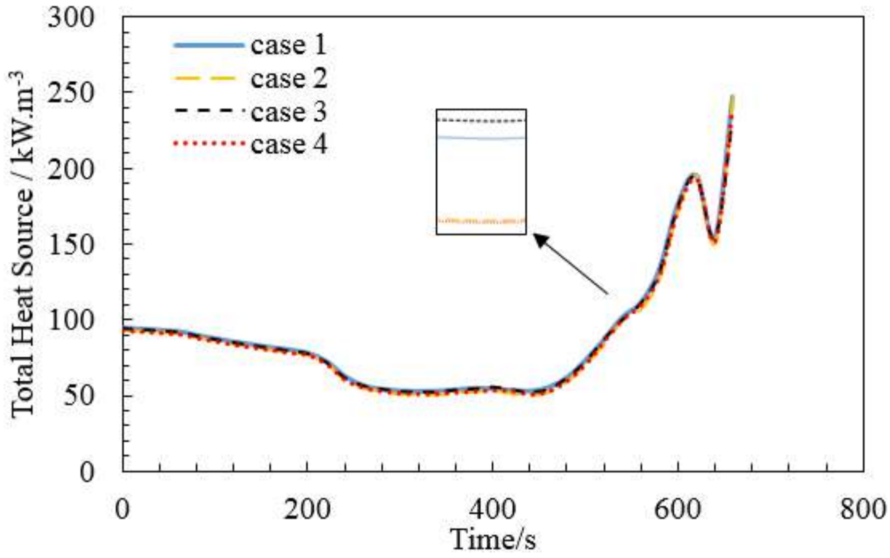

Figure 4.18: Comparison of the average heat source profiles under 4 I_t discharge current rate for the different cell design

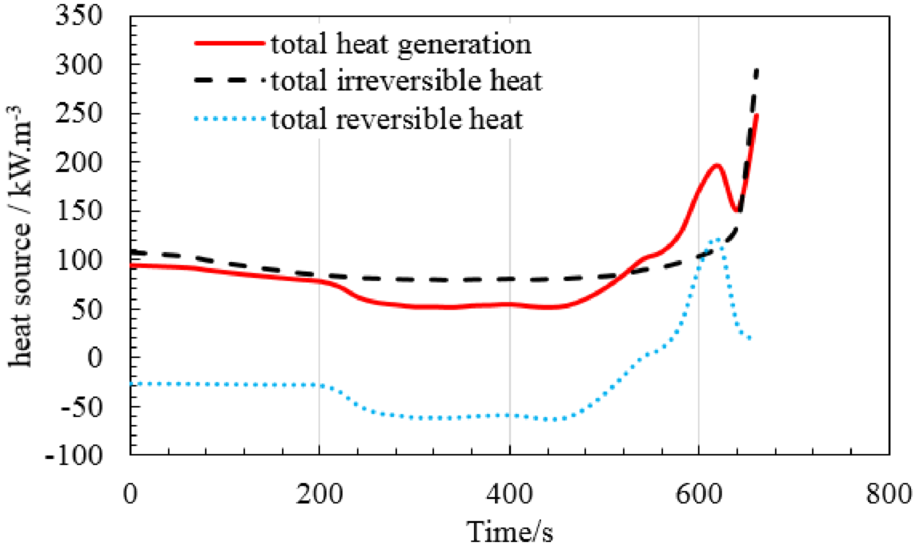

Figure 4.19: total, reversible and irreversible heat sources under 4 I_t discharge current rate for case 2 cell design

Figure 4.20 shows the temperature distribution through the different cell designs near the end of the discharge process. It can be seen that each cell design represents comparatively higher temperature near the positive tab (made of aluminium foil) than the rest of the battery, because of the high electrical resistivity and current density in this area. In addition, the temperature gradient is lower with cases 2 and case 4 due to the uniform potential and current distributions observed previously, which lead to lower heat source gradients. Uniform temperature distribution over the surface could be obtained by balancing the tab widths.

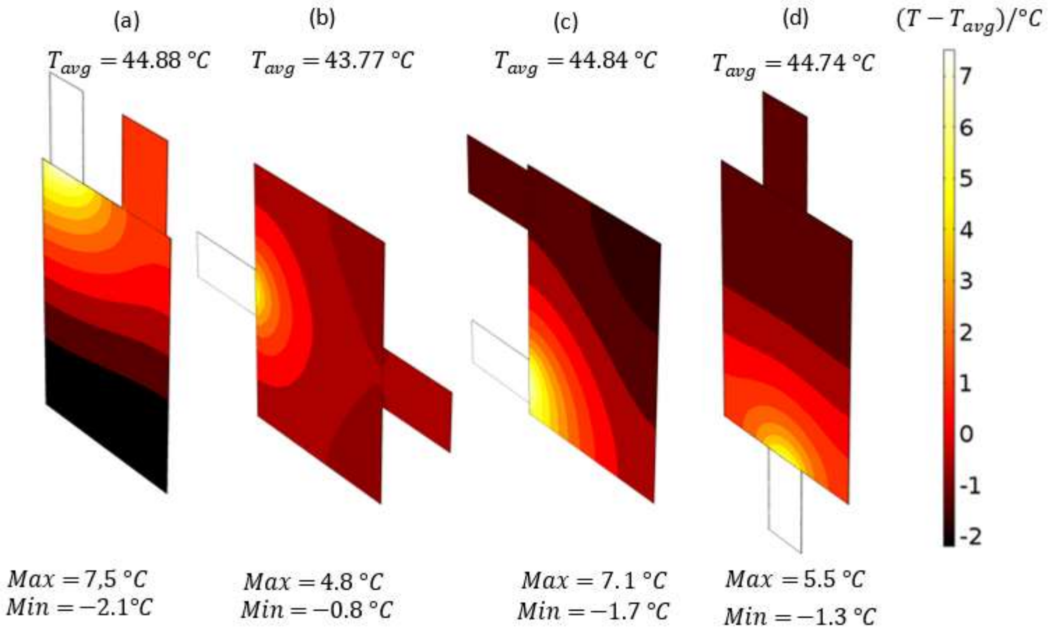

Figure 4.20: Temperature distribution over the cell under 4 I_t discharge current rate at 640s for different cell designs: (a) case 1, (b) case 2, (c) case 3 and (d) case 4

In summary, the statistical distributions of temperature, potential and current density are represented in Figure 4.21. Distributions are computed from the difference between the maximum and the minimum, and normalized by the maximum distribution obtained between the different cases ($\Delta M = \frac{\max(M_{max}-M_{min})}{\max\limits_{cases}(M_{max}-M_{min})}$), where M stands for the temperature, current density and potential. It is shown that case 2 and case 4 present more uniform temperature, potential and current distributions due to the symmetrical arrangement of their tabs (placed at the center of the cell), which minimize the maximum current pathways. At pack level, the battery design based on case 2 can be cycled more uniformly, requiring a less complex cooling system and strategy.

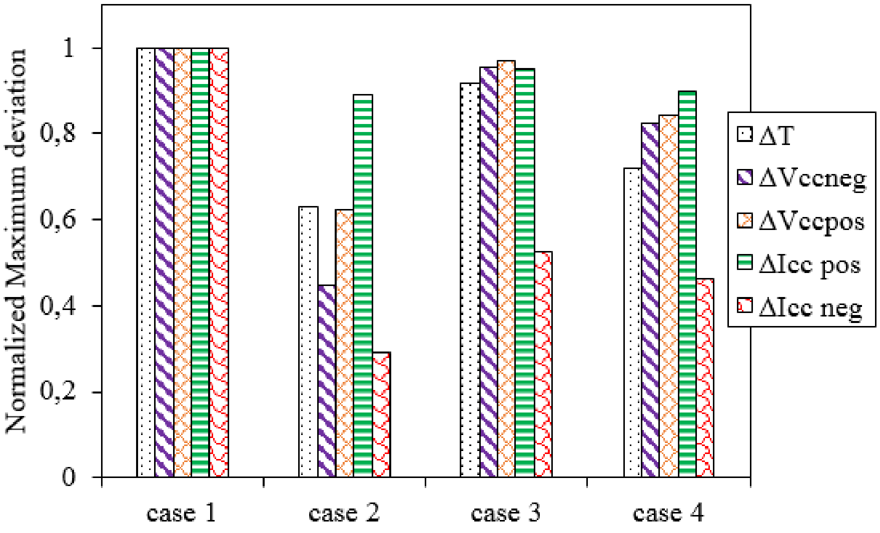

Figure 4.21: Summary of Comparison between cell designs under 4 I_t discharge current rate

As case 2 presents the most favorable cell design in term of thermal, voltage and current distributions, in-depth investigations are carried out with this case in order to highlight the impact of the tab width on the distribution. The values of the tab width investigated are summarized in Table 4.3. As shown in Figure 4.22, the temperature, potential and current density distributions become more uniform with the increase of the tab width, due to current density decreases when the surface increases. An increase of the tab width gives more uniform potential, current density and thermal distributions, leading to uniform utilization of the active material, which tends to improve battery performance by increasing the output voltage and capacity of the cell. It also tends to increase energy and power densities as established in the literature [44], [122].

	1*L_{tab}	2* L_{tab}	3* L_{tab}	4* L_{tab}
Positive tab (m)	0.04	0.08	0.12	0.16
Negative tab (m)	0.05	0.10	0.15	0.25

Table 4.3 : Value of investigated tab widths of the case 2 design

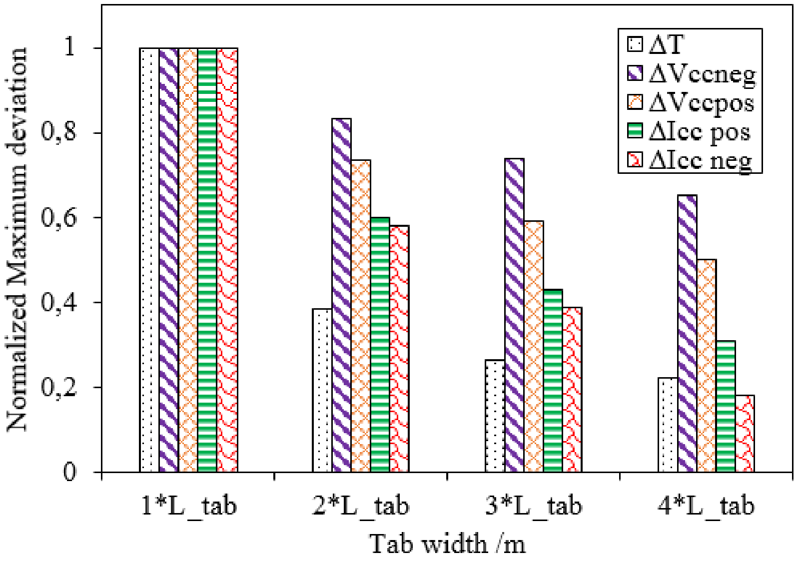

Figure 4.22: Influence of the tab width on the distribution under 4 It discharge current rate

4.5 Conclusion

Extensive three-dimensional simulations of large $LiFePO_4$ pouch cells have been carried out to investigate the impact of different pouch cell designs on performance and variable distributions. It has been shown that the cell designs with symmetrical configurations (case 2 and case 4) show uniform potential and current density gradient, which minimize the ohmic heat and lead to more uniform active material utilization and temperature distributions across the cell surface. Cell design with symmetrical configuration tends to minimize the maximum current pathways. It is found that the high potential, current density and temperature gradient are mainly located near the positive tab due to its high resistivity. Due to charge conservation, the potential distribution along the negative current collector at the beginning of discharge are responsible for the non-uniform active material utilization and the potential distribution in the positive current collector. In addition, the increase of the tab width makes the potential, current density and thermal distributions more uniform and improve the battery performance by increasing its output voltage. This also tends to increase the energy and power densities. At the pack level, the design of case 2 with a subsequent tab width can be cycled more uniformly and thereby allows a less complex cooling strategy.

Chapter 5: Numerical Analysis of Different Battery Thermal Management Systems

5. Numerical Analysis of Different Battery Thermal Management Systems

5.1 Goal

In this chapter, advanced numerical model for battery thermal management system (BTMS) have been developed and different BTMS designs, using liquid-cooling and Phase change material, have been investigated in order to optimize them. The battery module consists of 10 cells (45Ah Lithium iron phosphate pouch format). A one-dimensional electrochemical model (see chapter 4) coupled with a three-dimensional lumped thermal model was developed to describe the battery behavior. Furthermore, the flow channels are modeled by a one–dimensional non-isothermal flow model, and the plates are represented by a three-dimensional thermal model in order to estimate the heat dissipated from the batteries to the cooling plates. The finite element method (FEM) software COMSOL Multiphysics has been used to perform the simulations. At first, a preliminary analysis has been carried out for the comparison of different liquid cooling plate (cold plate) designs in order to select the most suitable and efficient cooling architecture, which allows to decrease the temperature and to obtain a more uniform temperature distribution over the surface of the battery cell. Secondly, the performances of the battery modules, using the best cold plate design at different locations are investigated and compared in order to select the most suitable and efficient cooling arrangement, which minimizes the temperature increase and gradient over the module. Finally, the passive cooling using phase change material embedded in aluminium-foam have been investigated and compared to the liquid cooling method. The impact on the cost of the different solutions are also discussed.

5.2 Introduction

Due to temperature issues and extension of battery system lifetime and performances, as mentioned in chapter 2, a Battery Thermal Management System (BTMS) is needed to maintain the operating temperature of the batteries within the optimum thermal envelope of 20°C - 40°C [39], [43]. Depending on the area of application, the temperature range during vehicle operation may vary between -30°C and 60°C [39].

The main functions of the BTMS are to regulate the temperature of the battery system and to achieve a uniform temperature across each battery cell and between cells in the module or pack, principally during high current rate charging and discharging processes. Therefore, the optimum design for BTMS is required in commercialization of electric vehicles. An effective design of BTMS help to enhance the battery performance, lifetime and effectiveness, and to reduce its complexity, size, weight and as well as the cost.

Four major cooling methods are widely used in electrically propelled vehicles: conventional air cooling [102], [123]–[126], liquid cooling [92], [96], [127]–[133], liquid-vapor phase change cooling [98], [134]–[139] and Phase Change Material (PCM) cooling [105], [140]–[142], or a combination of these methods. The conventional forced air-cooling is generally used in many HEVs, however the liquid cooling systems are advantageous for PHEV and BEV applications, where high amount of dissipated heat should be removed due to the wide operating range of the battery. In addition liquid cooling shows a heat transfer coefficient 1.5 to 3 times larger than air cooling [88] and required smaller cell to cell gap than the air cooling [143]. Recently, most of liquid cooling systems are based on cold plates (thin metal that include one or more internal channel through which a liquid is flowing) in order to increase the cooling efficiency and reducing the amount of liquid and the power consumption. Jarrett et al. [92], [131] investigated the optimization of a serpentine-channel cold plate in order to minimize the pressure drop and maximize the removal heat and temperature uniformity. Jin et al. [96] investigated ultra-thin mini-channel performance by comparing the oblique structure to the conventional channel and shows that the high performance was obtain with the oblique structure. We learned from these works that the designs of the cold plate can play a key role on the efficiency of the liquid cooling, however they didn't tackled the used of the cold plate in battery module.

Recently, some studies investigated the implementation of the cold plates on cell and pack levels. At cell level, Huo et al. [129], investigated numerically the influence of the number of cooling channel and effect of flow direction on the battery cell temperature during $5I_t$ discharge current rate. At pack level, Liu et al [132] investigated numerically the thermal behavior of a module of 20 prismatic batteries close to each other with two cold plates placed at the extremity, from the pack design, where high temperature increase was observed in the middle of the pack. Smith et al. [90] investigated the performance of the liquid-based BTMs where the cold plate was placed at the bottom of the battery module with 8 prismatic cell. However, these studies were carried out without taking into account the heat generated at the battery tab. From these studies, it can be concluded that the pouch cells are less investigated. In addition, the position of the cold plate on the battery modules can be improved.

In addition, PCM has been identified as a good solution for battery cooling system in PHEV and BEV applications [101], [103]. PCM on its own has relatively low thermal conductivity and to prevent high temperature increase, the generated heat must be removed quickly. For this reason, several techniques exist to improve the thermal conductivity of the PCM. Possible improvements are the encapsulation of PCM into metal-foam [102], [144]–[149], the metal is often made of aluminium, copper or graphite composite. Several modelling techniques represent the PCM as solid material [101], [103], [150] without taking into account the liquid phase after the melting. This phase can involve convection that can change the temperature distribution of the battery.

In this chapter, extended numerical models have been developed to simulate the existing and novel cold plate's designs in order to predict the optimal design which minimize the pressure drop of the water and also the temperature rise and distributions of the battery at various discharge processes. This comparison is carried out by using a single battery in the middle of the two cold plates with the same designs. In addition, the performances of the selected cold plate applied on battery module, with 10 pouch cells (as used in the previous chapter) connected in series, have been investigated. After evaluation of the effective position of the cold plate and its possibility to be associated with hot plate (without channel flow), the influence of liquid mass flow rate, liquid inlet temperature and ambient temperature of the battery module are also analyzed.

Secondly, PCM embedded in aluminium-foam system is used to cool the same battery module, as used previously in the first part. For this, an extended model of PCM that take into account the natural convection of the liquid arising from the melting of the PCM is used.

Finally, a comparison between the liquid cooling and PCM has been made in terms of performance and cost.

5.3 Liquid cooling method

5.3.1 Investigation of the cooling plate's designs

5.3.1.1 Model assumptions and geometry features

Figure 5.1 shows the pouch cell cooled by two cold plates with the same designs and dimensions. The cold plates are located on both sides of the pouch cell. The heat is generated by the battery, transferred into the cold plates, and removed throughout the cooling channels. Four cold plates' designs (Figure 5.2) are investigated at various discharge current rates (2 I_t, 4 I_t and 6 I_t) in order to illustrate the most efficient in terms of the maximum temperature rising and temperature distribution of the battery cell. The whole system is insulated in order to quantify the effectiveness's of the different cold plate designs and to represent the real situation in pack level where the battery are covered by protective material. The cooling plates and cooling channel are made of aluminium and copper, respectively.

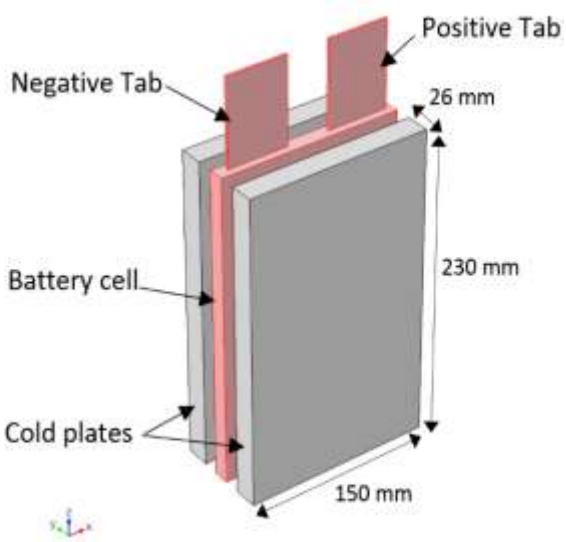

Figure 5.1: Battery cell cooled with two cold plates

The schematics of the different cold plate's designs are represented in Figure 5.2 and have the same dimensions of 150 mm in width, 26 mm in depth and 230 mm in height. The different cold plate designs differ from the structure of the cooling channels with an inner diameter of 16 mm:

- Design 1: characterized by 5-straight cooling channels distributed equidistantly along the width of the cold plates. The inlet connector channel is placed at the middle in order to have more flow rate at the middle of the cold plate. The outlet connector channel is placed at the middle of the bottom to recover the hot liquid. This design has the advantage of reducing the pressure drop inside the cooling channel.

- Design 2 comprises one cooling channel having an inlet and outlet ends on the left and right sides of the cold plate, respectively. The intermediate portion with a sinuous pattern has arranged vertically. This design has the advantage of conducting the total flow rate into the cooling channel.

- Design 3: characterized by 4-straight cooling channels, where the total flow rate is split uniformly into the different lines.

- Design 4 have the same characteristic than the design 2, however the intermediate portion with sinuous pattern is arranged horizontally.

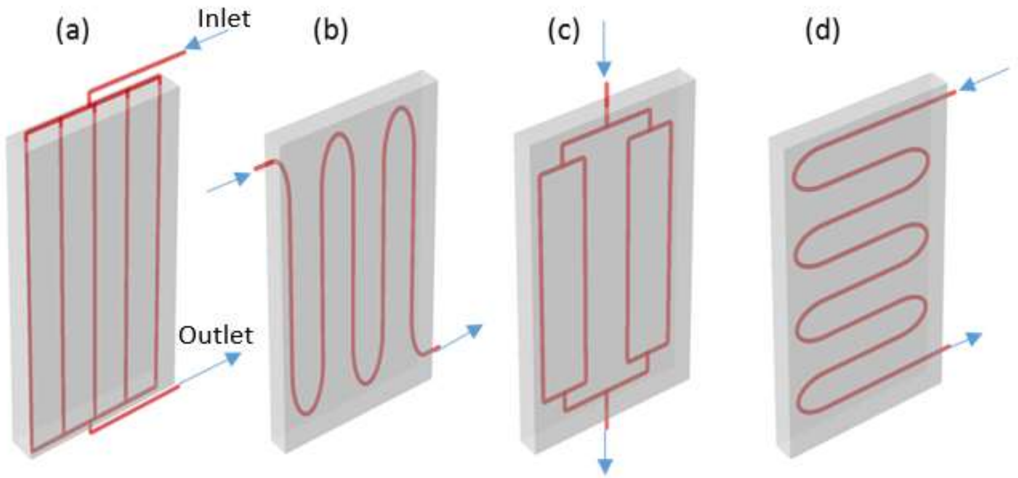

Figure 5.2: Different cold plate designs: (a) design 1, (b) design 2, (c) design 3 and (d) design 4

The simulation of heat transfer of the whole system requires a 3D geometry representation. Simulation of 3D flow and heat transfer inside the cooling channels is computationally expensive. As the diameter of the cooling channel is smaller (16 mm), the flow and heat transfer inside the cooling channels can be modelled with 1D pipe thermal-flow equations coupled with the 3D modelling of the cold plates. This technics have been never published regarding the BTMS modelling. The equations describing the cooling channel flow are fully coupled with the heat transfer equations of the cooling plate and battery.

5.3.1.2 Model development

5.3.1.2.1 Battery domain

The battery behavior is investigated by using a one-dimensional electrochemical model coupled with a lumped 3D-thermal model. This model was described in detail in chapter 4 and is able to accurately estimate the average voltage and heat source at different current rates. The heat source has mainly three contributions the reaction heat (q_{rea}), the reversible heat (q_{act}), and the electrical ohmic heat (q_{ohm}). The heat generation is evenly distributed within the electrode domain (Figure 5.4). The used input parameters of the electrochemical model are listed in Appendix II, Table 8.1 and Table 8.2. The electrochemical model is coupled with a 3D lumped thermal model (as shown in Figure 5.3), which requires as inputs the thermal parameters as estimated in chapter 3 section 3.3.4.

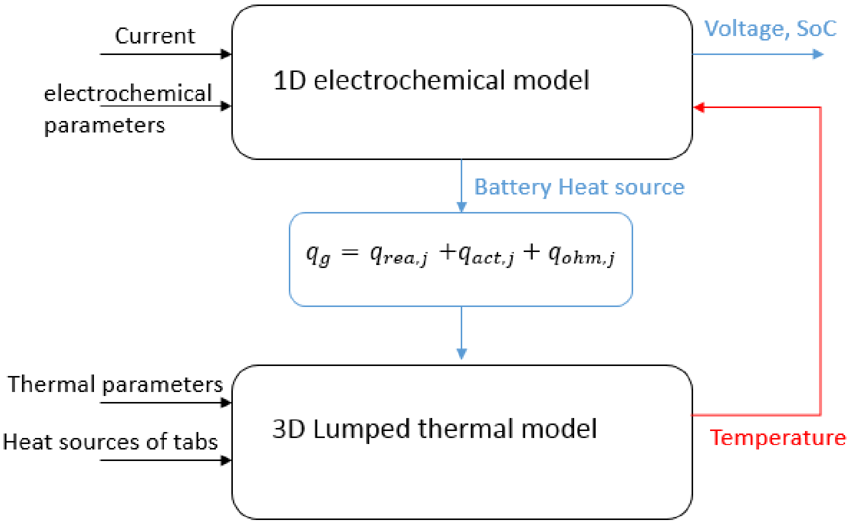

Figure 5.3: Battery model

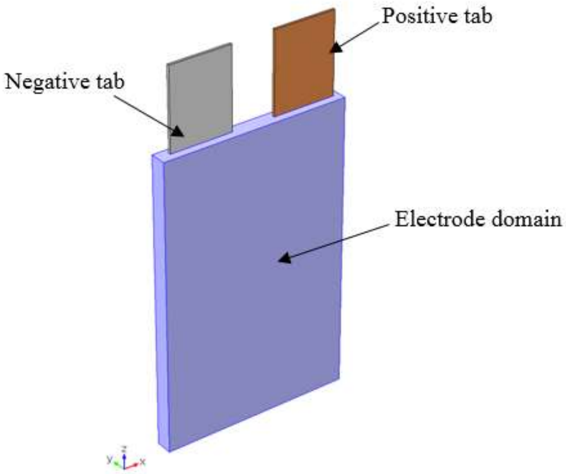

Figure 5.4: different battery domain

The energy balance equation of the battery cell (Figure 5.4) is formulated as:

$$\rho C_p \frac{dT}{dt} - \lambda \nabla^2 T = q_g \tag{5.1}$$

Where:

$\rho(\mathrm{kg/m^3})$: is the density of the battery,

$C_p(\mathrm{J\ kg^{-1}\ K^{-1}})$: is the specific heat capacity of the battery,

$\lambda(\mathrm{Wm^{-1}K^{-1}})$: is the thermal conductivity of the battery,

$q_g(\mathrm{Wm^{-3}})$: is the heat source generated by the battery,

$T(\mathrm{K})$: is the temperature of the battery.

- in the electrode domain, the heat source (q_g) is given by:

$$q_g = q_{rea,j} + q_{act,j} + q_{ohm,j} \tag{5.2}$$

Where:

$q_{rea,j}$ $(\mathrm{Wm^{-3}})$: is the reaction heat, computed from the electrochemical model,

$q_{act,j}(\mathrm{Wm^{-3}})$: is the activation heat, computed from the electrochemical model,

$q_{ohm,j}(\mathrm{Wm^{-3}})$: is the ohmic heat, computed from the electrochemical model,

- in the tabs domain, the heat source is given by:

$$q_g = \frac{R'' I_t^2}{V_{tab}}; \quad R'' = \rho'' \frac{l}{S} \tag{5.3}$$

Where:

$R''(\Omega)$: is the electrical resistance of the associated tab,

$I_t(\mathrm{A})$: is the current rate,

$V_{tab}(\mathrm{m}^3)$: is the volume of the associated tab,

$\rho''(\Omega\mathrm{m})$: is the resistivity of the associated tab,

$l(\mathrm{m})$: is the length of the associated tab,

$S(\mathrm{m}^2)$: is the cross-section of the associated tab,

The value of R'' are included in chapter 3, section 3.3.2.2, for both tabs of the considered battery type.

5.3.1.2.2 Cooling plate domain

5.3.1.2.2.1 Energy balance of the cold plate

The energy equation is given by:

$$\rho C_p \frac{\partial T}{\partial t} = \lambda \nabla^2 T \tag{5.4}$$

Where:

$\rho(\mathrm{kg/m^3})$: is the density of the cold plate,

$C_p(\mathrm{J\ kg^{-1}\ K^{-1}})$: is the specific heat capacity of the cold plate,

$\lambda(\mathrm{Wm^{-1}K^{-1}})$: is the thermal conductivity of the cold plate,

The cold plates are made of aluminium.

5.3.1.2.2.2 Flow and heat transfer in the cooling channels

Cooling channel with a large enough length/diameter ratio can be reduced to a 1D representation with cross section averaged velocity and pressure [151].

- The momentum and mass conservation of the 1D pipe flow in the cooling channels describe below are a simplified form of the Navier-Stokes equations:

$$\rho \frac{\partial v}{\partial t} = -\nabla p - f_D \frac{\rho}{2d_h} |v| v + F_{gravity} \tag{5.5}$$

$$\frac{\partial A\rho}{\partial t} + \nabla .(A \rho v) = 0 \tag{5.6}$$

Where:

v(m/s): is the averaged fluid velocity at the cross section of the cooling channel,

A(m^2): is the cross section of the cooling channel,

d_h(m): is the hydraulic diameter of the cooling channel,

ρ(kg/m^3): is the density of the water,

p(N/m^2): is the pressure,

$F_{gravity}$(N/m^3): represents the body force due to the gravity,

f_D is the Darcy friction factor, which describes the pressure drop due to the viscous shear. Among the different existing Darcy friction factor models in the literature [152], [153] for single phase flow, the Churchill relation [154] is more suitable to describe the water. This relation is valid for laminar flow (Reynolds number (Re) lower than 2000), turbulent flow (Reynolds number (Re) higher than 3000), and transitional region in between. In the Churchill relation, the Darcy friction factor is expressed as:

$$f_D = 8\left[\left(\frac{8}{Re}\right)^{12} + (A+B)^{-1.5}\right]^{\frac{1}{12}} \tag{5.7}$$

Where A and B are constants.

$$A = \left[-2.457\, ln\left(\frac{7}{Re}\right)^{0.9} + 0.27\left(\frac{e}{d_h}\right)\right]^{\frac{1}{12}} \tag{5.8}$$

$$B = \left(\frac{37530}{Re}\right)^{16} \tag{5.9}$$

The Reynolds number is equal to:

$$Re = \frac{\rho v d_h}{\mu} \tag{5.10}$$

Where μ (Pa.s) is the dynamic viscosity and $e(m)$ is the surface roughness.

The surface roughness is a function of the cooling channel material.

- The energy equation for the cooling channel flow is:

$$\rho A C_p \frac{\partial T}{\partial t} + \rho A C_p v.\nabla \mathrm{T} = \nabla.(A\lambda\nabla \mathrm{T}) + f_D \frac{\rho A}{2d_h}|v|^3 + Q_{wall} \tag{5.11}$$

Where:

C_p(J kg^{-1} K^{-1}): is the specific heat capacity of the water,

λ(Wm^{-1}K^{-1}): is the thermal conductivity of the water.

The second term on the left hand corresponds to the heat dissipated due to viscous shear. Q_{wall}(W/m), is the heat transferred from the cold plate to the water in the cooling channel through its wall and is expressed as:

$$Q_{wall} = h_{int}\, Z(T_{wall} - T) \tag{5.12}$$

Where

Z(m): is the wetted perimeter of the cooling channel,

h_{int}(W/m^2.K): is an overall heat transfer coefficient between the internal film of the cooling channel and the wall of the cold plates,

T_{wall}(°C): is the external temperature outside of the mini-channel given by the 3D heat transfer in the cold plate,

h_{int} has been estimated from the forced convection correlation, which depends on the Nusselt number (Nu) and Prandtl numbers (Pr), the flow regime and the design of the channel.

- for laminar flow regime with round pipe [155], the Nusselt number is given by:

$$Nu_{lam} = 3.66 \tag{5.13}$$

- for turbulent flow regime, the following Nusselt correlation has been used [156]:

$$Nu_{turb} = \frac{(f_D/8)(Re - 1000)Pr}{1 + 12.7\sqrt{f_D/8}(Pr^{2/3} - 1\ )} \tag{5.14}$$

The Prandtl number is expressed as:

$$Pr = \frac{\mu\, Cp}{\lambda} \tag{5.15}$$

h_{int} is expressed as:

$$h_{int} = Nu\frac{\lambda}{d_h} \tag{5.16}$$

With

$$Nu = \max(Nu_{lam}, Nu_{turb}) \tag{5.17}$$

5.3.1.2.2.3 Boundary and initial conditions

- Interface battery cell/cooling plates

The heat flux continuity is applied, where the heat from the battery is transferred to the cold plate:

$$-\lambda_{battery}\nabla \mathrm{T}|_{boundaries} = -\lambda_{cold\ plate}\nabla \mathrm{T}|_{boundaries} \tag{5.18}$$

- Interface cooling plate/channels

At the interface between the cold plate and cooling channel, the boundaries conditions are given by the continuity of the heat transfer fluxes. Indeed the heat from the cold plates is transferred to the channels:

$$-\lambda_{cold\ plate}\nabla \mathrm{T}|_{boundaries} = Q_{wall} \tag{5.19}$$

- At the inlet of the cooling channel, a temperature of T_{inlet} (°C) is specified:

$$T = T_{inlet} \tag{5.20}$$

- At the outlet of the cooling channel, an outflow condition is applied.
- At the external surface, the heat is dissipated through the ambient air by convection.

$$\lambda\nabla \mathrm{T}|_{boundaries} = h_{ext}(T - T_{amb}) \tag{5.21}$$

Where:

$h_{ext}(W/m^2.K)$: the convective heat coefficient between the interface battery and cooling plates included and ambient environment.

T_{amb} $(°C)$: the ambient air temperature.

- The initial temperature of the battery pack is defined as T_{ini}(°C):

$$T = T_{ini} \tag{5.22}$$

- In the inlet, the liquid velocity is equal to the ratio of volumetric flow rate and the cross-section of the cooling channel.

$$v = \frac{q_{v,0}}{A} \tag{5.23}$$

Where $q_{v,0}$ (m^3/s) is volumetric flow rate.

- In the outlet, the atmospheric pressure (p_a(Pa)) is assigned.

$$p = p_a \tag{5.24}$$

5.3.1.2.3 Numerical procedure

All equations are simultaneously solved numerically in COMSOL Multiphysics 4.3b by using the Finite Elements Method (FEM). As the governing equations are highly nonlinear, the performance and accuracy of the calculation depends heavily on the mesh and solver. The unstructured mesh was generated by using the swept method. To ensure the accuracy and the mesh independency of the solutions, 75791 hexahedral, 10058 triangular, 984 edge and 84 vertex elements are used over the entire computational domain after testing several grid densities with refining zones at the cooling channels. In order to reduce the memory usage and computational time, the equations are coupled using the segregated approach as shown in Figure 5.5. At each time step, two segregated steps are considered: first, the temperature and flow are solved by keeping the electrochemical variables constant, and second, the results of temperatures at each mesh nodes are used to update the corresponding local electrochemical parameters and then the local electrochemical variables of each mesh nodes are calculated. The process is repeated at each node until the convergence is reached for all variables. The direct solver PARDISO (Parallel Direct Sparse Solver Interface) was chosen as linear solver. For each time step, the convergence is reached where the relative tolerance is below 10^{-3} for all variables. Then, the time step progresses until the cut-off potential is reached

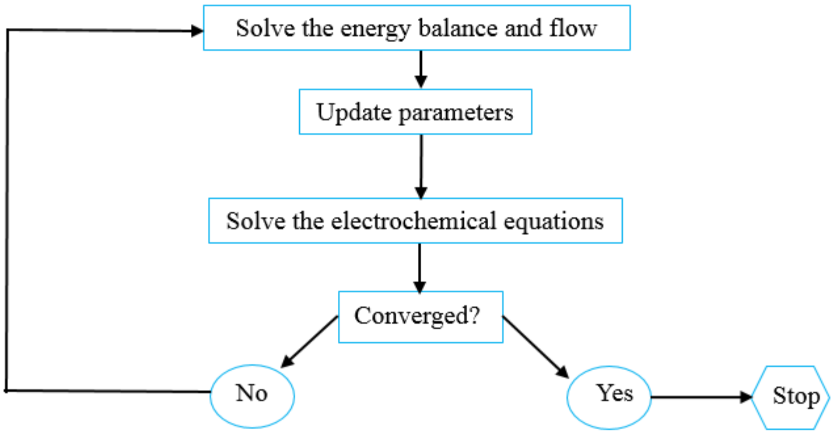

Figure 5.5: Procedure of the numerical solution at each time step

5.3.1.3 Results of the different cooling plate designs

Cold plates with different cooling channel designs are investigated in order to achieve better heat management. Based on the methodology as described above, during high discharge rate, the effect of the channel architecture, the exchanged heat flux with the environment air, ambient and inlet temperatures are evaluated in term of maximum and gradient temperatures.

5.3.1.3.1 Effect of the channel design

The battery cell is cycled between the maximum and the minimum voltages with a discharge rate of 6 I_t. The simulations of the different cooling plate design are performed by using the same conditions, physical and cooling parameters. The impact of the cold plate's designs on battery behavior are investigated by considering the heat removed by the refrigerant and the heat dissipated through the ambient air with a convective coefficient of 100 W/m^2.K. The water is used as a refrigerant with a volume flow rate of 30 l/min and an inlet and initial temperature of 20°C.

To evaluate the effect of the channel design, the evolution of the maximum and gradient temperatures of the battery cooled by the different cooling plate under 6 I_t discharge current, are presented in Figure 5.6 and Figure 5.7. It is clearly shown that all cooling plate's designs give almost similar temperature profile trends with a small difference. The results indicate more temperature drop with the design 4, follow by design 2, design 3 and design 1. The explanation can from the energy balance of the whole system, where the total amount of heat generated by the battery is distributed as follows:

- The heat removed by the liquid
- The heat dissipated by convection through the ambient air
- The remaining heat is stored inside the system and being responsible of temperature increases of the battery

As the external surfaces of the different cooling plate designs are the same, therefore the amount of heat dissipated by convection ($h_{ext}\ S\ (T_{surface} - T_{ambient})$ are the same for the different cases. The small differences may from to the heat removed by the water ($\rho\ q_v C_p(T_{outlet} - T_{inlet})$. The flow rate over the different branches of the channel are responsible for the temperature drop by increasing the heat transfer from the plates to the channel flow. Due to the division of the flow rate in the different channel branches of the design 1 and design 3, less temperature drops are observed, compared to the design 2 and 4, for which the flow rate remain the same and is equal to its total value. Regarding the temperature gradient as observed in Figure 5.7, the most uniform temperature distribution is obtained with the design 1 follow by design 3, design 4 and design 2 due to the uniform repartition of the flow rate through the plate, as illustrated in Figure 5.9. Furthermore, due to the low thermal conductivity of the battery in its normal direction, the cooling plate in direct contact with the battery leads a high temperature drop, in contrast a high gradient temperature is observed because of the high temperature in the middle and low temperature at the surface of the battery, as illustrated in Figure 5.8.

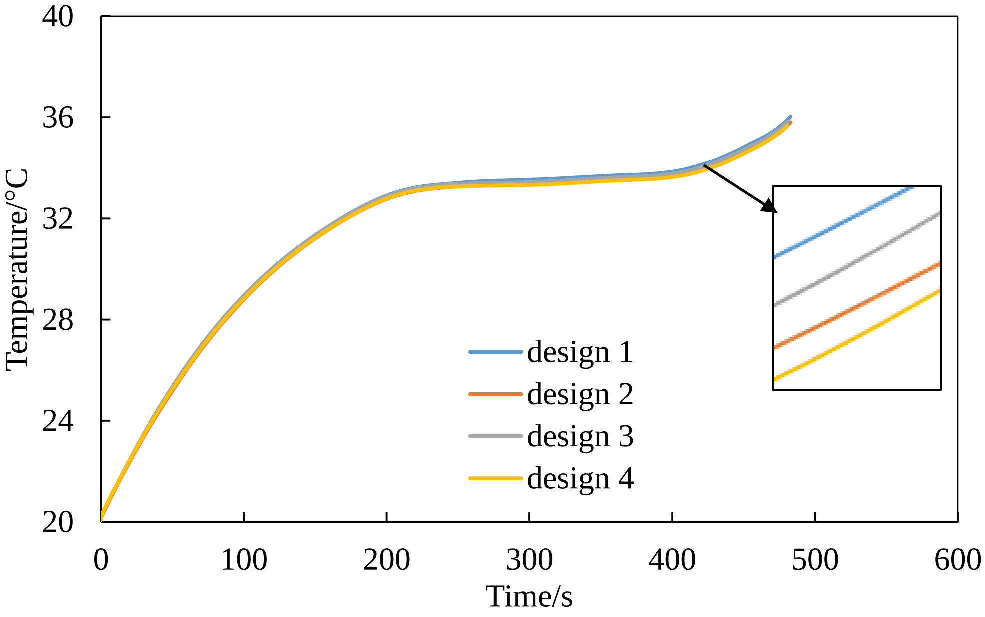

Figure 5.6 : Maximum battery cell temperature given by different cooling designs at $6I_t$ discharge current rate, Tinlet=20°C and Tamb=20°C with h=100 W/m².K.

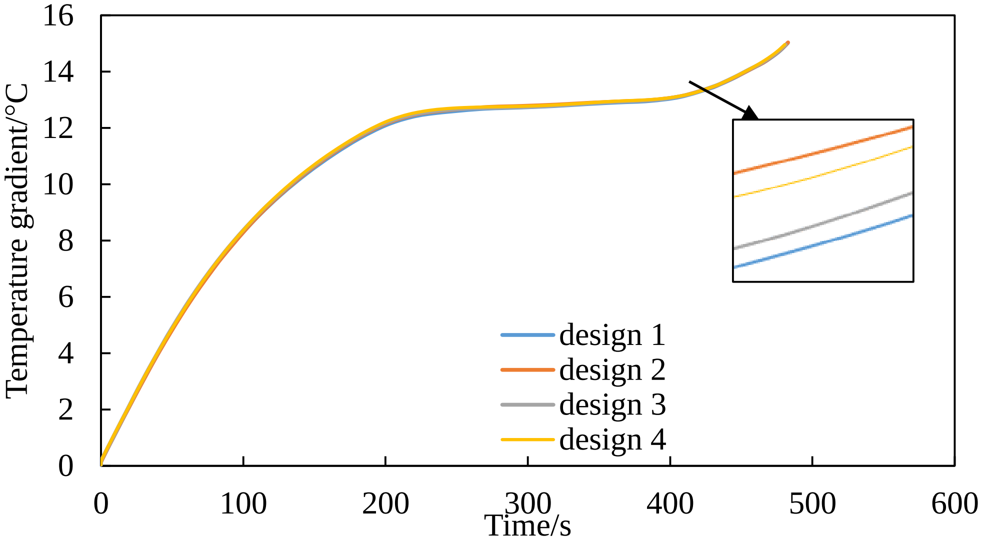

Figure 5.7: Cell temperature gradients with different cooling designs at 6I$_t$ discharge current rate, T_{inlet}=20°C and T_{amb}=20°C with h=100 W/m².K.

Design 1	**Design 2**	**Design 3**	**Design 4**
Max=36.16	Max=35.93	Max=36.25	Max=35.92

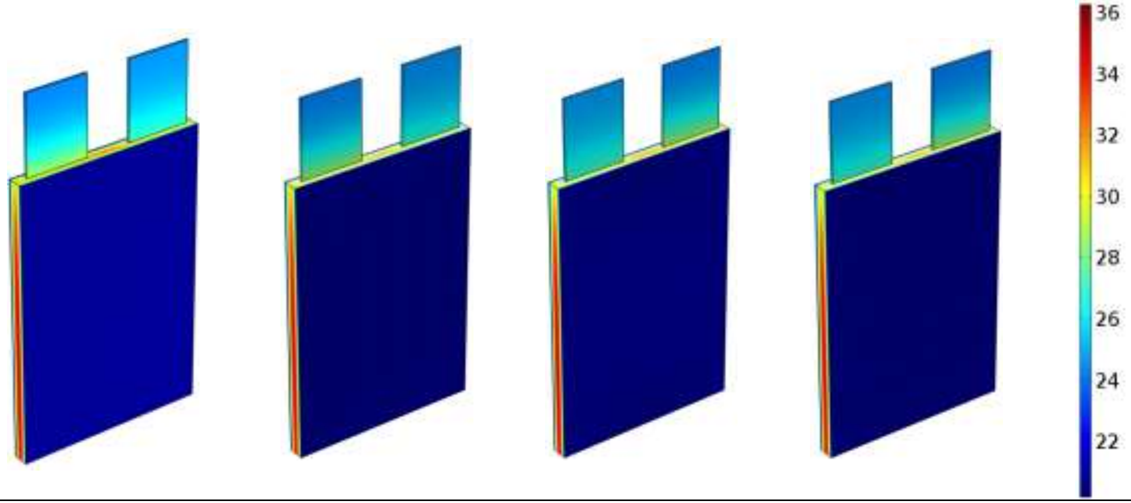

Min=20.45	Min =20.19	Min =20.20	Min =20.17

Figure 5.8: Temperature distribution over the cell at the end of 6 I$_t$ discharge current rate for different cold plate designs, Tinlet=20°C and Tamb=20°C with h=100 W/m².K.

Water	Design 1	Design 2	Design 3	Design 4
	Max=20.60	Max=20.37	Max=20.58	Max=20.38

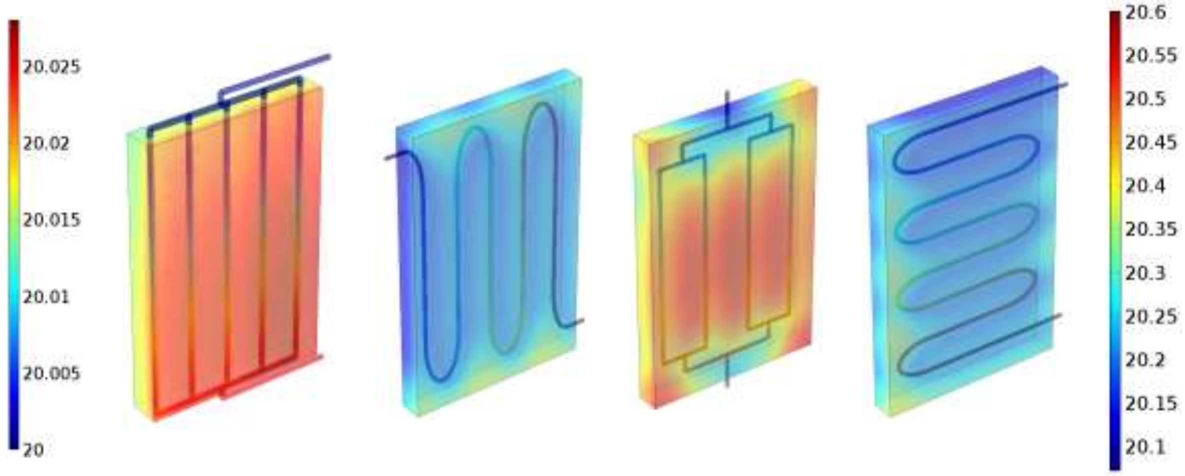

	Min=20.33	Min=20.07	Min=20.10	Min=20.07

Figure 5.9: Temperature distribution over the cell with different cold plate designs at the end of 6 I_t discharge current rate, Tinlet=20°C and Tamb=20°C with h=100 W/m^2.K.

5.3.1.3.2 Influence of inlet temperature

The performance of the different cooling plates was examined by considering different inlet temperatures (0°C and 40°C) of the liquid. At low inlet temperature, the plates act to cool the battery, as illustrated by the evolutions of the maximum and gradient temperatures in Figure 5.10 and Figure 5.11. These results corroborate the previous ones observed in Figure 5.6 and Figure 5.7. However, at high inlet temperature, the plates act to heat the battery, as illustrated as illustrated from the evolution of the maximum and gradient temperatures in Figure 5.12 and Figure 5.13, where the inverse trend is observed.

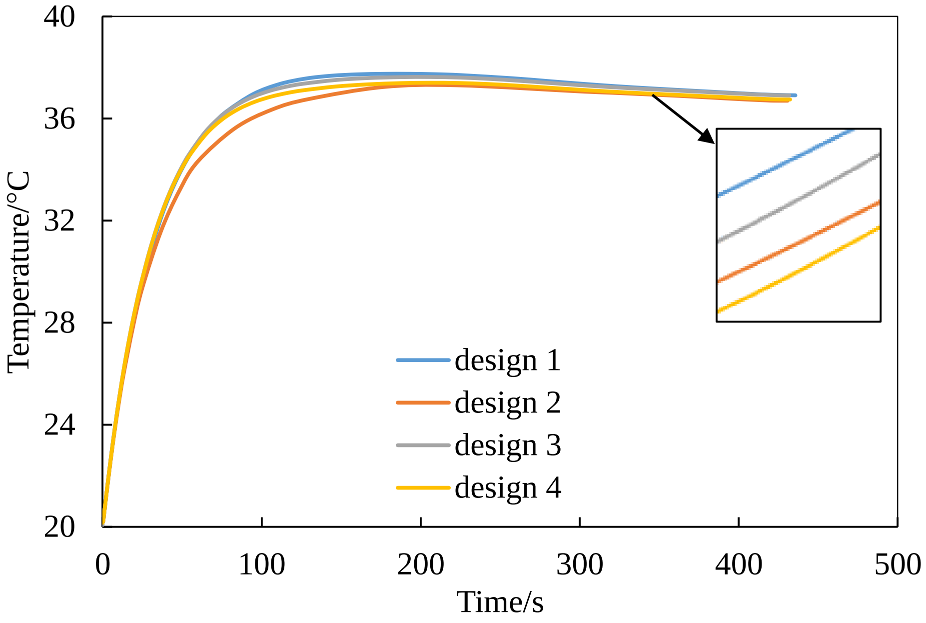

Figure 5.10: Maximum battery cell temperature given by different cooling designs at $6I_t$ discharge current rate, Tinlet=0°C and Tamb=20°C with h=100 W/m².K.

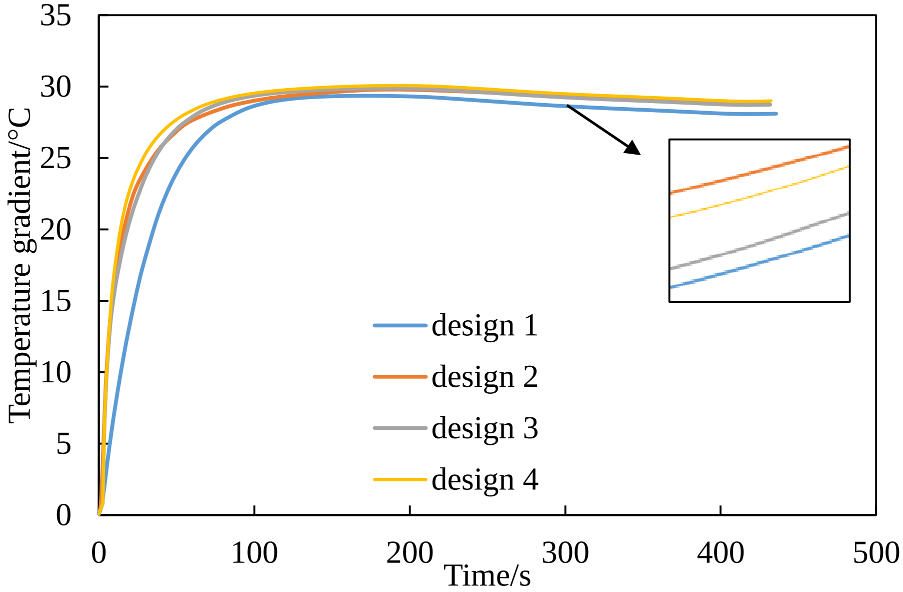

Figure 5.11: Cell temperature gradients with different cooling designs at $6I_t$ discharge current rate, Tinlet=0°C and Tamb=20°C with h=100 W/m².K.

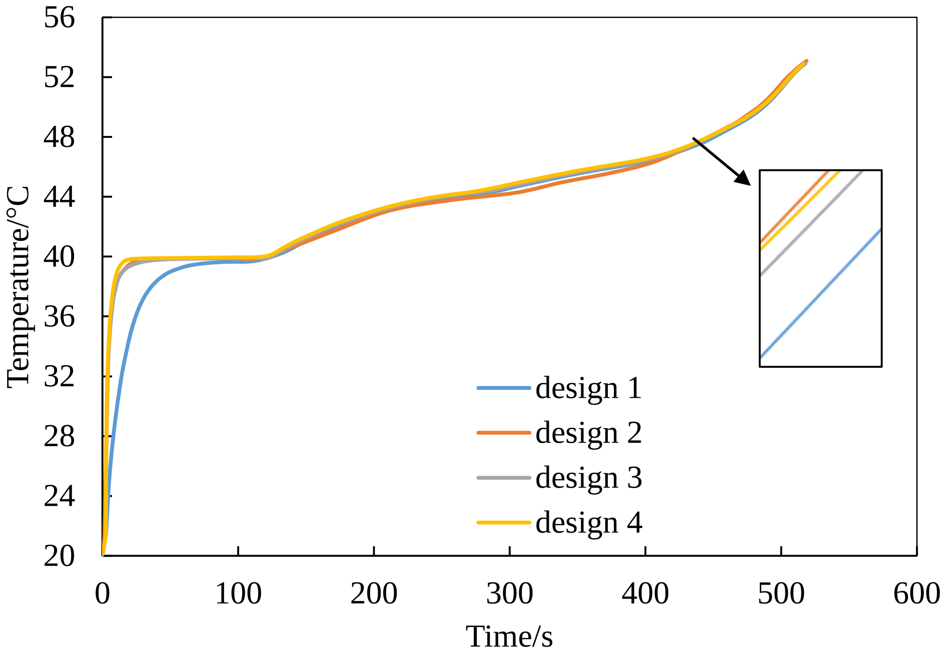

Figure 5.12 : Maximum battery cell temperature given by different cooling designs at $6I_t$ discharge current rate, Tinlet=40°C and Tamb=20°C with h=100 W/m².K.

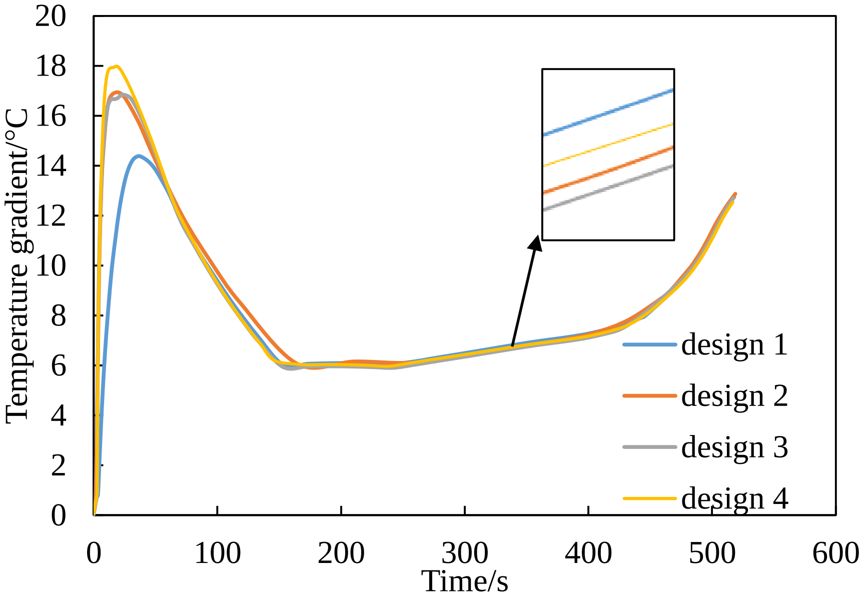

Figure 5.13: Cell temperature gradients with different cooling designs at $6I_t$ discharge current rate, Tinlet=40°C and Tamb=20°C with h=100 W/m².K.

In summary, it can be observed that the design 1 shows the lower temperature gradient than the other designs due to the uniform distribution of the flow rate into the different subdivision of the cooling channel.
In conclusion, as the difference between the maximum temperatures given by the different cold plate design is low, our main criteria of selection is dictated by the design with the lowest temperature gradient. Therefore, the design 1 is identified to be more appropriate to build an efficient BTMS

5.3.2 Impact of cooling plate location on the Battery module thermal management system

5.3.2.1 Model assumptions and geometry features

The battery module includes 10 Lithium iron phosphate pouch cells (32V, 45Ah) connected in series. The cold plates and hot plates (i.e. plates without cooling channels) have been placed at different positions in the module. The heat is removed from the battery module by the cold plates with design 1. The hot plates are used to conduct heat and to improve the uniformity of battery module temperature. Different positions of the cold plate in the battery module are investigated as illustrated in Figure 5.14, in order to select the suitable and efficient cooling arrangement of the cooling plates that minimizes the maximum temperature increase and the gradient in the module. The different battery module designs include:

- Design A: battery module with cold plates between the cells (no hot plates used),
- Design B: battery module with hot plates between the cells and cold plates at both the extremities of the module,
  Design C: battery module with hot plates between cells and cold plate at one of the longitudinal sides,
- Design D: battery module with hot plates between the cells and cold plates at the two of the longitudinal sides,
- Design E: battery module design with hot plates between cells and cold plate at the bottom side,
- Design F: battery module design with a cold plate at both extremities of the module and without hot plates between cells.

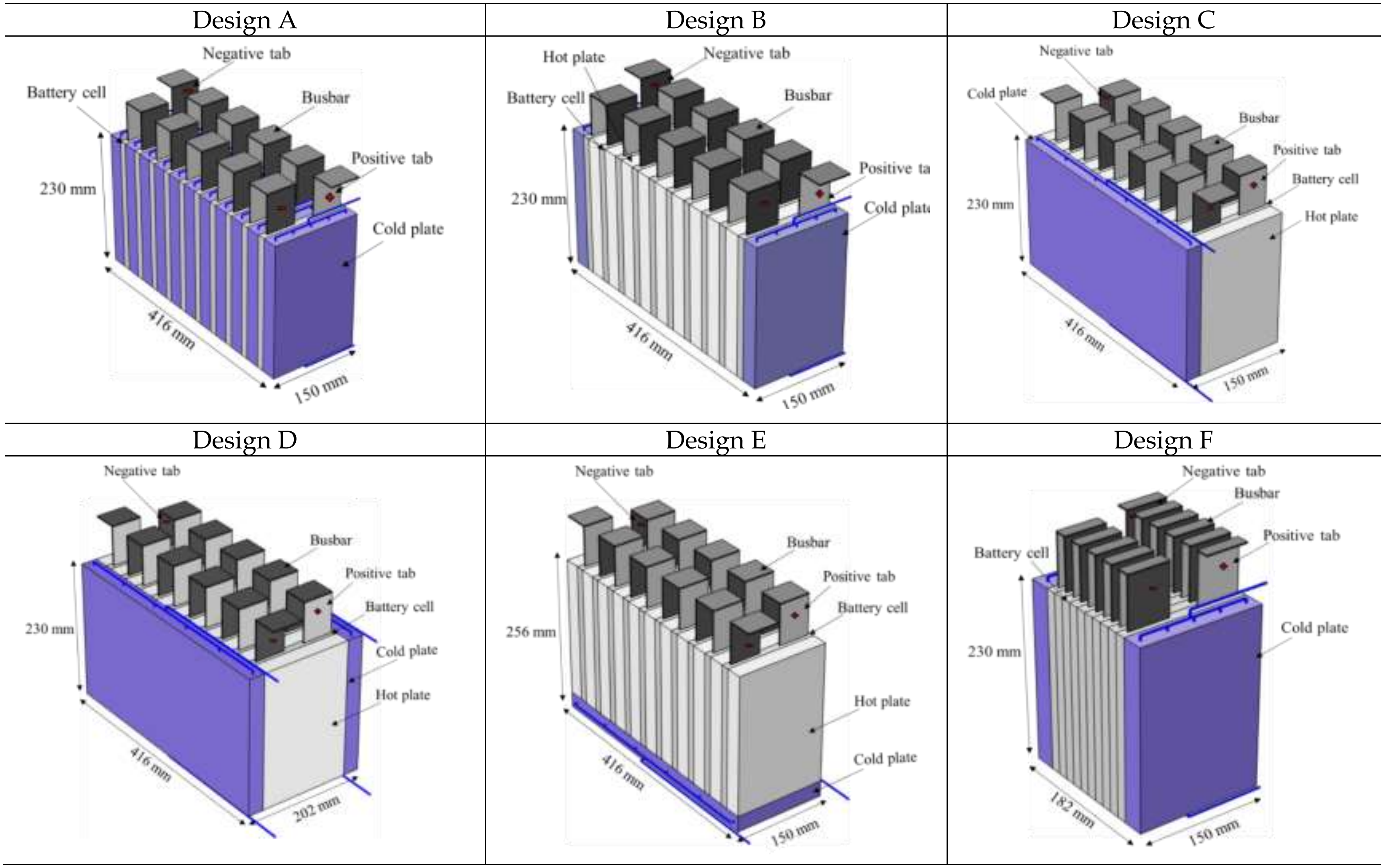

Design A

Design B

Design C

Design D

Design E

Design F

Figure 5.14: Different Battery module designs: Design (A, (B), (C), (D), (E), (F).

The battery module is assumed thermally insulated from the environment and therefore only the cold plates are able to remove the heat from the module. The cells are interconnected by copper busbars, which presented a same amount of heat source than the negative tab. The cells are assumed to have the same electrical and electrochemical behaviors. The comparisons of the different battery pack designs is based on the values of the maximum temperature of the cells and on the temperature gradient over the cells.

5.3.2.2 Results

5.3.2.2.1 Comparison of the different cooling plate location

The simulations of the different battery thermal management designs are performed at $4I_t$ discharge current rate and 20°C of operating and initial temperatures. A volume flow rate of 30 L/min and an inlet temperature of 20°C are used in the cooling channel inlet. Atmospheric pressure is set at the cooling channel outlet. The numerical simulation was implemented in Comsol Multiphysics version 4.3b. The same numerical methods described in section 5.3.2 have been used. The mesh independency is also investigated to ensure the accuracy of the numerical results.

As the cells in each module designs show almost the same maximum temperature profiles, except for design B, where the temperatures of the cells closest to the cold plates are different from those at the middle of the pack. Therefore, in Figure 5.15a the maximum temperature of one cell is represented for the module designs A, C, D, E and F while the maximum of two cells (one at the extremity and another one at the middle) is represented for the module design B.

The different battery module designs are compared based on the value of the maximum temperature evolution and on the temperature difference over the battery cells.

The maximum temperature profiles given by the different module designs show similar trends, with different maximum temperature increase. Without cooling, the maximum temperature is significantly higher (up to 55°C) and uniform. The design D shows the lowest maximum temperature increase, followed by designs A, C, E, and B, respectively. Regarding the temperature difference, as the cells in the different pack designs show almost the same temperature difference profiles, except for designs B and F, where the temperatures difference of the cells closest to the cold plates are different from those at the middle of the pack. Therefore, in Figure 5.15b the maximum temperature of one cell is represented for the module designs A, C, D, and E while the temperature differences of two cells (one at the extremity and another one at the middle) is represented for the module design B and F. It can be noticed that less temperature difference is obtained with the case of without cooling follow by the design B and F with only the cells placed at the middle of the module. For the entire module, with liquid cooling the lowest temperature gradient is obtain with the design D, whereas the design B and F show higher temperature gradient due to fact that one face of the cell (placed at the extremity of the pack) is cooled by cold plates. In addition the temperature gradient given by the design D is less than 5°C, as suggested by Pesaran et al. [88] in order to maximize the battery lifetime. For better understanding of the performance of the different module designs, the temperature distributions are plotted in Figure 5.16 and Figure 5.17 at the end of $4I_t$ discharge current rate.

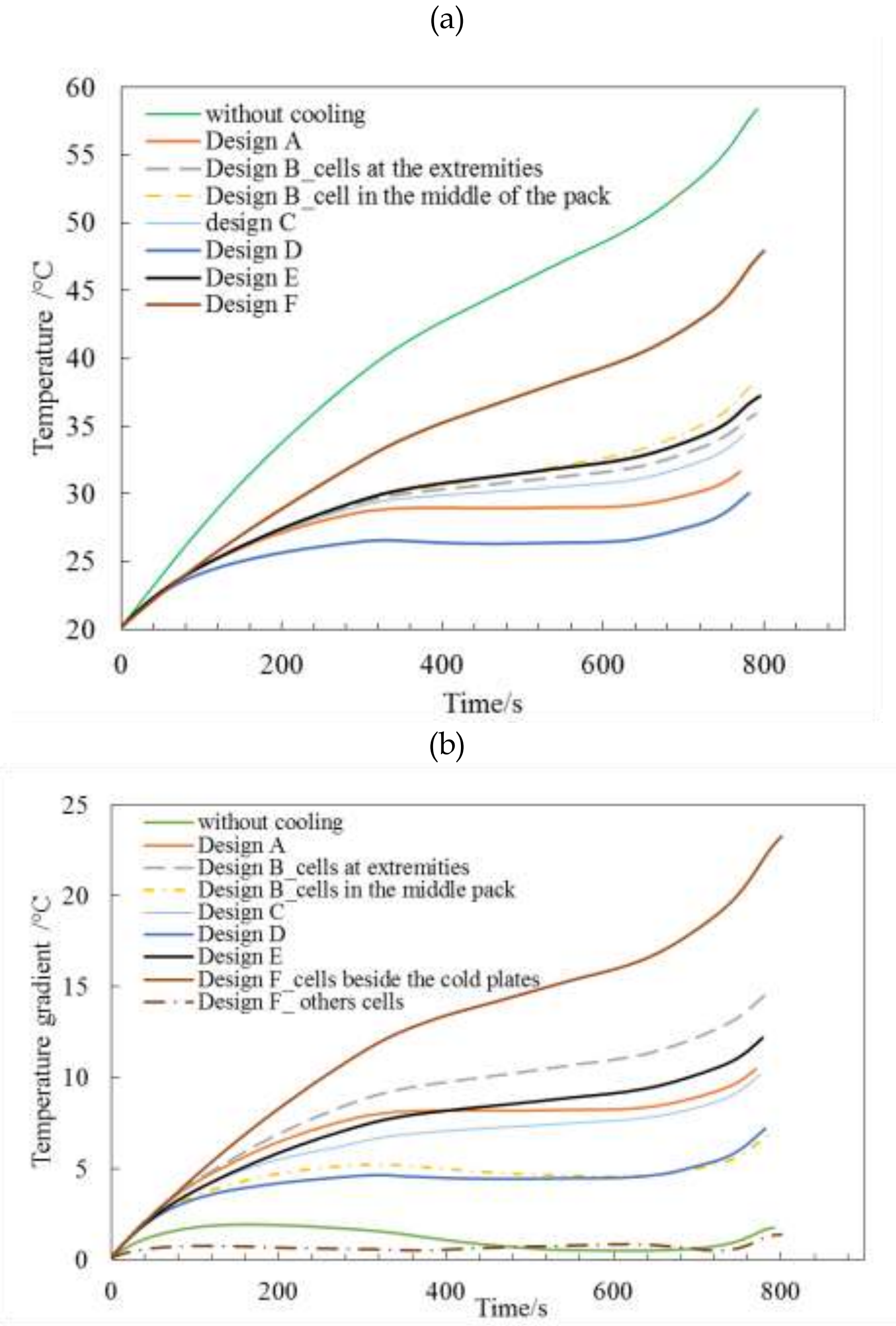

Figure 5.15: Comparison of the maximum temperature (a) and temperature gradient (b) profiles under 4 I_t discharge current rate for different battery module designs

Since the highest temperatures are reached at the end of the discharging processes with 4 I_t current rate, Figure 5.16 shows the temperature distribution over the different module designs at the end of the discharging processes. The highest temperatures are located on the tabs and the cells in the middle of the module, based on designs A, B, C, E and F. Design D shows uniform temperature distribution. Hot plates incorporated between the cells play important roles for better temperature uniformity. Indeed, the heat generated within the cells was dissipated through the hot plates to the cold plates. This figure shows how the location of the cold plate affects the temperature distribution in the battery module.

The main characteristics of the different designs include:

- Design A shows a low maximum temperature increase, located mainly located at the tabs and in the middle of each battery cell. However, the temperature gradient of each battery cell is still higher due to a low thermal conductivity in the normal direction of the cell.
- For designs B and F, due to the absence of cold plates between the cells, the temperature is uniformly distributed in the middle of the module, however, the maximum temperature increase remains high due to the location of cold plates at the extremities and due to the low thermal conductivity in the normal direction of the cell.
- The design C shows that the longitudinal position of the cold plate is reducing more the maximum temperature increases than the case of the cold plate in the transversal position, as observed with design B and F. However, due to the cooling at only one of the sides of the battery module, the temperature gradient remains higher.
- Design D shows the lowest maximum temperature increase and lowest temperature gradient because of the presence of the cold plates at both the longitudinal sides of the module.
- Design E shows that the position of the cold plate at the longitudinal bottom side is more effective than the cold plate in a traversal position, as observed in designs B and F.

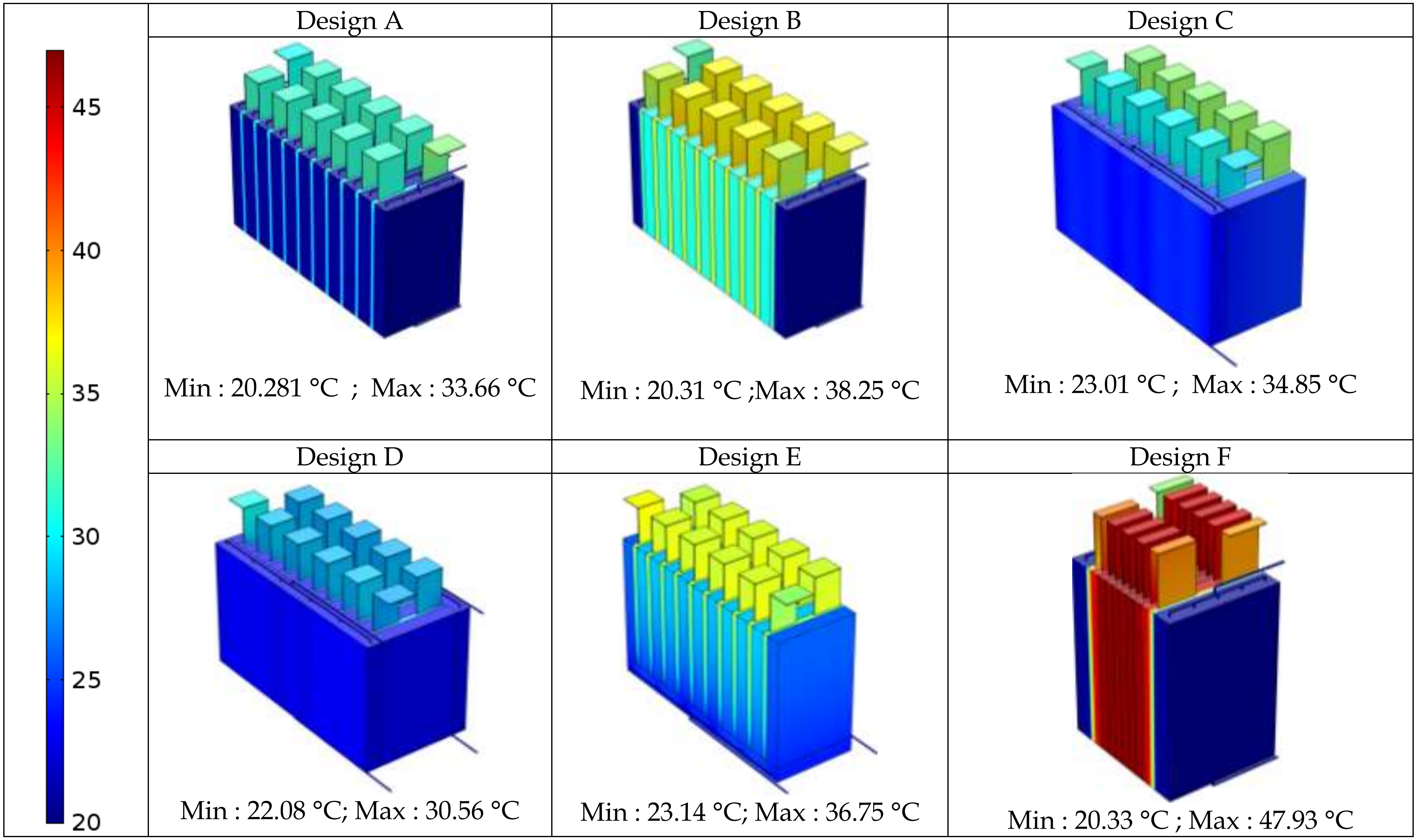

Figure 5.16: Temperature distribution over the different module designs at the end of 4 I_t discharge current rate and 20°C of initial temperature

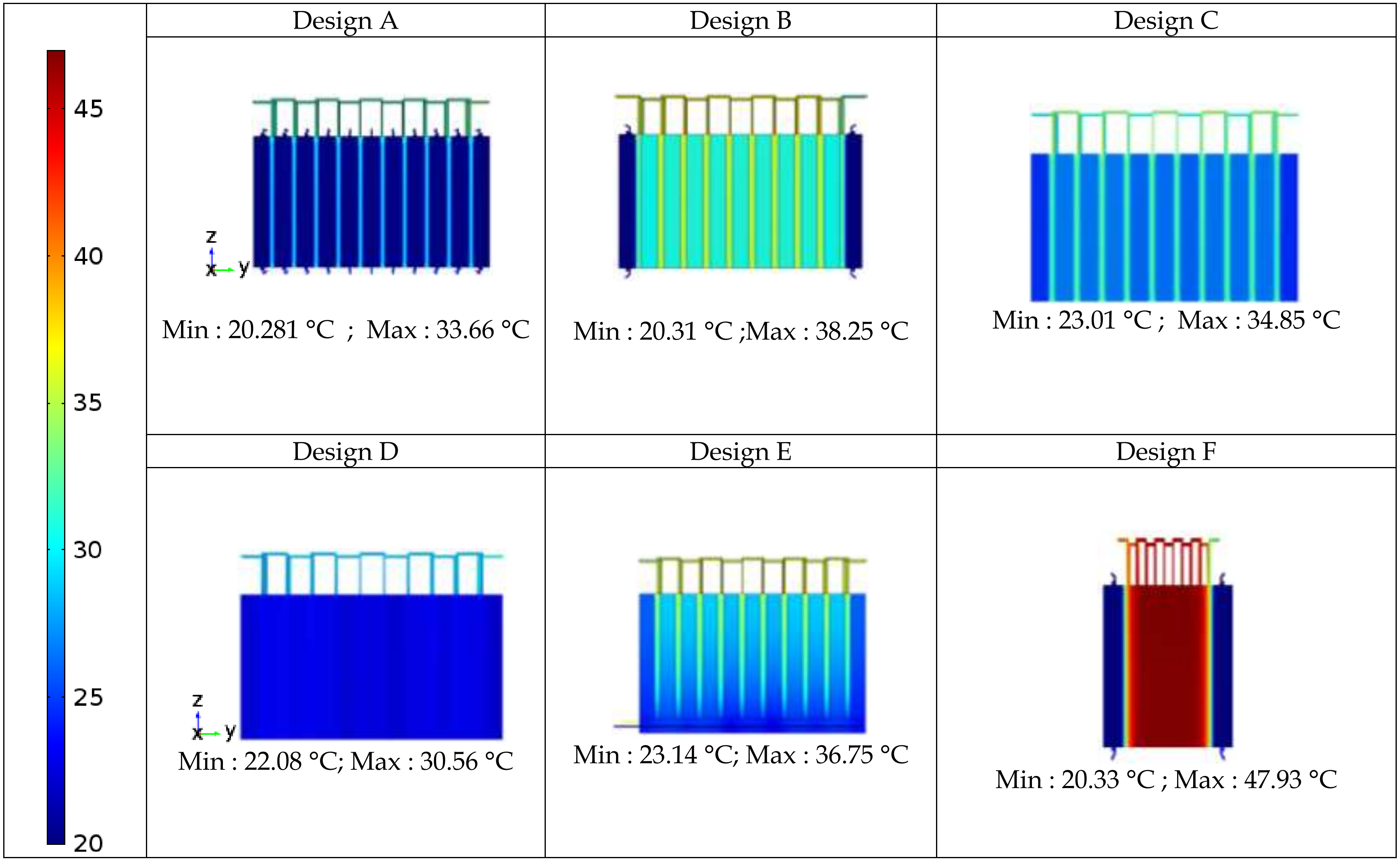

Figure 5.17: Temperature distribution over the different module designs in the zy plane at the end of 4 I_t discharge current rate and 20°C of initial temperature

In conclusion, the battery module with design D is identified as the most optimized one from the thermal point of view.

5.3.2.2.2 Influence of current rate

The performance of the battery module with design D is investigated at different discharge current rates ($2I_t$, $4I_t$ and $6I_t$). The evolution of the maximum temperature increases and temperature gradients are shown in Figure 5.18 and Figure 5.19, respectively. By increasing the current rate, the maximum temperature increase is due to the generated high heat source. With the liquid cooling method, the maximum temperatures dropped are 30°C, 20°C and 10°C compared to the no-cooling cases at the end of 6It, 4It and 2It discharge current rates, respectively. However the temperature gradients increase by 6°C, 4°C and 2°C at the end of $6I_t$, $4I_t$ and $2I_t$ discharge current rates. With high discharge rate, the maximum temperature increase and temperature gradient remain in the safety range (60°C and 5°C). Therefore, the simulation results indicate that the liquid cooling strategies can satisfy the requirement at any allowed operating discharge rate.

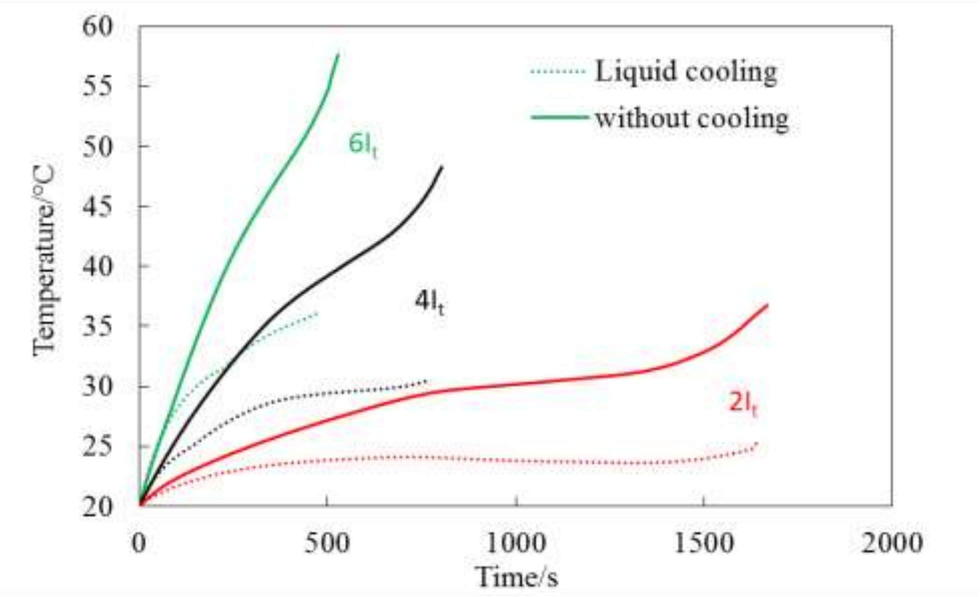

Figure 5.18: Evolution of the maximum temperature at different discharge current rates, 20°C of initial temperature and 30L/min of flow rate

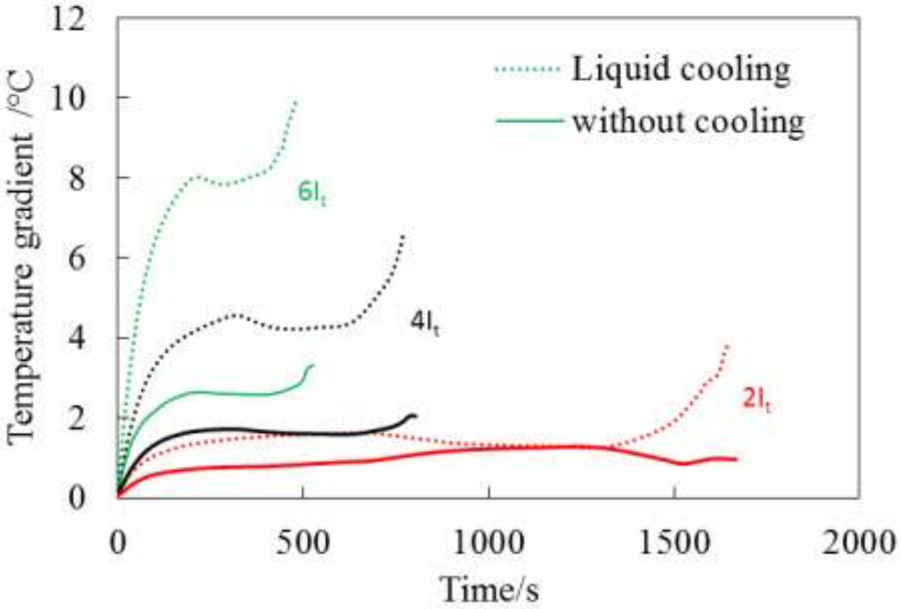

Figure 5.19: Evolution of the temperature gradient at different discharge current rates, 20°C of initial temperature and 30L/min of flow rate

5.3.2.2.3 Influence of the inlet and initial temperatures

The average temperatures of the battery with different inlet temperatures (0°C, 20°C, 40°C) and initial temperatures (0°C, 20°C, 40°C) at 4 It discharge process with a flow rate of 30L/min are illustrated in the Figure 5.20 and Figure 5.21. With a higher difference between the inlet and initial temperature, the inlet temperature became dominant at the end of discharge process; the temperature of the battery will stabilize near the value of the inlet temperature.

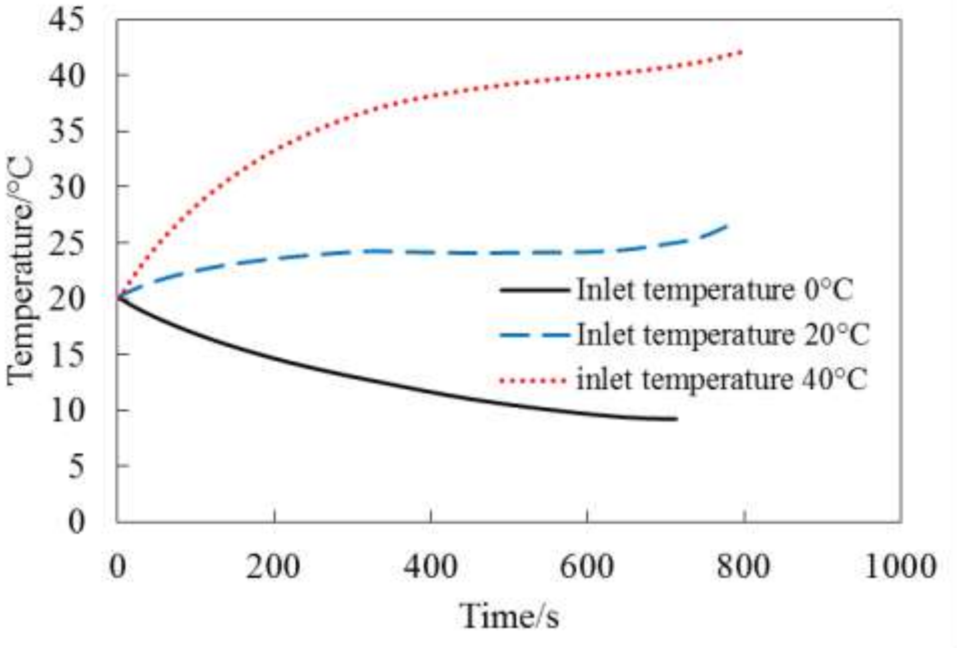

Figure 5.20: Comparison of the average temperature at 4 I_t discharge current rate and 20°C of initial temperature at different coolant inlet temperatures

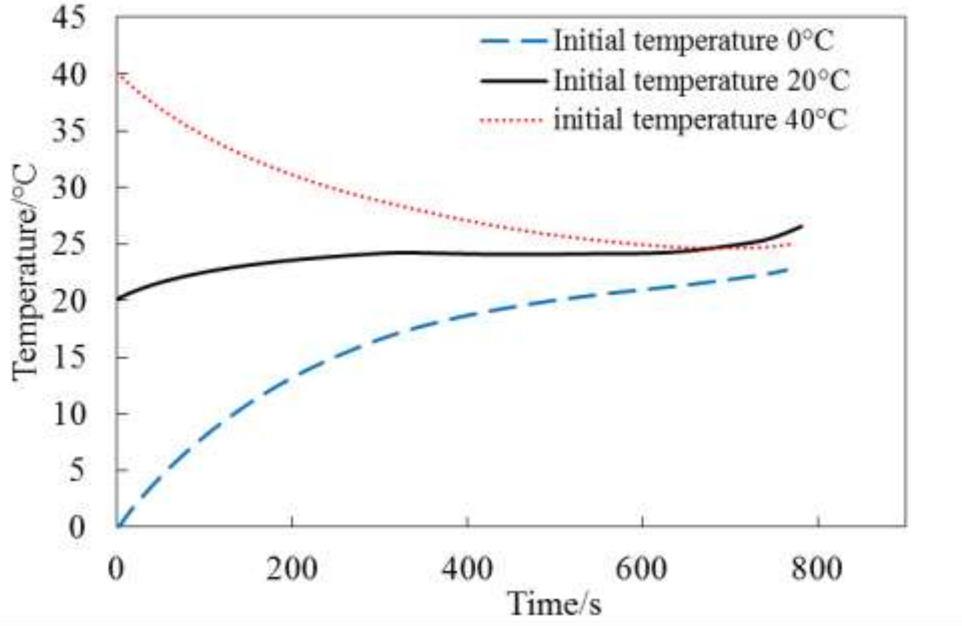

Figure 5.21: Comparison of the average temperature at 4 I_t discharge current rate and 20°C of inlet temperature at different initial temperatures

5.3.2.2.4 Influence of the flow rate

Figure 5.22 shows the evolution of the average battery temperature at various liquid flow rates (5L/min, 10 L/min, 30 L/min and 40 L/min) during discharge process with a current rate of 4 I_t. As expected, it has been shown that with higher flow rate the battery temperature increase is small and the temperature gradient (Figure 5.23) is higher, but remains lower than 5°C (except at the end of the discharge). Higher flow rate results in a higher heat removal by the cooling channel flow.

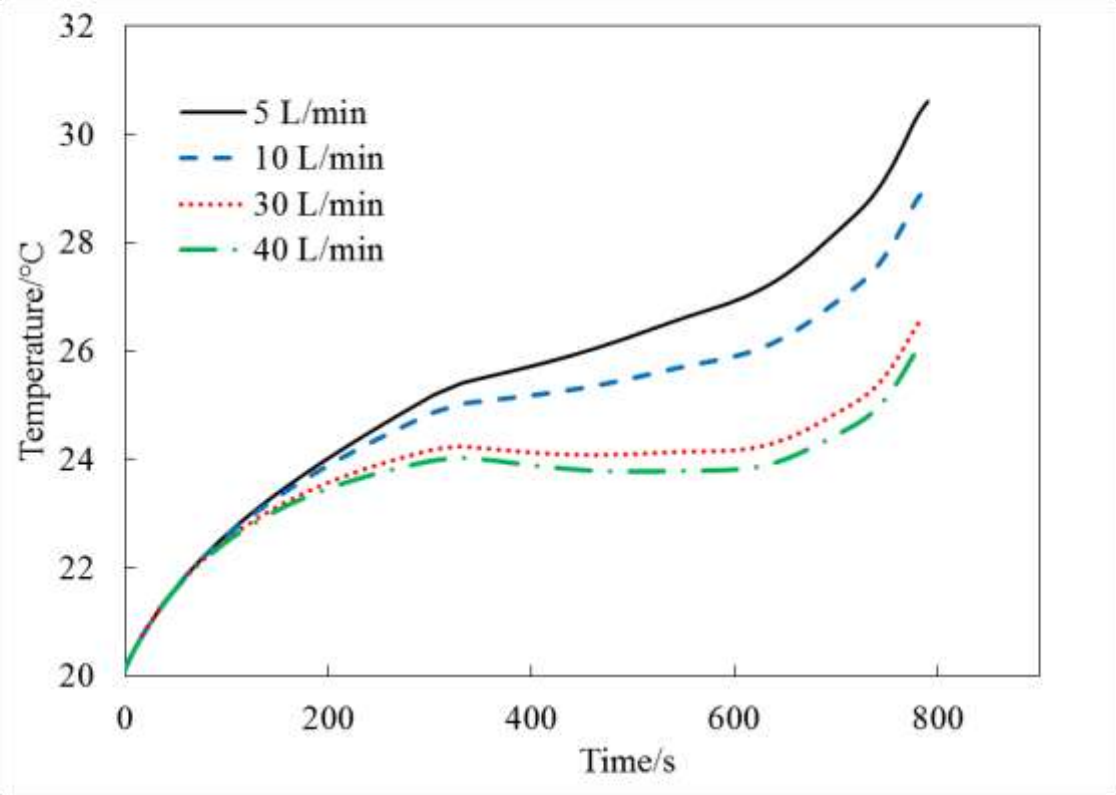

Figure 5.22: Comparison of the average temperature at 4 I_t discharge current rate at different flow rates

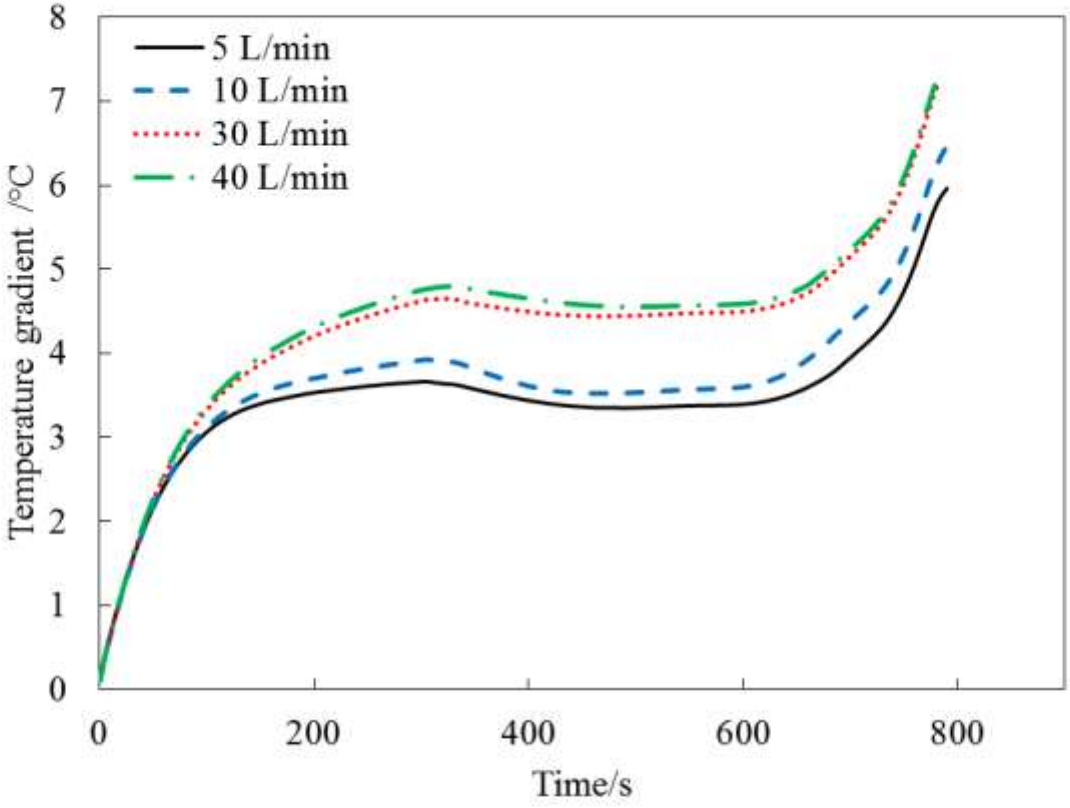

Figure 5.23: Comparison of the temperature gradient at $4I_t$ discharge current rate at different flow rates

The effect of the flow rate on the pressure drop has been investigated as well for design D. Figure 5.24 shows the pressure drop and the corresponding pump power required for various flow rates. As expected, liquid cooling, which requires higher flow rates also needs higher pumping power. As shown previously, with a flow rate of 30L/min, the maximum temperature of the battery pack is relatively low (up to 26°C) and remains within the safety range (between 20°C and 40°C). Therefore the required pumping power needed is about 6W.

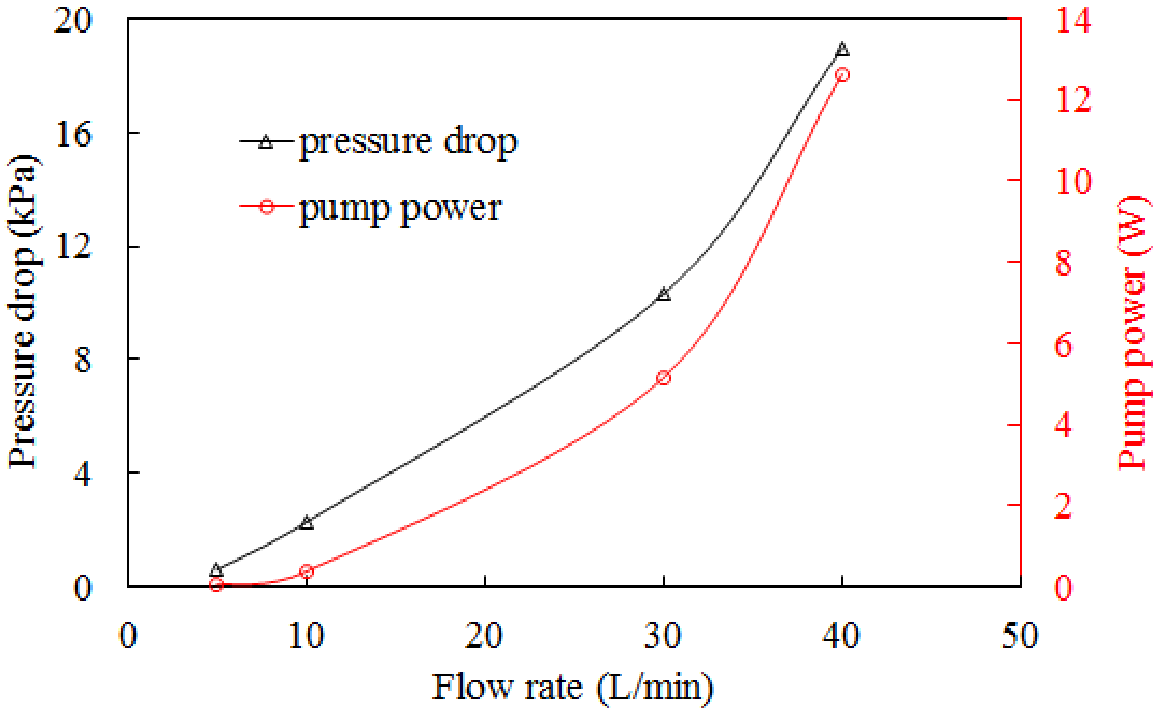

Figure 5.24: Evolution of pressure drop and required pump power at 4 I_t discharge current rate at different flow rates

5.4 Solid-liquid phase change material cooling method

5.4.1 Model Description

5.4.1.1 Geometry features and Model assumptions

The same battery pack with 10 $LiFePO_4$ pouch cells connected in series (32V, 4.5Ah), as previously used, has been selected for this study. The pack is cooled by PCM embed on aluminium-foam, as illustrated in Figure 5.25. The PCM absorbs the heat generated from the batteries while minimizing the temperature changes in the battery pack. As PCM, Paraffin wax is used in this study due to its high latent heat of fusion. Considering its low thermal conductivity, the Paraffin wax is embedded in aluminium-foam in order to increase the heat transfer. The impact of PCM thicknesses and initial temperatures are also investigated at 4 I_t discharge current rate. The battery pack is insulated.

The PCM absorbs the heat generated from the batteries while minimizing the temperature changes in the battery pack. The effectiveness of the PCM is governed by the melting point and latent heat of the material. Paraffin wax (Rubitherm RT-42) was used as the PCM in this study due to its high specific latent heat of fusion and its melting point in the operating temperature range of the battery pack.

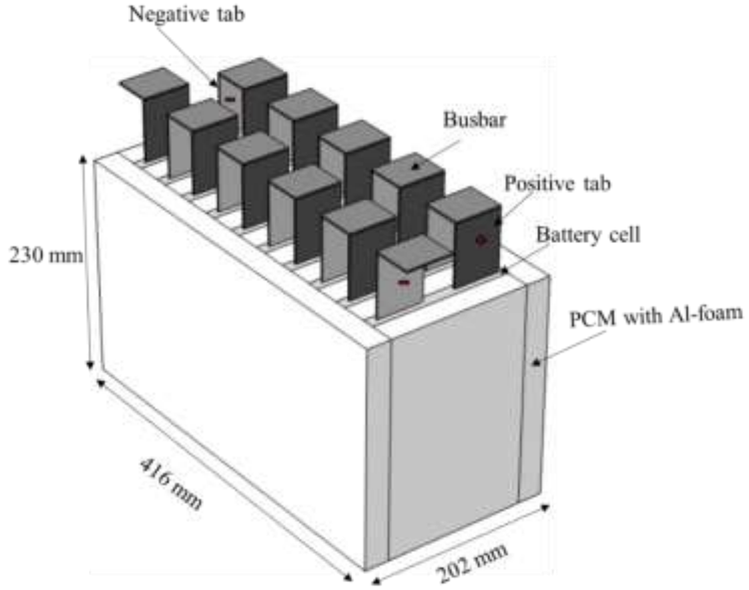

Figure 5.25: Battery pack cooled by PCM embed on aluminum-foam

5.4.1.2 Model development

5.4.1.2.1 Battery domain

The same battery model as described above in the liquid cooling system is used to compute the heat source. This model is coupled with the energy balance applied in PCM domain.

5.4.1.2.2 PCM domain

As shown above, the PCM is embedded in aluminium foam. The PCM is modelled by using the effective heat capacity method. This method is based on the idea of incorporating the phase change phenomenon into the heat capacity calculations [101], [157]. The energy balance of the PCM is expressed as follows:

$$\rho_{eff}\, C_{p_{eff}} \frac{\partial T}{\partial t} = \lambda_{eff}\, \nabla^2 T \tag{5.25}$$

Where

ρ_{eff}(kg/m^3): is the effective density of the PCM embedded in aluminium-foam,

$C_{p,eff}$(J /kg. K): is the effective heat capacity of the PCM embedded in aluminium-foam,

λ_{eff}(W/m^2. K): is the effective thermal conductivity.

The effective thermophysical properties of the PCM embedded in Al-foam depend on the state (liquid or solid) of the PCM and the aluminium properties.

- In the solid phase of the PCM where $T \leq T_s$, the thermophysical properties are given by:

$$\begin{gathered} C_{p_{PCM}} = C_{p_s} \\ \lambda_{PCM} = \lambda_s \\ \rho_{PCM} = \rho_s \end{gathered} \tag{5.26}$$

Where

ρ_s(kg/m^3): is the density of the solid state of the PCM,

$C_{p,s}$(J /kg. K): is the heat capacity of the solid state of the PCM,

λ_s(W/m^2. K): is the thermal conductivity of the solid phase of the PCM,

T_s(°C): is the start melting temperature of PCM.

- At the liquid phase of the PCM where $T \geq T_l$, the thermophysical properties are given by:

$$\begin{gathered} C_{p_{PCM}} = C_{p_l} \\ \lambda_{PCM} = \lambda_l \\ \rho_{PCM} = \rho_l \end{gathered} \tag{5.27}$$

Where

ρ_l(kg/m^3): is the density of the liquid state of the PCM,

$C_{p,l}$(J /kg. K): is the heat capacity of the liquid state of the PCM,

λ_l(W/m^2. K): is the thermal conductivity of the liquid phase of the PCM,

T_l(°C): is the end melting temperature of PCM.

- At the mushy phase $T_s < T < T_l$, where the solid and the liquid phases coexist the effective heat capacity of the material is a linear function of the latent heat (dH(J /kg. K)) of the PCM [158].

$$C_{p_{PCM}} = C_{p_s} + \frac{dH(T-T_s)}{(T_m-T_s)^2} \quad \text{if} \quad T_s < T < T_m$$

$$C_{p_{PCM}} = C_{p_s} + \frac{dH(2T_m-T-T_s)}{(T_m-T_s)^2} \quad \text{if} \quad T_m < T < T_l$$

$$T_m = \frac{(T_s + T_l)}{2} \tag{5.28}$$

$$\lambda_{PCM} = \frac{(\lambda_s + \lambda_l)}{2}$$

$$\rho_{PCM} = \frac{(\rho_s + \rho_l)}{2}$$

The effective thermophysical properties of the system PCM embedded in the aluminum-foam (with ε the associated porosity) is given by the following equations:

$$C_{p_{eff}} = \varepsilon C_{p_{PCM}} + (1-\varepsilon) C_{p_{Al}}$$

$$\lambda_{eff} = \varepsilon \lambda_{PCM} + (1-\varepsilon)\lambda_{Al} \tag{5.29}$$

$$\rho_{eff} = \varepsilon \rho_{PCM} + (1-\varepsilon)\rho_{Al}$$

By taking into account the convection flow of the liquid state of the PCM during phase change, the flow is represented by the volume average model based on Brinkman-Forchheimer extended Darcy model [159], which take into account the porous environment of the aluminium-foam,. Therefore the continuity and momentum equations are given by:

- The continuity equation which expressed the conservation of mass is formulated as:

$$\varphi \frac{\partial \rho_l}{\partial t} + \nabla.(\rho_l\, u) = 0 \tag{5.30}$$

Where
φ is the volume fraction of the liquid state in PCM,
u (m/s) is the velocity vector of the liquid state in PCM.

- The momentum equations are given by:

$$\rho_l \left[\frac{1}{\varphi}\frac{\partial u}{\partial t} + \frac{1}{\varphi}\nabla\left(\frac{u\,.\,u}{\varphi}\right)\right] = -\nabla P + \frac{\mu}{\varphi \rho_l}\nabla^2 u - \frac{\mu}{K}u - \frac{c_F \rho_l}{\sqrt{K}}|u|u + \rho_l g \beta (T_l - T_S) \tag{5.31}$$

Where

$P(\mathrm{Pa})$: is the pressure of the liquid state of the PCM,

$\mu(\mathrm{N.s.m^{-2}})$: is the kinetic viscosity of the liquid state of the PCM,

$K(\mathrm{m^2})$: is the permeability of the aluminum-foam,

c_F is the inertial coefficient,

$\beta(\mathrm{K^{-1}})$ is the thermal expansion coefficient of the liquid state of the PCM.

5.4.1.2.3 Boundary and initial conditions

- Interface battery cell/PCM

The heat flux continuity is applied, where the heat from the battery is transferred to the PCM:

$$-\lambda_{battery}\nabla\mathrm{T}|_{boundaries} = -\lambda_{eff}\nabla\mathrm{T}|_{boundaries} \tag{5.32}$$

- All other external boundaries are thermally isolated in order to test the efficiency of the cooling system. Therefore, non-heat exchange with the ambient environment is considered.

$$\lambda\nabla\mathrm{T}|_{boundaries} = 0 \tag{5.33}$$

- The initial temperature of the battery pack is defined as T_{ini}.

$$\mathrm{T} = \mathrm{T_{ini}} \tag{5.34}$$

5.4.1.2.4 Input parameters

The paraffin wax is used as a PCM and these different thermophysical properties are from the work of Khateeb et al. [160] and included in Table 5.1.

Parameters	**Symbol**	**Value**
Conductivity of the solid phase	λ_s ($\mathrm{Wm^{-1}K^{-1}}$)	0.29
Conductivity of the liquid phase	λ_l ($\mathrm{Wm^{-1}K^{-1}}$)	0.21
Conductivity of Aluminum	λ_{Al} ($\mathrm{Wm^{-1}K^{-1}}$)	218
Heat capacity of the solid phase	C_{p_s} ($\mathrm{kJ\ kg^{-1}K^{-1}}$)	1.77
Heat capacity of the liquid phase	C_{p_l} ($\mathrm{kJ\ kg^{-1}K^{-1}}$)	1.77
Heat capacity of Aluminum	$C_{p_{Al}}$ ($\mathrm{kJ\ kg^{-1}K^{-1}}$)	0.963
Porosity	ε	0.8
Density of the solid phase	ρ_s ($\mathrm{kg\ m^{-3}}$)	910
Density of the liquid phase	ρ_l ($\mathrm{kg\ m^{-3}}$)	822
Density of Aluminum	ρ_{Al} ($\mathrm{kg\ m^{-3}}$)	2700
Latent heat of melting	dH ($\mathrm{kJ\ kg^{-1}}$)	195
Start temperature of PCM melting	T_s (°C)	41
End temperature of PCM melting	T_l (°C)	44
Thermal expansion	β($\mathrm{K^{-1}}$)	$16.31\ 10^{-4}$

Table 5.1: Thermophysical properties for model materials [160]

5.4.2 Results

5.4.2.1 Influence of current rate

The equations are simultaneous solved in Comsol Multiphysics, with the same numerical procedure that has been used in the cold plate design in section 5.3.2. Figure 5.30 shows the maximum temperature profiles at different discharge current rates (2 I_t, 4 I_t and 6 I_t) of the battery module cooled by PCM with 26 mm of thicknesses. As observed previously, with the higher discharge current rate, the maximum temperature increase is higher.

Whether the temperature of the cell module is lower than the melting temperature of the PCM (41°C), then the temperatures of the cells follow the same trends, which lower values than the case of without cooling, as observed with the curve of 2It discharge current rate. The temperatures decrease of the cells cooled by the PCM is lower compared to the case of without cooling due the larger volume of the module with PCM. However, when it reaches the melting point, the heat from the batteries is absorbed by the PCM for the phase change while minimizing temperature changes in the module and then stabilized the cell temperature, as observed with the curve of 6It.

With the PCM cooling method, the maximum temperature drops are 10°C, 5°C and 2°C compared to the no-cooling case at the end of 6It, 4It and 2It discharge current rates, respectively. However, the maximum temperature gradients are decreasing by 2°C, 1.5°C and 0.5°C during 6It, 4It and 2It discharge current rates.

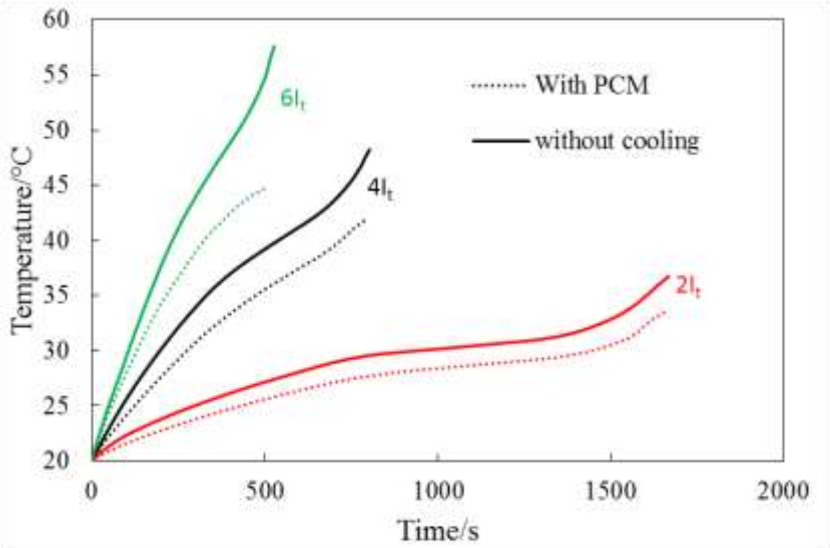

Figure 5.26: Maximum cell temperature profiles at different discharge current rates and 20°C of initial temperature

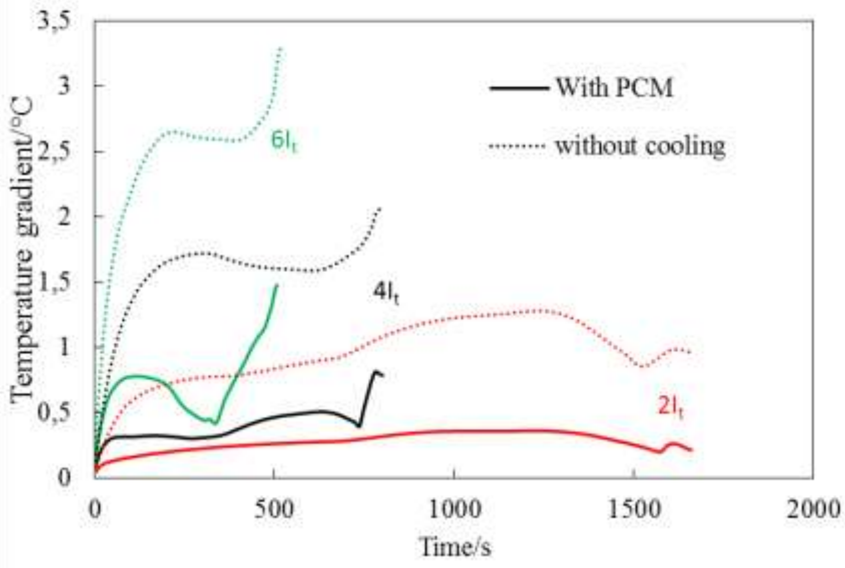

Figure 5.27: Temperature gradient profiles at different discharge current rates and 20°C of initial temperature

Figure 5.28 presents the temperature distributions of the pack cooled with PCM at the end of different discharge current rate. The temperature distributions are nearly uniform, with maximums located on the tab and busbars connections. Figure 5.29 shows the fraction of liquid due to the phase change at the end of different discharge current rates. It has been shown that higher fraction of liquid is present at 6It discharge current rate due to the high temperature of the cell.

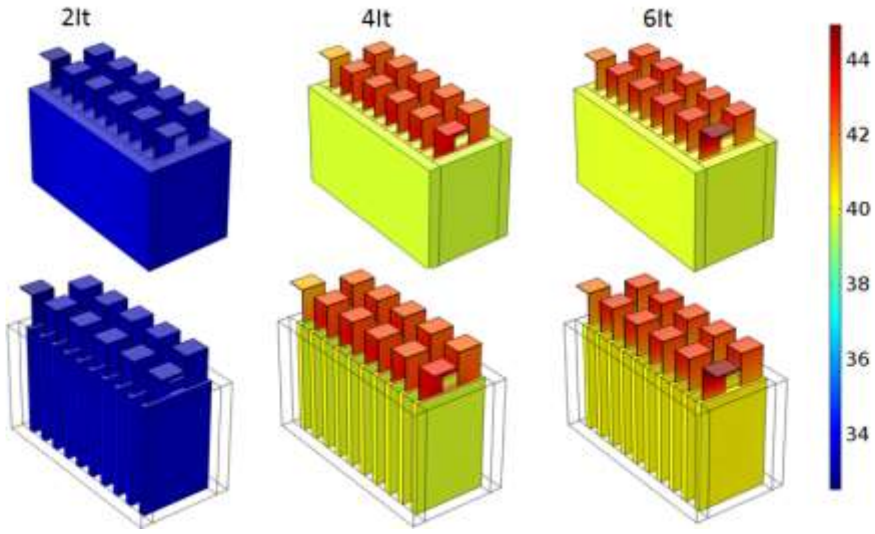

Figure 5.28: Temperature distribution over the battery pack at different discharge current rates at the end of the process

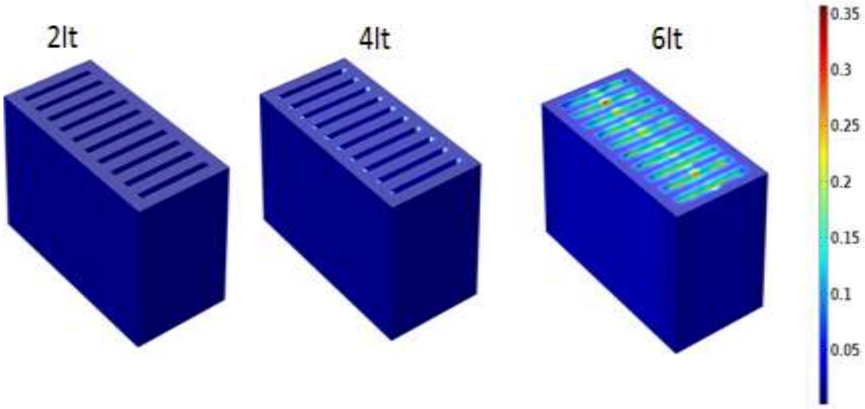

Figure 5.29: fraction of liquid over the PCM at different discharge current rates at the end of the process

5.4.2.2 Influence of PCM thickness

In addition, with larger thickness, the average cell temperatures become lower, but the temperature gradient becomes higher, as shown in Figure 5.31. The temperature gradient of the cell with PCM cooling method is relatively small (less than 2°C), except at the end of the discharge process.

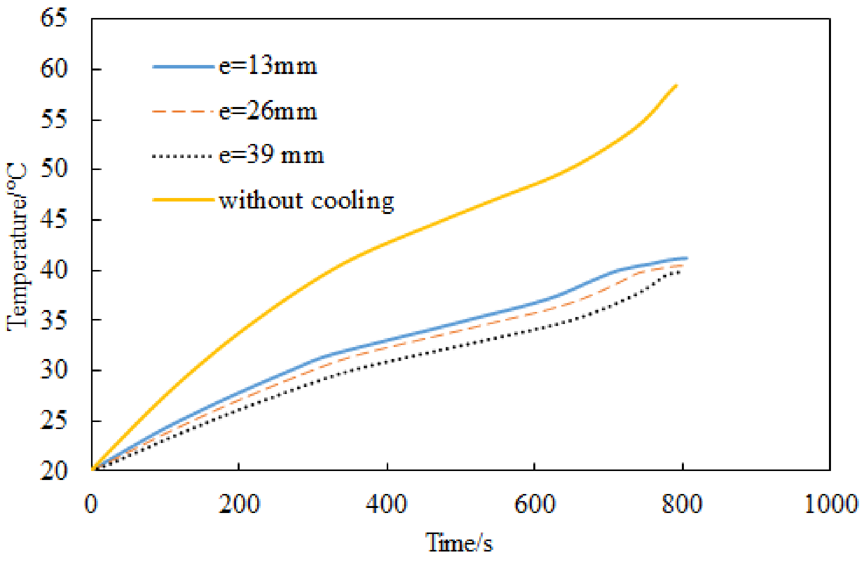

Figure 5.30: Maximum cell temperature profiles at 4 I_t discharge current rate and 20°C of initial temperature

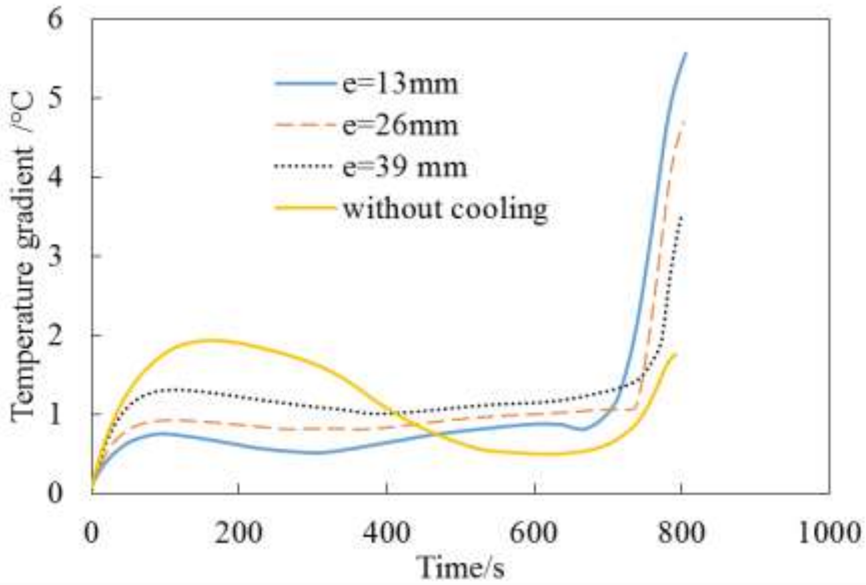

Figure 5.31: Temperature gradient profiles at 4 I_t discharge current rate and 20°C of initial temperature

5.4.2.3 Influence of initial temperature

The influence of initial temperature is investigated at 4 I_t discharge current rate. Two initial temperatures (20°C and 40°C) are used. From Figure 5.32, it has been shown that with an initial temperature of 20°C and 40°C, the temperature increased to around 21°C and 4°C, respectively. These results show that when the temperature difference between the initial temperature and the PCM melting temperature is low, the temperature increase of the battery module is lower as well.

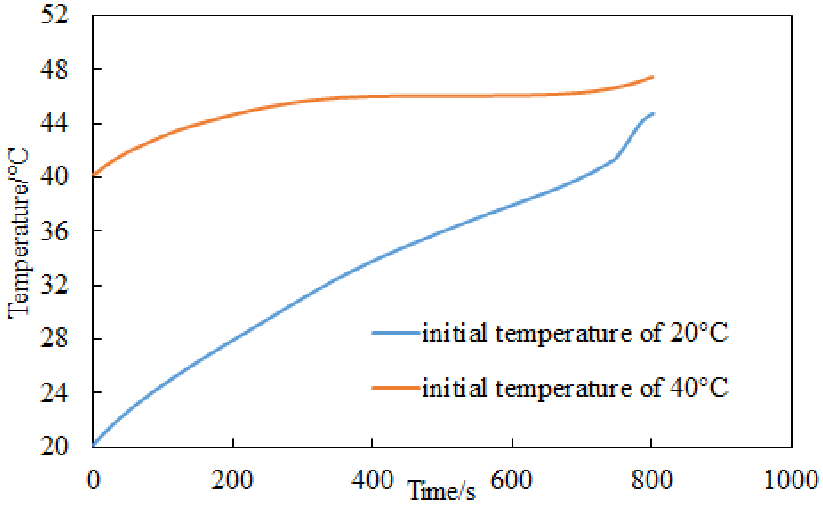

Figure 5.32: Maximum cell temperature profiles at 4 I_t discharge current rate at different initial temperatures

5.4.2.4 Combination of PCM with liquid cooling

As shown previously in section 5.3.2, the liquid cooling with design D was found as the most optimized one in term of lowering the maximum temperature and gradient temperature increase. Therefore, the liquid cooling is embedded on the PCM with respect to design D as shown in Figure 5.33.

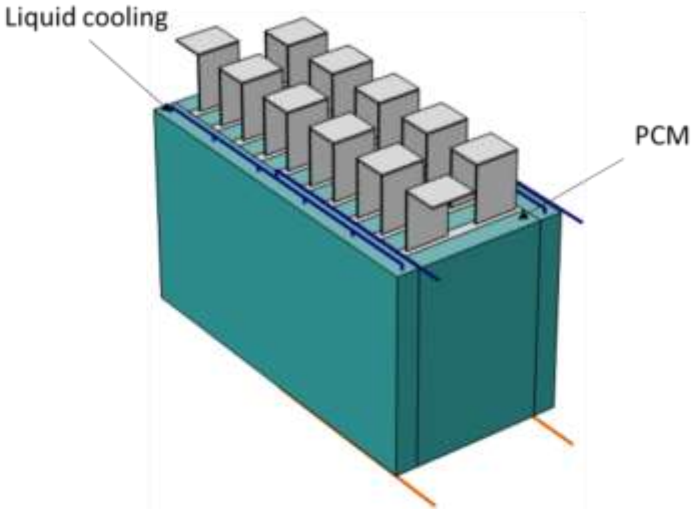

Figure 5.33: Design of PCM combining with liquid cooling

Figure 5.34 shows the temperature profiles of the cells cooling with PCM without liquid cooling and in combination with liquid cooling with an inlet temperature of 20°C and flow rate of 30L/min. It is illustrated that the PCM with liquid cooling shows less battery temperature increase. However, the temperature gradient remains higher as illustrated in Figure 5.35, due to the non-uniform cooling of the channel flows.

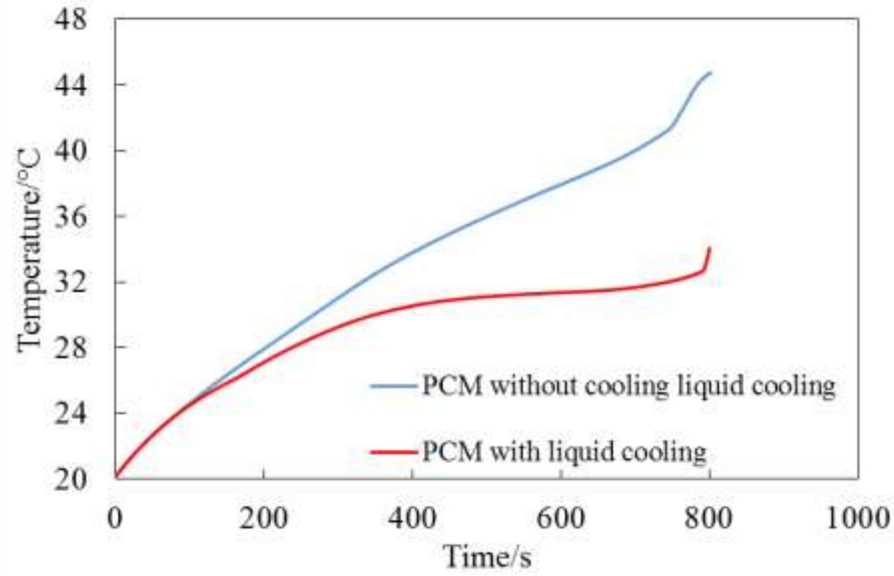

Figure 5.34: Maximum cell temperature profiles at 4 I_t discharge current rate at 20°C of initial temperatures

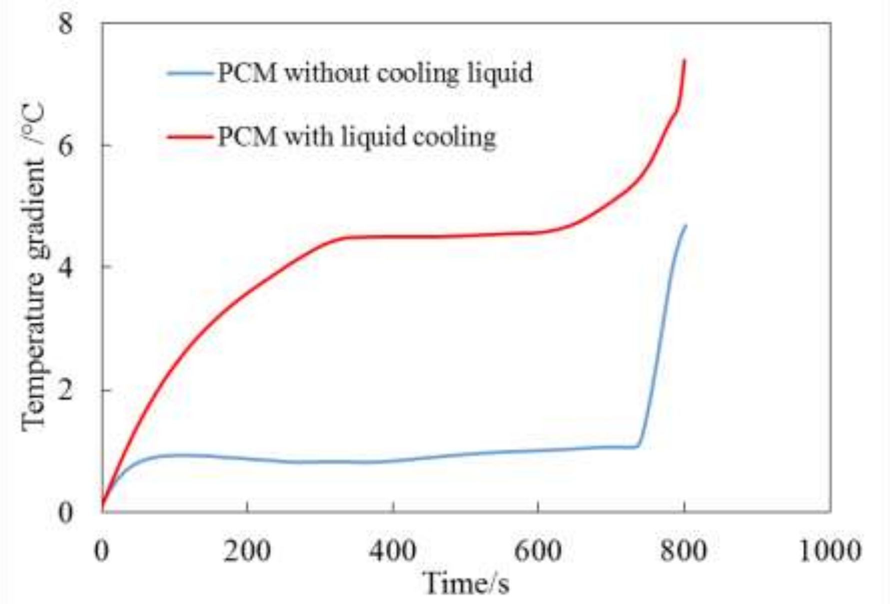

Figure 5.35: Temperature gradient profiles at 4 I_t discharge current rate at 20°C of initial temperatures

5.5 Comparison between liquid and PCM cooling methods

5.5.1 Performance comparison based on driving cycle

A performance comparison of both BTMS presented above is made by applying a driving cycle from Peugeot. The input current rate is presented in Figure 5.36. The positive values correspond to the charge current rate and the negative values correspond to the discharge current rate.

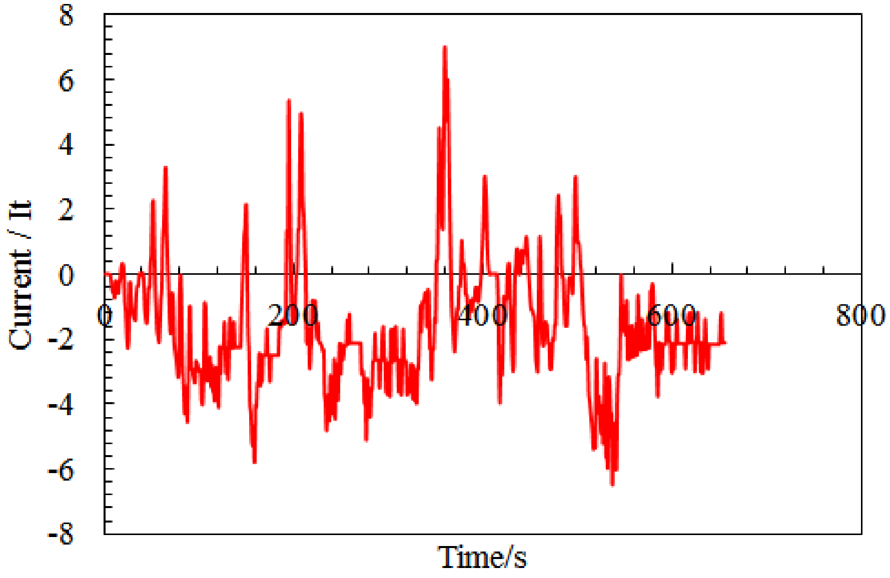

Figure 5.36: Peugeot driving cycle

Figure 5.37 shows the evolutions of the voltage during the driving cycle for both BTMS. The both profiles are similar.

It has been shown that the BTMS based on liquid cooling shows more temperature drop than the PCM cooling method as shown in Figure 5.38 and Figure 5.39. However, the temperature gradient given by the liquid cooling remains higher, as illustrated in Figure 5.39.

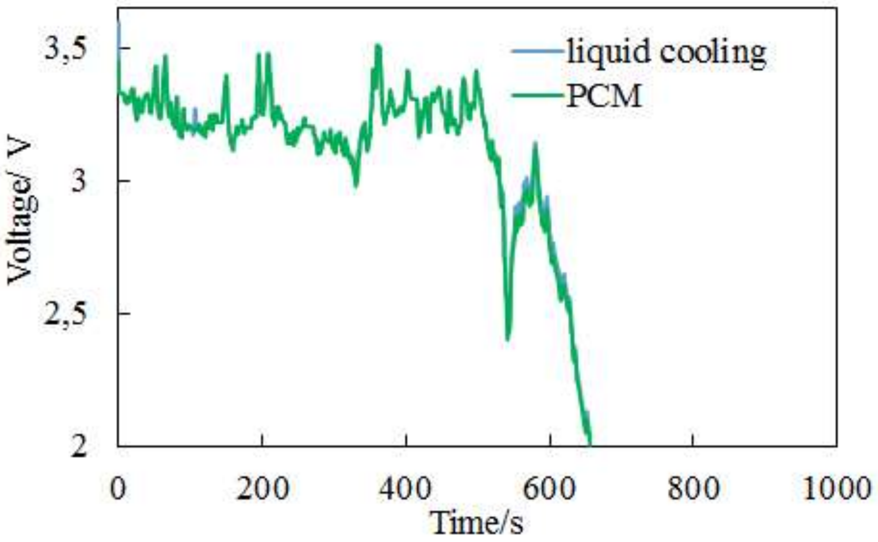

Figure 5.37: Evolution of the voltage during Peugeot driving cycle

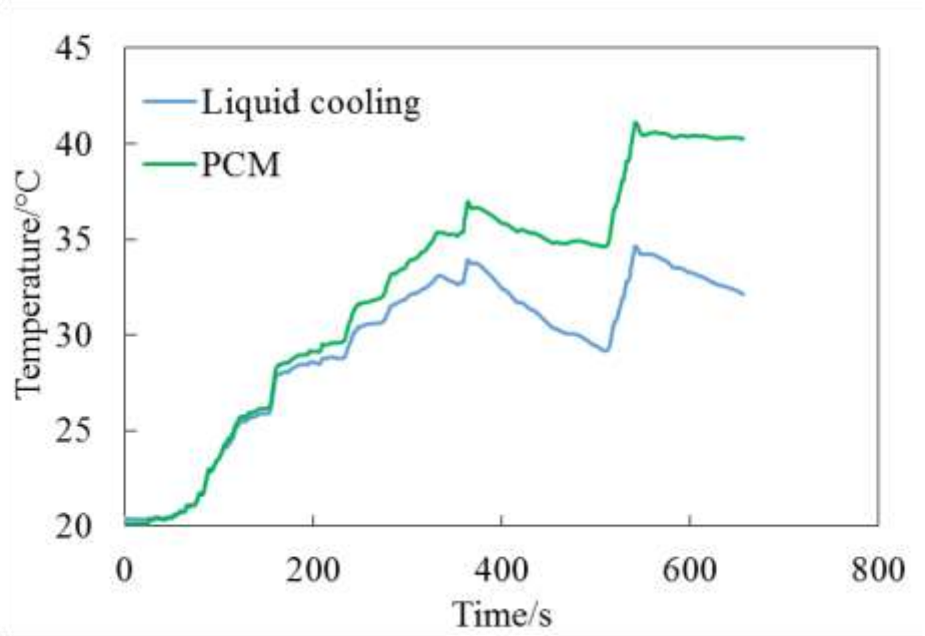

Figure 5.38: Evolution of the maximum temperature during Peugeot driving cycle

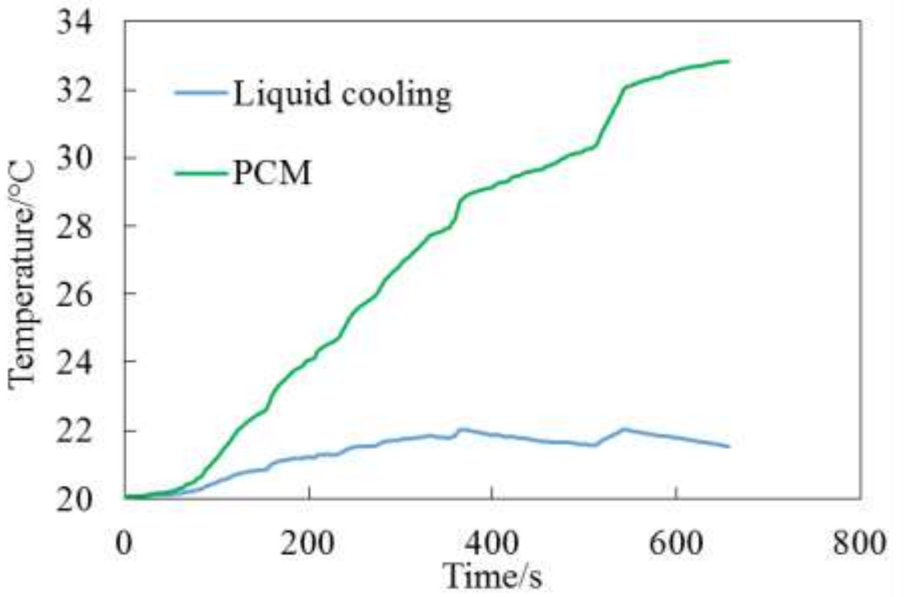

Figure 5.39: Evolution of the average temperature during Peugeot driving cycle

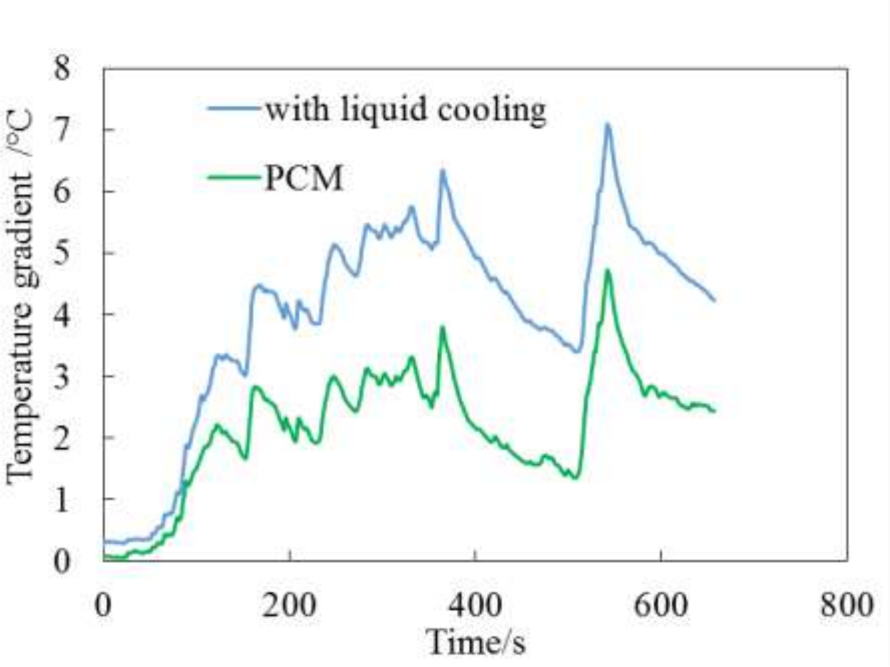

Figure 5.40: Evolution of the gradient temperature during Peugeot driving cycle

5.5.2 Cost comparison of the different cooling strategies

A cost comparison of the two BTMS as presented above, such as the liquid cooling and PCM are made with the price data of different components that composed the module. The mentioned prices should be considered as an approximation depending of the component supplier.

Cooling Strategies	Components	Units	Cost, euro
Liquid-cooling	Cold plate	2	500
	Hot plate	11	1190
	Pump	1	350
	Chiller	1	5150
		Total	7190
PCM embed on Al-foam	Aluminum foam	1	6256
	PCM Paraffin wax (Rubitherm RT-42)	1	1380
		Total	7636

Table 5.2: cost comparison of the different studied BTMSs

As shown in Table 5.2, liquid cooling have almost the same cost than the PCM. Nevertheless, many other aspects, such as the battery temperature specifications, ambient conditions, expected battery lifetime, consumption of the auxiliary system, maintenance, location flexibility, etc.…, should also be taken into account when selecting the best configuration. It should be noted that the proposed cost comparison is not based on series productions.

5.6 Conclusion

In this chapter different thermal management strategies such as liquid cooling and passive cooling using phase change material embedded in aluminium foam (liquid-solid phase change material) have been investigated by using the developed electrochemical-thermal model in chapter 4 coupled with fluid dynamics. The model has been developed in COMSOL Multiphysics. Firstly, different liquid cold plate's configurations has been investigated in order to obtain the efficient cooling architecture, which allows to decrease the temperature and to obtain a more uniform temperature distribution over the surface of the battery cell. It has been concluded that the cooling plate with design 1 successfully controls the maximum temperature and reduces the temperature gradient due to the high surface contact between the cooling channel and plates. Furthermore, the performances of a battery module with 10 cells have been investigated at different position of the cold plate. The both longitudinal sides have been found to be the best position of the cold plates. The hot plates are also used to make the temperature distribution of the cells more uniforms. Different operating conditions are also investigated. It has been shown that the flow rate of 30 L/min, represents an optimum value for lowering the maximum temperature increase, therefore the required pump power needed is about 6W. It has also been noticed that more the difference between the inlet and initial temperature is higher; the temperature of the battery tends to stabilize near the value of the inlet temperature at the end of the discharge process.

Secondly, the performances of a battery module have been investigated by using passive cooling with PCM embedded in aluminium-foam. Different discharge current rates have been simulated and show that with the PCM cooling method, the maximum cell temperature drops are 10°C, 5°C and 2°C, compared to the non-cooling case during the 6It, 4It and 2It discharge current rates, respectively. The temperature of the battery module increases steeply until the PCM reaches its melting temperature, where it stays nearly constant due to the high latent heat of the PCM. Therefore, the PCM melting temperature and latent heat are crucial parameters for the PCM selection. In addition, by increasing the thickness of the PCM, the average temperature of the battery module becomes lower, while the temperature gradient becomes higher. Furthermore, for an initial temperature of the battery module close to PCM melting temperature, the temperature increase of the battery module is lower.

Finally, a performance and cost comparison have been made between the liquid cooling and the PCM. The performance comparisons are made by applying a driving cycle from Peugeot for electric vehicles. More temperature (maximal and average) drop has been observed with the liquid cooling than the PCM cooling method. However, the temperature gradient given by the liquid cooling remains higher. A cost comparison based on non-series productions of the both cooling methods show that the liquid cooling have almost the same cost than the PCM. Nevertheless, many other aspects, such as the battery temperature specifications, ambient conditions, expected battery lifetime, consumption of the auxiliary system, maintenance, location flexibility etc. Should also be taken into account for the liquid cooling system.

Chapter 6: Conclusions, Contributions and Future Work

6. Conclusions, Contributions and Future Work

6.1 Conclusions and overview of work performed

After a brief presentation of the state-of-the-art of BEVs, HEVs and PHEVs, the main characteristics of the different lithium ion battery and their applications in some commercial vehicles are compared and analyzed. From chapter 2, it has been shown that the temperature is one of the major parameters influencing the battery performance and lifetime in many aspects. At cell level, the safety improvement can be made by acting on the cell chemistry or the cell design. At pack or module level the performance and safety can be improved by designing an optimal battery thermal management system.

In chapter 3, a 2D-thermal model is developed for a large size Li-ion pouch battery for BEVs, which is able to predict the surface temperature distribution of the battery at different operating conditions, accurately. The simulation results are in good agreement with the experimental results where the maximum relative error is between 7%. A novel battery thermal parameter estimation has been developed to estimate the related thermal parameters by using the thermal equivalent circuit model which is associated to the first order Cauer model. This model involves a primary calculation in order to calculate the percentage of heat flows through each side of the cell. These percentages of heat depend mainly on the surface of the sides.

In chapter 4, extensive three-dimensional simulations of large $LiFePO_4$ pouch cells have been carried out to investigate the impact of different pouch cell designs on performance and variable distributions. It has been shown that the cell designs with symmetrical configurations (case 2 and case 4) show uniform potential and current density gradient, which minimize the ohmic heat and lead to more uniform active material utilization and temperature distributions across the cell surface. Cell design with symmetrical configuration tends to minimize the maximum current pathways. It is found that the high potential, current density and temperature gradient are mainly located near the positive tab due to its high resistivity. Due to charge conservation, the potential distribution along the negative current collector at the beginning of discharge are responsible for the non-uniform active material utilization and the potential distribution in the positive current collector. In addition, the increase of the tab width makes the potential, current density and thermal distributions more uniform and improve the battery performance by increasing its output voltage. This also tends to increase the energy and power densities. At the pack level, the design of case 2 with a higher tab width can be cycled more uniformly and thereby allows a less complex cooling strategy.

In chapter 5, different thermal management strategies such as water cooling and passive cooling using phase change material embedded in aluminium foam (liquid-solid phase change material) have been investigated by using the developed electrochemical-thermal model in chapter 4 coupled with fluid dynamics. The model has been developed in COMSOL Multiphysics. Firstly, different liquid cold plate's configurations have been investigated in order to obtain the efficient cooling architecture, which allows to decrease the temperature and to obtain a more uniform temperature distribution over the surface of the battery cell. It has been found that the cooling plate with (design 1) successfully controls the maximum temperature and reduces the temperature gradient due to the high surface contact between the cooling channel and plates. Furthermore, the performances of a battery module with 10 cells have been investigated at different position of the cold plate. Both longitudinal sides have been found as the best position of the cold plates. The hot plates are also used to make the temperature distribution of the cells more uniforms. Different operating conditions are also investigated. It has been shown that the flow rate of 30 L/min, represents an optimum value for lowering the maximum temperature increase. Therefore the required pump power needed is about 6W for efficient cooling of the investigated cell module. In addition, when the inlet temperature is different from the initial temperature, therefore at the end of the discharge process, the cell temperature tends to the value of the inlet temperature.

Secondly, the performances of a battery module have been investigated by using passive cooling with PCM embedded in aluminium-foam. Different discharge current rates have been simulated and show that with the PCM cooling method, the maximum cell temperature drops are 10°C, 5°C and 2°C, compared to the no-cooling cases, during the $6I_t$, $4I_t$ and $2I_t$ discharge current rates, respectively. The temperature of the battery module increases steeply until the PCM reaches its melting temperature, where it stays nearly constant due to the high latent heat of the PCM. Therefore the PCM melting temperature and latent heat are crucial parameters for the PCM selection. In addition, by increasing the thickness of the PCM, the average temperature of the battery module becomes lower, while the temperature gradient becomes higher. Furthermore, for an initial temperature of the battery module close to PCM melting temperature, the temperature increase of the battery module is lower.

Finally an extended comparison has been made between the liquid cooling and the PCM. The performance comparisons are made by applying a typical driving cycle. More temperature (maximal and average) drop has been observed based on the liquid cooling than the PCM cooling method. However, the temperature gradient given by the liquid cooling remains higher. A cost approximation of both cooling methods is also compared and shows that the liquid cooling has almost the same cost than the PCM. Nevertheless, many other aspects, such as the battery temperature specifications, ambient conditions, expected battery lifetime, consumption of the auxiliary system, maintenance, location flexibility etc. Should also be taken into account regarding the design of the liquid cooling system.

6.2 Contributions

The major contributions of this work could be summarized as follows:

- Development of an extended 2D electrical-thermal model,
- The in-depth thermal characterization using a thermal camera,
- Development of a novel 3D thermal parameter estimation tool based on a thermal equivalent circuit model by calculating the ratio of heat throughout the different directions of the cell,
- Development of a fully coupled 3D electrochemical-thermal model,
- Investigation of the pouch cell design based on developed 3D electrochemical-thermal model,
- Development of an extended 1D pipe flow to simulate the liquid flow in a channel,
- Investigation of different cold plate designs,
- Development of a new liquid cooling battery thermal management system designs
- Development of an extended PCM new liquid cooling strategy by taking into accounts the convection flow in the aluminium-foam.

6.3 Future work

The presented work in this PhD dissertation gave rise to additional research opportunities concerning the following issues:

- Experimental investigation of the different pouch cell design,
- Reduced order of the fully electrochemical-thermal model in order to simulate the full battery cell by taking into account each cell layer. The results of such analysis can be compared to our work, where one cell layer has been considered, in order

to validate the made assumptions. Therefore, the battery reduced order model can be easily implemented in a BMS.

- Development of a BTMS model that takes into accounts the ageing phenomenon.
- Experimental investigation of the developed BTMSs used in this work in order to ensure the validity of the numerical results.
- Improvement of the cold plate's design.
- Investigation of the cooling plate with different refrigerant types.
- Investigation of different PCM with different melting points.
- Extension of the investigation of the battery module to pack level.

Appendix

7. Appendix I

7.1 Internal resistance as a function of SoC and temperature at different current rate

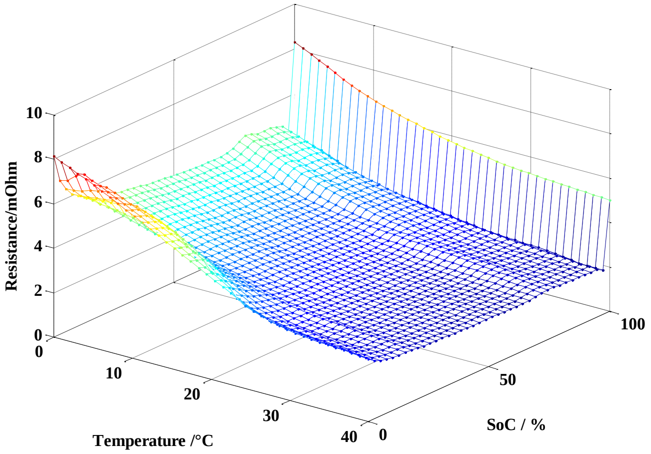

Figure 7.1: Internal resistance as a function of SoC and temperature at 1/3I$_t$ charge current rate

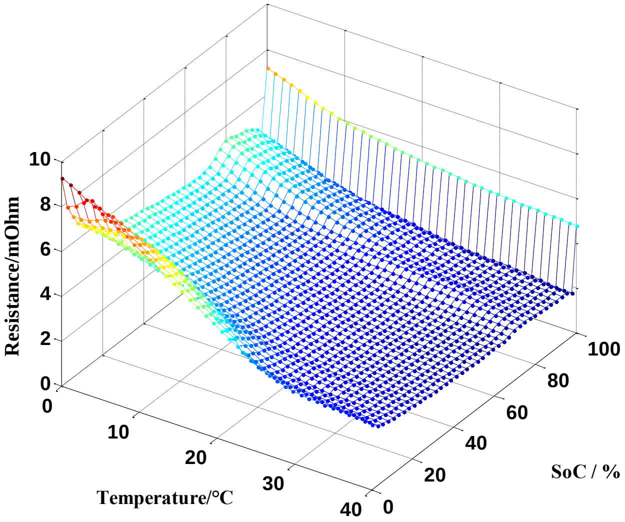

Figure 7.2: Internal resistance as a function of SoC and temperature at 1/3I$_t$ discharge current rate

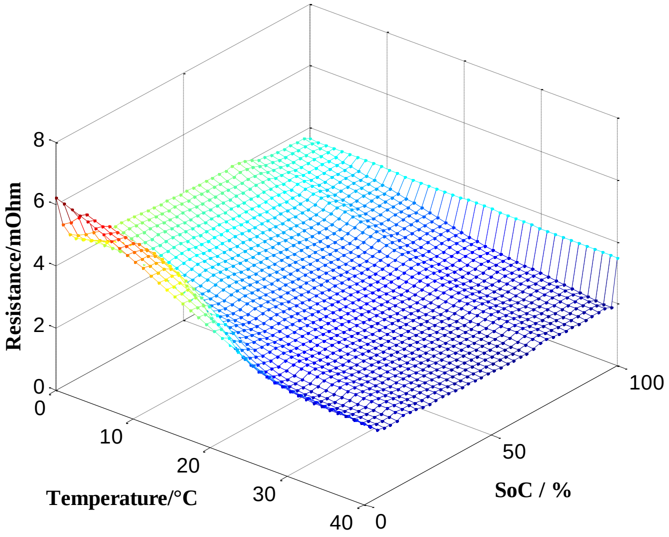

Figure 7.3: Internal resistance as a function of SoC and temperature at 2I_t charge current rate

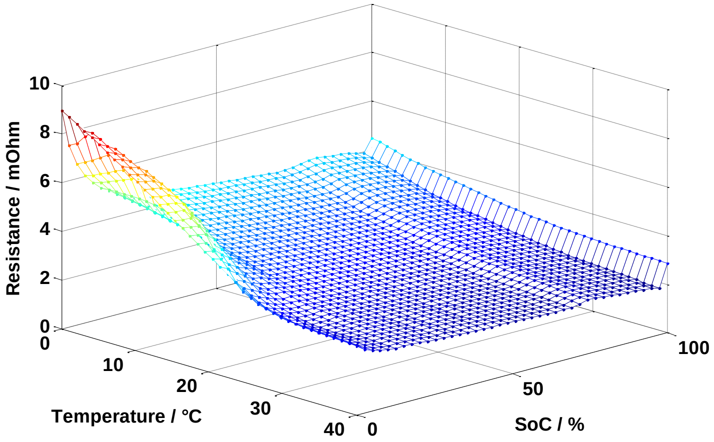

Figure 7.4: Internal resistance as a function of SoC and temperature at 2I_t discharge current rate

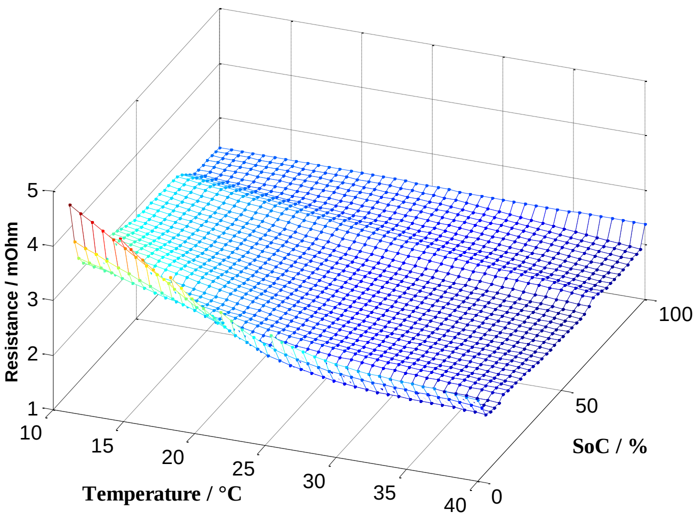

Figure 7.5: Internal resistance as a function of SoC and temperature at $3I_t$ charge current rate

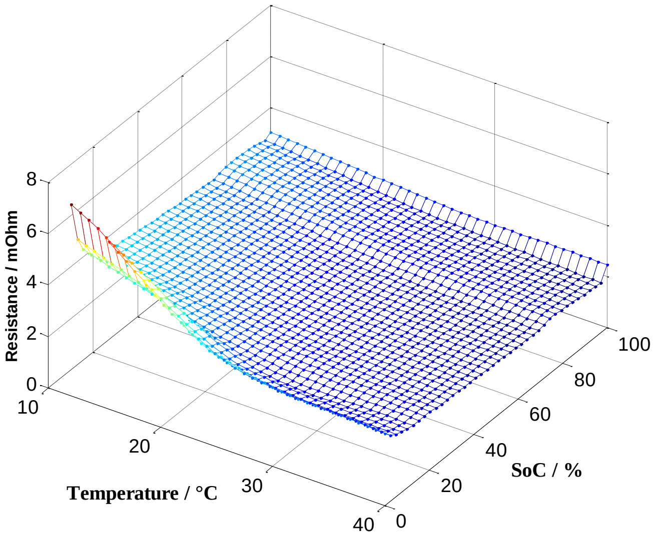

Figure 7.6: Internal resistance as a function of SoC and temperature at $3I_t$ discharge current rate

7.2 Comparison of the Thermal distributions based on experimental thermal imager and modeling at different current rates.

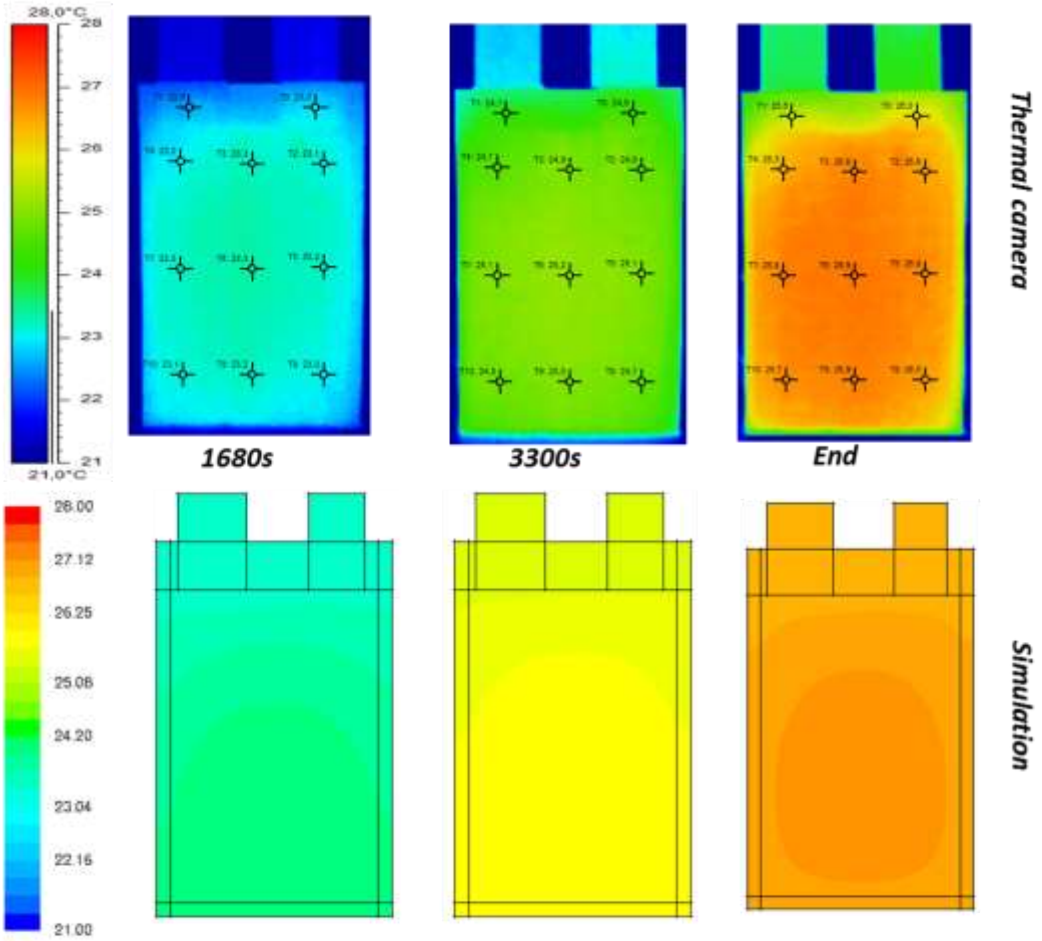

Figure 7.7: Thermal distributions based on experimental thermal imager and modeling at $2/3I_t$ charge current rate

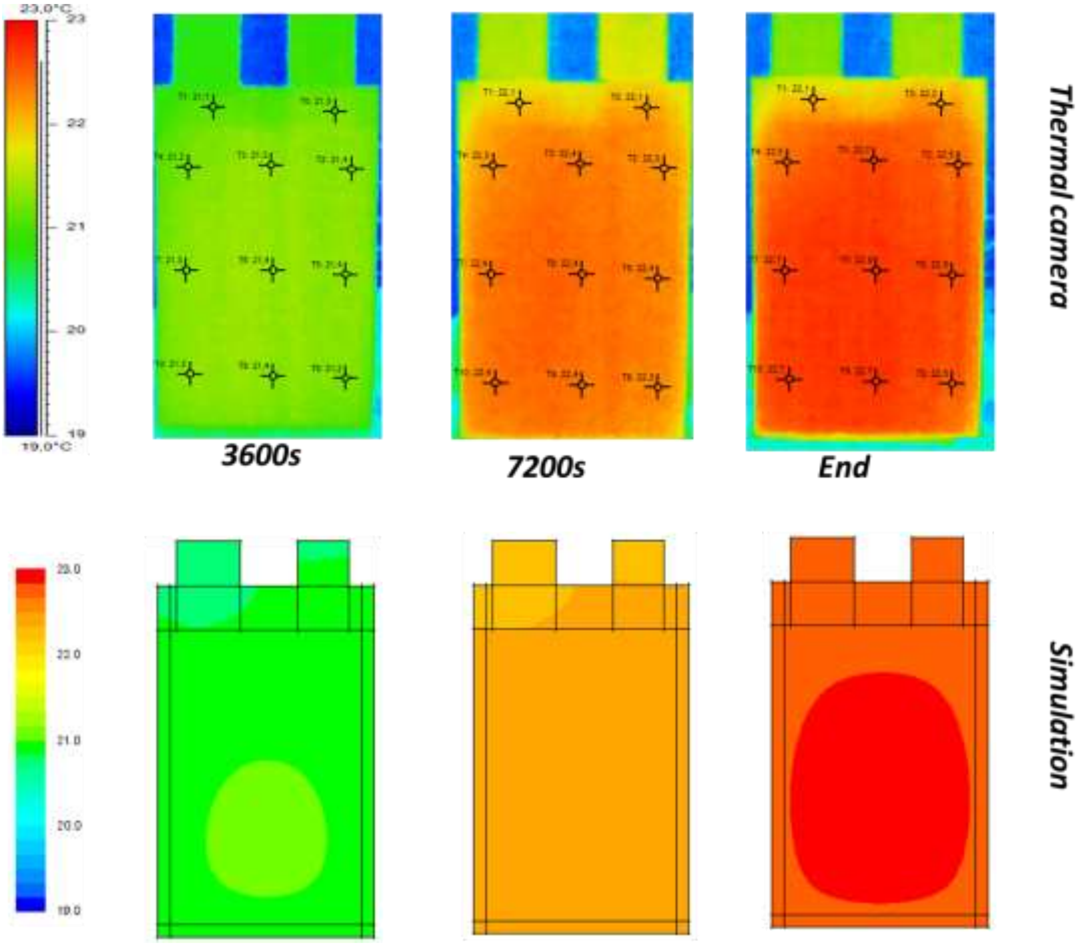

Figure 7.8: Thermal distributions based on experimental thermal imager and modeling at $1/3I_t$ charge current rate

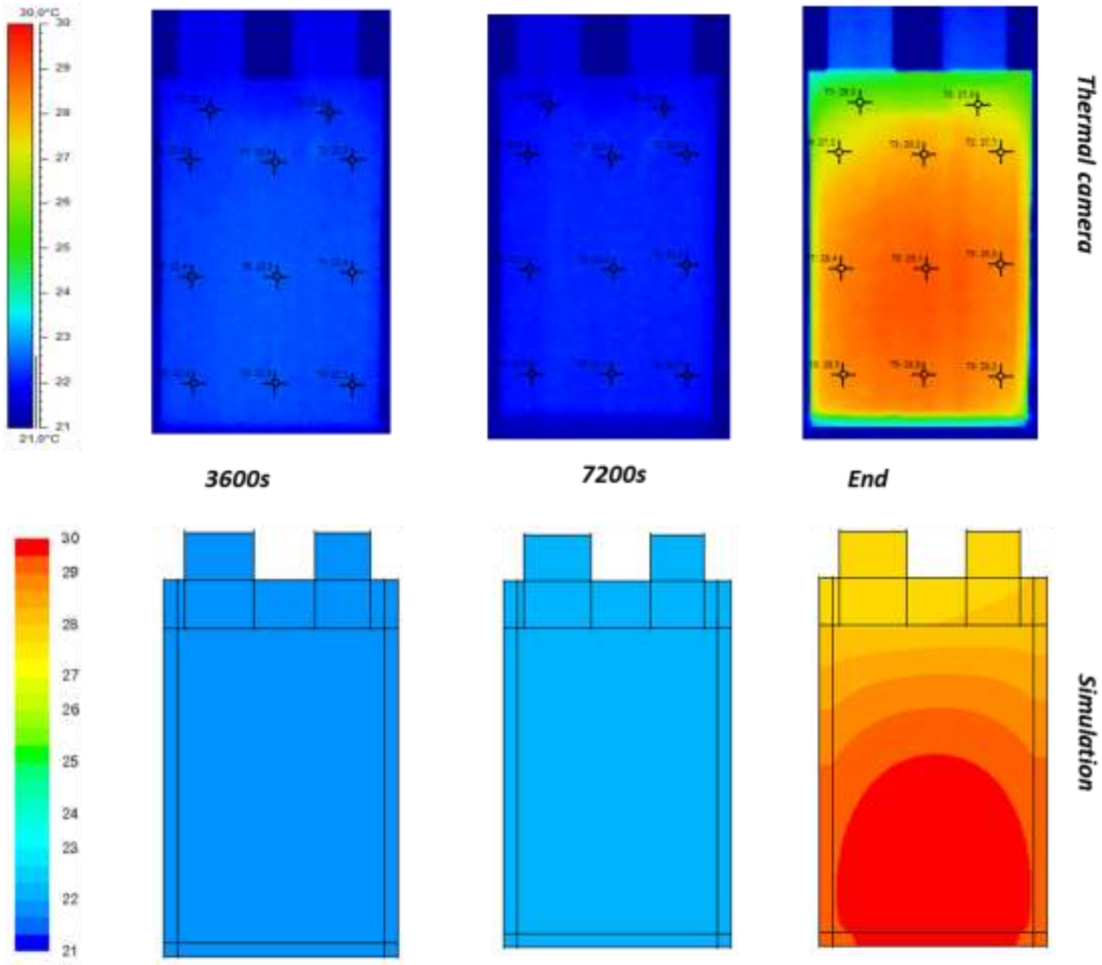

Figure 7.9: Thermal distributions based on experimental thermal imager and modeling at $1/3I_t$ discharge current rate

7.3 Entropy coefficient as a function of temperature at different SoC levels

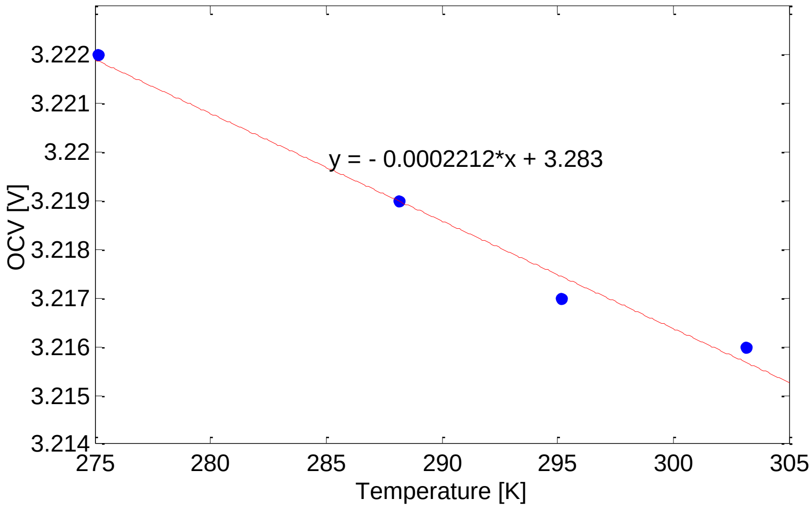

Figure 7.10: OCV at different temperature and 10% of SoC during charge process

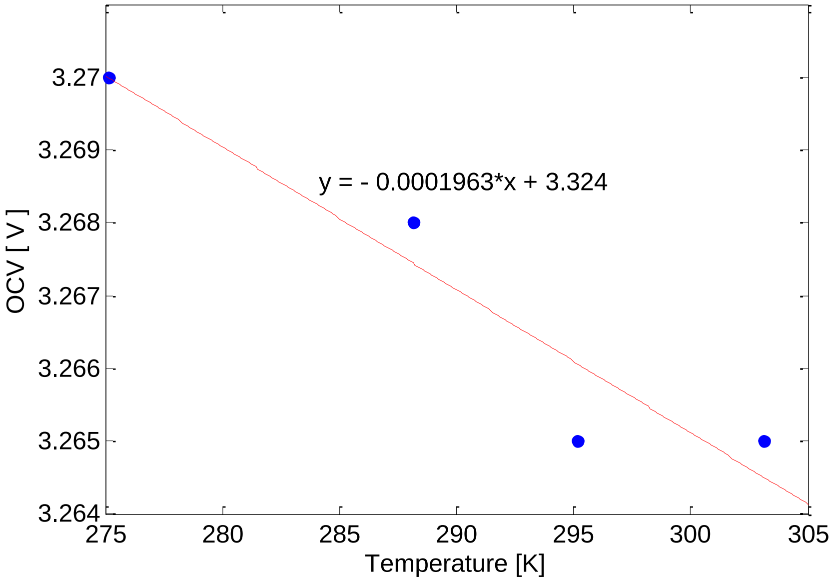

Figure 7.11: OCV at different temperature and 20% of SoC during charge process

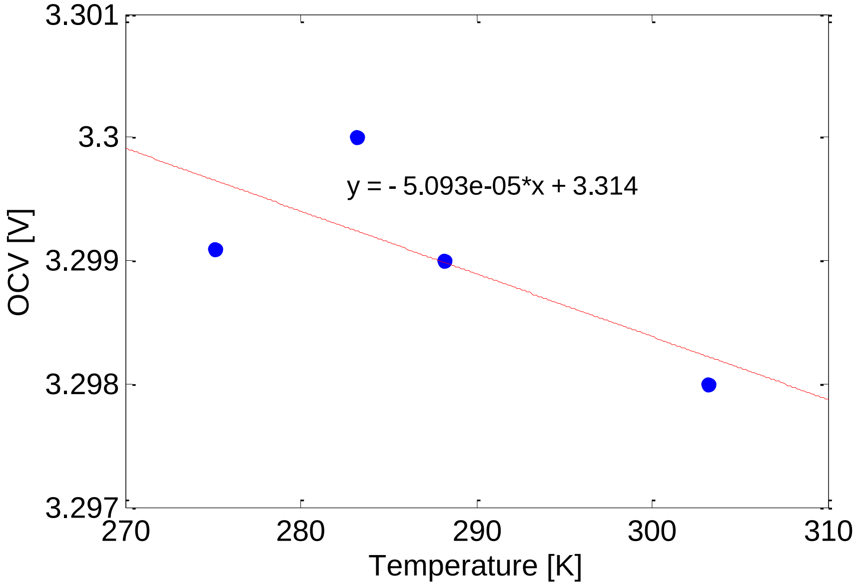

Figure 7.12: OCV at different temperature and 30% of SoC during charge process

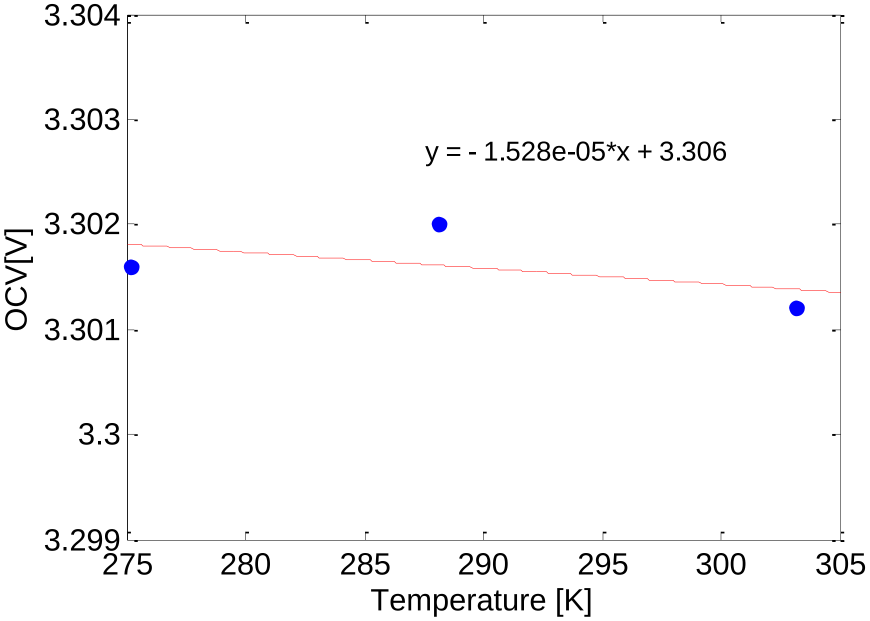

Figure 7.13: OCV at different temperature and 40% of SoC during charge process

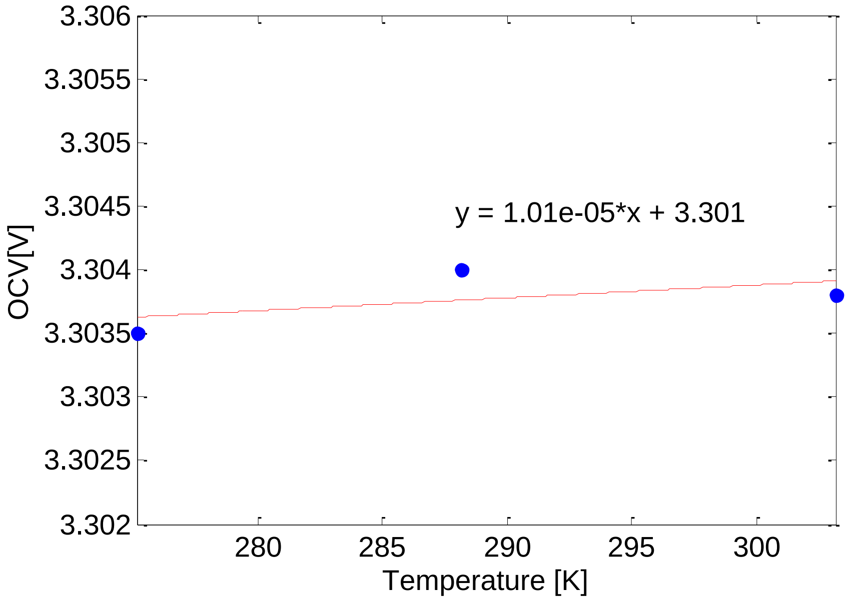

Figure 7.14: OCV at different temperature and 50% of SoC during charge process

8. Appendix II

8.1 Voltage distribution at the negative and positive current collectors

At 220s

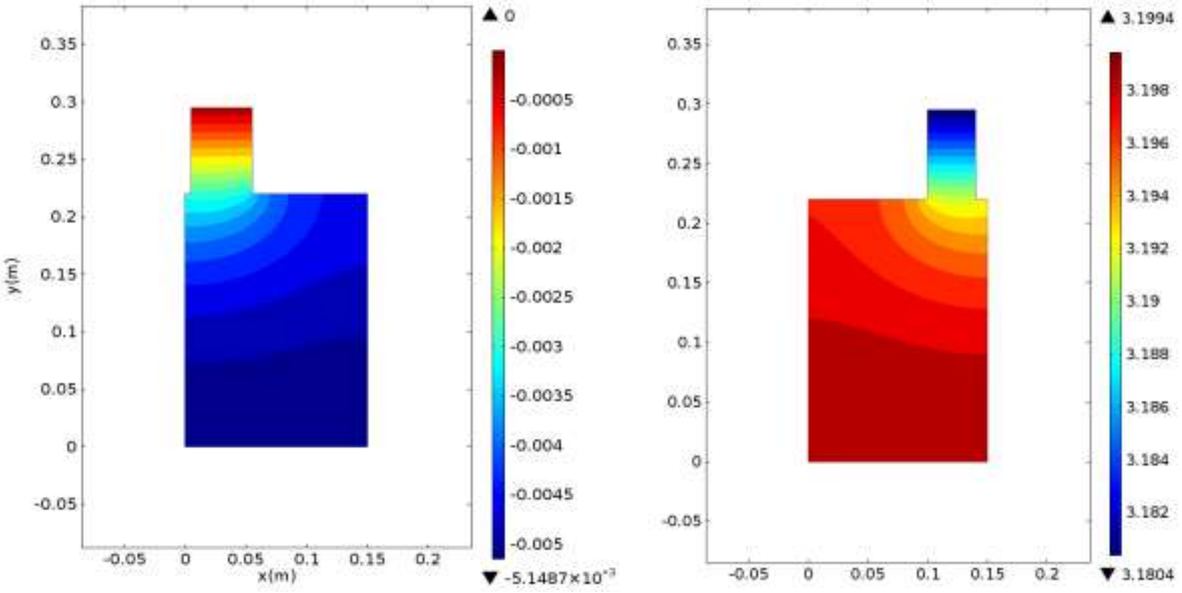

At 420s

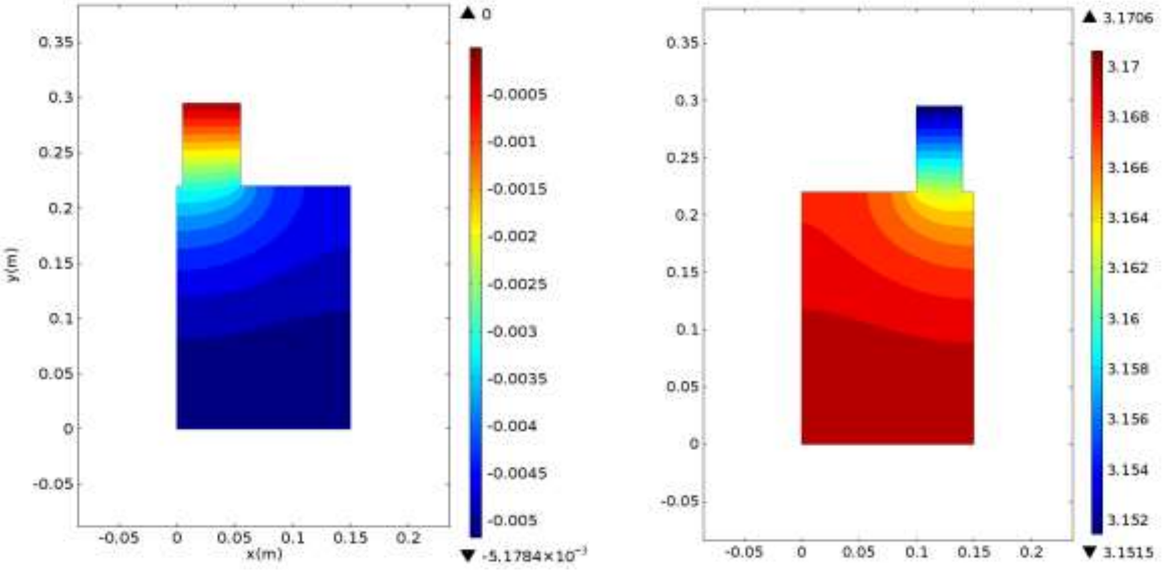

At 640s

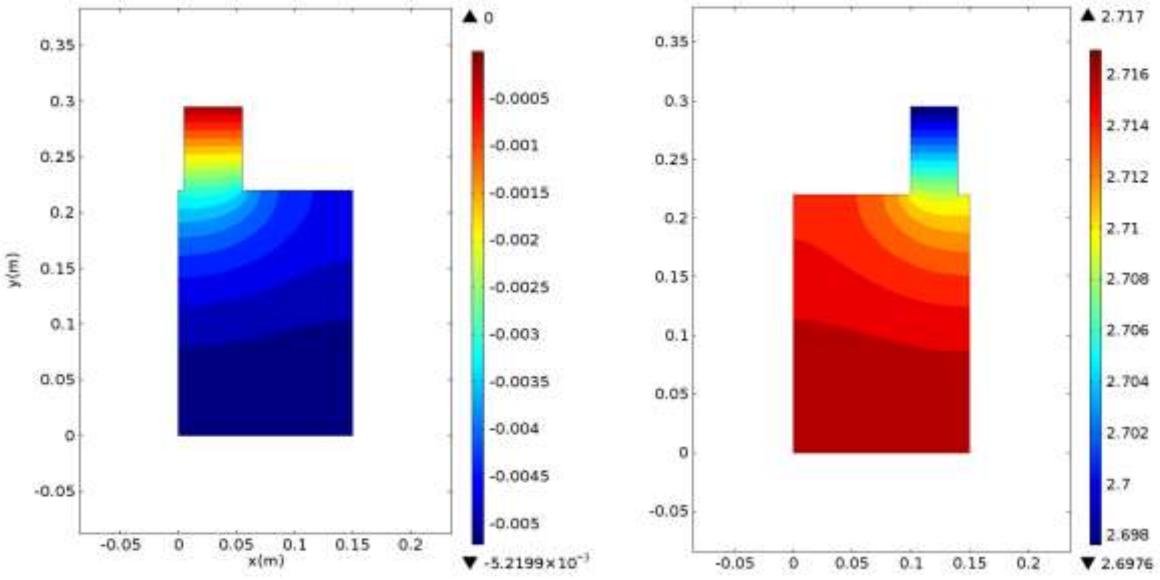

Figure 8.1: Voltage distributions based on simulation at 4I_t discharge current rate at different time steps

8.2 Temperature distribution at different time steps and 4It discharge rate

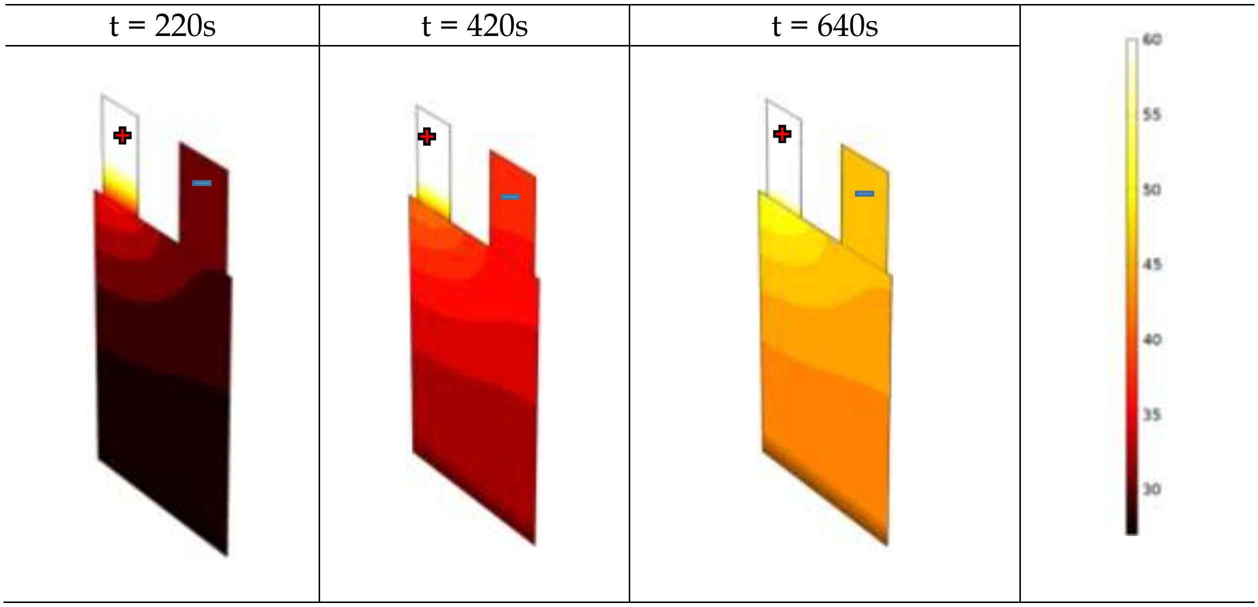

t = 220s

t = 420s

t = 640s

Figure 8.2: Temperature distributions based on simulation at $4I_t$ discharge current rate at different time steps

8.3 Input parameters for a 45 Ah LiFePO4 battery

Parameters	Symbol	Cu foil	Anode	Separator	Cathode	Al foil
Thickness	l_j[m]	$2\ 10^{-5}$	$3.4\ 10^{-5}$	$2.5\ 10^{-5}$	$8\ 10^{-5}$	$1\ 10^{-5}$
Particle radius	$R_{s,j,ref}$ [m]	-	$14.75\ 10^{-6}$	-	$1.15\ 10^{-6}$	-
Active material volume fraction	ε_1 [/]	-	0.56	-	0.435	-
Porosity	ε_2 [/]	-	0.268	0.54	0.306	-
Reaction rate coefficient	$k_{0,j,ref}$ [$m^{2.5}/mol^{0.5}$ s]	-	$1.764\ 10^{-11}$	-	$3.626\ 10^{-11}$	-
Reference Solid phase Li^+ diffusion	$D_{2,j}$ [m^2/s]	-	Eq (4.14)	Eq (4.14)	Eq (4.14)	
Electrolyte phase Li+ diffusion	$D_{1,j,ref}$ [m^2/s]	-	$3.9\ 10^{-14}$	-	$1.18\ 10^{-18}$	-
Maximum solid phase concentration	$c_{1,j,\ max}$ [mol/m^3]	-	31,370	-	22,806	-
Initial electrolyte concentration	$c_{2,0,}$ [mol/m^3]	-	2000	2000	2000	-
Stoichiometry at 0% SOC	$y_{0\%}$, $x_{0\%}$	-	0.1	-	0.83	-
Stoichiometry at 100% SOC	$y_{100\%}$, $x_{100\%}$	-	0.995	-	0.0005	-
Transference Number	t^+	-	-	0.363	-	-
Bruggman tortuosity factor	γ	-	1.5	1.5	1.5	-
Charge transfer coefficient,	α	-	0.5	-	0.5	-
Solid electronic conductivity	$\sigma_{1,j}$[S/m]	$6.63\ 10^{-7}$	100	-	0.5	$3.83\ 10^{-7}$
Ionic conductivity of electrolyte	$\sigma_{2,j}$[S/m]	-	Eq (4.17)	Eq (4.17)	Eq (4.17)	-
Activation energy for reaction	$Ea_{R,j}$[J/mol]	-	$4\ 10^3$	-	$4\ 10^3$	-
Activation energy for particle diffusion	$Ea_{D_{s,j}}$[J/mol]	-	$4\ 10^3$	-	$2\ 10^4$	-
heat capacity	Cp [J/kg.K]	385	1437	700	1260	900
density	ρ [kg/m^3]	8700	2660	492	1500	2700
thermal conductivity	λ [W/m.K]	398	1.04	1	1.48	170
Convective heat transfer	h [$W/m^2.K$]	0.03				
Total number of single cell	N	77				
Faraday's constant	F (C/ mol)	96487				-
Reference temperature	T_{ref} (K)	298.15				
Universal gas constant	R (J/ mol. K)	8.3145				-

Table 8.1: Input parameters for a 45 Ah $LiFePO_4$ battery [87], [121]

Parameters	Equations	Eq. Number
Diffusion coefficient of the solid phase	$D_{1,j} = D_{1,j,ref}\ exp\left[-\frac{Ea_{D_{1,j}}}{R}\left(\frac{1}{T}-\frac{1}{T_{ref}}\right)\right];\ (j = p, n)$	(4.14)
Diffusion coefficient of the liquid phase	$D_{2,j} = 10^{-4.43-\left(\frac{54}{T-229-0.005c_2}\right)-4}$	(4.15)
The reaction rate	$k_{0,j} = k_{0,j,ref}\ \ exp\left[-\frac{Ea_R}{R}\left(\frac{1}{T_{ref}}-\frac{1}{T}\right)\right];\ (j = p, n)$	(4.16)
The ionic conductivity	$\sigma_2 = 10^{-4}c_2 \times 1.2544(-8.2488 + 0.053248\,T - 0.00002987\,T^2 + 0.26235$ $\times 0.001\,c_2 - 0.0093063 \times 0.001\,c_2T + 0.000008069 \times 0.001\,c_2T^2$ $+ 0.22002 \times 10^{-6}c_2^2 - 0.0001765 \times 10^{-6}c_2^2T\,)^2$	(4.17)
Open circuit potential	$U_j = U_{ref,j} + (T - T_{ref})\ \frac{dU_j}{dT}$ $U_{ref,p} = 3.4323 - 0.4828\,exp\left(-80.2493(1-\theta_p)^{1.3198}\right) - 3.2474$ $\times 10^{-6}\exp\left(-20.2645(1-\theta_p)^{3.8003}\right) + 3.2482$ $\times 10^{-6}\exp\left(-20.2646(1-\theta_p)^{3.7995}\right)$ $U_{ref,n} = 0.6379 + 0.5416\,exp(-305.5309\,\theta_n)$ $+ 0.044\,tanh\left[-\frac{\theta_n - 0.1958}{0.1088}\right] - 0.1978\,tanh\left[\frac{\theta_n - 1.0571}{0.0854}\right]$ $- 0.6875\,tanh\left[\frac{\theta_n + 0.0117}{0.0529}\right] - 0.0175tanh[\frac{\theta_n - 0.5692}{0.0875}]$ $\theta_j = \frac{c_{2,j}}{c_{2,j,max}}$; $(j = p, n)$ State of charge (SOC)	(4.18)
Entropy coefficient	$\frac{dU_p}{dT} = -0.35376\theta_p^8 + 1.3902\theta_p^7 - 2.2585\theta_p^6 + 1.9635\theta_p^5 - 0.98716\theta_p^4 + 0.28857\theta_p^3$ $- 0.046272\theta_p^2 + 0.00321158\theta_p - 1.9186$ $\frac{dU_n}{dT} = -344.1347148 \times \frac{\exp(-32.9633287\theta_n + 8.316711484)}{1 + 749.0756003\exp(-34.79099646\theta_n + 8.887143624)}$ $- 0.85202788805\theta_n + 0.3622992229\theta_n^2 + 0.2698001697$	(4.19)

Table 8.2: temperature dependency of parameters [87], [121]

List of Publications

List of Publications

Publications in ISI Journals

J1 **A. Samba**, N. Omar, H. Gualous, Y. Firouz, P. Van den Bossche, J. Van Mierlo, and T. I. Boubekeur, "Development of an Advanced Two-Dimensional Thermal Model for Large size Lithium-ion Pouch Cells," *Electrochim. Acta*, vol. 117, pp. 246–254, Jan. 2014.

J2 N. Omar, H. Gualous, J. Salminen, G. Mulder**, A. Samba**, Y. Firouz, M. A. Monem, P. Bossche, and J. Mierlo, "Electrical double-layer capacitors: evaluation of ageing phenomena during cycle life testing," *Journal of Applied Electrochemistry,* vol. 44, issue 4, pp. 509-522, 2014, Springer.

J3 **A. Samba**, N. Omar, H. Gualous, O. Capron, P. Van den Bossche, and J. Van Mierlo, "Impact of Tab Location on Large Format Lithium-Ion Pouch Cell Based on Fully Coupled Tree-Dimensional Electrochemical-Thermal Modeling," *Electrochim. Acta*, vol. 147, pp. 319–329, Nov. 2014.

Publications in non-ISI Journals

J4 **A. Samba**, N. Omar, H. Gualous, P. Van den Bossche, and J. Van Mierlo, “Modélisation Electrothermique 2D d’une batterie lithium-ion de type « pouch »,” La Rev. 3EI, vol. 78, Octobre 2014.

J5 **A. Samba**, N. Omar, J. M. Timmermans, H. Gualous, P. Van den Bossche, J. Van Mierlo,” Assessment of Battery Thermal Management Designs Based on Liquid Cooling Method”, journal Sustainability, Special issue” Sustainability in Electrical Engineering”, Under review.

Contribution in Books

B1 P. Van den Bossche, N. Omar, **A. Samba**, M. Al Sakka,, H. Gualous and J. Van Mierlo, 11 - The Challenge of PHEV Battery Design and the Opportunities of Electrothermal Modeling, In Lithium-Ion Batteries, edited by Gianfranco Pistoia, Elsevier, Amsterdam, 2014, Pages 249-271, ISBN 9780444595133.

B2 N. Omar, Y. Firouz, M.A. Monem, **A. Samba**, H. Gualous, T. Coosemans, P. Van den Bossche and J. Van Mierlo, "Analysis of Nickel-Based Battery Technologies for Hybrid and Electric Vehicles", In Reference Module in Chemistry, Molecular Sciences and Chemical Engineering, Elsevier, 2014, ISBN 9780124095472.

Publications in Scientific Conferences

C1 **Samba, A**., Omar, N., Gualous, H., Van den Bossche, P., Van Mierlo, J., Boubekeur, T. I. Development of an Advanced 2D-Thermal Model for Large size Lithium-ion Pouch Cells, The 27th INTERNATIONAL ELECTRIC SYMPOSIUM & EXHIBITION, EVS, Barcelona, Spain, November 20, 2013

C2 **Samba, A.,** Omar, N., Gualous, H., Capron, O., H., Firouz, Y., M. A. Monem, J. Smekens, Van den Bossche, P., Van Mierlo, J. Thermal and Electrical Optimization Design of Pouch Battery Cell Based On Advanced Simulation Tool, 224th ECS conference, November 2013, San Francisco/ USA

C3 **Samba, A**., Omar, N., Gualous, H., Capron, O., H., Firouz, Y., Monem, M.,Van den Bossche, P., Van Mierlo, J. Sensitivity Analysis of Pouch Battery Cell Dimension and Design Based on Advanced Simulation Tool, Comsol conference, 2013, Rotterdam/ Netherlands

C4 Y. Firouz, N. Omar, M. A. Monem, **A. Samba**, J. Smekens, H. Gualous, Peter Van den Bossche, J. Van Mierlo Modeling and Characterization of Different Types of Lithium-Ion Batteries Under Various Conditions, 224th ECS conference, November 2013, San Francisco/ USA

C5 N. Omar, M. A. Monem, Y. Firouz, **A. Samba**, J. Smekens, H. Gualous, P. Van den Bossche, J. Van Mierlo, Lithium-Ion Batteries – Extended Analysis of Parameter Change and Development of a New Battery Model, 224th ECS conference, November 2013, San Francisco/ USA

C6 M. A. Monem, N. Omar, O. Hegazy, G. Mulder, B. Mantels, J. Smekens, Y. Firouz, **A. Samba**, P. Van den Bossche, J. Van Mierlo, Feasibility Study for Assessment the Effects of Charging Profile On the Performance of Commercial Lithium-Ion Batteries, 224th ECS conference, November 2013, San Francisco/ USA

C7 H. Gualous, N. Omar, **A. Samba**, P. Van den Bossche, J. Van Mierlo, Supercapacitor Calendar Ageing and Post Mortem Analysis, 224th ECS conference, November 2013, San Francisco/ USA

C8 O. Capron, **A. Samba**, N. Omar, H. Gualous, P. Van Den Bossche, and J. Van Mierlo, “Battery thermal modelling - Assessment of heat distribution and optimization of battery design concept,” in 2013 International Conference on Renewable Energy Research and Applications (ICRERA), 2013, pp. 304–309.

C9 O. Capron, **A. Samba**, N. Omar, H. Gualous, P. Van Den Bossche, and J. Van Mierlo, “Large and High Power Cylindrical Batteries – Analysis of the Battery Packs Temperature Distributions Using COMSOL Multiphysics ® and MATLAB ® Simulation Softwares,” in Comsol conferance 2014, CAMBRIDGE/UK.

C10 **A. Samba**. Modélisation Electro-thermique 2D d’une batterie lithium-ion de type “pouche”. Journées JCGE’2014 - SEEDS, Jun 2014, Saint-Louis, France. <hal-01083934>.

References

References

[1] R. Farreny, X. Gabarrell, and J. Rieradevall, "Energy intensity and greenhouse gas emission of a purchase in the retail park service sector: An integrative approach," *Energy Policy*, vol. 36, no. 6, pp. 1957–1968, Jun. 2008.

[2] Europen Environment Agency, *Final energy consumption by sector (CSI 027/ENER 016) - Assessment published Feb 2013*. Europen Environment Agency.

[3] U. Secretariat, *Technical report No 09 / 2014 Annual European Union greenhouse gas inventory 1990 – 2012 and inventory report 2014 Submission to the UNFCCC Secretariat*, no. 09. 2014.

[4] E. E. A. (EEA), *Approximated EU GHG inventory : Proxy GHG estimates for 2012*, No 14., no. 14. 2013.

[5] *European Council, Directive 93/59/EEC amending Directive 70/220/EEC on the approximation of the laws of the Member States relating to measures to be taken against air pollution by emissions from motor vehicles*. 1993.

[6] *European Parliament and Council, Directive 94/12/EC Council relating to measures to be taken against air pollution by emissions from motor vehicles and amending Directive 70/220/EEC*. 1994.

[7] *European Parliament and Council , Directive 98/69/EC relating to measures to be taken against air pollution by emissions from motor vehicles and amending Council Directive 70/220/EEC*. 1998.

[8] *European Parliament and Council, Regulation (EC) No 715/2007 on type approval of motor vehicles with respect to emissions from light passenger and commercial vehicles (Euro 5 and Euro 6) and on access to vehicle repair and maintenance information*. 2007.

[9] *European Commission, Regulation (EC) No 692/2008 implementing and amending Regulation (EC) No 715/2007 of the European Parliament and of the Council on type-approval of motor vehicles with respect to emissions from light passenger and commercial vehicles*. 2008.

[10] V. Marchal, D. Rob, C. Christa, C. Jean, L. Eliza, M. Bertrand, and van V. Jasper, "CHAPTER 3: CLIMATE CHANGE," in *OECD Environmental Outlook to 2050*, PRE-RELEAS., no. November, 2011.

[11] IEA, *Technology Roadmap Electric and plug-in hybrid electric vehicles*, no. 2011. OECD/IEA, 2011.

[12] J. Van Mierlo, *Simulation software for comparison and design of electric, hybrid electric and internal combustion vehicles with respect to respect to energy, emissions and performances*, PHD thesis. Vrije Universiteit Brussel, 2000.

[13] F. Orecchini, A. Santiangeli, and A. Dell'Era, *Lithium-Ion Batteries*. Elsevier, 2014, pp. 205–248.

[14] J. Warner, *Lithium-Ion Batteries*. Elsevier, 2014, pp. 127–150.

[15] http://www. greencarcongress. com. Green Car Congress, "Green Car Congress," *visited on 11/08/2014*.

[16] P. Van den Bossche, F. Vergels, J. Van Mierlo, J. Matheys, and W. Van Autenboer, "SUBAT: An assessment of sustainable battery technology," *J. Power Sources*, vol. 162, no. 2, pp. 913–919, Nov. 2006.

[17] A. SYSTEMS, "http://www.a123systems.com." .

[18] J. Salminen, T. Kallio, N. Omar, P. Van den Bossche, J. Van Mierlo, and H. Gualous, *Future Energy*. Elsevier, 2014, pp. 291–309.

[19] B. Xu, D. Qian, Z. Wang, and Y. S. Meng, "Recent progress in cathode materials research for advanced lithium ion batteries," *Mater. Sci. Eng. R Reports*, vol. 73, no. 5–6, pp. 51–65, May 2012.

[20] C. de las Casas and W. Li, "A review of application of carbon nanotubes for lithium ion battery anode material," *J. Power Sources*, vol. 208, pp. 74–85, Jun. 2012.

[21] J. B. Goodenough and Y. Kim, "Challenges for rechargeable batteries," *J. Power Sources*, vol. 196, no. 16, pp. 6688–6694, Aug. 2011.

[22] K. Zaghib, J. Dubé, A. Dallaire, K. Galoustov, A. Guerfi, M. Ramanathan, A. Benmayza, J. Prakash, A. Mauger, and C. M. Julien, *Lithium-Ion Batteries*. Elsevier, 2014, pp. 437–460.

[23] T.-F. Yi, L.-J. Jiang, J. Shu, C.-B. Yue, R.-S. Zhu, and H.-B. Qiao, "Recent development and application of Li4Ti5O12 as anode material of lithium ion battery," *J. Phys. Chem. Solids*, vol. 71, no. 9, pp. 1236–1242, Sep. 2010.

[24] P. Kubiak, J. Geserick, N. Hüsing, and M. Wohlfahrt-Mehrens, "Electrochemical performance of mesoporous TiO2 anatase," *J. Power Sources*, vol. 175, no. 1, pp. 510–516, Jan. 2008.

[25] K. Sawai, R. Yamato, and T. Ohzuku, "Impedance measurements on lithium-ion battery consisting of Li[Li1/3Ti5/3]O4 and LiCo1/2Ni1/2O2," *Electrochim. Acta*, vol. 51, no. 8–9, pp. 1651–1655, Jan. 2006.

[26] and H. V. Wenige R., Niemann M., Heider U., Jungnitz M., *Liquid electrolyte systems for advanced lithium batteries*. Chemical Engineering Research Information Center, 2010.

[27] T. Ohzuku and R. J. Brodd, "An overview of positive-electrode materials for advanced lithium-ion batteries," *J. Power Sources*, vol. 174, no. 2, pp. 449–456, Dec. 2007.

[28] I. Belharouak, W. Lu, D. Vissers, and K. Amine, "Safety characteristics of Li(Ni0.8Co0.15Al0.05)O2 and Li(Ni1/3Co1/3Mn1/3)O2," *Electrochem. commun.*, vol. 8, no. 2, pp. 329–335, Feb. 2006.

[29] J. Axsen, K. S. Kurani, and A. Burke, "Are batteries ready for plug-in hybrid buyers?," *Transp. Policy*, vol. 17, no. 3, pp. 173–182, May 2010.

[30] J. V. M. P. Van den Bossche, N. Omar, M. Al Sakka, A. Samba, H. Gualous, "11 - The Challenge of PHEV Battery Design and the Opportunities of Electrothermal Modeling, In Lithium-Ion batteries Advances and Applications," G. Pistoia, Ed. Amsterdam: Elsevier, 2014, pp. 249–271.

[31] S. Al Hallaj, H. Maleki, J. S. Hong, and J. R. Selman, "Thermal modeling and design considerations of lithium-ion batteries," *J. Power Sources*, vol. 83, no. 1–2, pp. 1–8, Oct. 1999.

[32] Q. Wang, P. Ping, X. Zhao, G. Chu, J. Sun, and C. Chen, "Thermal runaway caused fire and explosion of lithium ion battery," *J. Power Sources*, vol. 208, pp. 210–224, Jun. 2012.

[33] C.-Y. Jhu, Y.-W. Wang, C.-M. Shu, J.-C. Chang, and H.-C. Wu, "Thermal explosion hazards on 18650 lithium ion batteries with a VSP2 adiabatic calorimeter.," *J. Hazard. Mater.*, vol. 192, no. 1, pp. 99–107, Aug. 2011.

[34] G.-H. Kim, A. Pesaran, and R. Spotnitz, "A three-dimensional thermal abuse model for lithium-ion cells," *J. Power Sources*, vol. 170, no. 2, pp. 476–489, Jul. 2007.

[35] A. Vezzini, “Lithium-Ion Batteries,” in *Lithium-Ion Batteries*, Elsevier, 2014, pp. 345–360.

[36] L. Lu, X. Han, J. Li, J. Hua, and M. Ouyang, “A review on the key issues for lithium-ion battery management in electric vehicles,” *J. Power Sources*, vol. 226, pp. 272–288, Mar. 2013.

[37] C. E. . Shaffer and C. Y. . Wang, “Safety Analysis Design of Lithium-ion Battery EV Pack through Computer Simulation,” in *Battery Safety 2012*, 2012.

[38] M. Tarascon, J.M. and Armand, “nature,” *J. Nat.*, vol. 414, no. 15, p. 359, 2001.

[39] D. Linden and T. B. Reddy, *HANDBOOK OF BATTERIES*. .

[40] N. Omar, M. A. Monem, Y. Firouz, J. Salminen, J. Smekens, O. Hegazy, H. Gaulous, G. Mulder, P. Van den Bossche, T. Coosemans, and J. Van Mierlo, “Lithium iron phosphate based battery – Assessment of the aging parameters and development of cycle life model,” *Appl. Energy*, vol. 113, pp. 1575–1585, Jan. 2014.

[41] N. Omar, H. Gualous, J. Salminen, G. Mulder, A. Samba, Y. Firouz, M. A. Monem, P. Bossche, and J. Mierlo, “Electrical double-layer capacitors: evaluation of ageing phenomena during cycle life testing,” *J. Appl. Electrochem.*, Oct. 2013.

[42] A. Barré, B. Deguilhem, S. Grolleau, M. Gérard, F. Suard, and D. Riu, “A review on lithium-ion battery ageing mechanisms and estimations for automotive applications,” *J. Power Sources*, vol. 241, pp. 680–689, Nov. 2013.

[43] A. A. Pesaran, “Battery thermal models for hybrid vehicle simulations,” *J. Power Sources*, vol. 110, pp. 377–382, 2002.

[44] W. Zhao, G. Luo, and C.-Y. Wang, “Effect of tab design on large-format Li-ion cell performance,” *J. Power Sources*, vol. 257, pp. 70–79, Jul. 2014.

[45] K.-J. Lee, K. Smith, A. Pesaran, and G.-H. Kim, “Three dimensional thermal-, electrical-, and electrochemical-coupled model for cylindrical wound large format lithium-ion batteries,” *J. Power Sources*, vol. 241, pp. 20–32, Nov. 2013.

[46] U. S. Kim, C. B. Shin, and C.-S. Kim, “Effect of electrode configuration on the thermal behavior of a lithium-polymer battery,” *J. Power Sources*, vol. 180, no. 2, pp. 909–916, Jun. 2008.

[47] U. S. Kim, C. B. Shin, and C.-S. Kim, “Modeling for the scale-up of a lithium-ion polymer battery,” *J. Power Sources*, vol. 189, no. 1, pp. 841–846, Apr. 2009.

[48] P. Van den Bossche, N. Omar, A. Samba, M. Al Sakka, H. Gualous, and J. Van Mierlo, “The Challenge of PHEV Battery Design and the Opportunities of Electrothermal Modeling,” in *Lithium-Ion Batteries: Advances and Applications*, Elsevier 2., G. PISTOA, Ed. Amsterdam: Elsevier B.V, 2014, pp. 249–268.

[49] N. Omar, “Assessment of Rechargeable Energy Storage Systems for Plug-In Hybrid Electric Vehicles,” Vrije Universiteit Brussel, Brussels, Belgium, 2012.

[50] O. Tremblay, L. A. Dessaint, and A. Dekkiche, “Ageneric battery model for the dynamic simulation of hybrid electric vehicles.” Proceedings VPPC 2007, Texas, USA, 2007.

[51] and S. S. Wipke K., Cuddy M., Bharathan D., Burch S., Johnson V., Markel A., “Advisor 2.0:A second-generation advanced vehicle simulator for systems analysis.” NREL, 1999.

[52] Y. Tang, “On the feasibility of hybrid battery/ultracapacitor energy storage systems for next generation shipboard power systems,” *Proc. VPPC 2010*, 2010.

[53] V. H. Johnson, A. A. Pesaran, and B. Court, “Temperature-Dependent Battery Models for High-Power Lithium-Ion Batteries,” in *EVS 17*, 2000, pp. 1–15.

[54] U. S. D. S. of Energy, “FreedomCAR Battery Test Manual For IDAHO.” U.S. Department Secretary of Energy, 2003.

[55] D. Andre, M. Meiler, K. Steiner, C. Wimmer, T. Soczka-guth, and D. U. Sauer, “Characterization of high-power lithium-ion batteries by electrochemical impedance spectroscopy . I . Experimental investigation,” *J. Power Sources*, vol. 196, no. 12, pp. 5334–5341, 2011.

[56] M. Dubarry and B. Y. Liaw, “Development of a universal modeling tool for rechargeable lithium batteries,” *J. Power Sources*, vol. 174, no. 2, pp. 856–860, Dec. 2007.

[57] Y. Hu, S. Yurkovich, Y. Guezennec, and B. J. Yurkovich, “Electro-thermal battery model identification for automotive applications,” *J. Power Sources*, vol. 196, no. 1, pp. 449–457, Jan. 2011.

[58] E. K. L. Long, P. Bauer, “A practical circuit-based model for Li-ion battery cells in electric vehicle applications,” in *Telecommunications Energy Conference (INTELEC)*, 2011, pp. 1–9.

[59] S. Al-hallaj and J. R. Selman, "Thermal modeling of secondary lithium batteries for electric vehicle / hybrid electric vehicle applications," *J. Power Sources*, vol. 110, pp. 341–348, 2002.

[60] K. Thomas and J. Newman, "Heats of mixing and of entropy in porous insertion electrodes," *J. Power Sources*, vol. 119–121, pp. 844–849, Jun. 2003.

[61] Y. Inui, Y. Kobayashi, Y. Watanabe, Y. Watase, and Y. Kitamura, "Simulation of temperature distribution in cylindrical and prismatic lithium ion secondary batteries," *Energy Convers. Manag.*, vol. 48, no. 7, pp. 2103–2109, Jul. 2007.

[62] G. G. Botte, V. R. Subramanian, and R. E. White, "Mathematical modeling of secondary lithium batteries," *Electrochim. Acta*, vol. 45, no. 15–16, pp. 2595–2609, May 2000.

[63] W. B. Gu and C. Y. Wang, "Thermal-Electrochemical Modeling of Battery Systems," *J. Electrochem. Soc. 147 2910-2922*, vol. 147, no. 8, pp. 2910–2922, 2000.

[64] D. B. P. Huynh, D. J. Knezevic, and A. T. Patera, "A Laplace transform certified reduced basis method; application to the heat equation and wave equation," *Comptes Rendus Math.*, vol. 349, no. 7–8, pp. 401–405, Apr. 2011.

[65] S. Guo, J. Zhang, G. Li, and F. Zhou, "Three-dimensional transient heat conduction analysis by Laplace transformation and multiple reciprocity boundary face method," *Eng. Anal. Bound. Elem.*, vol. 37, no. 1, pp. 15–22, Jan. 2013.

[66] A. F. Barannyk, T. A. Barannyk, and I. I. Yuryk, "Generalized Separation of Variables for Nonlinear Equation," *Reports Math. Phys.*, vol. 71, no. 1, pp. 1–13, Feb. 2013.

[67] L. Jo´dar, "A separation of the variables method for solving coupled systems of second-order partial differential equations: exact, approximate solutions and error bounds," *J. Comput. Appl. Math.*, vol. 31, no. 2, pp. 243–251, Aug. 1990.

[68] R. Mahamud and C. Park, "Spatial-resolution, lumped-capacitance thermal model for cylindrical Li-ion batteries under high Biot number conditions," *Appl. Math. Model.*, vol. 37, no. 5, pp. 2787–2801, Mar. 2013.

[69] D. D. Mandaliya, A. S. Moharir, and R. D. Gudi, "An improved Green's function method for isothermal effectiveness factor determination in one- and two-dimensional catalyst geometries," *Chem. Eng. Sci.*, vol. 91, pp. 197–211, Mar. 2013.

[70] S. A. Khuri and A. Sayfy, "Variational iteration method: Green's functions and fixed point iterations perspective," *Appl. Math. Lett.*, vol. 32, pp. 28–34, Jun. 2014.

[71] H. Gualous, H. Louahlia-gualous, R. Gallay, and A. Miraoui, "Supercapacitor Thermal Modeling and Characterization in Transient State for Industrial Applications," vol. 45, no. 3, pp. 1035–1044, 2009.

[72] G. Guo, B. Long, B. Cheng, S. Zhou, P. Xu, and B. Cao, "Three-dimensional thermal finite element modeling of lithium-ion battery in thermal abuse application," *J. Power Sources*, vol. 195, no. 8, pp. 2393–2398, Apr. 2010.

[73] S. C. Chen, C. C. Wan, and Y. Y. Wang, "Thermal analysis of lithium-ion batteries," *J. Power Sources*, vol. 140, no. 1, pp. 111–124, Jan. 2005.

[74] C. Forgez, D. Vinh Do, G. Friedrich, M. Morcrette, and C. Delacourt, "Thermal modeling of a cylindrical LiFePO4/graphite lithium-ion battery," *J. Power Sources*, vol. 195, no. 9, pp. 2961–2968, May 2010.

[75] M. Al Sakka, H. Gualous, J. Van Mierlo, and H. Culcu, "Thermal modeling and heat management of supercapacitor modules for vehicle applications," *J. Power Sources*, vol. 194, no. 2, pp. 581–587, Dec. 2009.

[76] S. Al Hallaj, J. Prakash, and J. R. Selman, "Characterization of commercial Li-ion batteries using electrochemical – calorimetric measurements," *J. Power Sources*, pp. 186–194, 2000.

[77] W. Q. Li, Z. G. Qu, Y. L. He, and W. Q. Tao, "Experimental and numerical studies on melting phase change heat transfer in open-cell metallic foams filled with paraffin," *Appl. Therm. Eng.*, vol. 37, pp. 1–9, May 2012.

[78] E. Barsoukov, J. H. Jang, and H. Lee, "Thermal impedance spectroscopy for Li-ion batteries using heat-pulse response analysis," vol. 109, pp. 313–320, 2002.

[79] M. Fleckenstein, S. Fischer, O. Bohlen, and B. Bäker, "Thermal Impedance Spectroscopy - A method for the thermal characterization of high power battery cells," *J. Power Sources*, vol. 223, pp. 259–267, Feb. 2013.

[80] Y. He, "Rapid thermal conductivity measurement with a hot disk sensor," *Thermochim. Acta*, vol. 436, no. 1–2, pp. 122–129, Oct. 2005.

[81] R. Coquard, E. Coment, G. Flasquin, and D. Baillis, "Analysis of the hot-disk technique applied to low-density insulating materials," *Int. J. Therm. Sci.*, vol. 65, pp. 242–253, Mar. 2013.

[82] S. C. Nagpure, R. Dinwiddie, S. S. Babu, G. Rizzoni, B. Bhushan, and T. Frech, "Thermal diffusivity study of aged Li-ion batteries using flash method," *J. Power Sources*, vol. 195, no. 3, pp. 872–876, Feb. 2010.

[83] G. a. Swift, "Thermophysical Properties of Lithium Alloys for Thermal Batteries," *Int. J. Thermophys.*, vol. 32, no. 10, pp. 2102–2111, Sep. 2011.

[84] J. E. Soc, J. The, E. Society, P. A. Flowers, G. Mamantov, T. Journal, J. H. Taylor, W. S. Benedict, J. Strong, J. Chem, M. Doyle, T. F. Fuller, and J. Newman, "Modeling of Galvanostatic Charge and Discharge of the Lithium / Polymer / Insertion Cell," vol. 140, no. 6, pp. 1526–1533, 1993.

[85] K. Lee, K. Smith, and G. Kim, "A Three-Dimensional Thermal-Electrochemical Coupled Model for Spirally Wound Large-Format Lithium-Ion Batteries (Presentation), NREL (National Renewable Energy Laboratory)," *Sp. Power Work. Los Angeles, CA*, 2011.

[86] M. Guo and R. E. White, "A distributed thermal model for a Li-ion electrode plate pair," *J. Power Sources*, vol. 221, pp. 334–344, Jan. 2013.

[87] M. Xu, Z. Zhang, X. Wang, L. Jia, and L. Yang, "Two-dimensional electrochemical–thermal coupled modeling of cylindrical LiFePO4 batteries," *J. Power Sources*, vol. 256, pp. 233–243, Jun. 2014.

[88] A. A. Pesaran, "Battery Thermal Management in EVs and HEVs : Issues and Solutions," in *Advanced Automotive Battery Conference, Las Vegas, Nevada*, 2011.

[89] BEHR, "Thermal Management For Hybrid Vehicles," *Tech. Press Day*, no. Stuttgart, 2009.

[90] J. Smith, M. Hinterberger, P. Hable, and J. Koehler, "Simulative method for determining the optimal operating conditions for a cooling plate for lithium-ion battery cell modules," *J. Power Sources*, vol. 267, pp. 784–792, Dec. 2014.

[91] A. Jarrett and I. Y. Kim, "Influence of operating conditions on the optimum design of electric vehicle battery cooling plates," *J. Power Sources*, vol. 245, pp. 644–655, Jan. 2014.

[92] A. Jarrett and I. Y. Kim, "Design optimization of electric vehicle battery cooling plates for thermal performance," *J. Power Sources*, vol. 196, no. 23, pp. 10359–10368, Dec. 2011.

[93] E. T. G. Berdichevsky, K. Kelty, J. Straubel, "The Tesla Roadster Battery System." Tesla Motors2007, 2007.

[94] M. Wu, K. H. Liu, Y. Wang, and C. Wan, "Heat dissipation design for lithium-ion batteries," *J. Power Sources*, vol. 109, pp. 160–166, 2002.

[95] V. Barantsevich and V. Shabalkin, "Heat pipes for thermal control of ISS solar battery drive," *Appl. Therm. Eng.*, vol. 23, no. 9, pp. 1119–1123, Jun. 2003.

[96] L. W. Jin, P. S. Lee, X. X. Kong, Y. Fan, and S. K. Chou, "Ultra-thin minichannel LCP for EV battery thermal management," *Appl. Energy*, vol. 113, pp. 1786–1794, Jan. 2014.

[97] T. M. Bandhauer and S. Garimella, "Passive, internal thermal management system for batteries using microscale liquid–vapor phase change," *Appl. Therm. Eng.*, vol. 61, no. 2, pp. 756–769, Nov. 2013.

[98] Z. Rao, S. Wang, M. Wu, Z. Lin, and F. Li, "Experimental investigation on thermal management of electric vehicle battery with heat pipe," *Energy Convers. Manag.*, vol. 65, pp. 92–97, Jan. 2013.

[99] R. W. van Gils, D. Danilov, P. H. L. Notten, M. F. M. Speetjens, and H. Nijmeijer, "Battery thermal management by boiling heat-transfer," *Energy Convers. Manag.*, vol. 79, pp. 9–17, Mar. 2014.

[100] A. A. Pesaran, S. Burch, and M. Keyser, "An Approach for Designing Thermal Management Systems for Electric and Hybrid Vehicle Battery Packs Preprint," in *Fourth Vehicle Thermal Management Systems Conference and Exhibition London, UK May 24–27, 1999*, 1999, no. January.

[101] S. a Khateeb, M. M. Farid, J. R. Selman, and S. Al-Hallaj, "Design and simulation of a lithium-ion battery with a phase change material thermal management system for an electric scooter," *J. Power Sources*, vol. 128, no. 2, pp. 292–307, Apr. 2004.

[102] R. Sabbah, R. Kizilel, J. R. Selman, and S. Al-Hallaj, "Active (air-cooled) vs. passive (phase change material) thermal management of high power lithium-ion packs: Limitation of temperature rise and uniformity of temperature distribution," *J. Power Sources*, vol. 182, no. 2, pp. 630–638, Aug. 2008.

[103] R. Kizilel, R. Sabbah, J. R. Selman, and S. Al-Hallaj, "An alternative cooling system to enhance the safety of Li-ion battery packs," *J. Power Sources*, vol. 194, no. 2, pp. 1105–1112, Dec. 2009.

[104] N. R. Jankowski and F. P. McCluskey, “A review of phase change materials for vehicle component thermal buffering,” *Appl. Energy*, vol. 113, pp. 1525–1561, Jan. 2014.

[105] A. Mills and S. Al-Hallaj, “Simulation of passive thermal management system for lithium-ion battery packs,” *J. Power Sources*, vol. 141, no. 2, pp. 307–315, Mar. 2005.

[106] P. Van den Bossche, N. Omar, M. Al Sakka, A. Samba, H. Gualous, and J. Van Mierlo, *Lithium-Ion Batteries*. Elsevier, 2014, pp. 249–271.

[107] J. P. Holman, *Heat Transfer*, Mc Graw Hi. 2002.

[108] J. N. D. Bernardi, E. Pawlikowski, “A general energy balance for battery systems,” *J. Electrochem. Soc.*, vol. 132, no. 5, pp. 5–12, 1985.

[109] N. Omar, M. Daowd, P. Van Den Bossche, O. Hegazy, J. Smekens, T. Coosemans, and J. Van Mierlo, “Rechargeable Energy Storage Systems for Plug-in Hybrid Electric Vehicles—Assessment of Electrical Characteristics,” *Energies*, vol. 5, no. 12, pp. 2952–2988, Aug. 2012.

[110] N. Omar, M. Daowd, O. Hegazy, M. Al Sakka, T. Coosemans, P. Van den Bossche, and J. Van Mierlo, “Assessment of lithium-ion capacitor for using in battery electric vehicle and hybrid electric vehicle applications,” *Electrochim. Acta*, vol. 86, pp. 305–315, Dec. 2012.

[111] IEC, “IEC 61434: Secondary cells and batteries containing alkaline or other non-acid electrolytes - Guide to designation of current in alkaline secondary cell and battery standards,” 1996.

[112] V. Pop, H. J. Bergveld, P. H. L. Notten, J. H. G. Op het Veld, and P. P. L. Regtien, “Accuracy analysis of the State-of-Charge and remaining run-time determination for lithium-ion batteries,” *Measurement*, vol. 42, no. 8, pp. 1131–1138, Oct. 2009.

[113] M. Al Sakka, “Supercapacitors and DC/DC Converters for Fuel Cell Electric Vehicle,” Vrije Universiteit Brussel and Université de technologie de Belfort Montbeliard, 2010.

[114] M. Guo, G.-H. Kim, and R. E. White, “A three-dimensional multi-physics model for a Li-ion battery,” *J. Power Sources*, vol. 240, pp. 80–94, Oct. 2013.

[115] S. Tippmann, D. Walper, L. Balboa, B. Spier, and W. G. Bessler, “Low-temperature charging of lithium-ion cells part I: Electrochemical modeling and experimental

investigation of degradation behavior," *J. Power Sources*, vol. 252, pp. 305–316, Apr. 2014.

[116] X. Li, M. Xiao, and S.-Y. Choe, "Reduced order model (ROM) of a pouch type lithium polymer battery based on electrochemical thermal principles for real time applications," *Electrochim. Acta*, vol. 97, pp. 66–78, May 2013.

[117] L. H. Saw, Y. Ye, and a. a. O. Tay, "Electrochemical–thermal analysis of 18650 Lithium Iron Phosphate cell," *Energy Convers. Manag.*, vol. 75, pp. 162–174, Nov. 2013.

[118] L. H. Saw, K. Somasundaram, Y. Ye, and A. A. O. Tay, "Electro-thermal analysis of Lithium Iron Phosphate battery for electric vehicles," *J. Power Sources*, vol. 249, pp. 231–238, Mar. 2014.

[119] A. Samba, H. Louahlia-Gualous, S. Le Masson, and D. Nörterhäuser, "Two-phase thermosyphon loop for cooling outdoor telecommunication equipments," *Appl. Therm. Eng.*, vol. 50, no. 1, pp. 1351–1360, Jan. 2013.

[120] K. Somasundaram, E. Birgersson, and A. Sadashiv, "Thermal – electrochemical model for passive thermal management of a spiral-wound lithium-ion battery," *J. Power Sources*, vol. 203, pp. 84–96, 2012.

[121] J. Li, Y. Cheng, M. Jia, Y. Tang, Y. Lin, Z. Zhang, and Y. Liu, "An electrochemical–thermal model based on dynamic responses for lithium iron phosphate battery," *J. Power Sources*, vol. 255, pp. 130–143, Jun. 2014.

[122] K.-J. Lee, K. Smith, A. Pesaran, and G.-H. Kim, "Three dimensional thermal-, electrical-, and electrochemical-coupled model for cylindrical wound large format lithium-ion batteries," *J. Power Sources*, vol. 241, pp. 20–32, Nov. 2013.

[123] X. M. Xu and R. He, "Research on the heat dissipation performance of battery pack based on forced air cooling," *J. Power Sources*, vol. 240, pp. 33–41, Oct. 2013.

[124] H. Park, "A design of air flow configuration for cooling lithium ion battery in hybrid electric vehicles," *J. Power Sources*, vol. 239, pp. 30–36, Oct. 2013.

[125] Z. Rao and S. Wang, "A review of power battery thermal energy management," *Renew. Sustain. Energy Rev.*, Sep. 2011.

[126] F. He, X. Li, and L. Ma, "Combined experimental and numerical study of thermal management of battery module consisting of multiple Li-ion cells," *Int. J. Heat Mass Transf.*, vol. 72, pp. 622–629, May 2014.

[127] A. Tourani, P. White, and P. Ivey, "Analysis of electric and thermal behaviour of lithium-ion cells in realistic driving cycles," *J. Power Sources*, vol. 268, pp. 301–314, Dec. 2014.

[128] H. Park, "Numerical assessment of liquid cooling system for power electronics in fuel cell electric vehicles," *Int. J. Heat Mass Transf.*, vol. 73, pp. 511–520, Jun. 2014.

[129] Y. Huo, Z. Rao, X. Liu, and J. Zhao, "Investigation of power battery thermal management by using mini-channel cold plate," *Energy Convers. Manag.*, vol. 89, pp. 387–395, Jan. 2015.

[130] M. R. Giuliano, S. G. Advani, and A. K. Prasad, "Thermal analysis and management of lithium–titanate batteries," *J. Power Sources*, vol. 196, no. 15, pp. 6517–6524, Aug. 2011.

[131] A. Jarrett and I. Y. Kim, "Influence of operating conditions on the optimum design of electric vehicle battery cooling plates," *J. Power Sources*, Jul. 2013.

[132] R. Liu, J. Chen, J. Xun, K. Jiao, and Q. Du, "Numerical investigation of thermal behaviors in lithium-ion battery stack discharge," *Appl. Energy*, vol. 132, pp. 288–297, Nov. 2014.

[133] J. Xun, R. Liu, and K. Jiao, "Numerical and analytical modeling of lithium ion battery thermal behaviors with different cooling designs," *J. Power Sources*, vol. 233, pp. 47–61, Jul. 2013.

[134] T. M. Bandhauer and S. Garimella, "Passive, internal thermal management system for batteries using microscale liquid–vapor phase change," *Appl. Therm. Eng.*, vol. 61, no. 2, pp. 756–769, Nov. 2013.

[135] T. M. Bandhauer, "Electrochemical-Thermal Modeling and Microscale Phase Change for Passive Internal Thermal Management of Lithium Ion Batteries Electrochemical-Thermal Modeling and Microscale Phase Change for Passive Internal Thermal Management of Lithium Ion Batteries," no. December, 2011.

[136] R. Zhao, J. Gu, and J. Liu, "An experimental study of heat pipe thermal management system with wet cooling method for lithium ion batteries," *J. Power Sources*, vol. 273, pp. 1089–1097, Jan. 2015.

[137] Q. Wang, B. Jiang, Q. F. Xue, H. L. Sun, B. Li, H. M. Zou, and Y. Y. Yan, "Experimental investigation on EV battery cooling and heating by heat pipes," *Appl. Therm. Eng.*, Oct. 2014.

[138] T.-H. Tran, S. Harmand, B. Desmet, and S. Filangi, “Experimental investigation on the feasibility of heat pipe cooling for HEV/EV lithium-ion battery,” *Appl. Therm. Eng.*, vol. 63, no. 2, pp. 551–558, Feb. 2014.

[139] R. W. van Gils, D. Danilov, P. H. L. Notten, M. F. M. Speetjens, and H. Nijmeijer, “Battery thermal management by boiling heat-transfer,” *Energy Convers. Manag.*, vol. 79, pp. 9–17, Mar. 2014.

[140] N. Javani, I. Dincer, G. F. Naterer, and B. S. Yilbas, “Heat transfer and thermal management with PCMs in a Li-ion battery cell for electric vehicles,” *Int. J. Heat Mass Transf.*, vol. 72, pp. 690–703, May 2014.

[141] Y. Tian and C. Y. Zhao, “A numerical investigation of heat transfer in phase change materials (PCMs) embedded in porous metals,” *Energy*, vol. 36, no. 9, pp. 5539–5546, Sep. 2011.

[142] Z. Ling, Z. Zhang, G. Shi, X. Fang, L. Wang, X. Gao, Y. Fang, T. Xu, S. Wang, and X. Liu, “Review on thermal management systems using phase change materials for electronic components, Li-ion batteries and photovoltaic modules,” *Renew. Sustain. Energy Rev.*, vol. 31, pp. 427–438, Mar. 2014.

[143] S. Park and D. Jung, “Battery cell arrangement and heat transfer fluid effects on the parasitic power consumption and the cell temperature distribution in a hybrid electric vehicle,” *J. Power Sources*, vol. 227, pp. 191–198, Apr. 2013.

[144] Z. G. Qu, W. Q. Li, and W. Q. Tao, “Numerical model of the passive thermal management system for high-power lithium ion battery by using porous metal foam saturated with phase change material,” *Int. J. Hydrogen Energy*, vol. 39, no. 8, pp. 3904–3913, Mar. 2014.

[145] C. Y. Zhao, W. Lu, and Y. Tian, “Heat transfer enhancement for thermal energy storage using metal foams embedded within phase change materials (PCMs),” *Sol. Energy*, vol. 84, no. 8, pp. 1402–1412, Aug. 2010.

[146] S. S. Sundarram and W. Li, “The Effect of Pore Size and Porosity on Thermal Management Performance of Phase Change Material Infiltrated Microcellular Metal Foams,” *Appl. Therm. Eng.*, vol. 64, no. 1–2, pp. 147–154, Dec. 2013.

[147] M. M. Farid, A. M. Khudhair, S. A. K. Razack, and S. Al-Hallaj, “A review on phase change energy storage: materials and applications,” *Energy Convers. Manag.*, vol. 45, no. 9–10, pp. 1597–1615, Jun. 2004.

[148] J. R. Selman, S. Al Hallaj, I. Uchida, and Y. Hirano, “Cooperative research on safety fundamentals of lithium batteries,” *J. Power Sources*, vol. 97–98, pp. 726–732, Jul. 2001.

[149] A. Mills, M. Farid, J. R. Selman, and S. Al-Hallaj, “Thermal conductivity enhancement of phase change materials using a graphite matrix,” *Appl. Therm. Eng.*, vol. 26, no. 14–15, pp. 1652–1661, Oct. 2006.

[150] Z. Ling, J. Chen, X. Fang, Z. Zhang, T. Xu, X. Gao, and S. Wang, “Experimental and numerical investigation of the application of phase change materials in a simulative power batteries thermal management system,” *Appl. Energy*, vol. 121, pp. 104–113, May 2014.

[151] Comsol 4.4, “Pipe Flow Minicourse,” *Comsol Tutor. 4.4*, 2013.

[152] D. D. Joseph and B. H. Yang, “Friction factor correlations for laminar, transition and turbulent flow in smooth pipes,” *Phys. D Nonlinear Phenom.*, vol. 239, no. 14, pp. 1318–1328, Jul. 2010.

[153] F. E. Teruel, “Characterization of a porous medium employing numerical tools: Permeability and pressure-drop from Darcy to turbulence,” *Int. J. Heat Mass Transf.*, vol. 52, no. 25–26, pp. 5878–5888, Dec. 2009.

[154] S. W. Churchill, “Friction factor equations span all fluid-flow regimes,” *Chem. Eng.*, vol. 84, no. 24, p. 91, 1997.

[155] Incropera Frank P.; DeWitt David P.;, *Fundamentals of Heat and Mass Transfer (5th ed.)*, Wiley. Wiley, 2002, pp. 486–487.

[156] V. Gnielinski, “New Equations for Hat and Mass Transfer in Turbulent Pipe and Channel Flow,” *Int. Chem. Eng.*, vol. 16, p. 359, 1976.

[157] D. M. Stefanescu, *Science and engineering of casting solidification*, Springer. Springer, 2008.

[158] K. Peippo, P. Kauranen, and P. D. Lund, “A multicomponent PCM wall optimized for passive solar heating,” *Energy Build.*, vol. 17, no. 4, pp. 259–270, Jan. 1991.

[159] N. Donal A. and B. Adrian, *Convection in Porous Media*, Third. Springer, 2006, pp. 8–16.

[160] S. a. Khateeb, S. Amiruddin, M. Farid, J. R. Selman, and S. Al-Hallaj, “Thermal management of Li-ion battery with phase change material for electric scooters: experimental validation,” *J. Power Sources*, vol. 142, no. 1–2, pp. 345–353, Mar. 2005.

TITRE: Contribution à la modélisation et à la gestion thermique des Batteries Lithium -ion pour des Voitures Électriques

Résumé : L'avancée de la recherche sur les batteries a conduit à une utilisation massive des batteries Lithium-ion de grande capacité dans les véhicules électriques. De tels designs, en grand format, ont l'avantage de réduire le nombre de cellules interconnectées dans les packs de batteries. Dans les applications de transport, le temps de recharge des batteries constitue un frein au développement des véhicules électriques. L'augmentation du courant de charge peut soumettre à la batterie à des situations très critiques et peut ainsi entrainer une augmentation considérable de sa température. En long terme, ces phénomènes peuvent conduire à la réduction de sa durée de vie ainsi que ses performances et dans certains cas à l'emballement thermique. Afin d'éviter de telles situations, il est nécessaire d'optimiser la gestion thermique de manière à maintenir la batterie dans une gamme de températures de fonctionnement sûre. Ceci passe par la mise en place d'un modèle thermique capable de prédire la température d'une cellule et d'un pack de batterie à différentes conditions de fonctionnement et ensuite proposer différentes stratégies de refroidissements. Compte tenu de la forme et des dimensions du type de batterie utilisé (batterie « pouch ») un modèle électrothermique est développé afin de prédire la distribution de température de la cellule, ce modèle nécessite moins de paramètres d'entrée et possède une grande précision. En outre, un nouvel outil d'estimation des paramètres thermiques a été développé. Le comportement thermique de la batterie, soumise à des conditions de fonctionnements extrêmes, a été étudié avec ce modèle. De ces résultats, on remarque que la cellule de batterie présente une distribution thermique non-uniforme lorsque celle-ci est parcourue par des courants de grandes amplitudes. Ce constat nous amène à étudier le design des batteries de type « pouch » afin d'élire celle qui présente une distribution thermique et électrique plus uniformes. Pour se faire un modèle 3D électrochimique-thermique a été développé. Enfin, différentes stratégies de gestion thermique des batteries telles que: le refroidissement actif par liquide et passif utilisant un matériau à changement de phase (liquide-solide à changement de phase) incorporé dans une mousse d'aluminium, ont été étudiées puis comparées en appliquant un cycle de conduite, provenant d'un véhicule tout électrique de la gamme Peugeot. L'objectif principal est de réduire la complexité, le poids, le volume, le coût et également de maintenir à un haut niveau de sureté de fonctionnement du module de batterie.

Indexation rameau : Batteries, Lithium, Ion, modèle Mathématiques, thermique, électrochimie

---

TITLE: Battery electrical vehicles-Analysis of Thermal Modelling and Thermal Management

Abstract: Uitgebreid onderzoek naar Lithium-ion batterijen heeft een grootschalig gebruik van batterijen met een hoge capaciteit in Batterij Elektrische Voertuigen (BEVs) toegelaten. Dergelijke grote cellen hebben als voordeel dat het aantal cellen in een module en op pakket niveau kan verminderd worden. In tractie toepassingen, vormt een lange oplaadtijd een barrière voor het wijd gebruik van BEVs. Een stijging van de stroomgrootte kan de batterij onderwerpen aan gevaarlijke situaties en kan de batterijtemperatuur significant doen stijgen. Deze fenomenen reduceren de levensduur en performante van de batterij en in het slechtste geval kan oververhitting plaatsvinden. Om dit te vermijden is er nood aan een geoptimaliseerd warmtebeheer, zodat de batterij in haar veilig temperatuursbereik kan werken. Allereerst werd in dit proefschrift een tweedimensionaal elektrothermisch model ontwikkeld om de temperatuursdistributie over het oppervlak van de batterij te voorspellen. Dit model vereist minder input-parameters maar bereikt nog steeds een hoge nauwkeurigheid. Voorst werd het thermisch gedrag van de bestudeerde batterij onderzocht bij zowel verschillende omgevingscondities als bij schadelijk gebruik voor een beoordeling van de thermische stabiliteit. Rekening houdend met de grote temperatuursdistributie, is een geavanceerd driedimensionaal elektrochemisch thermisch model ontwikkeld om de impact van het cel design op de temperatuur-, spanning- en stroom-verdeling in te schatten. Het doel is een sterk niet-homogene distributie te vermijden. Het ontwikkeld model laat ons toe het cel design te optimaliseren om zo een zo hoog mogelijke levensduur en performante te garanderen. Tenslotte zijn verschillende warmtebeheer strategieën zoals vloeibare en passieve koeling gebruikmakend van *phase-changing materials* ingebed in een aluminium-foam (vloeistof-vaste fase verandering) onderzocht en grondig vergeleken door realistische BEV cycli op te leggen aan de batterij. Het voornaamste objectief van dit werk is een verlaging van de complexiteit, het gewicht, het volume en de kost zonder een hoge veiligheid van het batterijsysteem in het gedrang te brengen.

Trefwoorden: Batterijen, Lithium, Ion, Matematica model, Thermish, Elecktrochemie

Adresse : LUSAC, 60 rue Max Pol Fouchet, CS 20082, 50130 Cherbourg-Octeville